University of California
Santa Barbara

Quantum Simulation of Strongly-Driven Systems Using Ultracold Lithium and Strontium

A dissertation submitted in partial satisfaction
of the requirements for the degree

Doctor of Philosophy
in
Physics

by

Ruwan Senaratne

Committee in charge:

Professor David Weld, Chair
Professor Ania Jayich
Professor Andreas Ludwig

June 2018

The Dissertation of Ruwan Senaratne is approved.

Professor Ania Jayich

Professor Andreas Ludwig

Professor David Weld, Committee Chair

June 2018

Quantum Simulation of Strongly-Driven Systems Using Ultracold Lithium and Strontium

by

Ruwan Senaratne

To my father, my inspiration,

to my mother, my motivation,

&

to those who sacrificed their lives for peace in Sri Lanka.

Acknowledgements

It is impossible to finish a graduate education without having a long list of people to thank. Throughout my graduate school experience, I have looked forward to this small soap-box upon which I may briefly stand and proclaim my gratitude to all the people who have made my achievements possible. However, now that the time comes to write these acknowledgements, I find it difficult. I fear that I may not do justice to all that people have done for me, and worse, that I may forget to mention some people. I apologize in advance for both oversights.

Being a member of the Weld Lab has been the defining feature of my existence over the past six-plus years. During this time, the group has gone through much change. Starting from David, Zach, a few undergraduates, a computer and a temporary lab-space, the group has grown large, and now runs experiments on two ultracold gas apparatus. None of this would have been possible if it were not for David's vision and leadership, but most fundamentally, his love of science. David has the great attribute of being very knowledgeable and creative while remaining humble and frank about what he does not understand. He taught me to speak with precision, and what zinc does not smell like. He did not bat an eye when I laid out my break-neck plan to graduate, and proof-read this dissertation in one sleep-deprived night between DAMOP and my defense. It has been an honor to learn from him and to learn with him. Science needs more people like David.

One of David's greatest achievements was assembling the collection of graduate students that would form the heart of the Weld Lab. I have spent more time with Zach, Shankari, Kurt and Kevin than anyone who is not in my family, and it shows. Other graduate students in our department have at times likened us to a cult, but this is only because *they jelly*. Zach was our leader due to reasons of history and height, and he did

more to shape the culture in our office and lab than anyone else. Zach taught me the value in doing things the right way, and how to roast a pig. He welcomed me into his family and his state, and the Geigers became one of my families-away-from-family. He would almost always put up with my shenanigans and was my go-to partner-in-crime, and for that I am ever grateful to him.

Shankari brought with her the intensity we needed to succeed in laid-back Santa Barbara. Her drive and conviction put the rest of us to shame, and made us all better. She bought-in to the culture that Zach had created, and thereby ensured its longevity. Shankari and I have worked together on two machines and seven bakes, and we have seen it all together. She and I together negotiated the throes of younger-sibling malaise on the strontium-side of the lab. She taught me the value of just getting things done, no matter how much time, effort and sleeplessness it takes. She put up with having to sit next to me and to listen to whatever cynical nonsense I was spouting at the time for several years. None of the scientific results we achieved on the strontium machine would have been possible without her.

Kurt has made his impact felt ever since he *kurted* his way into the lab. His radiance and enthusiasm kept Zach and I going when we were in the doldrums of magnet-winding. He graciously allowed us to insert his name into almost every song written. He was even not that angry at me at having to deal with the consequences of the infamous Ultra-Mag-Trap word. He is a very deep thinker, and I have learned that whenever you disagree with him, that probably means you're wrong. His mastery of electronics and of MATLAB kept me out of the D. L. and the source code, for which I am very grateful.

Kevin was all-in from day one, and even though he may not still think of us senior grad students as demi-gods, his admiration of us and our work was most appreciated. His willingness to cut optical pathways between the lines got the job done, and he has made a *massive* contribution to the group. Over my last couple of quarters working day-to-day

on the lithium machine, he taught me to never train someone who his taller, fitter and browner (questionable) than you are to do your job. Though he has since switched to Instagram, he introduced me to Snapchat and was instrumental in its adoption as the data-recording platform of choice for the group. I will miss the sophomoric banter we shared on the left-side.

Apart from this core-group of graduate students with whom I worked for the majority of my graduate education, two post-docs, a few younger graduate students, and many undergraduates and volunteer researchers made important contributions to our group. Slava was our first post-doc, and he was incredibly valuable as the only person in the group other than David who had experience working with ultracold atoms at the time. He introduced me to a different perspective on our field and taught me that it is okay to disagree with David sometimes. Some of his contributions to the lab have made it through the annealing of several years.

Toshi, our second and current post-doc, has brought with him equanimity and an immense arsenal of technical skills and nth-hand equipment purchased on eBay. His patience and methodical consideration of issues-at-hand has been critical in the scientific push on each machine. His love of molecules and efficiency are impressive. He has a way of melting away your stress as he groans and corrects your Japanese pronunciation. He and I have shared many late-night dinners, and both his proof-reading and his construction of a trance playlist were crucial in the writing of this dissertation.

Peter, Misha and Quinn, our junior graduate students, have made many contributions to the lab while juggling coursework and teaching responsibilities. Bryance and Eric, two graduate students who worked in our lab for a time, also made substantial contributions. I admire Peter's ability to respond to all of the teasing he gets from the older members of the lab with a smile, and Misha's love of atomic physics. While I have not had the chance to work with Quinn closely, I have confidence that he has what it takes to

be a great experimentalist. I very much look forward to hearing about their scientific accomplishments over the next few years. A whole army of undergraduates and volunteer researchers worked in our lab, and I cannot attempt to name them all without risking leaving someone out. It was a pleasure to help mentor them, and some of them became close friends. Many of them have gone on to graduate school in AMO physics, and I am sure they will continue to succeed.

Many members of the Physics Department and the California NanoSystems Institute have helped me over the years. Jennifer Farrar, Mike Deal, Dave Prine, Dan Stack, Erin Ferguson, Jean Dill, Glenn Schiferl, Rick Barber, Jeff Dutter, Guy Patterson, Mark Scheckherd, Doug Rehn, Andy Segale, Holly Woo, Daniel Daniels, Lynne Leininger, Sonya Alvarado and Jess Henry have all made my life easier and helped make this work possible. I would like to thank all of the professors from whom I took classes and for whom I taught. In particular I would like to thank my committee members, Professors Ania Jayich and Andreas Ludwig, both of whom I had the pleasure of teaching for, for their mentorship over the years. I would also like to thank Professor Andrew Jayich for many fruitful discussions over the past couple of years, and for being generous with time and advice. Professor Dave Cannell was very generous in allowing us to use his lab-space, and we inherited many pieces of equipment from his lab, including the optical table that is now the strontium laser table. I deeply appreciate the Martinis and Mazin Groups' generosity in regularly lending us their leak checker, the Sherwin Group's generosity in loaning us a 405 nm ECDL, and the Young Group's generosity in loaning us the piezo-driver that we use for the phason experiment.

Although work consumes most of your life during graduate school, it is important to make the most of the free-time you do have. During my time in Santa Barbara I met many wonderful people with whom to spend my precious free-time. For five rip-roaring years I lived in Kaiser House with several people, including, at various times, Paul,

Kaushal, Ben, Mark, Eric, Amit, James and Josh. Thank you for being good friends and housemates, and for putting up with everything. We had some good times. For many years I would have a standing lunch date during the work-week with several people, including Hunter, Jessica, Darren, Blake and Lucas. Thank you for the conversation, and for waiting for my food to arrive before starting to eat. I have had many great experiences with Bill, Brayden, Teddy, Charlie, Laura, Christina, Ram, Sean and Devon. Thank you to everyone who came to Kaiser when we needed a fourth. A common feature of all of my years in grad school has been trivia, whether at Woodstock's, Draughtsmen or Old King's Road. Thank you James, Will and Tim for many enjoyable hours of quizzing, and thank you to all the people who played trivia with me at some point over the years. Additionally, thank you to all of my friends from far and wide who came to visit me in Santa Barbara, including friends from school in Sri Lanka, and friends from college.

People who know me will say that I care about few things more than cricket. Being a fan of Sri Lankan cricket has taken me through good times and bad, and I spent many sleepless nights during grad school following test matches in Asia. My first visit to Santa Barbara was the day after Sri Lanka's defeat in the 2011 World Cup Final, and it is a testament to the beauty of this town that I managed to enjoy that visit at all. High points in grad school include the 2014 World Twenty20 victory, the 2014 series win in England, and the 2016 whitewash of Australia at home. I also played cricket with many people in Santa Barbara and in Los Angeles over the course of the past seven years. Often my partner-in-cricketing-crime was Amit, who would keep me going despite my workload and general laziness. I managed to convince several of my American friends to play and watch cricket with me, and to them I am thankful.

Lastly, and most importantly, I would like to thank my family. My parents have molded their lives around my existence for my entire existence. My sister and I were born while they were graduate students, a challenge that I cannot begin to contemplate.

They did this so that my sister and I would be US citizens, and this act has made my life and education in this country over the past eleven years possible. Later in life they brought me home, where I learned to become a Sri Lankan, to drink tea and to breath cricket. To make this possible, my father had to live apart from us in Saudi Arabia, and my mother had to give up her scientific career. For these sacrifices, and innumerable other things, I am forever grateful. My sister has been my best-friend for my entire life. As we moved around the globe as children, she and I had each other. She has always been there ahead of me, a trailblazer clearing the path for me. I would not be where I am today if it were not for her.

Curriculum Vitæ

Ruwan Senaratne

Education

2018	Ph.D. in Physics (Expected), University of California, Santa Barbara.
2014	M.A. in Physics, University of California, Santa Barbara.
2011	A.B. in Physics and Mathematics, Harvard College.

Publications

R. Senaratne, S. V. Rajagopal, T. Shimasaki, P. E. Dotti, K. M. Fujiwara, K. Singh, Z. A. Geiger, D. M. Weld. *Quantum simulation of ultrafast dynamics using trapped ultracold atoms*. Nat. Comm. **9**, 2065 (2018).

Z. A. Geiger, K. M. Fujiwara, K. Singh, **R. Senaratne**, S. V. Rajagopal, M. Lipatov, T. Shimasaki, R. Driben, V. V. Konotop, T. Meier, D. M. Weld. *Observation and uses of position-space Bloch oscillations in an ultracold gas*. Phys. Rev. Lett. **120**, 213201 (2018).

K. M. Fujiwara, Z. A. Geiger, K. Singh, **R. Senaratne**, S. V. Rajagopal, M. Lipatov, T. Shimasaki, D. M. Weld, *Experimental Realization of a Relativistic Harmonic Oscillator*, arXiv 1712.09501 (2017).

S. V. Rajagopal, K. M. Fujiwara, **R. Senaratne**, K. Singh, Z. A. Geiger, and D. M. Weld, *Quantum Emulation of Extreme Non-Equilibrium Phenomena with Trapped Atoms*, Ann. Phys. **529**,1700008 (2017).

R. Senaratne, S. V. Rajagopal, Z. A. Geiger, K. M. Fujiwara, V. Lebedev, and D.M. Weld, *Effusive atomic oven nozzle design using an aligned micrcapillary array*, Rev. Sci. Instrum. **86**, 023105 (2015).

Abstract

Quantum Simulation of Strongly-Driven Systems Using Ultracold Lithium and Strontium

by

Ruwan Senaratne

Weakly-interacting atoms in a Bose-Einstein condensate coherently occupy the ground-state of their container. This phenomenon, coupled with the technical ability to produce precise, isolated and dynamically-tunable trapping potentials, makes ultracold atoms a versatile platform for simulating quantum mechanical systems. This thesis details the construction of two apparatus at the University of California, Santa Barbara for the production of Bose-Einstein condensates of lithium and strontium atoms respectively. Results of the first experiment performed on the strontium apparatus, a quantum simulation of ultrafast dynamics, are presented. In this experiment, driven cold atoms simulate ultrafast ionization dynamics in attosecond laser pulses, counter-intuitively emulating some of the fastest processes in atomic physics with some of the slowest. A sequence of experiments which demonstrate the correspondence with ultrafast science are described, including the direct observation of carrier-envelope-phase dependent sub-cycle unbinding dynamics. Preliminary results from a second experiment, studying phasonic excitations in a quasiperiodic lattice, are also discussed.

Contents

Chapter 1

Introduction

Atoms are fundamental to both human experience and to the development of quantum mechanics. Spectroscopic measurements of the discrete energy levels in atoms were one of the main motivations behind the development of the theory. The successful calculation of the spacings of the energy levels in a hydrogen atom is why we continue to study quantum mechanics one hundred years later. Thus it should perhaps not be surprising that to this day atoms provide the most simple and precise realizations of the theory that was developed to study them. The quantum theory was later extended to treat not only the internal structure of atoms, but also their interactions with each other - both in the few-body and many-body regimes. Experimentally, however, such study hinged upon the ability to produce and probe cold atomic gases, as the effects predicted by the quantum theory are energetically suppressed at human, or even cryogenic, temperatures. The development of the laser in the 1960s [1] and the advent of laser cooling allowed for the production of such gases, and the 1980s and 1990s led to a new era in experimental atomic physics [2, 3, 4]. The crowning achievement of this drive was the production of Bose-Einstein condensates (BECs) in dilute gases of bosonic alkali atoms in 1995 [5, 6]. The defining feature of such condensates is the macroscopic occupation of a single

quantum state, making them exquisite test subjects for quantum mechanics. In a highly productive few years, experimentalists were able to observe few-body processes such as Feshbach resonances [7], as well as many-body phenomena, such as collective excitations [8, 9]. Yet again, atoms, and the magnetic and optical traps that were used to contain them, showcased their utility in producing clean quantum mechanical systems.

1.1 Quantum simulation using ultracold atoms

A paradigm shift in ultracold atomic physics ocurred in 2001, with the experimental observation of a quantum phase transition predicted to exist in a condensed matter system - the superfluid to Mott insulator transition [10]. In this experiment, the cleanliness, isolation and tunabiliy of ultracold atomic systems were harnessed to emulate the Hubbard model - a system of chargeless interacting bosons in a periodic potential. Thus the field of quantum simulation using ultracold atoms was born. Experimental atomic physicists were now no longer limited to studying systems of atoms, but now could hope to use cold atoms to study other systems. In certain theoretical systems - such as those involving interactions or fermionic statistics - cold atoms presented a pathway to simulating systems that are computationally intractable for reasonable system sizes. Due to the relative ease of producing spatially periodic potentials, much of the work in cold atom quantum simulation focused on condensed matter systems. In such experiments, the atoms emulate the electrons in a solid, while an optical lattice emulates the periodic crystalline potential. Such experiments were, and continue to be, very successful, despite the atoms being used in many cases being neutral bosons and the potentials being sinusoidal rather than periodicically spaced Coulomb potentials[11, 12, 13]. A major focus for many cold atom groups is the production of magnetic ground states of varations of the Hubbard model [14, 15, 16]. One of the main challenges faced by these groups is the

difficulty in producing samples of cold atoms with low enough temperature and entropy to make such ground states accessible.

1.2 Time-dependent and non-equilibrium systems

There has been much recent theoretical and experimental interest in non-equilibrium, driven and infinite-temperature systems [17, 18]. The non-equilibrium or, in the case of periodic driving, Floquet physics is rich in complexity and has suffered a dearth of experimental realizations, due to the difficulty in dynamically tuning the Hamiltonian of a solid state system, and the inaccessibility of relevant timescales. This relatively unexplored avenue for quantum simulation was our first target for quantum simulation experiments in the Weld Lab. In an effort that consumed the majority of my graduate school experience, we constructed two cold atom machines; one using lithium atoms, and the other using strontium atoms. With the lithium experiment, we aimed to study non-equilibrium dynamics in a cold atom realization of the Kapitza pendulum [19], as well as explore the prospects of Floquet engineering the bandstructure of a periodically driven optical lattice [20]. Using the strontium experiment, we aimed to use cold atoms to study the physics of electrons bound to atoms or molecules that experience a strong time-varying electric field, such as those experienced during a laser pulse. This would represent an almost completely new sub-field for quantum emulation using cold atoms [21, 22, 23, 24]. In addition to such strong-field physics emulations, we planned to study the dynamics of quasiperiodic systems, which have remained relatively inaccessible to calculation and to solid-state experiments.

1.3 Dissertation overview

In this dissertation I will discuss the work I performed in the construction of our two BEC machines, as well as the results from experiments that I performed in conjuction with others on the strontium machine. In Chapter 2 I will discuss some basic atomic physics, atom cooling and trapping, and Bose-Einstein condensation. In Chapters 3 and 4, I will present the relevant atomic properties of ^{7}Li and ^{84}Sr and the cooling trajectories we use to bring these atoms to quantum degeneracy. In Chapters 5 and 6 I will discuss the design and construction of the two experiments. Chapter 7 is largely a reproduction of the paper "Quantum simulation of ultrafast dynamics using trapped ultracold atoms" published in *Nature Communications*, which discusses the results of the first experiment we ran on the Sr apparatus. Chapter 8 discusses our current efforts on studying phasonic excitations in a quasiperiodic lattice, as well as other research goals on the Sr experiment. Appendix A contains a reproduction of the paper entitled "Effusive atomic oven nozzle design using an aligned microcapillary array" published in *Review of Scientific Instruments*. Appendix B contains details on our vacuum procedures, Appendix C contains a list of useful tips and Appendix D contains some drawings of custom parts used in the two experiments.

1.4 Permissions and Attributions

Much of the content of this dissertation is heavily influenced by *Atomic Physics* by Christopher Foot [25] and *Advances in Atomic Physics* by Claude Cohen-Tannoudji and David Guery-Odelin [26]. Florian Schreck's and Simon Stellmer's theses were particularly useful in our pushes for Li and Sr BECs respectively, and in the writing of this dissertation [27, 28]. Many experimental details for the Li experiment were found in Zachary Geiger's

dissertation [29].

1. The content of chapter 7 is the result of a collaboration with Shankari V. Rajagopal, Toshihiko Shimasaki, Peter E. Dotti, Kurt M. Fujiwara, Kevin Singh, Zachary A. Geiger and David M. Weld, and has previously appeared in *Nature Communications* [30]. It is reproduced here with the permission of SpringerNature: `http://nature.com/reprints/permission-requests.html`.

2. The content of Appendix A is the result of a collaboration with Shankari V. Rajagopal, Zachary A. Geiger, Kurt M. Fujiwara, Vyacheslav Lebedev and David M. Weld, and has previously appeared *Review of Scientific Instruments* [31]. It is reproduced here with the permission of AIP Publishing: `http://publishing.aip.org/authors/copyright-reuse`.

Chapter 2

Theory

In order to perform quantum simulation experiments using atoms, one must be able to cool atoms to temperatures at which quantum effects dominate, control their internal degrees of freedom, apply potentials to the atoms as desired and detect their final state. An understanding of atomic level structure, as well as atomic interactions with D.C. magnetic fields, on-resonant and off-resonant electromagnetic fields, and other atoms, is necessary to achieve all of these objectives. Furthermore, Bose-Einstein condensation has become a weapon in the experimentalist's armory, used to produce samples of atomic gases in a near-single quantum state. Thus it is necessary to understand the statistical mechanics behind Bose-Einstein condensation, as well as the framework of spontaneous symmetry breaking that predicts the existence of the superfluid state.

2.1 Atomic physics in a nutshell

The theory of atoms is at once old and new. The idea that matter is made up of fundamental blocks is over two thousand years old, and was present in Greece and India [32]. However, atoms only came into vogue in modern science in the early 19th century,

when John Dalton postulated that matter must be exist in discrete packets due to the stoichiometry of chemical reactions. This atomic theory was later supported by Robert Brown's observation of the random walks undergone by pollen particles in air. However, it was not until Einstein's *annus mirabilis* that a statistical mechanical description of Brownian motion was developed [33]. Further experimentation by Jean Perrin confirmed this description [34], finally ending the debate on the discrete nature of matter, for which, in part, he was awarded the Nobel Prize in Physics in 1926. It is stunning how recent the conclusion of this debate is, particularly given that there is perhaps no concept in science that so thoroughly permeates human thought than atomism.

2.1.1 Level structure

Electrons in atoms occupy discrete energy levels due to the boundary condition implied by an attractive Coulomb potential (that the amplitude of the wave function must go to zero at infinity). For a single spin-less non-relativistic electron system, the solutions to the radial part of the Schrödinger equation (which in this case is separable) are Laguerre polynomials, which are enumerated by a positive integer, n, known as the principal quantum number, which specifies the energy of the electron. The solutions to the angular part of the Schrödinger equation are also necessarily discrete (due to the periodic boundary condition for angular displacement), and are the spherical harmonics, which are eigenstates of the $\mathbf{L^2}$ and the $\mathbf{L_z}$ operators, where $\vec{\mathbf{L}} = \vec{\mathbf{r}} \times \vec{\mathbf{p}}$ is the orbital angular momentum operator. The spherical harmonics are enumerated by a non-negative integer L, which is the orbital angular momentum quantum number, and an integer $|m_L| < L$, which is the magnetic quantum number and represents the projection of the orbital angular momentum along the $\hat{z}$-axis. Since electrons also carry intrinstic spin angular momentum (denoted $\vec{\mathbf{S}}$), it is convenient to define $\vec{\mathbf{J}} = \vec{\mathbf{L}} + \vec{\mathbf{S}}$, where $\vec{\mathbf{L}}$ and $\vec{\mathbf{S}}$

indicate sums over all valence electrons, if necessary. Atomic physicists commonly use the Russell-Saunders notation to denote the angular momentum state of such valence electrons, in the form ${}^{2S+1}L_J$, where L is denoted by the first letter of the historical names sharp, principle, diffuse or fine ($L = 0$, 1, 2 and 3 respectively). Further, for cases where the total nuclear spin $\vec{\mathbf{I}}$ is non-zero, it is common to define $\vec{\mathbf{F}} = \vec{\mathbf{I}} + \vec{\mathbf{J}}$, the total angular momentum, and specify the eigenvalue of its square.

In order to calculate the energies of these states, one must take into account several effects, which collectively create what is known as fine structure in the energy spectrum of atoms. The energetically largest effects are due to taking into consideration the relativistic form of the kinetic energy of the electron. Another relativistic effect, namely that the electron experiences an effective magnetic field as its travels relativistically through the electric field of the nucleus, is known as spin-orbit coupling, as this term can be expressed as being proportional to $\vec{\mathbf{L}} \cdot \vec{\mathbf{S}}$ (the constant of proportionality depends on the radial part of the wave function). A third significant relativistic effect which is implied by the Dirac equation is the Darwin term[1], which is proportional to a δ-function at the origin. Since only the $L = 0$ spherical harmonic has non-zero value at the origin this term only affects the energies of S-orbital electrons. Together, these three effects serve to break the degeneracy between electrons of equal n but differing J[2].

For atoms with nuclear spin, there are further shifts in the energy levels which result in what is known as hyperfine structure. This is due to an interaction of the magnetic moment of the nucleus with the magnetic field created by the electron. Since the magnetic moment of a nucleon is three orders of magnitude smaller than that of an electron, this effect is smaller than that of the spin-orbit coupling. However, it is sufficient to lift the degeneracy between states of equal L and S but differing F.

[1] Due to Charles Darwin, grandson of a noted naturalist.

[2] A relatively small effect known as the Lamb shift, due to vacuum fluctuations modelled by quantum electrodynamics, further breaks the degeneracy between S and P orbital electrons with equal J.

The picture is further complicated by the addition of more electrons to the atom. The presence of complete inner shells of electrons (i.e. orbitals to which no further electrons may be added due to Pauli exclusion) serves to break the degeneracy between electrons of equal n and J, but differing L. This variation of the energies of different orbitals is known as the quantum defect[3], and is a much larger effect than fine structure, particularly for lighter atoms with fewer closed shells. For atoms with multiple valence electrons, one must perform degenerate perturbation theory in order to calculate the energy differences between electronic configurations that have equal n and L but differing S. For two-valence electron atoms such as alkaline-earths, the electronic structure can be separated into two ostensibly disjoint substructures with different values of S (0 and 1). This can be viewed as a result of the fact that the Hamiltonian features SU(2) $\otimes$ SU(2) symmetry. Therefore the Hilbert space must decompose into a direct sum of subspaces associated with irreducible representations of SU(2) - in this case the one-dimensional[4] and three-dimensional[5] representations. Electron states with spin 0 are known as singlet states, and electron states with spin 1 are known as triplet states.

2.1.2 Zeeman shift

The energy levels of an atom may be altered by its environment. An applied DC magnetic field shifts the energy levels, and is known as the Zeeman effect. The magnitude and sign of the effect is dependent on the eigenvalues of the J_z operator (or F_z for atoms with non-zero nuclear spin). Due to this reason, these m_J or m_F states are often known as Zeeman sub-levels. For atoms with no nuclear spin, the magnetic moment of the

[3]Thusly known as it is well-modeled for alkalis by using an effective principle quantum number in Bohr's formula for the energy levels of hydrogen atoms.

[4]The one-dimensional representation of SU(2) is unsurprisingly trivial (since SU(2) is non-abelian), and are associated with operators that act on spin 0 vectors in Hilbert space.

[5]The three-dimensional representation of SU(2) is a three-dimensional generalization of the Pauli matrices (which form the two-dimensional and defining representation of SU(2) and are used to represent spin $\frac{1}{2}$ operators) and is associated with operators that act on spin 1 vectors in Hilbert space.

valence electrons is given by

$$\vec{\boldsymbol{\mu}} = -\frac{g_L \mu_{\mathrm{B}}}{\hbar}\vec{\mathbf{L}} - \frac{g_S \mu_B}{\hbar}\vec{\mathbf{S}}, \tag{2.1}$$

where μ_{B} is the Bohr magneton, $g_L \approx 1$ is the electron orbital g-factor and $g_S \approx 2$ is the electron spin g-factor. In the regime where the energy of the Zeeman shift is smaller than the energy of the spin-orbit coupling, the Zeeman perturbation can be expressed in terms of $\vec{\mathbf{J}}$, and the energy of the perturbation to first order[6] can be expressed in terms of L, S, J and m_J, as

$$E_{\mathrm{Zeeman}} = g_J m_J \mu_{\mathrm{B}} B = \left(\frac{3}{2} + \frac{S(S+1) - L(L+1)}{2J(J+1)}\right) m_J \mu_B B, \tag{2.2}$$

where g_J is known as the Landé g-factor, and the magnetic field has magnitude B and is assumed to point along the $\hat{z}$-axis. Atoms in states for which the product $g_J m_J$ is positive are attracted to regions of low magnetic field, whereas atoms in states for which it is negative are attracted to regions of high magnetic field. The $m_J = 0$ states have no Zeeman shift to first order. For atoms with non-zero nuclear spin, I, the Zeeman shift is similarly given by

$$E_{\mathrm{Zeeman}} = g_F m_F \mu_{\mathrm{B}} B, \tag{2.3}$$

where

$$g_F = g_J \frac{F(F+1) - I(I+1) + J(J+1)}{2F(F+1)} + g_I \frac{F(F+1) + I(I+1) - J(J+1)}{2F(F+1)}. \tag{2.4}$$

Since $g_I/g_J = m_e/m_p$ the second term can be ignored in most cases.

In the high magnetic field regime where the Zeeman shift cannot be treated as a per-

[6]This can be carried out to higher orders. To second order, the result is known as the quadratic Zeeman shift.

turbation to the spin-orbit coupling[7], the spin and orbital angular momenta are effectively decoupled, and contribute to the Zeeman energy separately.

2.1.3 Atom-photon interactions

At the heart of any atomic physics lab is the atom-photon interaction. Resonant interactions allow us to slow, cool, optically pump and image atoms, while non-resonant interactions are used for trapping and are the only means of producing periodic potentials on the length scales required for quantum simulation experiments. A semi-classical theory (one that treats the atom quantum mechanically but treats the perturbing light as a classical oscillating electric field) is very successful at modelling all the relevant phenomena for a sufficiently two-level system through time-dependent perturbation theory, though spontaneous emission must be introduced by hand as a decay mechanism. For a linearly polarized, monochromatic oscillating electric field, the perturbing Hamiltonian is given by

$$H_{\mathrm{E}}(t) = e\,\vec{\mathbf{r}} \cdot \vec{\mathbf{E_0}} \cos(\omega t) = e\,\mathrm{E}_0\, z\, \cos(\omega t), \tag{2.5}$$

where $e\,\vec{\mathbf{r}}$ is the electric dipole operator for an electron at a location $\vec{\mathbf{r}}$. Further assuming that the unperturbed ground state $|1\rangle$ has normalized population $|c_1|^2$ and the unperturbed excited state $|2\rangle$ has normalized population $|c_2|^2$, one can derive the rates of change of the population of the two states by substitution into the time-dependent

[7] Known as the Paschen-Back regime.

Schrödinger equation, which gives

$$\begin{aligned} \dot{c_1} &= -\mathrm{i}\,\frac{\Omega}{2}\,c_2\,\mathrm{e}^{\mathrm{i}\delta t} \\ \dot{c_2} &= -\mathrm{i}\,\frac{\Omega}{2}\,c_1\,\mathrm{e}^{-\mathrm{i}\delta t}, \end{aligned} \tag{2.6}$$

where

$$\begin{aligned} \delta &= \omega - \omega_0 \\ \Omega &= \frac{1}{\hbar}\,\langle 1|\,e\,\mathrm{E}_0\,z\,|2\rangle\,. \end{aligned} \tag{2.7}$$

Here ω_0 is the resonant frequency given by the energy splitting between the two states and Ω is known as the Rabi frequency. Note that we have made the so-called rotating wave approximation, and discarded terms proportional to $\mathrm{e}^{\mathrm{i}\,(\omega+\omega_0)\,t}$ or $\mathrm{e}^{-\mathrm{i}\,(\omega+\omega_0)\,t}$, as they oscillate with a period much shorter than any relevant timescale. The two first-order differential equations in equation 2.6 can be combined to give one second-order differential equation, which can be solved to give the time dependence of the populations of the two levels. Assuming the initial condition of $|c_1(0)|^2 = 1$, the excited state normalized population is given by

$$|c_2(t)|^2 = \frac{\Omega^2}{\Omega^2+\delta^2}\sin^2\Big(\frac{\sqrt{\Omega^2+\delta^2}\,t}{2}\Big). \tag{2.8}$$

These oscillations in population between the ground and excited states are known as Rabi oscillations, and at zero detuning they occur at the Rabi frequency. These perfect, coherent oscillations are disturbed and ultimately destroyed upon the addition of spontaneous emission, which can be added in by hand as a population-proportional damping term on the rate of change of the excited state population. The constant of

proportionality in this damping term is given by $\Gamma = \frac{1}{\tau} = (2\,\pi) \times \gamma$, where τ is the lifetime of the excited state, and γ is the linewidth of the transition between the two states. For interrogation times that are long compared to τ, the excited state normalized population reaches a steady state value, which is given by

$$P_2 = \lim_{\tau/t \to 0} |c_2(t)|^2 = \frac{\Omega^2/4}{\delta^2 + \Omega^2/2 + \Gamma^2/4} = \frac{1}{2} \frac{I/I_{\rm sat}}{1 + I/I_{\rm sat} + 4\delta^2/\Gamma^2}, \tag{2.9}$$

where I is the laser intensity and $I_{\rm sat}$ is the saturation intensity, which is given by

$$\begin{aligned} \frac{I}{I_{\rm sat}} &= \frac{2\Omega^2}{\Gamma^2} \\ I_{\rm sat} &= \frac{\hbar \omega_0^3\, \Gamma}{12 \pi c^2} = \frac{\pi h c\, \Gamma}{3\lambda^3}. \end{aligned} \tag{2.10}$$

In the limit of low light intensity, where photons emitted through stimulated emission events can be ignored, the scattering rate of incident photons is equal to the rate of spontaneous emission events, due to conservation of energy in the above long-time limit. Therefore the absorption rate in this regime is given by

$$R_{\rm abs} = \Gamma\, P_2 = \frac{\Gamma}{2}\, \frac{I/I_{\rm sat}}{1 + I/I_{\rm sat} + 4\delta^2/\Gamma^2}. \tag{2.11}$$

This absorption profile is a Lorentzian with a full-width at half-maximum of $2\Gamma_{\rm PB}$, where

$$\Gamma_{\rm PB} = \Gamma \left(1 + \frac{I}{I_{\rm sat}}\right), \tag{2.12}$$

and is known as the power-broadened linewidth.

This process of resonant scattering of photons is used remove momentum from atoms during laser cooling, and the absorption of resonant photons and the flourescence of spontaneously emitting atoms are both used to image and count atoms. Of course no

atom is a truly two-level system. For most atoms, the presence of other states means that there is no closed or approximately closed cycling transition which can be used for laser cooling. Furthermore, for atoms such as the alkalis and certain two-valence electron atoms, which have reasonably-cycling transitions, degeneracies in either the ground or excited state or both complicate the picture painted above. In these cases atom-photon interactions are used to control the internal states of atoms, as the polarization of the incident photon determines what angular momentum can be delivered to the atom, and thus which state the electron will be excited to. Circularly polarized light that is right-handed with respect to the quantization axis (in practice an applied magnetic field) is said to have σ^+ polarization, and an electron that is excited with such a photon gains one unit of angular momentum (i.e. m_J increases by one unit). Conversely, circularly polarized light that is left-handed with respect to the quantization axis is said to have σ^- polarization, and an electron that is excited with such a photon loses one unit of angular momentum. Light that is linearly polarized with respect to the quantization axis is said to be π polarized, and imparts no angular momentum on an excited electron. The absorption rate of photons is dependent on the polarization of the light, as it determines to which state(s) an electron can be excited. The application of σ^+-polarized light on a $J \rightarrow J' = J + 1$ transition transfers the population of atoms to the ground state with largest m_J, and the application of σ^--polarized light transfers the population of atoms t that with lowest m_J. This process is known as optical pumping, and these states with extremal values of $|m_J|$ are known as stretched states.

2.1.4 AC Stark shift

As mentioned in the previous section, non-resonant interactions between atoms and photons are also widely used in atomic physics laboratories. In addition to the Zeeman

shift, the AC Stark shift is used to externally alter the internal energy levels of an atom. The DC Stark shift is observed when an atom experiences an electric field that is constant in time. The AC Stark shift refers to energy level shifts that occur in the presence of a rapidly oscillating electric field, such as that experienced in electromagnetic radiation. The AC effect is qualitatively different to the DC effect, in that the sign of the effect is dependent on the frequency of the oscillation of the electric field.

One can treat the AC Stark shift as a time-independent second-order perturbation of strength $\hbar\Omega$ on the excited state and the dressed ground state, which has an energy of the ground state energy plus the energy of one drive photon ($\hbar\omega$). The energy splitting of these two states is thus $\hbar\delta$ and the time-independent Schrödinger equation for such a system reads

$$\hbar \begin{pmatrix} \delta/2 & \Omega/2 \\ \Omega/2 & -\delta/2 \end{pmatrix} \begin{pmatrix} \psi_{\mathrm{D}} \\ \psi_2 \end{pmatrix} = E \begin{pmatrix} \psi_{\mathrm{D}} \\ \psi_2, \end{pmatrix} \tag{2.13}$$

where ψ_{D} is the dressed ground state and ψ_2 is the excited state. Solving for the eigenvalues of the Hamiltonian and taking the non-resonant limit, where $\Omega/\delta \to 0$, gives the following energies for the two states:

$$\begin{aligned} E_{\mathrm{D}} &= \hbar\left(\frac{\delta}{2} + \frac{\Omega^2}{4\delta}\right) \\ E_2 &= -\hbar\left(\frac{\delta}{2} - \frac{\Omega^2}{4\delta}\right). \end{aligned} \tag{2.14}$$

To obtain the energy of the perturbed bare ground state, one simply must subtract the energy of a drive photon. The shift of the ground state energy from the unperturbed value is

$$\Delta E_{\mathrm{ACS}} = \hbar\frac{\Omega^2}{4\delta} = \frac{3\pi c^2}{2\omega_0^3}\frac{\Gamma}{\delta}I, \tag{2.15}$$

where we have expressed the Rabi frequency in terms of the laser intensity I, using

equation 2.10. The sign of the shift depends on the sign of the detuning of the light. For blue-detuned light δ is positive, and the ground state atom is repelled from regions of high light intensity. For red-detuned light δ is negative, and the ground state atom is attracted to regions of high light intensity. The magnitude of the AC Stark shift is also dependent on the polarization of the light, as this determines the value of the matrix element which defines the Rabi frequency (see equation 2.7).

Since real atoms are not truly two-level systems, there is a whole forest of transitions that need to be considered when calculating the AC Stark polarizability of an atom, but typically when far from any resonances, only the main transition needs to be considered. However, the resonance frequency for a transition will depend upon the AC Stark shifts of both the ground state and the excited state. The latter depends on the resonance frequencies for transitions to some third state. Typically, at the wavelengths used to apply AC Stark shifts, the detuning from excited state to excited state transitions is large, and the AC Stark shift of the excited state is negligible. There also can exist a "magic" wavelength for which the AC Stark shift of the ground and excited state are equal, so the resonance frequency is unshifted from the bare transition. Such magic wavelength traps or lattices are useful for optical clocks, where shifts in the clock frequency are undesirable, or for experiments where *in situ* addressing of an optical transition is required.

2.1.5 Atom-atom interactions

Atom-atom interactions become important at the sufficiently high densities that can be obtained in a magnetic or optical dipole trap. Elastic atomic collisions are well modeled by standard quantum scattering theory, which solves for the wave function in the center of mass frame of the scattering particles by using the time-independent Schrödinger equation. At a distance r which is large compared to the length scale of

the interaction potential, the wavefunction is a sum of an incoming plane wave, and an outgoing spherical wave [35]. Thus, in this regime the wave function is given by

$$\psi(\vec{\mathbf{k_i}}, \vec{\mathbf{r}}) = \frac{1}{(2\pi)^{3/2}}\big[\mathrm{e}^{(\mathrm{i}\vec{\mathbf{k_i}}\cdot\vec{\mathbf{r}})} + f(\vec{\mathbf{k_i}}, \vec{\mathbf{r}})\frac{\mathrm{e}^{\mathrm{i}k_i r}}{r}\big], \tag{2.16}$$

where $f(\vec{\mathbf{k_i}}, \vec{\mathbf{r}})$, the scattering amplitude, is given by

$$f(\vec{\mathbf{k_i}}, \vec{\mathbf{r}}) = \frac{m}{4\pi\hbar^2}\int \mathrm{d}^3\vec{\mathbf{r}}'\mathrm{e}^{-\mathrm{i}\frac{k_i}{r}\vec{\mathbf{r}}\cdot\vec{\mathbf{r}}'}V(\vec{\mathbf{r}}')\psi(\vec{\mathbf{r}}'). \tag{2.17}$$

Here m is the mass of one atom (assuming a homonuclear interaction) and $V(\vec{\mathbf{r}})$ is the interaction potential. For sufficiently weak interactions, one may assume that f only depends upon the incident plane wave[8] and is given by

$$f(\vec{\mathbf{k_i}}, \vec{\mathbf{k_f}}) = \frac{m}{4\pi\hbar^2}\int \mathrm{d}^3\vec{\mathbf{r}}'\mathrm{e}^{-\mathrm{i}(\vec{\mathbf{k_f}}-\vec{\mathbf{k_i}})\cdot\vec{\mathbf{r}}'}V(\vec{\mathbf{r}}'), \tag{2.18}$$

where $\vec{\mathbf{k_f}} = \frac{k_i}{r}\vec{\mathbf{r}}$.

For a spherically symmetric interaction potential, the scattering amplitude is only dependent on the initial plane wave momentum and the angle between the initial and final wave vectors. The probability of the atom scattering into any infinitesimal solid angle, or the differential cross-section, is given by $|f(k_i, \theta, \varphi)|^2$, and the total scattering cross-section is given by[9]

$$\sigma_{\mathrm{T}} = \int \mathrm{d}\Omega\frac{\mathrm{d}\sigma}{\mathrm{d}\Omega} = \int \mathrm{d}\Omega|f(k_i, \theta, \varphi)|^2 = \frac{4\pi}{k}\mathrm{Im}(f(k, 0)), \tag{2.19}$$

where the last equality is known as the optical theorem[10]. For a spherically symmetric

[8] This is known as the Born approximation.

[9] Here we use $k = k_i$.

[10] So-called due to a similar theorem from optical scattering (developed by Lord Rayleigh and others) relating the index of refraction to the forward scattering amplitude for light.

potential, it is convenient to introduce an expansion of the wave function in terms of $m = 0$[11] spherical harmonics,

$$\psi(\vec{\mathbf{r}}) = \sum_{\ell=0}^{\infty}(2l+1)P_\ell(\cos\theta)\frac{u_{k,\ell}(r)}{r}, \tag{2.20}$$

where $P_\ell(x)$ is the ℓth Legendre polynomial and $u_{k,\ell}(r)$ is a wave function satisfying the radial Schrödinger equation:

$$\left[\frac{\mathrm{d}^2}{\mathrm{d}r^2} + k^2 - \frac{\ell(\ell+1)}{r^2} - \frac{m}{\hbar^2}V(r)\right]u_{k,\ell}(r) = 0. \tag{2.21}$$

The extra term proportional to $\frac{1}{r^2}$ is known as the centrifugal barrier, and indicates a potential barrier at short length scales for non-zero angular momentum components of the scattering amplitude. In the regime where r is large relative to the incoming plane wave wavelength, the wave function has the form given in equation 2.16, and can be expanded in terms of the spherical harmonics as

$$\psi(\vec{\mathbf{k_i}}, \vec{\mathbf{r}}) = \frac{1}{(2\pi)^{3/2}}\sum_{\ell=0}^{\infty}(2l+1)P_\ell(\cos\theta)\big[\frac{\mathrm{e}^{\mathrm{i}k_i r} - (-1)^\ell \mathrm{e}^{-\mathrm{i}k_i r}}{2\mathrm{i}kr} + \frac{f(k_i,\theta)\mathrm{e}^{\mathrm{i}k_i r}}{r}\big]. \tag{2.22}$$

Due to unitarity (i.e. conservation of probabilty) and rotational invariance (i.e. conservation of angular momentum), the coefficients of the incoming and outgoing spherical waves must have equal magnitude for each ℓ. Thus the outgoing spherical wave can only differ from the incoming spherical wave by a phase, and the scattering amplitude must equal

$$f(k_i,\theta) = \sum_{\ell=0}^{\infty}(2l+1)P_\ell(\cos\theta)\frac{\mathrm{e}^{2\mathrm{i}\delta_\ell(k_i)} - 1}{2\mathrm{i}k_i} = \frac{1}{k_i}\sum_{\ell=0}^{\infty}(2l+1)P_\ell(\cos\theta)\mathrm{e}^{\mathrm{i}\delta_\ell(k_i)}\sin\left(\delta_\ell(k_i)\right) \tag{2.23}$$

[11] Here m refers to the index of spherical harmonics, not mass.

and therefore the radial wave function at large r is given by

$$\frac{u(k_i,r)}{r} = \frac{1}{(2\pi)^{3/2}}\Big[\frac{\mathrm{e}^{2\mathrm{i}\delta_\ell(k_i)+\mathrm{i}k_i r} - (-1)^\ell \mathrm{e}^{-\mathrm{i}k_i r}}{2\mathrm{i}k_i r}\Big] = \frac{\mathrm{e}^{\mathrm{i}(\frac{\pi}{2}\ell+\delta_\ell(k_i))}}{(2\pi)^{3/2}}\frac{\sin\left(k_i r + \delta_\ell(k_i) - \frac{\pi}{2}\ell\right)}{k_i r}. \tag{2.24}$$

Using equations 2.19 and 2.23, as well as the normalization condition for the Legendre polynomials ($P_\ell(1) = 1$), one finds the total scattering amplitude to be

$$\sigma_{\mathrm{T}} = \frac{4\pi}{k_i^2}\sum_{\ell=0}^{\infty}(2l+1)\sin^2(\delta_\ell(k_i)). \tag{2.25}$$

In the case of indistinguishable particles, a scattering event with angle θ is indistinguishable from one with angle $\theta - \pi$. Therefore the total scattering amplitude is given by

$$f_{\mathrm{Identical}}(k,\theta) = f(k,\theta) + \epsilon f(k,\theta-\pi), \tag{2.26}$$

where $\epsilon = 1$ for bosons, and $\epsilon = -1$ for fermions. This is a result of the fact that the overall wave function must be symmetric for bosons and antisymmetric for fermions upon particle exchange. Further, using the symmetry properties of Legendre polynomials ($P_\ell(-x) = (-1)^\ell P_\ell(x)$), one finds that

$$\begin{aligned}\sigma_{\mathrm{T,Bosons}} &= \frac{8\pi}{k_i^2}\sum_{\ell\,\mathrm{even}}(2l+1)\sin^2(\delta_\ell(k_i)) \\ \sigma_{\mathrm{T,Fermions}} &= \frac{8\pi}{k_i^2}\sum_{\ell\,\mathrm{odd}}(2l+1)\sin^2(\delta_\ell(k_i))\end{aligned} \tag{2.27}$$

At the low energy scales that are relevant to cold atom experiments, one only considers s-wave ($\ell = 0$) scattering events. This can be viewed as being a result of the centrifugal barrier in equation 2.24 - at temperatures corresponding to energy scales lower than the barrier, the phase $\delta_\ell(k_i)$ is close to zero, as the incoming wavevector is simply relected

off of the barrier. At sufficiently low temperatures, only s-wave scattering produces a non-negligible phase shift, since for $\ell = 0$ there is no centrifugal barrier. Therefore the scattering cross-section for bosons is well-approximated by purely s-wave scattering events, and the scattering cross-section for fermions is well-approximated by zero[12].

It is possible to recast $\delta_0(k_i)$ as a length scale a known as the scattering length. The radial wave function at large r in equation 2.24 can be expanded around $k_i r = 0$ (which corresponds to a low energy scale) to give

$$u(k_i, r)_{k_i r=0} = \frac{\mathrm{e}^{\mathrm{i}\delta_0(k_i)}}{(2\pi)^{3/2} k_i}\big[\sin(\delta_0(k_i)) + k_i r\cos(\delta_0(k_i))\big] = \frac{\mathrm{e}^{\mathrm{i}\delta_0(k_i)}\cos(\delta_0(k_i))}{(2\pi)^{3/2}}(r-a), \quad (2.28)$$

where

$$a = -\lim_{k_i\to 0}\tfrac{\tan\delta_0(k_i)}{k_i} \quad \text{or} \quad \lim_{k_i\to 0}\delta_0(k_i) = -k_i a. \quad (2.29)$$

Using this low-energy expansion in equation 2.27, one can show that the scattering cross-section for identical bosons is

$$\sigma_{\mathrm{T,Bosons}} = 8\pi a^2. \quad (2.30)$$

For an attractive potential the sign of the the scattering length can be either positive or negative, as the existence of bound states leads to divergences in a. Due to these divergences, the magnitude of the scattering length is not bounded and in particular can be much larger than the length scale of the interaction potential. A positive scattering length corresponds to a negative phase shift in the outgoing spherical wave, which corresponds to an effective repulsive interaction. Conversely a negative scattering length corresponds to an attractive interaction[13]. Additionally, the phase shift and effective scattering length depend on the incident momentum k_i, and therefore the gas temperature. For atoms with

[12] This can be viewed as a manifestation of the Pauli exclusion principle

[13] A negative phase shift corresponds to the large-r wave function being "pushed" away from the origin, while a positive phase shift corresponds to the large-r wave function being "pulled" in towards the origin.

$a < 0$ at $\mathrm{T} = 0\,\mathrm{K}$, it is possible to have a zero-crossing of the effective scattering length at finite temperature. This is the case in ^{7}Li for the $^2S_{1/2}\ |F = 2, m_F = 2\rangle$ hyperfine state, and it leads to complications in the cooling procedure.

2.1.6 Scattering in an ultracold gas

Elastic scattering allows an interacting gas of atoms to thermalize without a change in total energy. The rate of thermalization is an important parameter in evaporative cooling, where the hottest atoms are removed from a gas, and the reamaining atoms are allowed to re-thermalize to a lower temperature. The elastic collision rate for a single atom, Γ_{el}, is given by

$$\Gamma_{\mathrm{el}} = \bar{n}\bar{v}\sigma_{\mathrm{T}}, \tag{2.31}$$

where $\bar{n}$ is the mean number density of the cloud, and $\bar{v}$ is the mean velocity of the atoms. It is typical to asumme that σ_{T} variation with T is not relevant at the temperature scale in an ultracold gas[14]. For a linearly trapped gas (as in a magnetic quadrupole trap, see Section 2.3.2), $\Gamma_{\mathrm{el}} \propto N/T^{5/2}$. For a harmonically trapped gas (as in an optical trap, see Section 2.3.3), $\Gamma_{\mathrm{el}} \propto N/T$.

Inelastic scattering events are typically undesirable in an ultracold gas, as they can lead to heating. There are a few relevant inelastic processes. Spin-exchange can occur during a collision. Such exchanges must conserve the orbital angular momentum quantum numbers (l and m_l) for each atom, and the sum of the total spin projection must be conserved ($m_{F_1} + m_{F_2}$). Therefore these are avoided by spin-polarizing into the highest available spin-state for a given orbital. Magnetic dipole-dipole interactions during a collision can lead to spin-changes as well. During three-body collisions, a molecule can be formed by a pair of atoms while the third atom carries away energy and momentum.

[14] This is not always true, as with the $|F = 2, m_F = 2\rangle$ state in ^{7}Li, which has a scattering-cross-section zero-crossing at 6 mK.

Since such collisions require three atoms, the three-body recombination rate for a single atom depends on n^2. This limits experimentally achievable densities to approximately 10^{13} cm^{-3}.

2.1.7 Feshbach resonances

Resonance effects lead to complications in the treatment of elastic scattering given above. We have discussed how the permittance of bound states leads to divergences in the s-wave scattering length[15]. For $l \neq 0$ collisions, there may also exist quasi-bound states due to the centrifugal barrier in the inter-atomic potential that may cause a resonant enhancement of the scattering length. It is also possible for the scattering to be resonantly enhanced by proximity to a bound state in a different channel under an interaction that mixes channels. This is known as a Feshbach resonance.

When two atoms collide, the inter-atomic potential is determined by the quantum state of the pair of atoms. For different sets of initial quantum numbers, known as channels, the available bound states are therefore different. Due to off-diagonal terms in the interaction Hamiltonian, such as dipole-dipole spin interactions, different channels can be coupled. The channel corresponding to the quantum state of the colliding pair of atoms is known as the entrance or open channel, and other channels are known as closed channels. If there is a bound state of a closed channel that is close in energy to the energy of the colliding pair, it can have a resonant effect on the scattering of the atoms if there is sufficient coupling between the two channels. To model a Feshbach resonance it is sufficient to consider only one closed channel, and one relevant bound state. The inter-channel coupling mixes the open and closed (bound state) eigenstates, producing "dressed" states, and the open channel eigenstates are perturbed by the proximity to

[15]Such divergences lead to a resonantly enhanced scattering length if there is a bound state near the threshold energy of the potential.

the bound closed state, as in standard degenerate perturbation theory. This produces a resonance in the scattering length when the energy difference between the open channel energy and the bound state energy is equal to the energy of the coupling between the open and closed eigenstates. Such resonances are experimentally useful due to two reasons.

The first is that magnetic Feshbach resonances allow for the tuning of the scattering length through a divergence by simply tuning an applied magnetic field. The effective scattering length as a function of magnetic field strength B is

$$a = a_{\mathrm{bg}}\left(1 - \frac{\Delta B}{B - B_0}\right), \tag{2.32}$$

where a_{bg} is the zero-field, zero-temperature scattering length. The effective scattering length goes through a divergence at a magnetic field strength of B_0, and is equal to zero at a magnetic field ΔB higher than this divergence field. Such magnetic Feshbach resonances are used experimentally to tune the scattering length from $-\infty$ to $+\infty$.

The second is that Feshbach resonances can be used to produce loosely bound molecules [36], known as Feshbach molecules, by adiabatically tuning the scattering length from being negative to positive[16]. Such Feshbach bound states exhibit universal scaling properties, and can be used to produce ground-state molecules through stimulated Raman adiabatic passage (STIRAP) [37].

2.2 Laser cooling

The ability to laser cool atoms revolutionized experimental atomic physics. Low temperature atoms are easier to trap and exhibit many phenomena beyond those exhibited by the ideal gas, which is governed by 19th century thermodynamics. This technical

[16]For repulsive effective interactions, the molecular state is of lower energy than that of the free atoms, so can be accessed by adiabatically tuning from negative to positive effective scattering length.

breakthrough and its theoretical understanding were the subject of the 1997 Nobel Prize award. The most basic and central laser cooling technique is Doppler cooling, in which the Doppler shift is used to selectively scatter photons off of atoms that are traveling towards the laser beam, resulting in slowing, and, when done in 3 dimensions, cooling. This technique is at the heart of optical molasses, transverse cooling, Zeeman slowing and magneto-optical trapping, and allows for cooling to the Doppler cooling limit. Sub-Doppler cooling methods, such as Sisyphus cooling and gray molasses, allow for cooling below this limit.

2.2.1 Optical molasses

An atom which is scattering photons from a laser beam experiences a force in the direction of the laser beam. This is due to the atoms gaining momentum in the direction of the photon k-vector after absorption, and on average gainng no momentum upon spontaneous emission, due to a symmetric distribution of emission events. The force experienced by the atom is the photon momentum, $\hbar k$, multiplied by the scattering rate (see equation 2.11), and is thus given by

$$F_{\text{scatt}} = \hbar k R_{\text{abs}} = \hbar k \frac{\Gamma}{2} \frac{I/I_{\text{sat}}}{1 + I/I_{\text{sat}} + 4\delta^2/\Gamma^2}. \tag{2.33}$$

In order for this force to perform cooling, it must only exert on atoms that are traveling towards the laser beam. Atoms that have a velocity component v in the direction counter to the propagation of the laser beam experience a positive (blue-detuned) Doppler shift in the laser frequency, which is given by

$$\Delta_{\text{D}}\omega = kv. \tag{2.34}$$

Therefore, if the laser detuning is chosen to be negative (red-detuned), only atoms that are traveling towards the laser with velocity such that the Doppler shift is close to that detuning will scatter photons appreciably. Assuming N pairs of counter-propagating red-detuned laser beams, the force exerted on the atom in the regime where the Doppler shift is small compared to the magnitude of the detuning and the linewidth of the transition is given by [38]

$$\vec{\mathbf{F}} = 4\hbar k^2 \frac{I}{I_{\text{sat}}} \frac{2\delta/\Gamma}{(1 + 2NI/I_{\text{sat}} + 4\delta^2/\Gamma^2)^2} \vec{\mathbf{v}}. \tag{2.35}$$

In this regime, the force is proportional to the velocity of the atom, and is thus a damping force for negative detuning, which should reduce the atoms' velocities to arbitrarily close to zero, inspiring the name optical molasses. The maximum damping coefficient is $\hbar k^2/4N$ and is achieved for $\delta = -\Gamma/2$ and $I = I_{\text{sat}}/N$. It is common to use 2d optical molasses as a stage of transverse cooling to improve the collimation of an atomic beam, and these parameters are used to cool the transverse degrees of freedom of the atomic motion in as short an interaction region as possible.

The process of optical molasses also causes heating, due to spontaneous emission and due to atoms with zero mean velocity along one beam axis absorbing photons from both beams. Both of these processes lead to the atom undergoing a random walk in position and momentum space, leading to a non-zero mean momentum squared, which is given by the number of random walk steps multiplied by the photon momentum squared. An equilibrium temperature may be calculated by equating the heating and cooling rates, and is given by

$$T_{\text{Molasses}} = \frac{\hbar\Gamma}{4k_{\text{B}}} \frac{1 + 2NI/I_{\text{sat}} + (2\delta/\Gamma)^2}{2|\delta|/\Gamma}, \tag{2.36}$$

where k_{B} is Boltzmann's constant. This molasses temperature is minimized at low laser

intensity and for $\delta = -\Gamma/2$, and gives the Doppler cooling limit of

$$T_{\text{Doppler}} = \frac{\hbar\Gamma}{2k_{\text{B}}}. \tag{2.37}$$

Optical molasses is very successful at producing cold clouds of atoms, but it does not produce a restoring force, and therefore does not trap the atoms. Often it is used after a magneto-optical trapping stage to further lower the temperature of the atoms.

2.2.2 Zeeman slowing

In order to trap atoms, it is necessary to cool them below the trap depth for a conservative trap like a magnetic or off-resonance optical trap, or to slow them below the capture velocity, v_{c}, of a non-conservative trap, such as a magneto-optical trap. For atoms with low vapor pressure, it is necessary to heat the solid to hundreds of degrees Celsius above room temperature, producing a hot vapor which is then collimated into a beam, where the most probable velocity is extremely high - more than a mile per second in some cases. In order to slow such fast-traveling atoms to below a typical capture velocity of ~ 50 m/s, it is common to employ a counter-propagating resonant laser beam to scatter photons off of the atoms in the atomic beam until there is a sufficient population of atoms with velocity in the beam direction at or below v_{c}. The scattering force given in equation 2.33 causes the atoms to accelerate, and the peak acceleration is obtained in the limit of high laser intensity and is given by

$$a_{\text{max}} = \frac{\hbar k\Gamma}{2m}, \tag{2.38}$$

where m is the mass of the atom. This peak deceleration gives a minimum length scale over which slowing may occur, given a maximum initial velocity along the beam

direction $v_{\max}$, and an exit velocity along the beam direction of v_c. Typically a safety parameter $\eta < 1$ is introduced to scale the peak acceleration in order to take into account experimental inefficiencies. The velocity of atoms, which enter the slowing region at $z = 0$ with velocity $v_{\max}$ at any point z in the slowing region is given by

$$v(z) = (v_{\max} - v_c)\left(1 - \frac{2\,\eta\,a_{\max}\,z}{v_{\max}^2 - v_c^2}\right)^{1/2} + v_c. \tag{2.39}$$

A complication in this process is that as the velocity of the atoms in the direction of the beam continuously decreases towards the capture velocity, so does the Doppler shift, which is given by kv. As v typically decreases by an order of magnitude from the beginning to the end of such an atomic beam slower, the laser detuning must also be spatially-varying to match this decrease in order to maintain deceleration. In practice, it is common to use a spatially-varying external magnetic field to apply a spatially-varying linear Zeeman shift to counter the spatially-varying Doppler shift. Such atomic beam slowers are known as Zeeman slowers. Using equations 2.2 & 2.39, we find the required magnetic field profile for such a slower, which is

$$B(z) = \frac{k\,v(z)}{\mu_B(g_{J'}m_{J'} - g_J m_J)} + B_{\text{offset}}, \tag{2.40}$$

where the prime denotes excited state quantum numbers. A constant magnetic field offset, B_{offset}, may be applied in general, and results in a shift in the laser detuning used for the Zeeman slower. It is desirable to have the Zeeman shift at the exit of the Zeeman slower to be far from zero to prevent atoms from being cooled significantly below v_c (in particular to prevent the atoms from being turned around by the slower) and to ensure that the Zeeman slower laser beam detuning is large so as not to disrupt the magneto-optical trap. It is also desirable to have a zero-crossing in the magnetic field of the Zeeman slower at some point along the length of the slower, to prevent the absolute value of the

magnetic field at either end from being very large. Such a zero-crossing also allows for transitions with different values of $g_{J'}m_{J'} - g_J m_J$ to be on resonance in that section of the slower. This is useful for "repumping" atoms back into a desirable hyperfine manifold. Therefore it is common to use a negative B_{offset} of a few hundred gauss[17]. The magnetic field of the Zeeman slower can point longitudinally (along the beam dimension), in which case the field is typically produced by a tapered solenoid electromagnet, or transversely, in which case the field is typically produced using permanent magnets.

Scattering photons from one direction off of the atoms leads to heating in the transverse dimensions, as the atoms undergo a random walk in this 2d space. This leads to the phenomenon known as "beam explosion," where the atomic beam expands in the transverse dimension. This effect is largest for light-mass atoms. In addition to beam explosion, the k-vector of an atom with a small transverse velocity component curves away from the beam direction as the atom is selectively slowed in the beam direction. In order to mitigate both of these effects, it is common to position the end of the Zeeman slowing region to be as close to the trapping region as possible and to use transverse cooling at the final stages of slowing.

2.2.3 Sub-Doppler laser cooling

Several methods exist to laser cool atoms below the Doppler cooling limit. The most commonly-used technique is known as Sisyphus or polarization gradient cooling, in which counter-propagating laser beams (resonant with a $J \neq 0 \rightarrow J' = J + 1$ transition) with opposite polarization are used to produce a periodic spatial modulation of the local light-field polarization. Optical pumping between two or more ground states as the atom

[17]When using a Zeeman slower with a magnetic field zero-crossing section and an atom with non-zero m_J states, it is important for the spatial gradient of the magnetic field as it passes through zero to be small enough to allow the spin to flip along with the quantization axis. Such slowers are known as spin-flip Zeeman slowers.

moves through this periodic polarization gradient results in energy being removed from the atom. This is because the atom climbs up a potential hill, where it becomes resonant with photons which optically pump it to a state which sees a potential minimum at that position. Due to the periodic potential gradient, this process repeats, drawing comparison to the unfortunate Greek mythological character. Here the cooling limit is set by the minimal unit of energy that can be removed from the system, i.e. the maximal energy difference between the AC Stark shifts of ground states with maximal $|m_J|$.

In atoms where such transitions are not possible due to the level structure, or due to parasitic transitions to undesirable hyperfine ground states, other sub-Doppler cooling techniques may be used. A technique known as gray molasses or electromagnetically-induced transparency (EIT) cooling is particularly successful in cooling lithium and potassium [39, 40, 41, 42]. Here, the two ground-state hyperfine manifolds are coherently mixed with each other through the application of two frequencies of light: one near-detuned from the transition from one ground state to an excited state (with $J' = J$ or $J-1$), and the other near-detuned from the transition from the other ground state to the same excited state[18]. If the detuning of these two lasers are equal, the ground states are now superpositions of the bare ground states, where one of the dressed states couples to the light field (the bright state) and thus exhibits an AC Stark shift, and the other does not (the dark state). If standing waves of these two frequencies of light are applied to the atoms, the dark state is motionally coupled to the bright state - i.e. dark state atoms with non-zero velocity are transferred to the bright state through a non-adiabatic process. Additionally, the standing wave produces a spatially dependent AC Stark shift on the bright state. If the two lasers are equally blue-detuned from the excited state,

[18]This is an example of a Raman process, where an atom simultaneously absorbs a photon from one light-field, and undergoes stimulated emission due to the second light-field. Sub-Doppler cooling techniques of both free and trapped atoms based on Raman processes exist. Raman processes can also be used to coherently move population from one state to another, as in the case of stimulated Raman adiabatic passage (STIRAP).

this results in cooling though a Sisyphus-like process, as the bright state atom climbs a potential hill before being transferred to the dark state, where it remains until it has moved to a position where the AC Stark shift for the bright state is minimal [43]. The cooling limit of gray molasses is not completely understood.

2.3 Trapping and evaporative cooling

Trapping atoms is advantageous in experiments where large numbers of atoms are desired, as a trap with a lifetime long compared to the trap-loading rate can be used to collect atoms, and necessary to increase the density of an atomic gas to levels where atom-atom interactions are relevant. The first trapping stage in many ultracold atom experiments is the magneto-optical trap, in which optical molasses beams are used in conjuction with a magnetic-field minimum to produce a restoring force on the atoms. Such traps are used to collect and cool atoms from a slow atomic beam. Subsequently, conservative traps such as magnetic and off-resonant optical traps are used to increase the density of the atomic gas, and to perform forced evaporative cooling. Evaporative cooling occurs naturally in a conservative trap where the temperature of the gas is similar to the trap depth. During this cooling, hot atoms escape the trap via elastic collisions, while the remaining atoms rethermalize to a lower temperature. This cooling is not effective when the temperature of the gas is much smaller than the trap depth, as elastic collisions no longer produce atoms with energy sufficient to escape the trap. However by reducing the trap depth concurrently, one can force evaporation to continue, leading to ultracold, dense gases with phase space densities on the order of unity. If the ratio of elastic to inelastic scattering events is sufficiently large, and the trap depth is lowered sufficiently slowly for rethermalization to occur, this induces "runaway evaporation," where the temperature of the gas is proportional to the atom number to a power larger than one (i.e. the cooling

power of evaporative cooling increases as more atoms are removed). Once a degenerate quantum gas is produced, a common approach is to load the atoms into the ground band of an optical latice, which is a periodic optical potential produced by a standing wave of light.

2.3.1 Magneto-optical traps

As discussed in section 2.2.1, optical molasses does not produce a restoring force, which is necessary to trap atoms. In order to produce such a restoring force, position dependence must be introduced into the scattering force. In a magneto-optical trap (commonly abbreviated and referred to as a MOT), this position dependence is engineered by applying a spatially dependent Zeeman shift. In order to produce a position-dependent force that would lead to trapping, a magnetic field that either increases or decreases towards the trap center in all directions is required. As local magnetic field maxima are impossible for static fields [44], the only option is to produce a local magnetic-field minimum. The simplest arrangement that has such a local minimum is a quadrupole field, which has a magnetic field zero at the origin. Such a field arrangement is produced by a pair of anti-Helmholtz coils[19], which produce an approximately linear magnetic field gradient in the axial and radial dimensions[20]. The simplest case of a MOT is for a $J = 0 \rightarrow J = 1$ transition, where the excited state energies are shifted by the Zeeman shift, but the ground state is unperturbed. If red-detuned light is used, as in molasses,

[19]The Helmholtz condition for equally-sized circular coils is that the separation of the coils is equal to their radii. When the directions of current flow in these two coils are the same, they produce a magnetic field with zero-curvature at the point halfway between the coils along the axis of the coils. Anti-Helmholtz coils refer to an arrangement where the directions of current flow in these two coils are opposite to each other, and this produces a quadrupolar field in the region between the coils, where field-gradient curvature is minimized at the point halfway between the coils along the axis of the coils. See section 5.5.1 for quantitative details on Helmholtz coils.

[20]The magnitude of the axial magnetic-field gradient is twice that of the radial magnetic-field gradient, as a result of $\vec{\nabla} \cdot \vec{\mathbf{B}} = 0$. By similar logic, if the magnetic field along the axial dimension points towards the magnetic-field zero, the magnetic field along the radial dimension points away from the magnetic-field zero (and vice versa).

the light will be resonant with atoms with zero mean velocity only if the excited state is lowered in energy by the Zeeman shift, and that Zeeman shift is similar to the detuning of the light. If one defines the quantization axis as pointing along the magnetic field, this implies that only σ^- transitions (assuming $g_{J'}$ is positive, see equation 2.2) will be resonant. For a red-detuned laser beam with polarization such that the light is σ^--polarized on the side of the magnetic-field zero that is nearer the laser beam, the light will be σ^+-polarized on the side of the trap beyond the magnetic-field zero, and therefore will not be absorbed by atoms in this region with zero mean velocity. The atoms experience a drag force as in optical molasses, but also a restoring force that is proportional to their distance away from the magnetic-field zero. Atoms are cooled via the damping force and trapped via the restoring force.

The magnetic-field gradient and the detuning of the laser beams sets a length scale (i.e. the position away from the magnetic-field zero where the Zeeman shift of the relevant excited state is equal to the laser detuning) which determines the size of the trapping region. Of course, the diameter of the laser beams must be larger than this trapping region for it to be a meaningful length scale. The capture velocity, v_c of the MOT is set by the laser beam diameter and the maximal acceleration in equation 2.38[21], and is of the order of 50 m/s for typical MOTs. The temperature of a MOT is typically higher than the Doppler cooling limit (see equation 2.37), both due to the high laser intensities and detunings used[22] and due to photon-mediated atom-atom repulsive interactions, which become relevant at high densities and saturation parameters, and increase the physical size of a MOT beyond that expected for a gas of a given temperature in the restorative trap. These atom-atom interactions and the near-total absorption of the laser beams by a sufficiently populated MOT limit the total number of atoms one can trap with this

[21] MOTs are operated in the saturated regime.

[22] Intensity and detuning are typically chosen to maximize atom number in the MOT.

technique to around 10^{10}. It is common to have a second "compressed" MOT (cMOT) stage after the trapped atom number has saturated to further reduce the temperature. If the ground state has hyperfine structure, it may be necessary to have a "repumping laser" to transfer the atoms out of the undesirable ground-state hyperfine state to continue to scatter photons of the main "cooling laser." During the cMOT stage, the repumper power can be reduced, while the cooler is brought closer to resonance. This has the effect of moving the atoms towards the magnetic-field zero (and thus increasing density), and collecting atoms in the dark hyperfine ground state, where they no longer scatter photons, and therefore experience no heating. This cold, dense cloud is a good starting point for sub-Doppler cooling, or loading into a conservative trap.

2.3.2 Magnetic traps

A magnetic trap is a region of space that encloses a local magnetic-field minimum. Atoms in Zeeman sublevels of atoms that are shifted down in energy by the application of a magnetic field (i.e. low-field seeking states) are trapped as long as they experience a positive magnetic-field gradient. Practically, the magnetic-field gradient in the vertical dimension must be large enough to produce a force that is larger than gravity, and the temperature of the gas sets the size of the volume that is occupied by the gas. The simplest way to arrange for this, as in the case of a MOT, is by engineering a quadrupolar field using anti-Helmholtz coils (see Section 5.5.1 for a discussion of Helmholtz and anti-Helmholtz coils). Near the field-zero the potential experienced by the atoms is

$$V(r,z) = \frac{F_z}{2}(r^2 + 4z^2)^{1/2}, \tag{2.41}$$

where z is the dimension of the strongest magnetic field-gradient (i.e. the axis of the coils), and r is the radial dimension in the plane perpendicular to this axis, and $F_z =$

$g_F m_F \mu_B G_z$, where G_z is the magnetic-field gradient along the z-axis. The probability distribution of the atoms in the trap is

$$P(r, z, \vec{\mathbf{p}}) = \frac{1}{Z} \exp\Bigg[- \frac{1}{k_{\mathrm{B}} T} \Bigg(V(r, z) + \frac{|\vec{\mathbf{p}}|^2}{2m} \Bigg) \Bigg], \tag{2.42}$$

where Z, the partition function is

$$Z = \frac{1}{(2\pi\hbar)^3} \int_0^{\infty} \mathrm{d}r \int_{-\infty}^{+\infty} \mathrm{d}z \int \mathrm{d}\vec{\mathbf{p}}\, 2\pi r P(r, z, \vec{\mathbf{p}}) = 4\pi \Bigg(\frac{2 k_{\mathrm{B}} T}{F_z \Lambda_{\mathrm{DB}}} \Bigg)^3, \tag{2.43}$$

where $\Lambda_{\mathrm{DB}} = \sqrt{2\pi\hbar^2 / m k_{\mathrm{B}} T}$ is the thermal de Broglie wavelength. Since the energy dependence on postion and momentum is separable, the momentum dependence can be integrated out to give a spatial distribution,

$$P_{\mathrm{S}}(r, z) = \frac{1}{\Lambda_{\mathrm{DB}}^3 Z} \exp\Bigg[- \frac{1}{k_{\mathrm{B}} T} \Big(V(r, z) \Big) \Bigg]. \tag{2.44}$$

This distribution is peaked at the trap center, where, for a cloud with N atoms, the peak number density is

$$n_P = \frac{N}{\Lambda_{\mathrm{DB}}^3 Z} = \frac{N F_z^3}{32\pi (k_{\mathrm{B}} T)^3}. \tag{2.45}$$

Integrating out the momentum and radial degrees of freedom of the probability distribution gives the axial spatial distribution of the atoms, sometimes known as the Fujiwara function, which is

$$P_{\mathrm{F}}(z) = \frac{F_z}{4 k_{\mathrm{B}} T} \Big(1 + \frac{F_z}{k_{\mathrm{B}} T} |z| \Big) \exp\Bigg[- \frac{F_z}{k_{\mathrm{B}} T} |z| \Bigg]. \tag{2.46}$$

This density and axial distribution are completely determined by the temperature and magnetic-field gradient (assuming a specific $g_F m_F$). The full-width at half-maximum of

the axial distribution can be found numerically, and is

$$\sigma_{\mathrm{FWHM}} = 3.3567\,\frac{k_B T}{F_z}. \tag{2.47}$$

The peak phase-space density is

$$\rho_{\mathrm{P}} = n_{\mathrm{P}}\Lambda_{\mathrm{DB}}^3 = \frac{N F_z^3}{32\pi}\left(\frac{2\pi\hbar^2}{m}\right)^{3/2}\frac{1}{T^{9/2}}, \tag{2.48}$$

which similarly only depends on temperature and magnetic-field gradient. For an adiabatic ramp of the magnetic-field gradient, ρ is constant, and therefore gives a relationship between temperature and magnetic-field gradient, which is $T \propto G_z^{2/3}$. Similarly, for adiabatic compression, $\sigma \propto G_z^{-1/3}$, and $n_{\mathrm{P}} \propto G_z$. Adiabatic compression of the magnetic trap increases the elastic scattering rate, since $\Gamma_{\mathrm{el}} \propto \bar{n}\bar{v} \propto n_{\mathrm{P}} T^{1/2} \propto G_z^{4/3}$. However, the increase in density associated with adiabatic compression also leads to an increased three-body recombination rate.

It is common to perform forced evaporative cooling in a magnetic trap by inducing transitions to high-field seeking states (either in the same or a different hyperfine manifold), typically with radio frequency (RF) radiation. This type of evaporative cooling is thus known as RF-assisted evaporation. For a given frequency of RF radiation that is blue-detuned from the zero-magnetic-field frequency, atoms at positions defined by the surface of an ellipse will be resonant with the radiation, as the Zeeman shift caused by the magnetic field at these locations is equal to the detuning, and will be ejected from the trap[23]. In practice, the RF radiation is swept from a value that corresponds to an ellipse that is larger than the volume occupied by the atoms down towards the zero-magnetic-field frequency. This process selectively removes the hottest atoms first, as they make the

[23] A similar procedure can be used to measure the temperature of magnetically trapped atoms, which is known as RF thermometry.

largest excursions away from the magnetic-field zero. In addition to this RF sweep, the magnetic-field gradient is reduced to prevent increase in density in order to avoid three-body collisions which lead to heating. The first Bose-Einstein condensates produced in dilute atomic gases were results of RF-assisted evaporative cooling in magnetic traps.

The presence of a sharp kink in the magnetic field at the magnetic-field zero in a quadrupolar trap can lead to a non-adiabatic spin-flip from a low-field seeking to a high-field seeking state, known as a Majorana spin-flip. This leads to both atom loss and heating of the trapped atoms, as the coldest atoms are most likely to enter the region close to magnetic-field zero where they may undergo a spin-flip. This is particularly an issue for cold, dense clouds, and thus typically manifests after some amount of evaporative cooling. To avoid this Majorana heating, it is common to use a blue-detuned high-power off-resonant laser focused at the magnetic-field zero location to push atoms away from this region by the AC Stark shift. Such a laser used in this context is known as a plug beam, and is in a sense the opposite of an optical trap[24].

2.3.3 Optical traps

Unlike magnetic traps, which only trap atoms with certain quantum numbers, optical dipole traps (ODTs) can be used to trap any atom. In an optical trap, the dipole force pushes atoms towards regions of high-intensity of light that is red-detuned from the transition frequency. The AC Stark shift is given by equation 2.15, and the potential

[24]It is also possible to use more complicated arrangements of electromagnets, such as in a Ioffe-Pritchard trap, where the local magnetic-field minimum is non-zero. This is advantageous as it avoids the issue of Majorana losses that quadrupolar traps suffer from. Alternatively, a time-averaged orbiting potential (TOP) can be used to move the magnetic-field zero around in a circle, which allows for trapping atoms within this circle.

energy at any position in the trap is given by [45]

$$U_{\mathrm{ODT}}(\vec{\mathbf{r}}) = \frac{3\pi c^2}{2\omega_0^3}\frac{\Gamma}{\delta} I(\vec{\mathbf{r}}). \tag{2.49}$$

As in magnetic traps, the gradient of the laser intensity has to be sufficiently high in the vertical dimension to hold the atoms against gravity. Scattering of the trap photons leads to heating, and is therefore undesirable. Taking the large-detuning limit of equation 2.11, which is the typical regime of optical traps, the scattering rate at a position $\vec{\mathbf{r}}$ in the trap is given by

$$R_{\mathrm{scatt}}(\vec{\mathbf{r}}) = \frac{\Gamma^3}{8\delta^2}\frac{I(\vec{\mathbf{r}})}{I_{\mathrm{sat}}} = \frac{3\pi c^2}{2\hbar\omega_0^3}\frac{\Gamma^2}{\delta^2} I(\vec{\mathbf{r}}). \tag{2.50}$$

Since the potential depth scales as Γ/δ whereas the scattering rate scales as Γ^2/δ^2, it is advantageous to operate ODTs at high detunings, typically hundreds of terahertz.

The simplest ODT consists of a single focused $\mathrm{TEM}_{0,0}$ mode Gaussian beam. The intensity profile of such a beam with power P is

$$\begin{aligned} I(r,z) &= \frac{2P}{\pi w^2(z)} \mathrm{e}^{(-2r^2/w^2(z))}, \\ w(z)^2 &= w_0^2\big(1 + (z/z_{\mathrm{R}})^2\big), \\ z_{\mathrm{R}} &= \frac{\pi w_0^2}{\lambda}, \end{aligned} \tag{2.51}$$

where the beam points along the z-axis, the focus is located at $z = 0$, and r is a radial coordinate. The $1/\mathrm{e}^2$ radius at the focus is known as the waist, w_0, and the distance along the axis from the focus to the point where the $1/\mathrm{e}^2$ radius is $\sqrt{2}w_0$ is known as the Rayleigh length, z_{R}. If the temperature of the gas of atoms is small compared to the potential depth, the atoms are mostly confined to a small region near the focus, where

the potential is well approximated by a harmonic potential, which can be written

$$V_{\mathrm{ODT}}(r,z) \approx \frac{3\pi c^2}{2\omega_0^3}\frac{\Gamma}{\delta}\frac{2P}{\pi w_0^2}\left[1-2\left(\frac{r}{w_0}\right)^2-\left(\frac{z}{z_R}\right)^2\right] = V_0\left[1-2\left(\frac{r}{w_0}\right)^2-\left(\frac{z}{z_{\mathrm{R}}}\right)^2\right], \quad (2.52)$$

and the radial and axial approximate trap frequencies are given by

$$\begin{aligned} \omega_r &= 2\pi\nu_r = 2(V_0/mw_0^2)^{1/2} \\ \omega_z &= 2\pi\nu_z = (2V_0/mz_{\mathrm{R}}^2)^{1/2} \end{aligned} \quad (2.53)$$

The probability distribution of thermal atoms[25] in an ODT is

$$P(r,z,\vec{\mathbf{p}}) = \frac{1}{Z}\exp\left[-\frac{1}{k_{\mathrm{B}}T}\left((V_0 - V_{\mathrm{ODT}}(r,z)) + \frac{|p|^2}{2m}\right)\right] \quad (2.54)$$

where Z, the partition function, is

$$Z = \frac{1}{2\pi\hbar}\int_0^\infty \mathrm{d}r \int_{-\infty}^\infty \mathrm{d}z \int \mathrm{d}^3\vec{\mathbf{p}}\, P(r,z,\vec{\mathbf{p}}) = \frac{w_0^2 z_R}{4\Lambda_{\mathrm{DB}}^3}\left(\frac{\pi k_{\mathrm{B}}T}{V_0}\right)^{3/2}. \quad (2.55)$$

Since the energy dependence on position and momentum is separable, the momentum dependence can be integrated out to give a spatial distribution,

$$P_S(r,z) = \frac{1}{\Lambda_{\mathrm{DB}}^3 Z}\exp\left[-\frac{1}{k_{\mathrm{B}}T}(V_0 - V_{\mathrm{ODT}}(r,z))\right]. \quad (2.56)$$

This distribution is peaked at the trap center, where the peak number density is

$$n_{\mathrm{p}} = \frac{4N}{w_0^2 z_{\mathrm{R}}}\left(\frac{V_0}{\pi k_{\mathrm{B}}T}\right)^{3/2} = 2N\nu_r^2\nu_z\left(\frac{2\pi m}{k_{\mathrm{B}}T}\right)^{3/2} \quad (2.57)$$

[25]The Maxwell-Boltzmann distribution is used to describe thermal atoms. As the temperature approaches the critical temperature, Bose-Einstein statistics play a dominant role (see Section2.4.1 for details).

Thus for a thermal cloud the spatial distribution of the trap is a Gaussian, and the number density is determined by the atom number, cloud temperature, and trap geometry. The Gaussian widths of the thermal cloud are determined by the temperature and the trap geometry, and are given by

$$\begin{aligned}\sigma_r &= w_0\sqrt{\frac{k_{\mathrm{B}}T}{4V_0}} = \frac{1}{2\pi\nu_r}\sqrt{\frac{k_{\mathrm{B}}T}{m}} \\ \sigma_z &= z_{\mathrm{R}}\sqrt{\frac{k_{\mathrm{B}}T}{2V_0}} = \frac{1}{2\pi\nu_z}\sqrt{\frac{k_{\mathrm{B}}T}{m}}.\end{aligned} \tag{2.58}$$

The peak phase-space density is

$$\rho_{\mathrm{P}} = n_{\mathrm{P}}\Lambda_{\mathrm{DB}}^3 = \frac{4N}{w_0^2 z_{\mathrm{R}}}\left(\frac{2V_0}{m}\right)^{3/2}\left(\frac{\hbar}{k_{\mathrm{B}}T}\right)^3 = 2N\nu_r^2\nu_z\left(\frac{h}{k_{\mathrm{B}}T}\right)^3, \tag{2.59}$$

which similarly only depends on number, temperature and trap geometry. For an adiabatic ramp of laser power, ρ is constant, and therefore gives a relationship between temperature and laser power, which is $T \propto P^{1/2}$. Similarly, $\sigma \propto P^{-1/4}$ and $n \propto P^{3/4}$.

An ODT is highly anisotropic, due to the weak confinement along the ODT axis. To further confine the atoms in this dimension it is common to add a second ODT with axis at approximately 90° to the original ODT. This type of arrangement is called a crossed ODT (XODT). Along the axial dimension of either ODT, the trap depth is effectively that of a single ODT, and along the dimension orthogonal to both ODTs, the trap depth is the sum of the trap depths of the two ODTs.

An XODT can be loaded out of a magnetic trap in which RF-assisted evaporation has further cooled the gas, or a narrow-line MOT where the temperature of the atoms is sufficiently low. Transfer between traps is usually achieved by simply ramping up the optical trap while ramping down the magnetic field-gradient or the MOT beam powers. For heavy atoms, gravity can play a useful role in pushing the atoms into the optical

trap. Alternatively, an XODT with a large trap-volume can be loaded directly during or after a sub-Doppler cooling stage, such as Sisyphus cooling or gray molasses.

Since the trap depth is directly proportional to the laser power, forced evaporative cooling can be performed by simply lowering the laser power[26]. Since no magnetic fields are used in an optical trap, an external magnetic field may be used to tune the scattering length of elastic collisions to an optimum value using a Feshbach resonance. Such optical evaporation allows for the condensation of atoms with a non-magnetic ground state, as well as atoms with an unfavorable background scattering length when used in conjunction with a Feshbach resonance.

2.3.4 Optical lattices

The final stage of many quantum simulation experiments using quantum degenerate gases is loading the atoms into one or more optical lattices. An optical lattice is a standing wave of light, which produces a periodic pattern of nodes and antinodes of the electric field, which leads to a periodic pattern of laser intensity. The simplest way to produce an optical lattice is to retro-reflect a red-detuned laser beam such that both beams are focused at the atoms. This produces a standing wave of electromagnetic radiation, with a node at the plane of the retro-mirror. The lattice potential at a point near the focus (relative to the Rayleigh length) for a retro-reflected laser beam is given by

$$V_{\text{lattice}}(z) = V_0 \sin^2(kz). \tag{2.60}$$

Note that the lattice spacing is half the laser wavelength, and the lattice depth is four times that for an ODT produced by the same beam sans retro-reflection. Such a one-

[26]One drawback of this simplistic evaporation protocol is that the trap frequencies decrease as the square root of laser power (see equation 2.53), leading to poorer thermalization. It is possible to counter this decrease in trap frequencies by implementing more complex trap protocols [46].

dimensional optical lattice results in a series of pancake shaped clouds, as the atoms experience approximately harmonic confinement in the radial dimensions as in an ODT. Along the axial dimension there is tight confinement provided by the interference pattern, which may be approximated by a harmonic potential near the lattice well, and has a lattice site frequency of

$$\omega_{\text{lattice}} = 2\pi\nu_{\text{lattice}} = \left(\frac{2V_0k^2}{m}\right)^{1/2} = \frac{\sqrt{4E_{\text{R}}V_0}}{\hbar}, \tag{2.61}$$

where m is the mass of the atom, and $E_{\text{R}} = \hbar^2k^2/2m$ is the recoil energy, defined as the kinetic energy gained by the atom upon absorbing a photon from the light field. In addition to this tight confinement, there is a weak harmonic potential along the axial dimension as in an ODT. Other more complicated geometries of interfering beams may produce lattices with different geometries and periodicities relative to the wavelength of light used. Three mutually-orthogonal retro-reflected laser beams may be used to produce a cubic lattice, and this is a common arrangement for quantum simulation experiments which aim to study condensed matter systems.

Optical lattices are clean realizations of separable periodic potentials, and therefore their eigenstates are Bloch waves, which are labeled by quasi-momentum $q_i \in [-\pi/a_i, \pi/a_i]$[27], where a is the lattice periodicity in the dimension i, and $n \in \mathbb{N}$, which is the band index. Such Bloch waves take the form

$$\psi_{n,\vec{\mathbf{q}}}(\vec{\mathbf{r}}) = \mathrm{e}^{\mathrm{i}\vec{\mathbf{q}}\cdot\vec{\mathbf{r}}}u_{n,\vec{\mathbf{q}}}(\vec{\mathbf{r}}), \tag{2.62}$$

where $u_{n,\vec{\mathbf{q}}}(\vec{\mathbf{r}})$ is a spatially periodic function. For a retro-reflected lattice, the band-structure, or the energy of each eigenstate $\psi_{n,q}$, is solely determined by the dimensionless

[27] i.e. the first Brillouin zone.

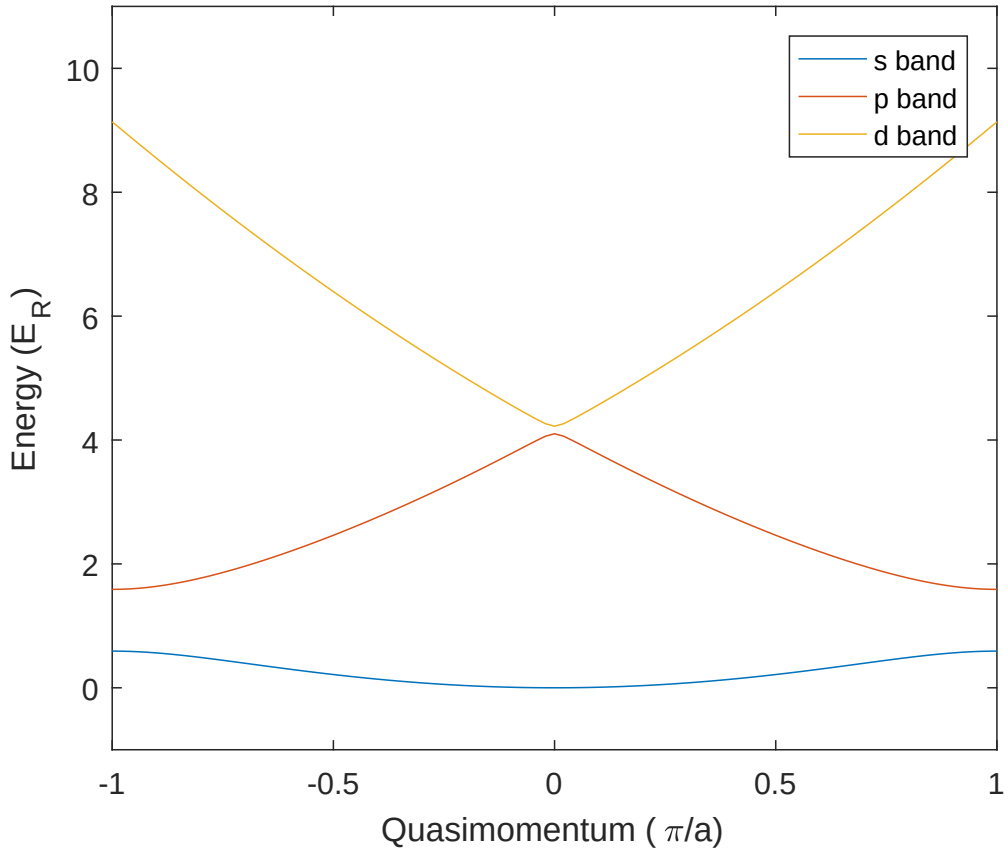

Figure 2.1: Band-structure of a retro-reflected optical lattice with lattice depth 2 recoil energies. The lowest three bands are shown. The atomic orbital labels s, p, and d are used to label the lowest three bands respectively.

quantity V_0/E_R. The band-structure can be computed numerically straight-forwardly by diagonalizing the Hamiltonian in the plane-wave basis over the first Brillouin zone. The band-structure for a 2 E_R and a 5 E_R retro-reflected lattice are shown in Figures 2.1 and 2.2 respectively. Transitions between the ground band and the first three excited bands are plotted in Figure 2.3.

It is convenient to define Wannier functions, which are super-positions of Bloch waves in the same band (or multiple bands in the case of bands with similar energy) that are

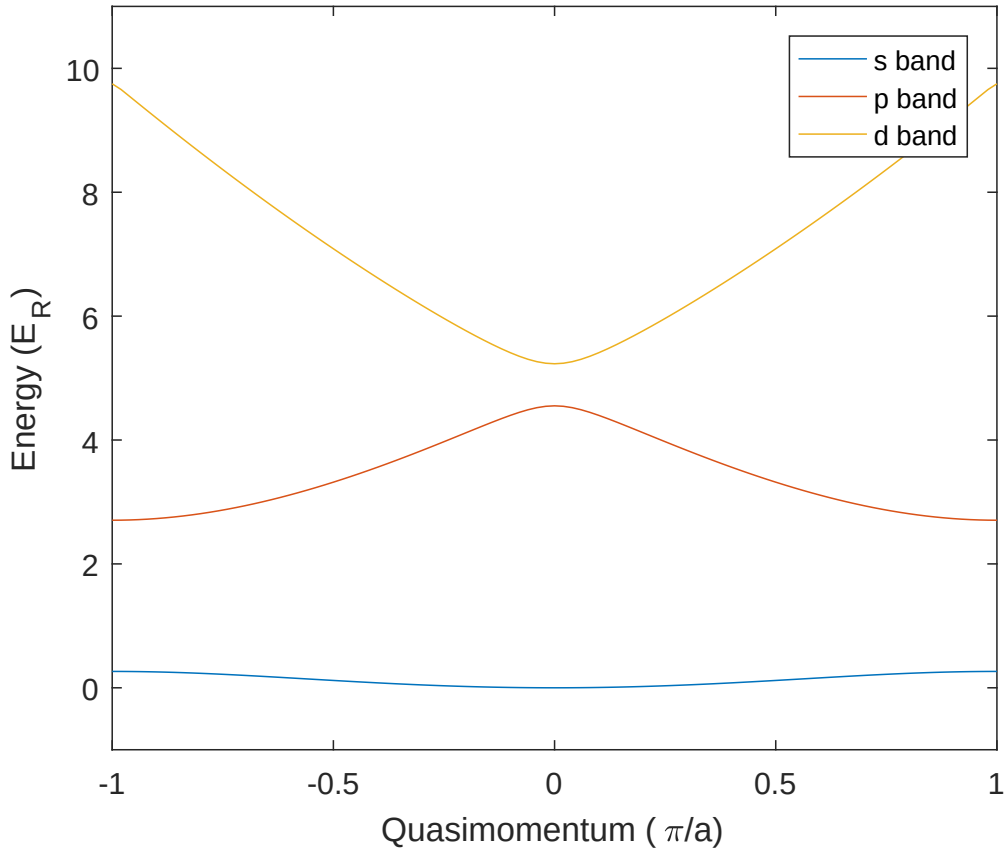

Figure 2.2: Band-structure of a retro-reflected optical lattice with lattice depth 5 recoil energies. The lowest three bands are shown. The atomic orbital labels s, p, and d are used to label the lowest three bands respectively.

localized[28] at a particular lattice vector $\vec{\mathbf{R}}$ and may be chosen to be real[29] [47, 48]. Explicitly, a Wannier function is defined as

$$w_{n,\vec{\mathbf{R}}}(\vec{\mathbf{r}} - \vec{\mathbf{R}}) = \int_{\mathrm{BZ}} \mathrm{d}^3\,\vec{\mathbf{q}} \mathrm{e}^{-\mathrm{i}\vec{\mathbf{q}}\cdot\vec{\mathbf{R}}} \psi_{n,\vec{\mathbf{q}}}(\vec{\mathbf{r}}). \tag{2.63}$$

[28]There is a freedom of choice of gauge in this transformation. For an isolated band n, a Wannier function may be multiplied by the unitary operator $\mathrm{e}^{\mathrm{i}\phi_n(\vec{\mathbf{q}})}$ for any scalar function $\phi_n(\vec{\mathbf{q}})$ and the result is also a Wannier function. This gauge freedom is more complicated for mixed bands. By choosing a specific gauge, maximally localized Wannier functions can be calculated.

[29]This is true for any Hermitian Hamiltonian. It is further conjectured that all maximally localized Wannier functions may be chosen to be real.

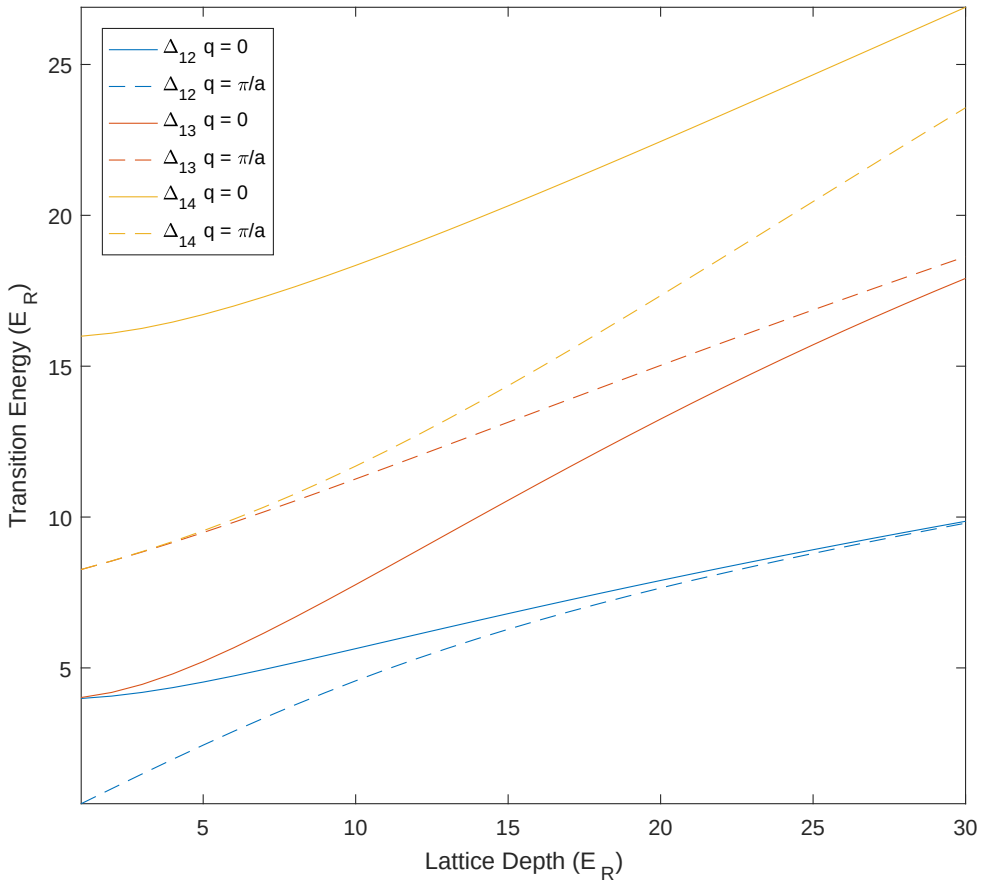

Figure 2.3: Transition energies as a function of lattice depth for transitions between the ground band and the first three excited bands of an optical lattice formed by retro-reflecting a laser beam. Transition energies are given for eigenstates at the center and edge of the Brillouin zone. Transition energies and lattice depths are given in terms of recoil energies.

Such Wannier functions may be used to calculate tunnelining matrix elements between lattice sites, as well as on-site interaction energies do to s-wave interactions. The tunneling energy between two sites i and j in a specific band is given by [49]

$$J_{i,j} = \int \mathrm{d}^3\vec{\mathbf{r}}\, w(\vec{\mathbf{r}} - \vec{\mathbf{R}_i})\left(-\frac{\hbar^2}{2m}\nabla^2 + V_{\text{lattice}}(\vec{\mathbf{r}})\right) w(\vec{\mathbf{r}} - \vec{\mathbf{R}_j}), \tag{2.64}$$

while the on-site interaction energy between two atoms is given by[30]

$$U_i = \frac{4\pi a_s \hbar^2}{m} \int \mathrm{d}^3\vec{\mathbf{r}}\, w(\vec{\mathbf{r}} - \vec{\mathbf{R}_i})^4. \tag{2.65}$$

For neutral atoms in an optical lattice, typically only nearest neighbor interactions are relevant, and for a sufficiently uniform trapping potential J and U are constant across the lattice. A useful estimate for U can be found by approximating the Wannier functions as the ground states of 3d harmonic oscillators[31]. If the geometric mean of the oscillator radial frequencies in each dimension is $\bar{\omega}$ and the geometric mean of the ground-state length-scales ($\sqrt{\hbar/m\omega}$) is $\bar{a_0}$, the interaction energy can be approximated as

$$U = \frac{2\hbar\bar{\omega}}{\sqrt{2\pi}} \frac{a_s}{a_0}. \tag{2.66}$$

Assuming that there are no more than two atoms per site, and they all occupy the lowest vibrational levels of each lattice site, the Hamiltonian governing the atoms is

$$H = -J \sum_{\langle i,j \rangle} b_i^\dagger b_j + \frac{U}{2} \sum_i b_i^\dagger b_i (b_i^\dagger b_i - 1) + \sum_i \mu_i b_i^\dagger b_i. \tag{2.67}$$

The first sum is taken over nearest neighbors, and represents tunneling between neighboring lattice sites. The second term counts the number of doubly occupied sites and penalizes them energetically by a factor U. The third term accounts for the harmonic trapping potential, which is accounted for in μ_i, the local chemical potential This is known as the Bose-Hubbard model, and its similarity to the Hamiltonians governing

[30] This assumes the interaction potential is $V_{\mathrm{int}}(\vec{\mathbf{r}} - \vec{\mathbf{r}}') = \frac{4\pi a_s \hbar^2}{m} \delta(\vec{\mathbf{r}} - \vec{\mathbf{r}}')$, which gives a scattering length equal to a_s the s-wave scattering length (in an appropriate limit).

[31] This approximation is less useful for calculating an estimate for J, as the weight of a Wannier function at a neighboring lattice site is substantially different to that of a harmonic oscillator ground state (since the potentials are substantially different this far away from the original lattice site). An excellent MATLAB code bank for calculating Wannier functions and Hubbard model parameters has been made available online by the Jaksch group [50].

electrons in solids is the starting point for many quantum simulation experiments. In order to reach the regime where the Bose-Hubbard Hamiltonian governs the atoms in a lattice, one must load into the ground band of the lattice. This is most straight-forwardly achievable by using a quantum degenerate gas.

2.4 Bose-Einstein condensation and superfluidity

The production of a Bose-Einstein condensate (BEC) in a dilute gas was long a goal of cold atom experiments, and was achieved in 1995. Two properties of BECs have made them enduring experimental tools beyond this initial quest. Firstly, a BEC produces large numbers of atoms in the ground state of a trap, which can then, for example, be loaded into the ground band of a lattice. Secondly, in practice, the BEC is also a superfluid[32], since the atomic gases used have weak repulsive interactions. This implies that not only are the atoms in the ground state of a trap, but the wavefunctions of these atoms have the same phase due to spontaneous breaking of the U(1) symmetry of the Schrödinger equation. Hence a superfluid BEC is a collection of large numbers of atoms with a single wavefunction, and is thus the apotheosis of quantum control.

2.4.1 Bose-Einstein condensation of a non-interacting Bose gas

The Bose-Einstein distribution was first developed by Bose in 1924 in the context of light quanta, and was later extended to atoms by Einstein. It gives the fractional occupation of states with energy ϵ for a gas of bosons that can equilibrate with a reservoir

[32]Superfluidity, a fluid with zero viscosity, was first observed in liquid helium-4, and Bose-Einstein condensation was proposed as the mechanism for this phenomenon. At typical temperatures, the condensate fraction in superfluid helium is $\sim$ 10%, and is limited by quantum depletion due to strong interactions.

at temperature T with which it can exchange particles, and is given by [51, 52, 53]

$$f_{\mathrm{BE}}(\epsilon) = \frac{1}{\mathrm{e}^{(\epsilon-\mu)/k_{\mathrm{B}}T} - 1}, \tag{2.68}$$

where μ, the chemical potential is the energy required to add a particle to the ensemble. The chemical potential must be less than the energy of the lowest energy state[33], which can be assumed to be zero in the thermodynamic limit. It is convenient to define the fugacity, $z = \mathrm{e}^{\mu/k_{\mathrm{B}}T} \leq 1$. The number of atoms at a given z is

$$N = N_{\mathrm{g}} + N_{\mathrm{e}} = \frac{z}{1-z} + \int_0^\infty \mathrm{d}\epsilon \, \frac{z\, g(\epsilon)}{\exp(\epsilon/k_{\mathrm{B}}T) - z}, \tag{2.69}$$

where $g(\epsilon)$ is the density of states, which, for a harmonic potential with a trap frequency of ν_j in the j-dimension, is

$$g(\epsilon) = \frac{\epsilon^2}{2h^3\nu_x\nu_y\nu_z}. \tag{2.70}$$

The population in the ground state is considered outside of the integral because $g(0) = 0$, which incorrectly sets the ground state occupation to zero. It can be shown that N_{e} is bounded from above by

$$N_e \leq \frac{(k_{\mathrm{B}}T)^3}{h^3\nu_x\nu_y\nu_z}\zeta(3), \tag{2.71}$$

where ζ is the Riemann zeta function, and equality holds when $z = 1$. On the other hand, N_{g} is unbounded as $z \to 1$. Therefore if number is increased at constant temperature, when the number of atoms exceeds the above bound they must exist in the ground state.

A more natural case is if particle number is fixed and temperature is decreased. In this case, when the bound drops below the number of particles in the system, the remaining particles enter the ground state. This temperature below which occupation of the ground

[33] If the chemical potential was larger than the energy of the lowest energy state, the value of the Bose-Einstein distribution would be negative for that state.

state begins to grow is known as the critical temperature, and is given by

$$T_{\mathrm{c}} = \frac{h\bar{\nu}}{k_{\mathrm{B}}}\left(\frac{N}{\zeta(3)}\right)^{1/3}, \tag{2.72}$$

where $\bar{\nu}$ is the geometric mean of the trap frequencies. The fraction of particles occupying the ground state as a function of temperature is

$$\frac{N_{\mathrm{g}}}{N} = 1 - \left(\frac{T}{T_{\mathrm{c}}}\right)^3, \tag{2.73}$$

and becomes unity at $T = 0\,\mathrm{K}$. This transition from a thermal Bose gas where there are negligible numbers of particles in the ground state, to a gas with macroscopic occupation of the ground state is called Bose-Einstein condensation, and the particles collected in the ground state are known as the Bose-Einstein condensate.

It is also instructive to consider the density of the thermal component at T_{c}. The number density as a function of position for a thermal Bose gas may be calculated by integrating out the momentum contribution to the energy (i.e. the kinetic energy) out of the Bose-Einstein distribution [54].

$$n_{\mathrm{T}}(\vec{\mathbf{r}}) = \frac{1}{(2\pi\hbar)^3}\int \mathrm{d}^3\,\vec{\mathbf{p}}\, f_{\mathrm{BE}}(\epsilon) = \frac{1}{(2\pi\hbar)^3}\int \mathrm{d}^3\vec{\mathbf{p}}\,\frac{z}{\exp(V(\vec{\mathbf{r}}) + |\vec{\mathbf{p}}|^2/2m)/k_{\mathrm{B}}T) - z} \tag{2.74}$$

At the transition, $z \to 1$ and the thermal density is

$$n_T(\vec{\mathbf{r}}) = \left(\frac{mk_{\mathrm{B}}T}{2\pi\hbar^2}\right)^{3/2}\sum_{l=1}^{\infty}\frac{\exp(lV(\vec{\mathbf{r}})/k_{\mathrm{B}}T)}{l^{3/2}} = \frac{1}{\lambda_{\mathrm{DB}}^3}\sum_{l=1}^{\infty}\frac{\exp(lV(\vec{\mathbf{r}})/k_{\mathrm{B}}T)}{l^{3/2}}, \tag{2.75}$$

where λ_{DB} is the thermal de Broglie wavelength. The quantity $n\lambda_{\mathrm{DB}}^3$ is equal to the phase-space density, ρ, of the gas, and at the center of the trap, where we set the potential to

be zero, the critical phase-space density for condensation is

$$\rho_{\mathrm{c}} = \sum_{l=1}^{\infty} \frac{1}{l^{3/2}} = \zeta(3/2) \approx 2.612. \tag{2.76}$$

The critical temperature may be thought of the temperature below which the inter-particle spacing is of similar length to the thermal de Broglie wavelength. Equivalently, the transition occurs at phase-space densities of O(1).

2.4.2 Superfluidity in a weakly-interacting Bose gas

The Bose-Einstein condensation transition occurs for non-interacting bosons, and is purely a feature of bosonic quantum statistics. For weakly-interacting bosons there also exists a quantum phase transition (a phase transition that occurs at $T = 0\,\mathrm{K}$), which is known as the superfluid transition. The most successful theoretical framework for superfluidity was developed by Landau, for which he was awarded the Nobel Prize in 1962. The second-quantized Hamiltonian for bosons with a two-point interaction is [55]

$$H - \mu N = \int \mathrm{d}^3\vec{\mathbf{r}}\, \psi^\dagger(\vec{\mathbf{r}}) \left[-\frac{\nabla^2}{2m} - \mu \right] \psi(\vec{\mathbf{r}}) + \frac{1}{2} \int \mathrm{d}^3\vec{\mathbf{r}} \int \mathrm{d}^3\vec{\mathbf{r}}\,' \psi^\dagger(\vec{\mathbf{r}}) \psi^\dagger(\vec{\mathbf{r}}\,') V(\vec{\mathbf{r}} - \vec{\mathbf{r}}\,') \psi(\vec{\mathbf{r}}) \psi(\vec{\mathbf{r}}\,'). \tag{2.77}$$

The grand canonical partition sum is

$$\mathcal{Z} = \operatorname*{Tr}_{\mathcal{B}} \mathrm{e}^{-\beta(H-\mu N)} = \int \mathcal{D}[\phi^*(\vec{\mathbf{r}}, \tau), \phi(\vec{\mathbf{r}}, \tau)]\, \mathrm{e}^{-S}, \tag{2.78}$$

where the trace is taken over the bosonic Fock space, and the second term is a path integral over coherent states, where τ is an imaginary time parameter that parametrizes $\beta = 1/k_{\mathrm{B}}T$, and S is the action. For a hard-sphere potential V, which can be expressed

as

$$V(\vec{\mathbf{r}} - \vec{\mathbf{r}}') = V_0\,\delta(\vec{\mathbf{r}} - \vec{\mathbf{r}}'), \tag{2.79}$$

where $V_0 > 0$ for repulsive interactions, the action reads

$$S = \int \mathrm{d}\tau \int \mathrm{d}^3\vec{\mathbf{r}}\,[\phi^*\partial_\tau\phi + \frac{1}{2m}(\vec{\nabla}\phi^*)\cdot(\vec{\nabla}\phi) - \mu|\phi|^2 + \frac{V_0}{2}|\phi|^4], \tag{2.80}$$

where the coherent states are functions of $\vec{\mathbf{r}}$ and τ. The first term in the action originates from insertions of the identity during the Trotter decomposition of the trace. For $\mu > 0$ the effective potential

$$V(\phi) = \frac{V_0}{2}\left(|\phi|^2 - \frac{\mu}{V_0}\right)^2|\phi|^2, \tag{2.81}$$

exhibits the classic Mexican hat shape which is emblematic of spontaneous symmetry breaking. The potential and action is minimized for

$$\phi_0 = \sqrt{\frac{\mu}{V_0}}\mathrm{e}^{\mathrm{i}\varphi_0}, \tag{2.82}$$

where φ_0 is a phase freedom which is due to the U(1) symmetry of the Hamiltonian and action. The expectation value of the $\psi(\vec{\mathbf{r}},\tau)$ operator is

$$\langle\psi(\vec{\mathbf{r}})\rangle_{H-\mu N} = \frac{1}{\mathcal{Z}}\operatorname*{Tr}_{\mathcal{B}}\mathrm{e}^{-\beta(H-\mu N)}\psi(\vec{\mathbf{r}}) = \frac{1}{\mathcal{Z}}\int \mathcal{D}[\phi^*(\vec{\mathbf{r}},\tau),\phi(\vec{\mathbf{r}},\tau)]\,\phi(\vec{\mathbf{r}},\tau)\,\mathrm{e}^{-S} \tag{2.83}$$

and for $\mu > 0$ and $T \to 0$ K

$$\langle\psi(\vec{\mathbf{r}},\tau)\rangle_{H-\mu N} \to \sqrt{\frac{\mu}{V_0}}\mathrm{e}^{\mathrm{i}\varphi_0}. \tag{2.84}$$

Similarly, the the two-point correlation function for $\mu > 0$ and $T \to 0$ K is

$$\langle \psi^\dagger(\vec{\mathbf{r}})\psi(\vec{\mathbf{r}}')\rangle_{H-\mu N} \underset{|\vec{\mathbf{r}}-\vec{\mathbf{r}}'|\to\infty}{\longrightarrow} \langle \psi^\dagger(\vec{\mathbf{r}})\rangle\langle\psi(\vec{\mathbf{r}}')\rangle = \frac{\mu}{V_0}, \tag{2.85}$$

where we have applied the cluster property. This fulfills the criterion for spontaneous symmetry breaking, as the system shows off-diagonal long-range order[34]. One can show that the expectation value of the number operator in this limit (where the system is in the ground state) is macroscopic. The coherent-state operator can be re-written in terms of local density and phase, as

$$\phi(\vec{\mathbf{r}},\tau) = \sqrt{\rho(\vec{\mathbf{r}},\tau)}\mathrm{e}^{\mathrm{i}\varphi(\vec{\mathbf{r}},\tau)}. \tag{2.86}$$

The action can be rewritten in terms of the ρ and φ operators, and one can show that equations of motion of the symmetry-breaking state are those of a fluid with zero viscosity, and that two systems with different phase exhibit the Josephson effect.

2.4.3 The Thomas-Fermi regime

It is useful to consider a mean-field approach to the case of weakly interacting bosons. Given a multi-particle Hamiltonian of the form

$$H = \sum_{i=1}^{N}\left[\frac{|\vec{\mathbf{p}}_i|^2}{2m} + V(\vec{\mathbf{r}}_i)\right] + g\sum_{i<j}\delta(\vec{\mathbf{r}}_i - \vec{\mathbf{r}}_j), \tag{2.87}$$

[34]For $\mu < 0$ the two-point correlation function goes to zero.

where $g = 4\pi\hbar^2 a_s/m$[35], one can develop a mean-field equation for a large number of particles, all with the same wavefunction[36], as is in the case of a BEC. Having minimized the energy while holding the particle number fixed, one obtains

$$-\frac{\hbar^2}{2m}\nabla^2\psi(\vec{\mathbf{r}}) + V(\vec{\mathbf{r}})\psi(\vec{\mathbf{r}}) + g|\psi(\vec{\mathbf{r}})|^2\psi(\vec{\mathbf{r}}) = \mu\psi(\vec{\mathbf{r}}). \tag{2.88}$$

Here the equality comes from equating the energy of the wavefunction to μN to ensure that particle number is fixed. This is known as the time-independent Gross-Pitaevskii equation (GPE), and it can be used to calculate the ground-state of a weakly-interacting Bose gas in a harmonic potential. For a sufficiently large cloud, the interaction and potential terms dominates the kinetic term, which can be neglected. This is known as the Thomas-Fermi approximation, and in this regime the GPE has the solution

$$|\psi(\vec{\mathbf{r}})|^2 = \frac{1}{g}\Big(\mu - V(\vec{\mathbf{r}})\Big), \tag{2.89}$$

for $\mu - V(\vec{\mathbf{r}}) \geq 0$. Elsewhere, the density is zero. For a harmonic potential, given by

$$V(\vec{\mathbf{r}}) = \frac{1}{2}m(\omega_x^2 x^2 + \omega_y^2 y^2 + \omega_z^2 z^2), \tag{2.90}$$

the spatial density profile is therefore an inverted parabola, with peak value μ/g. The length-scales of this spatial distribution (i.e. half the distance between density zeros along a dimension i) are $R_i = (2\mu/m\omega_i^2)^{1/2}$. The chemical potential can be computed by enforcing that the integral of the density function over all space (in actuality only the

[35]This value for U_0 is used to reproduce the scattering length obtained from using the actual interatomic potential.

[36]This approximation is valid for weak interactions. For a system like superfluid helium, where interactions are strong, there is significant "depletion" of the condensate due to interactions and there are particles with other, longer-length-scale wavefunctions.

region specified by these length-scales) is equal to the number of particles, N. Thus,

$$\begin{aligned} N = \int \mathrm{d}\vec{\mathbf{r}}\,|\psi(\vec{\mathbf{r}})|^2 &= \frac{\mu}{g\omega_x\omega_y\omega_z}\left(\frac{2\mu}{m}\right)^{3/2}\int_0^1 \mathrm{d}R\int_0^\pi \mathrm{d}\theta\int_0^{2\pi}\mathrm{d}\phi\, R^2\sin(\theta)(1-R^2) \\ &= \frac{8\pi\mu}{15g\omega_x\omega_y\omega_z}\left(\frac{2\mu}{m}\right)^{3/2}, \end{aligned} \tag{2.91}$$

and the chemical potential is

$$\mu = \left(\frac{m}{2}\right)^{3/5}\left(\frac{15gN\omega_x\omega_y\omega_z}{8\pi}\right)^{2/5} = \frac{\hbar^2}{2m}\left(\frac{15Na_\mathrm{s}}{a_x^2a_y^2a_z^2}\right)^{2/5}, \tag{2.92}$$

where $a_i = \sqrt{\hbar/m\omega_i}$ are the length scales of the harmonic oscillator in each dimension. Thus the length-scales of the spatial distribution are

$$R_i = \left(\frac{\hbar\bar{\omega}}{m\omega_i^2}\right)^{1/2}\left(\frac{15Na_\mathrm{s}}{\bar{a}}\right)^{1/5}, \tag{2.93}$$

where $\bar{\omega}$ and $\bar{a}$ are the geometric means of the oscillator radial frequencies and length-scales, respectively. The R_i are known as the Thomas-Fermi radii, and can be substantially larger than the a_i.

In order to study the dynamics of a condensate, one can construct the time-dependent Gross-Pitaevskii equation,

$$\mathrm{i}\hbar\frac{\partial\psi(\vec{\mathbf{r}})}{\partial t} = \left[-\frac{\hbar^2}{2m}\nabla^2 + V(\vec{\mathbf{r}}) + g|\psi(\vec{\mathbf{r}})|^2\right]\psi(\vec{\mathbf{r}}). \tag{2.94}$$

The time-dependent GPE successfully predicts the hydrodynamic modes of a superfluid gas.

Chapter 3

^{7}Li atomic properties & cooling

Lithium is the lowest atomic number alkali metal. Two stable isotopes exist, ^{7}Li, a boson, and ^{6}Li a fermion[1]. Both isotopes have been cooled to quantum degeneracy. To this date in the Weld group we have solely trapped and cooled ^{7}Li, which has a natural abundance of $\sim 92.5\%$, though our apparatus is in principle capable of co-trapping both isotopes. A few different pathways to achieving degeneracy exist, but it is possible with only one resonant laser, at 671 nm, with MHz scale linewidths. At this time, the most common way to produce this light is with direct laser diodes[2] in an external-cavity diode laser (ECDL) set up, and with tapered amplifiers for power amplification. The background s-wave scattering rates of bosonic lithium hyperfine sub-levels are not sufficiently large and positive to achieve efficient evaporation and condensation, but a broad Feshbach resonance at approximately 730 Gauss allows for the tuning of the scattering length[3]. Further, tuning the scattering length tunes the Hubbard model parameter U (see equation 2.65), which allows for the exploration of a rich quantum phase space. The low mass

[1] ^{6}Li is one of only two stable fermionic alkali metal isotopes, the other being ^{40}K. Both are widely used in quantum simulation experiments where Fermi statistics are required.

[2] These diodes are on the lower edge of wavelengths accessible by non-GaN-based semi-conductors, and aren't as high-powered or tunable as diodes in the range 780-980 nm.

[3] The Feshbach resonance in ^{6}Li has been used to produce Feshbach molecules, and to explore the BEC-BCS (Bardeen-Cooper-Schrieffer) crossover.

of Li leads to relatively large J (see equation 2.64), which is also desirable[4]. For these reasons, Li is a popular atom for ultracold atom quantum simulation experiments.

3.1 ^{7}Li level structure & laser cooling

As an alkali metal, lithium has a single valence electron, which exists in a $2s$ shell when unexcited, so $S = 1/2$, $L = 0$ and $J = 1/2$, giving a Russell-Saunders term $^2S_{1/2}$. ^{7}Li has a nuclear spin, $I = 3/2$, leading to hyperfine structure[5]. The ground-state is split into two hyperfine levels, $F = 2$ and $F = 1$, which are split by 803.5 MHz. The optical transitions that are typically addressed are between the $2s$ hyperfine manifolds to the $2p$ hyperfine manifolds, and are within approximately 10 GHz of each other for both isotopes, at approximately 671 nm, with linewidths of approximately 6 MHz[6]. The $2p$ orbital splits into two fine-structure levels, which are split by 10.052 GHz. Historically this splitting was observed as a doublet in spectographs of atomic fluorescence, and the $^2S_{1/2} \rightarrow {}^2P_{1/2}$ transitions are known as D1 transitions, while the $^2S_{1/2} \rightarrow {}^2P_{3/2}$ transitions are known as D2 transitions. The $^2P_{1/2}$ level is split into $F' = 2$ and $F' = 1$ hyperfine levels, and the $^2P_{3/2}$ level is split into four hyperfine levels, labeled $F = 0, 1, 2$ and 3. The hyperfine splitting in the $^2P_{1/2}$ manifold is 92.03 MHz, while the splittings in the $^2P_{3/2}$ are much smaller. The most experimentally relevant states are the the $F' = 2$ and $F' = 3$ hyperfine levels which, are split by 9.39 MHz, which is on the order of the linewidth of the transitions, and are therefore not resolvable. See Fig. 3.1 for an energy

[4]For atoms in lattices produced by a retro-reflected laser the tunneling rate can be expressed in terms of only the recoil energy. Thus, tunneling depends inversely on mass. Having fast tunneling times allows for longer relative experimental sequences, which is advantageous for adiabatic processes. Perhaps more significantly, nearest-neighbor interactions in neutral-atom lattice experiments are solely provided by superexchange, the energy scale of which is $\propto J^2/U$, which sets a temperature scale of < 1 nK. Thus, understandably, the most successful demonstrations of anti-ferromagnetic ordering with cold atoms have been achieved with ^{6}Li.

[5] ^{6}Li also has a nuclear spin, I=1/2.

[6]Further laser cooling on the narrower 323 nm transition between the $2s$ and $3p$ orbtals has been demonstrated [56].

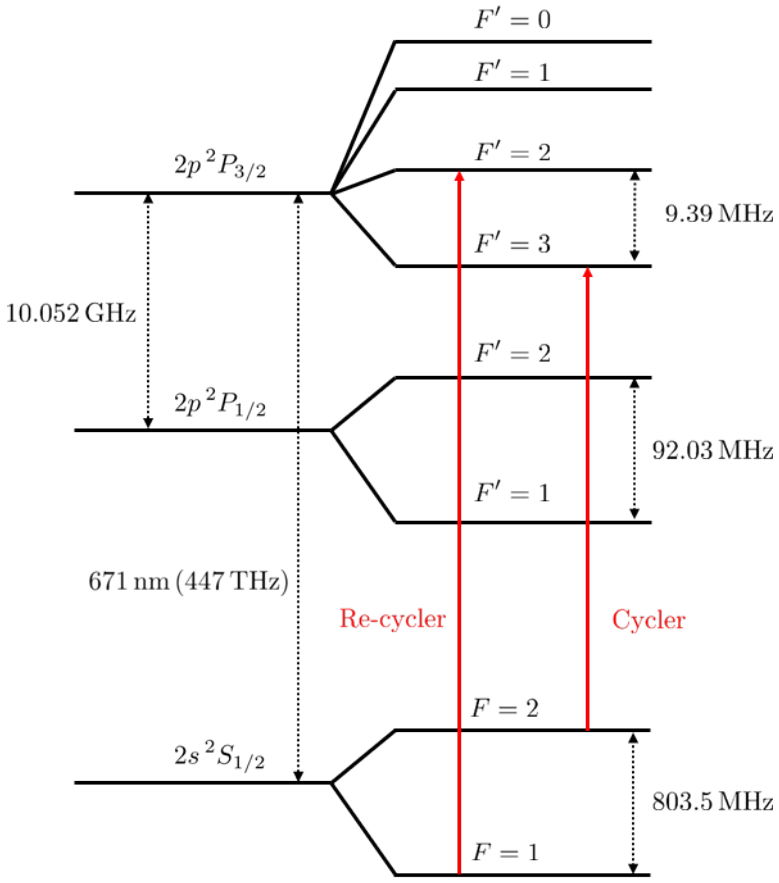

Figure 3.1: A level diagram depicting experimentally relevant energy levels in ^{7}Li.

level diagram of ^{7}Li, which summarizes these details.

The only cycling transitions available are the $\sigma^{\pm}$ D2 transtitions between $^2S_{1/2}\,|F = 2, m_F = \pm 2\rangle$ and $^2P_{3/2}\,|F' = 3, m_{F'} = \pm 3\rangle$ hyperfine sub-levels. However in practice, since the splitting between the $F' = 3$ and $F' = 2$ manifolds in the $^2P_{3/2}$ state is only 9.39 MHz, imperfect polarization leads to population of the $F' = 2$ sub-levels, which introduces a leak into the ground-state $F = 1$ manifold. In order to scatter sufficient photons off of ^{7}Li atoms to slow, cool or image them, a "re-cycling" laser is required[7],

[7]In order to laser cool Rb, a similar laser is required to repump atoms out of a dark hyperfine state. However since the excited-state hyperfine splitting is large relative to the linewidth in this case, the main cooling transition is "more" cycling, and the power ratio between cooler and repumper is high. For ^{7}Li it is effectively $1:1$, leading us to call what is traditionally called the "cooler" the "cycler" and what is traditionally called the "repumper" the "re-cycler."

Electron spin, S	1/2
Nuclear spin, I	3/2
Ground-state hyperfine splitting	803.5 MHz
Cycling transition	$2s\,^2S_{1/2}\,F = 2 \rightarrow 2p\,^2P_{3/2}\,F' = 3$
Recycling transition	$2s\,^2S_{1/2}\,F = 1 \rightarrow 2p\,^2P_{3/2}\,F' = 2$
Wavelength, λ_0	670.975 nm
Linewidth, $\Gamma/2\pi$	5.87123 MHz
Doppler temperature, T_{D}	141 μK
Recoil temperature, T_{R}	3 μK
Saturation intensity, I_{sat}	2.54 mW/cm^2

Table 3.1: Selected ^{7}Li properties.

resonant with the D2 transition from $^2S_{1/2}\,F = 1 \rightarrow {}^2P_{3/2}\,F' = 2$, and 812.9 MHz detuned from the cycler. Some properties of ^{7}Li related to laser cooling are summarized in Table 3.1.

3.2 ^{7}Li magnetic properties

The ground-state hyperfine manifolds are split into 8 Zeeman sub-levels. The $F = 2$ hyperfine manifold has 5 Zeeman sub-levels, with m_F = -2, -1, 0, 1 and 2, and the $F = 1$ hyperfine manifold has 3 Zeeman sub-levels, with m_F = -1, 0 and 1. The Landé g-factor g_F is 1/2 for the $F = 2$ manifold, and is $-1/2$ for the $F = 1$ manifold, leading to the sub-levels to have opposite Zeeman shifts at low-field for the two different hyperfine manifolds. Thus there are three magnetically-trappable states: $|F = 2, m_F = 2\rangle$, $|F = 2, m_F = 1\rangle$ and $|F = 1, m_F = -1\rangle$. Of these the most desirable for magnetic-trapping is the $|F = 2, m_F = 2\rangle$ sub-level, as it experiences the deepest potential for a given magnetic-field gradient[8] and is immune to spin-changing collisions[9]. It is straightforward to force evaporation from the magnetic trap by driving magnetic dipole transi-

[8]Additionally, due to the decoupling of nuclear and electron spin at high-field, the $|F = 1, m_F = -1\rangle$, which starts off trappable, becomes anti-trappable above 140 G.

[9]Total m_F must be conserved during a spin-changing collision in order to conserve spin angular momentum.

Hyperfine Manifold	g_F
$^2S_{1/2}\,F=2$	1/2
$^2S_{1/2}\,F=1$	-1/2
$^2P_{3/2}\,F=3$	2/3
$^2P_{3/2}\,F=2$	2/3
$^2P_{1/2}\,F=2$	1/6

Table 3.2: Landé g-factors for experimentally relevant ground-state and excited-state hyperfine manifolds.

tions from the $|F=2,m_F=2\rangle \rightarrow |F=1,m_F=1\rangle$, which is anti-trapped. The g-factors for experimentally relevant hyperfine manifolds are listed in Table 3.2.

It is useful to consider the relative Zeeman shifts between states involved in laser cooling. As discussed in section 3.1, the cycling transitions are between the $^2S_{1/2}\,F=2$ and $^2P_{3/2}\,F'=3$ hyperfine levels. The relative Zeeman shifts between Zeeman sub-levels related via $\sigma^{\pm}$ transitions between these two hyperfine manifolds are given in Table 3.3. The relative Zeeman shifts for the re-cycling transition, between the $^2S_{1/2}\,F=2$ and $^2P_{3/2}\,F'=2$ hyperfine levels, are given in Table 3.4.

D1 transitions are used to optically pump atoms into the $|F=2,m_F=2\rangle$ ground state before loading into the magnetic trap[10]. A bias magnetic-field is used during this process to set a quantization axis, so therefore it is useful to consider the Zeeman shifts between these hyperfine levels. The relative Zeeman shifts for σ^+ D1 optical pumping transitions are given in Table 3.5.

Magnetic dipole transitions are used to eject hot $|F=2,m_F=2\rangle$ atoms from the magnetic trap during RF-assisted forced evaporation. We use a stimulated emission process to transfer the atom from the $|F=2,m_F=2\rangle$ state to the the $|F=1,m_F=1\rangle$ state, which is anti-trapped by a magnetic-field minimum due to its negative g-factor

[10]Optical pumping is also possible on the D2 transition, but leads to continuous cycling on the $|F=2,m_F=2\rangle \rightarrow |F=3,m_F=3\rangle$ transition, and therefore heating. D1 optical pumping between the $^2S_{1/2}\,F=2$ and $^2P_{1/2}\,F'=2$ hyperfine levels is self-terminating, as there are no possible σ^+ transions out of the $|F=2,m_F=2\rangle$ state.

Ground State	Excited State	Transition Shift (MHz/G)
$\|F=2, m_F=\pm 2\rangle$	$\|F'=3, m_{F'}=\pm 3\rangle$	$\pm$ 1.40
$\|F=2, m_F=\pm 1\rangle$	$\|F'=3, m_{F'}=\pm 2\rangle$	$\pm$ 1.17
$\|F=2, m_F=0\rangle$	$\|F'=3, m_{F'}=\pm 1\rangle$	$\pm$ 0.93
$\|F=2, m_F=\mp 1\rangle$	$\|F'=3, m_{F'}=0\rangle$	$\mp$ 0.70
$\|F=2, m_F=\mp 2\rangle$	$\|F'=3, m_{F'}=\mp 1\rangle$	$\mp$ 0.47

Table 3.3: Transition shifts for $\sigma^{\pm}$ D2 cycling transitions at low-field.

Ground State	Excited State	Transition Shift (MHz/G)
$\|F=1, m_F=\pm 1\rangle$	$\|F=2', m_{F'}=\pm 2\rangle$	$\pm$ 2.57
$\|F=1, m_F=0\rangle$	$\|F=2', m_{F'}=\pm 1\rangle$	$\pm$ 0.93
$\|F=1, m_F=\mp 1\rangle$	$\|F=2', m_{F'}=0\rangle$	$\mp$ 0.70

Table 3.4: Transition shifts for $\sigma^{\pm}$ D2 re-cycling transitions at low-field.

(see Table 3.2). Additionally, this magnetic dipole transition is used to transfer atoms from the $|F=2, m_F=2\rangle$ state to the $|F=1, m_F=1\rangle$ state in the optical trap by using adiabatic rapid passage. The Zeeman shift for this transition is 2.1 MHz/G.

3.3 ^{7}Li scattering properties

The background scattering length between Li atoms can be decomposed into a singlet and a triplet contribution, based on the total spin of the colliding pair of atoms. For ^{7}Li the triplet s-wave scattering length is -27.6 a_0 and the singlet s-wave scattering length is 33 a_0 [57, 58].For collisions between two atoms of the $|F=2, m_F=2\rangle$ state (i.e. the state that is magnetically trapped), the collisions are purely triplet in character, and

Ground State	Excited State	Transition Shift (MHz/G)
$\|F=2, m_F=1\rangle$	$\|F'=2, m_{F'}=2\rangle$	1.17
$\|F=2, m_F=0\rangle$	$\|F'=2, m_{F'}=1\rangle$	0.23
$\|F=2, m_F=-1\rangle$	$\|F'=2, m_{F'}=0\rangle$	-0.70
$\|F=2, m_F=-2\rangle$	$\|F'=2, m_{F'}=-1\rangle$	-1.63

Table 3.5: Transition shifts for σ^{+} D1 optical pumping transitions at low-field.

therefore the background s-wave scattering length is -27.6 a_0. At non-zero temperature this scattering length has a zero-crossing at 6.6 mK, as discussed in section 2.1.5, which makes evaporative cooling inefficient even in clouds at a temperature of 1 mK. In order to efficiently evaporate in the magnetic trap, the temperature must be lowered via laser cooling. We achieve this by using gray molasses cooling on the $D1$ transition to lower the cloud temperature to approximately 50 μK before loading into the magnetic trap.

At these cloud temperatures RF evaporation proceeds, but a BEC is not stable to attractive interactions above a certain atom number [59], and therefore it is common to transfer the atoms to the $|F = 1, m_F = 1\rangle$ state (in an optical trap, as this state is not magnetically trappable), which has a background s-wave scattering length of 5.1 a_0 [60, 61], but more importantly has a broad Feshbach resonance which can be used to tune the interactions [62], with $B_0 = 736.8(2)$ G, $B_\Delta = -192.3(3)$ G and $a_{\mathrm{BG}} = -24.5^{+3.0}_{-0.2}\, a_0$ (see equation 2.32 for definitions of these parameters)[11]. The magnetic field at which the scattering length diverges (B_0) is accessible with conventional electromagnets, and the breadth of the resonance (parameterized by B_Δ) relaxes constraints on the precision of the applied magnetic field.

3.4 Preparation of a large flux of cold atoms

A Li atom begins its life-cycle in the machine in the oven. The oven consists of a reservoir, which was initially loaded with 25 g of Li, that is heated above the melting temperature to 450 °C, and a collimating nozzle made of microcapillaries, which is heated to 550 °C (see Section 5.3.2 for details on the Li oven). This produces a collimated atomic beam, with beam divergence given by the aspect ratio of the microcapillaries, which is 1 : 50, which corresponds to a solid angle roughly four times the solid angle subtended

[11] This fit is only accurate near the resonance. It does not feature the zero-crossing in scattering length at low magnetic fields which leads to a positive background scattering length.

by the MOT, which is roughly 2 cm in diameter and 2 m away. In order to further collimate the beam, we employ transverse cooling in the transverse cooling cube of the oven manifold (see Section 5.3.3 for details on the oven manifold). A Zeeman slower is used to modify the speed distribution of the atomic beam to increase the fraction of atoms with speeds lower than the capture velocity of the MOT (see Sections 2.2.2 and 5.4 for details on Zeeman slowing and the Li Zeeman slower). Due to the low mass of Li, beam explosion is particularly problematic, and transverse cooling after the Zeeman slower is also used. The initial MOT-loading rate is $\sim 5 \times 10^8$ atoms/s and is a lower bound on the flux of slowed atoms through the MOT region.

3.4.1 Pre-slower transverse cooling

Transverse cooling is 2d optical molasses (see Section 2.2.1 for a discussion of optical molasses). The drag co-efficient produced by molasses beams is given by equation 2.33, and is maxmized for a detuning of $-\Gamma/2$ and intensity of $I_{\rm sat}/N$, where N is the dimension of cooling (here, 2). For these parameters, the drag coefficient is $\hbar k^2/8$, where k, the wavenumber, is $2\pi/\lambda$, where λ is the resonance wavelength, 671 nm. Therefore as the atoms move through the transverse cooling region their transverse velocities decrease exponentially with time, with a time constant of $\hbar k^2/8m$, where m is the mass of the atom. In ^{7}Li this corresponds to a time constant of 10 μs, and, for atoms traveling at 1000 m/s, a distance of 1 cm. Of course, molasses has a lower temperature limit given by the Doppler temperature, and for this detuning and intensity, the lower temperature limit is twice the Doppler temperature[12]. This corresponds to a root-mean-squared speed of 1 m/s for ^{7}Li. For atoms traveling at the extremal angle defined by the aspect ratio of

[12]Molasses also has a capture velocity of $\Gamma/2k$, which for Li is 2 m/s. This is much smaller than the transverse velocities of atoms traveling at 1000 m/s at the extremal angle defined by the aspect ratio of the microcapillaries (20 m/s) and is perhaps why pre-Zeeman slower transverse cooling has not been effective in our Li experiment.

the microcapillaries, the ratio of this lower speed limit to their speed is roughly $1/e^3$, and therefore an interaction region of 3 cm is required to maximally collimate the beam. This is close to the maximal interaction length possible in a 2.75" conflat cube[13]. For optimal power efficiency, the laser beams used for transverse cooling should have a rectangular profile, with length 3 cm and width determined by the width of the atomic beam (0.5 cm). We use cylindrical optics to produce a beam shape close to these dimensions. We use light with detuning $-\Gamma/2$ and use a power of 2.5 mW, with a $1:1$ ratio of cycler to re-cycler power. In practice we only use transverse cooling in the vertical dimension due to power constraints. We believe that the transverse cooling beams have the added benefit of angling the atomic beam downwards, which better aligns it with the MOT, due to a misalignment between the oven and main chamber sections.

3.4.2 Zeeman slowing

At the temperatures necessary to produce a substantial vapor pressure of Li, the fraction of atoms in the speed distribution of the atomic beam below the capture velocity of the MOT is negligible. Therefore some method of modifying the speed distribution to enlarge this fraction is necessary. We employ a decreasing-field spin-flip Zeeman slower that is designed to slow atoms traveling at 1000 m/s or below to 50 m/s (see Sections 2.2.2 and 5.4 for details on Zeeman slowing and the Li Zeeman slower). The Zeeman slower laser beam was originally set to be focused to the size of the nozzle at the nozzle, with an initial beam diameter filling 1" optics, but was then empirically adjusted to maxmize load rate. The beam has a power of 60 mW and is detuned by 390 MHz from the cycling transition. Sidebands are added the beam with a home-made electro-optic modulator that operates at 813.5 MHz. The positive sideband serves as the recycling light, while the negative sideband is off of resonance. The power in the sidebands is roughly 30% of

[13]The clear aperture of a 2.75" conflat window is 1.3".

the carrier power. The slower is designed to use σ^+ transitions in the decreasing-field section of the slower, where the magnetic field points away from the MOT. Therefore the slower light is initially set to have right-handed circular polarization using two quarter waveplates, before it is empirically optimized while maximizing the loading rate of the MOT.

3.4.3 Post-slower transverse cooling

During Zeeman slowing the beam diameter expands due to three reasons. Firstly, the beam simply expands based on the angle set by the aspect-ratio of the microcapillaries in the nozzle, or based on the ratio of the speed of the atoms to the lowest transverse speed obtained via transverse cooling (see Section 3.4.1). Secondly, the slowed-beam expands due to the preferential reduction in its longitudinal velocity as it is slowed. Thirdly, the slowed-beam expands due to heating in the transverse dimension caused by the emitting of photons with directional components in the transverse plane. This is known as beam explosion, and is the only source of expansion that is capable of causing the atoms in our atomic beam to clip on the Zeeman slower tube while moving towards the MOT. To maximize the fraction of atoms that reach the MOT after the Zeeman slowing stage, we employ a second stage of transverse cooling in a 1.33" conflat cube after the increasing-field section of the Zeeman slower (see Section 5.4 for a discussion of the Li Zeeman slower design). We use a single laser beam to transversely cool both dimensions, by cycling it through the two axes with mirrors and retro-reflecting it. The laser beam is collimated and fills the 1.33" conflat window (which has a clear aperture of 0.6") and has a cycler power of 1.8 mW and a re-cycling power of 1 mW. Since the relevant atoms in this region are traveling at the MOT capture velocity or less, the required interaction length is very small. We empirically set the polarization with a quarter wave-plate; there are

non-negligible magnetic fields at this location due to the proximity to the increasing-field section of the Zeeman slower[14].

3.5 Initial trapping, cooling and spin-polarization

The magneto-optical trap (MOT) is the first trapping and truly[15] cooling stage of the experiment. See Section 2.3.1 for a discussion of the operation of a MOT. In the Li experiment it is operated mainly as an accumulation stage, during which atoms below the capture velocity (v_c) of the MOT are trapped from the Zeeman-slowed atomic beam. The compressed MOT stage, which is immediately after the MOT stage, is used to increase the density and lower the temperature of the MOT cloud, without a reduction in atom number.

3.5.1 MOT

The MOT was designed to be operated with 3 pairs of beams: one pair in the vertical dimension (beams 1 & 2), entering through the re-entrant windows, and two pairs in the horizontal plane (beams 3, 4, 5 & 6), each at a 31.5° angle to the atomic beam. Such a low angle is atypical of cold atom experiments, and was necessitated by our main chamber design which prioritized optical access. The $1/e^2$ diameters of the MOT beams are 32 mm, but are effectively clipped on 1" lenses. The beams are approximately collimated and are mildly focused or defocused to ensure power-balancing on the MOT and subsequent compressed MOT (cMOT). The deceleration from the capture velocity is provided by the two MOT beams that are in the horizontal plane and have non-zero

[14] A polarization maintaining (PM) fiber is used for this light, and therefore the light is linearly polarized coming out of the fiber.

[15] Transverse cooling and the Zeeman slower do modify the speed distribution of the atoms, but do not result in cooling.

components counter to the propagation of the atomic beam. Assuming 8.25 mW of power in each of these beams, a detuning of -4.5 Γ and an interaction length equal to the projection of the 1" beam diameter on to the atomic beam dimension, we find the capture velocity of the MOT is 32 m/s. This calculation assumes a constant scattering rate through the deceleration, and neglects the Doppler and Zeeman shifts (which can be thought of as approximately canceling each other), but is a useful estimate.

The six MOT beams are produced by a custom Oz Optics non-polarization-maintaining (non-PM) 2 : 6 fiber splitter, and are expanded and collimated either with a collimation package and telescope, or simply a fast lens. Our first MOT was made using 3 retro-reflected beams, but this arrangement limited the MOT size, as the optical density of the MOT was sufficient to greatly lower the intensity of the forwards-propogating beam in the location of the MOT. We later upgraded the MOT setup to include a fourth pair of MOT beams (beams 7 & 8), that are in the horizontal beam and 90° to the the atomic beam. These beams provide extra confinement in this dimension, which was weak in the 6-beam configuration due to the 58.5° angle between the horizontal beams and this axis. The extra 2 beams were produced by using two Thorlabs TW630R5A2 2:2 non-PM fiber splitters that are butt coupled to the two most powerful outputs of the 2:6 fiber splitter[16]. The power in beams 1, 2, 7 & 8 are $\sim$ 20 mW, while the powers in beams 3, 4, 5 & 6 are $\sim$ 9 mW.

Two quarter waveplates are used on each beam axis to set the circular polarization required by the magnetic field-gradient configuration. The magnetic field is arranged to point outwards from the field zero along the vertical axis, and inwards towards the field zero along the horizontal axis. As discussed in Section 3.1, the cycling transitions used are the $^2S_{1/2}\ |F = 2, m_F = \pm 2\rangle \rightarrow\ ^2P_{3/2}\ |F' = 3, m_{F'} = \pm 3\rangle$ transitions, and the

[16]Fiber outputs from the original 2 : 6 fiber splitter were used for beams 7 & 8, and the fiber outputs from the 2:2 fiber splitters were used for beams 3, 4, 5 & 6. This was to provide as symmetric confinement as possible in the horizontal plane.

recyling transitions used are the $^2S_{1/2}\ F = 1 \rightarrow\ ^2P_{3/2}\ F' = 2$ transitions. The two inputs on the fiber splitter are used to separately couple the cycling and re-cycling light. A red-detuned MOT requires the transitions to have net-positive Zeeman shift, and therefore the σ^- transitions are used (see Section 3.2) for the relative transition shifts of the cycling and re-cycling transitions). We chose to wire our magnets such that, when in the anti-Helmholtz configuration, the magnetic field points outwards from the field-zero in the vertical dimension, and inwards towards the field-zero in the horizontal dimensions (see Section 5.5 for details on the Li magnets). This determines that right-handed circularly polarized light should be used for the vertical beams, and left-handed circularly polarized light should be used for the horizontal beams[17].

The magnetic-field gradient used for the MOT is 20 G/cm in the vertical dimension, which corresponds to a current of $\sim$ 40 A in the inner set of magnet coils (see Section 5.5). Our cycling light detuning of $-4.5\,\Gamma$ corresponds to a length scale of 1 cm, which is appropriate given our 1" MOT Beams. The re-cycling detuning is $-2.5\,\Gamma$, which corresponds to a length scale of 0.3 cm. These MOT parameters result in a MOT number of $\sim 5 \times 10^9$ atoms after a load time of $\sim$ 10 s, with a temperature of $\sim$ 1 mK and a phase-space density of $\sim 10^{-7}$.

3.5.2 Compressed MOT

The MOT is initially optimized to maximize loading rate and atom number at the expense of temperature and density. A subsequent compressed MOT (cMOT) stage is used to optimize both of these parameters without a loss in atom number. In this stage the magnetic field-gradient is ramped from 20 G/cm to 100 G/cm in the vertical dimension over the course of 28 ms. This corresponds to an increase from 40 A to 200

[17]Note that our Thorlabs PAN5710VIS polarimeter measures polarization ellipticity with handedness defined in the direction opposite to the laser beam k-vector.

A in the inner coils of the magnets (see Section 5.5 for a discussion of the Li magnets). After this ramp, the cycler detuning is decreased from $-4.5\,\Gamma$ to $-2\,\Gamma$ over the course of 1 ms, without a significant change in power. The re-cycler detuning is held constant, but its power is decreased by a factor of 4. The increased magnetic-field gradient and the decrease in cycler detuning both serve to reduce the size of the elliptical surface-of-resonance for zero-velocity atoms. This leads to the atoms being pushed towards the field-zero, and an increase in density of the cloud. As the re-cycler is effectively turned off, atoms only scatter a few cycling photons before going into the dark $F = 1$ ground-state manifold, and this prevents further heating and leads to effective cooling. However, this trap is very lossy, which is why it is only held for 1 ms. After this stage, the temperature drops from 1 mK to 0.5 mK and the density doubles, without any change in atom number.

3.5.3 Gray molasses

The process of loading into a magnetic trap heats the atoms, as they gain energy from the potential created by the magnetic-field gradient. Due to the zero-crossing of the s-wave scattering length at 6 mK discussed in Section 3.3, the temperature of the trapped cloud must be substantially below 1 mK to achieve sufficient scattering for forced evaporative cooling (see Section 2.3 for a discussion of evaporative cooling). To minimize the temperature of the atoms before loading them into the magnetic trap, we use sub-Doppler cooling between the MOT and the magnetic trap. Since Sisyphus cooling is not possible in Li due to the unresolved nature of the $J' = 3/2$ excited-state manifold, we employ a gray molasses on the D1 transitions from the ground-state hyperfine manifolds to the $J' = 1/2$ excited-state manifold (see Sections 3.1 and 2.2.3 for discussions of the level structure of ^{7}Li and sub-Doppler cooling, respectively.).

The gray molasses beams operate on the $^2S_{1/2}\,F = 2 \rightarrow {}^2P_{1/2}\,F' = 2$ and $^2S_{1/2}\,F =$

$1 \rightarrow {}^2P_{1/2}\, F' = 2$ transitions, both with detunings of $+4.5\,\Gamma$ (i.e. the Raman condition is satisfied, as the relative detuning between these beams is zero). There are two input beams, each with a power of 50 mW; one which is introduced vertically from below the chamber and is retro-reflected above the chamber, and one which is cycled through all of the horizontal viewports that are at acute angles to the atomic beam (i.e. the viewports that are used for MOT beams 3, 4, 5 & 6) and retro-reflected. The retro-reflection produces the standing wave of intensity that is necessary for gray molasses. The light addressing atoms in the $F = 1$ ground-state is produced by a home-built EOM, which adds sidebands at 803.5 MHz, with an intensity of 1-2% of the carrier frequency. The magnetic-field gradient is clamped to zero within 250 μs with an insulated-gate bipolar transistor (IGBT) (see Section 5.5.4 for a discussion of magnet switching). The gray molasses beams are applied for 1 ms, and cool the atoms to 60 μK, with a reduction in atom number to 3×10^9.

3.5.4 Optical pumping

As discussed in Section 3.2, 3 out of the 8 ground states have positive g-factors, and are therefore magnetically trappable. Of these three states, the most desirable state is the $|F = 2, m_F = 2\rangle$ state, as it is most tightly confined, and is not susceptible to spin-changing collisions when in a spin-polarized gas. Therefore it is desirable to transfer as many as possible of the atoms to this state before loading into the magnetic trap. This is best executed immediately after gray molasses, as the MOT and gray molasses both "stir" the ground-state spins, and is achieved via optical pumping (see Section 2.1.3 for a discussion of optical pumping). Since optical pumping involves spontaneous emission events, it leads to heating for atoms that are below the Doppler temperature, and thus it is desirable to scatter as few photons as possible during the process. This is

best accomplished by optically pumping with σ^+-polarized light on the D1 transitions, $^2S_{1/2}\,F = 2 \rightarrow {}^2P_{1/2}\,F' = 2$ and $^2S_{1/2}\,F = 1 \rightarrow {}^2S_{1/2}\,F' = 2$, as once the atoms are in the $|F = 2, m_F = 2\rangle$ ground-state no further σ^+ transitions can occur. For this purpose we use the vertical gray molasses beam, and a small vertical bias magnetic field to provide a quantization axis[18]. The polarization with respect to the quantization axis (σ^+) is the same for both before and after the reflection of the beam on the gray-molasses retro-mirror. Applying optical pumping light from both directions helps ensure that there is no net-momentum applied to the cloud. The light is stepped towards resonance[19] with the $F = 2$ hyperfine states, and the intensity of the sidebands applied by the gray molasses EOM is increased to be equal with the carrier. We empirically set the duration of the optical pumping stage to be 450 μs for a pumping beam power of 70 mW, after which almost all of the atoms are in the $|F = 2, m_F = 2\rangle$ state.

3.6 Conservative trapping and evaporative cooling

After gray molasses there is no further laser cooling in our Li experiment. All further cooling is done via forced evaporation (see Section 2.3 for a discussion of evaporative cooling), which is performed in conservative traps, such as magnetic quadrupole traps and optical dipole traps. While it is possible to trap ^{7}Li in an optical trap directly after the MOT, it requires 100s W of optical power at 1064 nm to produce the required trap depths and volumes. Therefore we load the atoms into a plugged magnetic quadrupole trap, which can have very high trap depths and volumes, and perform RF-assisted forced evaporation (see Section 2.3.2 for a discussion of magnetic trapping and RF-assisted evaporation). Due to the negative background scattering length of $|F = 2, m_F = 2\rangle$ atoms,

[18]This field is $\sim$ 1 G, and does not produce significant Zeeman shifts. See Table 3.5 for a list of relevant transition shifts

[19]Technically this happens with a separate acousto-optic modulator pathway that is realigned with the vertical gray molasses beam.

it is not possible to produce large BECs with this state in the magnetic trap. Therefore, after increasing the phase-space density of the atoms to 10^{-2}, we transfer them to a far-off resonance optical dipole trap, where we tune the scattering length of the $|F = 1, m_F = 1\rangle$ state using a magnetic Feshbach resonance and evaporatively cool to quantum degeneracy via trap weakening.

3.6.1 RF-assisted evaporation in the plugged magnetic quadrupole trap

The magnetic trap is snapped on at a magnetic-field gradient strength of 80 G/cm in the vertical dimension (G_z) in 100 μs using a high-voltage capacitor bank (see Section 5.5.4 for details on the switching of the magnets), before being ramped up to its maximum value of 420 G/cm in a few 100 ms using analog control of the high-current power supplies. This initial snap on is diabatic with respect to the thermalization rate of the atoms, which is given by the rate of elastic scattering, and therefore heats the atoms, but it minimizes the decrease in density caused by the expansion of the atoms between gray molasses, optical pumping and the magnetic trap. The slow ramp up is adiabatic with respect to the thermalization rate of the atoms, and the phase-space density remains constant during this procedure, and the number density (n) increases, proportionally to magnetic-field gradient (see Section 2.3.2 for a general discussion of magnetic trapping). The rate of two-body atom-atom interactions, such as elastic scattering, in an atom cloud is proportional n^2. Therefore it is desirable to increase G_z before evaporation.

We apply radio frequency (RF) radiation at 927 MHz during the compression, which is resonant with the $|F = 2, m_F = 2\rangle \rightarrow |F = 1, m_F = 1\rangle$ magnetic dipole transition[20] for atoms at locations where the magnetic field is ~ 60 G. The $|F = 1, m_F = 1\rangle$ state is

[20]This transition has a zero-field resonance equal to the ground-state hyperfine splitting of 803.5 MHz, and a transition shift of 2.1 MHz/G (see Section 3.2).

anti-trapped, and therefore these atoms are ejected from the trap. The effect of the RF radiation is to remove the hottest atoms from the trap, which make larger excursions away from the trap center. Whenever such an atom moves through a location where the magnetic field is 60 G, it is ejected from the trap. We hold the frequency at 927 MHz for 50 ms after the adiabatic compression, before commencing forced evaporation. We lower the RF frequency from 885 MHz to 805.3 MHz over the course of 4 s. The rate at which we lower the frequency was set empirically. In the first two stages of evaporative cooling, the frequency is lowered from 885 to 829 MHz linearly over the course of 1.5 s. In the final stage, the frequency is lowered from 829 to 805.3 MHz over the course of 2.5 s, while the magnetic-field gradient is lowered by a factor of 10, from 420 G/cm to 42 G/cm.

This lowering of the field gradient allows us to keep the cloud number density at or below 10^{13} cm^{-3}, which is helpful to avoid three-body collisions, which scale as n^3. An additional source of loss and heating are Majorana losses, which are important at high-field gradients and low temperatures. We prevent these losses by using a blue-detuned optical plug beam focused to within $5 - 10\,\mu$m of the field-zero. We use a 10 W 532 nm laser that is focused to a waist of 30 μm. This produces a potential hill with height equivalent to 0.5 mK that prevents the atoms from nearing the field-zero. The beam is turned on during the ramping-on of the magnetic trap and turned off at the end of RF evaporation over 300 ms. Shimming any stray magnetic fields (including the Earth's magnetic field) is critical, as they cause the magnetic-field zero to move during the ramping of the magnetic-field gradient.

3.6.2 Optical trap

We load the atoms from the post-evaporation magnetic trap into a crossed optical dipole trap (XODT). The two beams have powers of 8 W each and are focused to 90 μm waists, which produce individual trap depths of 30 μK. The intersection point of the individual optical dipole traps (ODTs) is offset from the trap center, to avoid the effects of the plug beam. Once the atoms are loaded into the XODT, we apply RF frequency again to transfer the atoms from the $|F = 2, m_F = 2\rangle$ state to the $|F = 1, m_F = 1\rangle$ state. We sweep the frequency from 809.56 MHz to 807.45 MHz over the course of 65 ms, which transfers 98% of the atoms via adiabatic rapid passage. At this stage the magnetic field is ramped to 722 G, which corresponds to a scattering length of 294 a_0. The ODT powers are ramped exponentially to 2 W over the course of 4.5 s with a time constant of 2.25s. This produces a BEC of approximately 10^5 atoms at a temperature of approximately 100 nK. Further details on the Li cooling sequence can be found in Zachary Geiger's dissertation [29].

Chapter 4

^{84}Sr atomic properties & cooling

Strontium is an alkaline-earth metal. Four stable isotopes exist, ^{84,86,88}Sr which are bosons, and ^{87}Sr, which is a fermion. All isotopes have been cooled to quantum degeneracy. To this date in the Weld group we have trapped and cooled all isotopes in MOTs and have produced BECs of ^{84}Sr, which, with a natural abundance of $\sim 0.5\%$ is the least abundant isotope. However, our apparatus should be capable of producing degenerate gases of the other isotopes if desired. Since Sr has two valence electrons, it has a richer electronic structure than the alkalis, and at minimum three resonant lasers are required to bring Sr to degeneracy. However, it is possible to produce all three of these wavelengths with visible-light direct-diodes in external-cavity diode laser (ECDL) configurations[1]. Due to its two valence electrons, Sr has a spinless singlet ground-state structure. Intercombination transitions, which are S-changing transitions, between this singlet ground state and triplet excited states, which are forbidden by selection rules, proceed to some extent due to spin-orbit coupling, and have narrow linewidths [2]. These

[1] At the time we began construction of the Sr experiment, direct diodes were not readily available at 461 nm, and we opted for a frequency-doubled 922 nm diode-laser system.

[2] To obtain a sub-linewidth light source for these transitions it is typically necessary to lock the laser to a high-finesse cavity. However, this is not necessary to produce cold enough laser-cooled clouds to produce a degenerate gas.

narrow-linewidth transitions enable Doppler cooling to very low temperatures (and even to quantum degeneracy [63]), some of the most precise atomic clocks [64], and the engineering of spin-orbit coupling in an optical lattice [65]. The bosonic isotopes lack nuclear spin, and therefore only have one ground state, with both electrons occupying the $5s$ orbital. The fermionic isotope has a large nuclear spin of $I = 9/2$, resulting in ten degenerate hyperfine sub-levels in the ground state. The s-wave scattering lengths between two of these hyperfine sub-levels are equal for any pair of different sub-levels. This leads to an SU(10) symmetry between these degenerate nuclear spin-states, which has inspired numerous proposals to study exotic magnetism [66], as well as proposals to use these states as qubits [67]. For these reasons, Sr has been a popular choice for ultracold atom experiments in recent years.

4.1 ^{84}Sr level structure & laser cooling

As an alkaline-earth metal, Sr has two valence electrons, and therefore the electronic structure splits into two parts; singlet, $S = 0$, states, and triplet, $S = 1$, states. When unexcited, both electrons occupy the $5s$ orbital, and are in a singlet configuration, giving the ground-state a Russell-Saunders term of $^1S_0$. The bosonic isotopes lack nuclear spin, and therefore $F = J$, and the ground state is non-degenerate, and non-magnetic. Two states in which one of the electrons is excited to the p-orbital are used for laser cooling: the singlet $5s5p\,^1P_1$ state (with a transition wavelength of approximately 461 nm and a linewidth of 30.5 MHz), and the triplet $5s5p\,^3P_1$ state (with a transition wavelength of approximately 689 nm and a linewidth of 7.4 kHz). The fine structure splitting in the ^3P_J manifold is several THz. See Fig. 4.1 for an energy level diagram of bosonic Sr, which summarizes these details.

The lifetimes of the ^3P_J states are significant in the Sr cooling process. The least long-

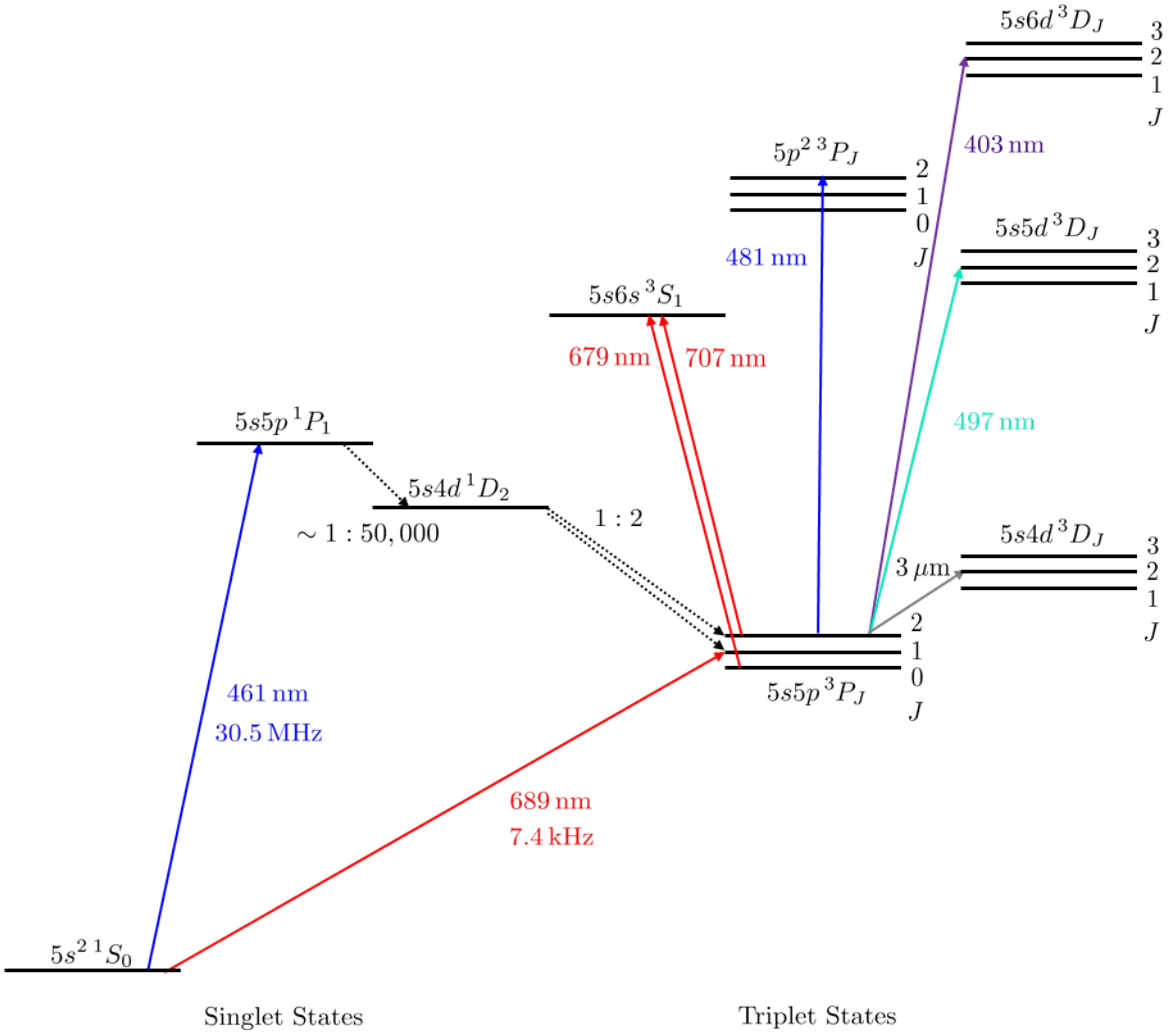

Figure 4.1: A level diagram depicting experimentally relevant energy levels in bosonic Sr.

lived of these states is the $^3P_1$ state that is used for laser cooling, which has a lifetime of 21 μs. Atoms in this state may decay down to the ground state via an electric-dipole transition, which is forbidden by selection rules ($\Delta S \neq 0$), but proceeds in Sr due to non-negligible spin-orbit coupling due to the high atomic number. The $^3P_2$ state has a calculated lifetime of the order of 1000 s[3], and its main decay paths are through a magnetic-dipole transition to the $^3P_1$ state and a magnetic-quadrupole transition to the

[3]This lifetime was measured to be approximately 100 s, though this was limited by blackbody radiation at $\sim 3\mu$m exciting transitions to the $5s4d\,^3D_J$ manifold. At $T = 0$ K the lifetime was estimated to be approximately 500 s [68].

Electron spin, S	0
Nuclear spin, I	0
Blue transition	$5s^2\,{}^1S_0 \rightarrow 5s5p\,{}^1P_1$
Wavelength, λ_{461}	460.7 nm
Linewidth, $\Gamma_{461}/2\pi$	30.5 MHz
Doppler temperature, $T_{\mathrm{D},461}$	732 μK
Recoil temperature, $T_{\mathrm{R},461}$	537 nK
Saturation intensity, $I_{\mathrm{sat},461}$	40.8 mW/cm^2
Red transition	$5s^2\,{}^1S_0 \rightarrow 5s5p\,{}^3P_1$
Wavelength, λ_{689}	689.2 nm
Linewidth, $\Gamma_{689}/2\pi$	7.4 kHz
Doppler temperature, $T_{\mathrm{D},689}$	178 nK
Recoil temperature, $T_{\mathrm{R},689}$	240 nK
Saturation intensity, $I_{\mathrm{sat},689}$	2.95 μW/cm^2
Repump transition	$5s5p\,{}^3P_2 \rightarrow 5s6d\,{}^3D_2$
Wavelength, λ_{403}	403 nm
Linewidth, $\Gamma_{403}/2\pi$	O(1) MHz

Table 4.1: Selected ^{84}Sr properties.

ground $^1S_0$ state. The $^3P_0$ state has a calculated lifetime of the order of thousands of years, and it decays to the ground state via two-photon electric-dipole-magnetic-dipole transitions [69][4].

The transition to the $5s5p\,{}^1P_1$ state on the 461 nm transition is not completely cycling; the state has a $1:50,000$ branching ratio into the lower-lying $5s4d\,{}^1D_2$ state, from where the electron decays to the $5s5p\,{}^3P_1$ and $^3P_2$ states with a 2:1 branching ratio. The atoms in the $^3P_1$ state decay back to the ground state with a lifetime of 21 μs, but the lifetime of the $^3P_2$ state is on the order of 1000 s, and therefore these atoms must be "repumped" to the $^3P_1$ state, from where they may decay back to the ground state. For this purpose we use a transition to the $5s6d\,{}^3D_2$ state, which is at approximately 403 nm, and has a linewidth on the order of a MHz. There are several other possible repumping schemes,

[4]This lifetime is reduced in ^{87}Sr to approximately 100 s, due to the hyperfine interaction, which couples the $^3P_0$ state to the $^1P_1$ and $^3P_1$ states, and thereby allows electric-dipole decay to the ground-state. This is the transition that is used in Sr clocks.

which are depicted in Fig. 4.1. Some properties related to laser cooling bosonic Sr are listed in Table 4.1.

4.2 ^{84}Sr magnetic properties

The ground state of bosonic strontium has no magnetic moment, and therefore cannot be magnetically trapped. However, as discused in section 4.1, atoms excited to the $^1P_1$ state with the 461 nm transition leak into the $^3P_2$ state. The g-factor for this state is 3/2, and therefore the $|J = 2, m_J = 2\rangle$ and $|J = 2, m_J = 1\rangle$ states are magnetcally trappable, and are thus magnetically trapped during the operation of an un-repumped MOT on $^1S_0 \rightarrow {}^1P_1$ transition with sufficiently high magnetic-field gradient. The g-factors for experimentally relevant excited states in bosonic Sr are listed in Table 4.2.

State	g_J
$^1P_1$	1
$^3P_1$	3/2
$^3P_2$	3/2
$^3D_2$	7/6

Table 4.2: Landé g-factors for experimentally relevant excited states of bosonic Sr.

The Zeeman shifts of transitions from the ground state are solely determined by the excited state Zeeman shifts, and are zero for π transitions. The Zeeman shifts for $\sigma^{\pm}$ transitions on the $^1S_0 \rightarrow {}^1P_1$ and $^1S_0 \rightarrow {}^3P_1$ transitions are listed in Table 4.3.

Ground State	Excited State	Transition Shift (MHz/G)
$^1S_0$ $\|J = 0, m_J = 0\rangle$	$^1P_1$ $\|J = 1, m_J = \pm 1\rangle$	$\pm$ 1.40
$^1S_0$ $\|J = 0, m_J = 0\rangle$	$^3P_1$ $\|J = 1, m_J = \pm 1\rangle$	$\pm$ 2.10

Table 4.3: Transition shifts for $\sigma^{\pm}$ cycling transitions.

The Zeeman shifts of transitions from the magnetically trappable $^3P_2$ states depend on both upper-state and lower-state Zeeman shifts, and are listed in Table 4.4.

Lower State	Upper State	Transition Shift (MHz/G)
$^3P_2\ \|J=2, m_J=2\rangle$	$^3D_2\ \|J=2, m_J=2\rangle$	-0.93
$^3P_2\ \|J=2, m_J=2\rangle$	$^3D_2\ \|J=2, m_J=1\rangle$	-2.57
$^3P_2\ \|J=2, m_J=1\rangle$	$^3D_2\ \|J=2, m_J=2\rangle$	1.17
$^3P_2\ \|J=2, m_J=1\rangle$	$^3D_2\ \|J=2, m_J=1\rangle$	-0.47
$^3P_2\ \|J=2, m_J=1\rangle$	$^3D_2\ \|J=2, m_J=0\rangle$	-2.1

Table 4.4: Transition shifts for all possible transitions from magnetically trappable $^3P_2$ states to the $^3D_2$ state.

4.3 Sr scattering properties

The s-wave scattering length is isotope dependent, as the additions of neutrons to the nucleus changes the details of the inter-atomic potential. As discussed in section 2.1.5, the energy of the highest-energy bound state in the inter-atomic potential significantly impacts the scattering length, and each introduction of another allowed bound state leads to a divergence in the scattering length. As the mass of the Sr nucleus is tuned upwards, a new bound state is permitted between nucleon numbers of 84 and 86. This leads to the scattering length of ^{86}Sr being very large and positive, and the scattering length of ^{87}Sr (for two fermions in differing m_F states) and ^{88}Sr decreasing towards, and slightly below zero. The scattering length of ^{84}Sr is 123 a_0, which is suitable for evaporative cooling, and is why we use this isotope for producing BECs, even though it is the least abundant isotope. The homonuclear scattering lengths are listed in Table 4.5. Since Sr has a non-magnetic ground-state (or nearly non-magnetic in the case of the fermion), no magnetically-tunable Feshbach resonances exist for collisions between ground-state atoms.

Isotope	s-wave Scattering Length (a_0)
^{84}Sr	122.7(3)
^{86}Sr	823(24)
^{87}Sr	96.2(1)
^{88}Sr	-1.4(6)

Table 4.5: s-wave scattering lengths in units of a_0 for homonuclear scattering of the four stable isotopes of Sr [70, 71]. The scattering length of ^{87}Sr is listed for interactions between different spin states.

4.4 Preparation of a large reservoir of cold atoms

A Sr atom begins its life-cycle in the machine in the oven. The oven consists of a reservoir, which was initially loaded with 25 g of Sr, and then reloaded with 100 g at the end of 2016, that is heated to 600 °C, and a collimating nozzle made of microcapillaries, wihch is heated to 650 °C (see Section 6.3.2 for details on the Sr oven). This produces a collimated atomic beam, with beam divergence given by the aspect ratio of the microcapillaries, which is 1 : 50, which corresponds to a solid angle roughly 35 times the solid angle subtended by the MOT, which is roughly 5 mm in diameter 1.5 m away. In order to further collimate the beam, we employ 1d transverse cooling in the atomic beam shutter cube (see Section 6.3.3 for details on the Sr oven manifold). A Zeeman slower is used to modify the speed distribution of the atomic beam to increase the fraction of atoms with speeds lower than the capture velocity of the MOT (see Sections 2.2.2 and 6.4 for details on Zeeman slowing and the Sr Zeeman slower). The initial magnetic trap loading rate is $\sim 5 \times 10^5$ atoms/s for ^{84}Sr, and is a lower bound on the flux of slowed atoms through the MOT region.

4.4.1 Transverse Cooling

We planned to employ transverse cooling in the transverse cooling cube immediately after the nozzle to gain the maximum benefit from collimating the atomic beam (see

Section 6.3.3 for details on the Sr oven manifold). However, these windows were made opaque by the deposition of Sr, and, in the second iteration of the Sr oven manifold, the optical density of Sr gas in the cube was too high to address the atomic beam. For these reasons, we performe transverse cooling in the atomic beam shutter cube, where only the horizontal dimension is accessible. Following the discussion in Section 3.4.1 we find that for an optimal drag coefficient in 1d that the time constant is 29 μs, corresponding to a distance of 5 cm to slow the atoms to the velocity limit of molasses with these conditions. We only have access to $\sim$ 1 cm. We apply 20 mW of 461 nm light with a detuning of $-\Gamma/2$. The beam is shaped with cylindrical lenses to have a shape that matches the profile of the atomic beam. This improves the magnetic trap loading rate by a factor of 2.

4.4.2 Zeeman Slowing

At the temperatures necessary to produce a substantial vapor pressure of Sr, the fraction of atoms in the speed distribution of the atomic beam below the capture velocity of the MOT is negligible. Therefore some method of modifying the speed distribution to enlarge this fraction is necessary. We employ a decreeasing-field "spin-flip"[5] Zeeman slower that is designed to slow atoms traveling at 600 m/s or below to 50 m/s (see Sections 2.2.2 and 6.4 for details on Zeeman slowing and the Sr Zeeman slower). The Zeeman slower light is introduced to the machine through a 1.33" conflat window that is directly opposite the port through which the atomic beam enters the main chamber. The light is coupled into a polarization-maintaining (PM) fiber, and is collimated with a collimation package and expanded with a 1" telescope, which both are mounted directly to the optical table. We use 2" mirrors mounted on standard optics to elevate the beam

[5]Of course, there is no spin in the ground-state of ^{84}Sr. The slower has a magnetic-field-zero crossing, as in an alkali spin-flip Zeeman slower.

and angle it upwards at 16° to match the angle of the atomic beam. An initial iteration of the Zeeman slower light involved directly plugging the fiber into cage-mounted optics that were mounted to the Zeeman slower window heating collar[6]. However, this set up did not allow us to independently control the angle and the position of the Zeeman slower light, and we replaced it with the current set up.

The Zeeman slower laser beam was originally set to be focused to the size of the nozzle at the nozzle, with an initial beam diameter matched to the clear aperture of the 1.33" conflat window through which the beam enters the chamber. Since then, the beam focus has been adjusted to maxmize the magnetic trap loading rate. The beam has a power of 80 mW and is detuned by 740 MHz from the transition. The slower currents were configured to use σ^- transitions in the decreasing-field section of the slower, where the magnetic field points towards the MOT. Therefore the slower light is initially set to have right-handed circular plarization with respect to its own k-vector using two quarter waveplates, before it is empirically optimized while maximising the loading rate of the MOT. Due to the large mass of Sr, beam explosion is not significant, and we do not do any transverse cooling after the slower.

4.4.3 461 nm magneto-optical trap

The first MOT in the Sr cooling sequence is operated on the broad 461 nm transition. It was designed to be operated with 3 retro-reflected beams. The horizontal MOT beams are at 45° to the atomic beam, and have a power of 5 mW each. The vertical MOT beam is at a 85° angle to the atomic beam and has a power of 10 mW. The $1/e^2$ diameters of the MOT beams are ~ 7.5 mm, but the Gaussian beam profile is clipped by the 0.6" clear aperture of the 1.33" conflat windows used for the horizontal beams. The deceleration

[6]This collar is used to mount a second window outside of vacuum a small distance from the vacuum window. A bandheater is used to heat this region, and maintains the vacuum window at a uniform high temperature to avoid Sr deposition.

from the capture velocity is provided by the two horizontal MOT beams that are in the horizontal plane and have component counter to the propagation of the atomic beam. Assuming 5 mW in each of these beams, a detuning of $-\Gamma$ and an interaction length equal to the projection of the 7.5 mm beam diameter on to the atomic beam dimension, we find the capture velocity of the MOT is 34 m/s. This calculation assumes a constant scattering rate through the deceleration, and neglects the Doppler and Zeeman shifts (which can be thought of as approximately canceling each other), but is a useful estimate. The magnetic-field gradient used for the MOT is 54 G/cm, which is produced by running 288 A through a pair of large (roughly) anti-Helmholtz coils (see Section 6.5 for a discussion of the design, construction and operation of the Sr magnets). The MOT is operated for 10s, during which $\sim 5 \times 10^6$ atoms in the $^3P_2$ $|J = 2, m_J = 2\rangle$ and $|J = 2, m_J = 1\rangle$ states are loaded into the magnetic trap, with a temperature of ~ 1 mK. The number of atoms in the MOT itself can be a few orders of magnitude lower [72]. Due to the low atom number in the MOT, it is difficult to perform absorption imaging on the MOT, and therefore Zeeman slower and MOT diagnostics are determined by performing absorption imaging on the magnetically trapped atoms after a repump flash. Figure 4.2 shows a photograph of a repumped 461 nm MOT of ^{88}Sr atoms.

As discussed in Chapter 6, the Sr main chamber is a Kimball spherical octagon, with 16 1.33" conflat flanges, which form 8 diametrically opposed pairs. The axes of cylindrical symmetry of these flanges intersect at the center of the chamber, and are each angled at 16° to the horizontal plane. The atomic beam enters through one of the upper 1.33" flanges, and is therefore angled downwards by 16°. The "horizontal" MOT beams enter the main chamber through upper 1.33" flanges that are on the opposite side of the main chamber. Projected onto the horizontal plane, these MOT beams are at 45° to the atomic beam. Projected onto the vertical plane along the atomic beam, they are at 32°, to the atomic beam. The MOT beams are retro-reflected back through

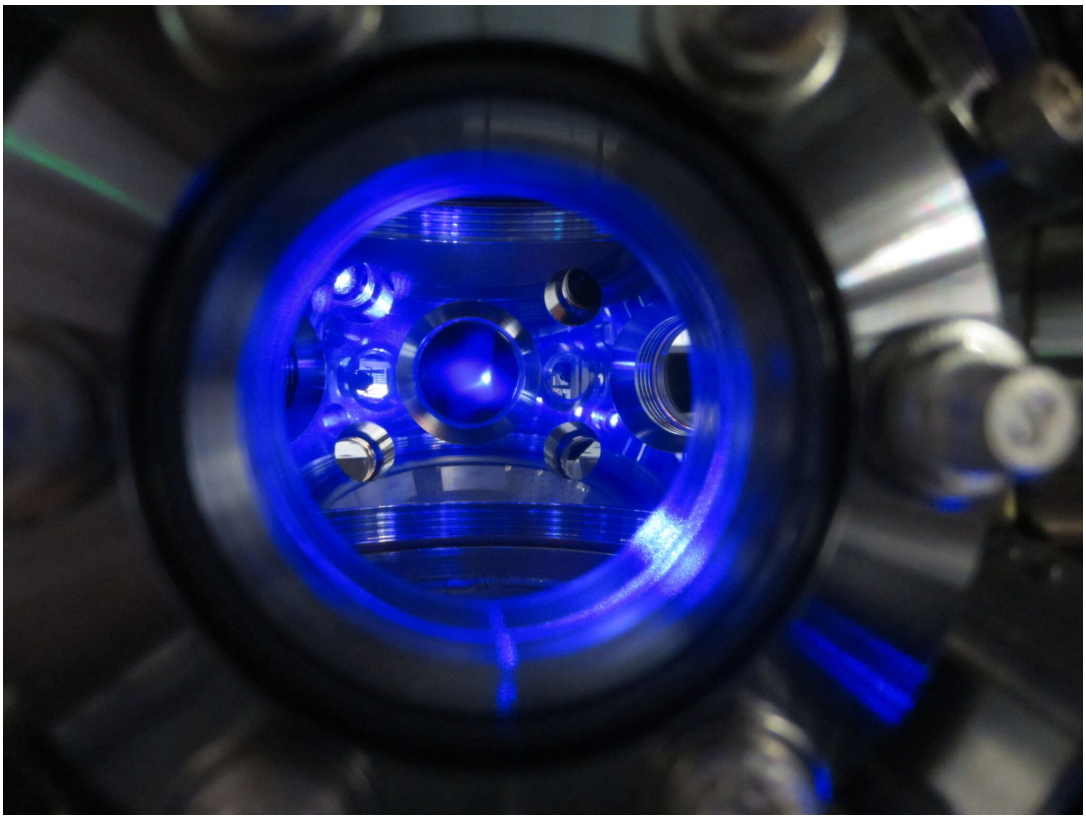

Figure 4.2: A photograph of a repumped 461 nm MOT of ^{88}Sr atoms.

the opposing 1.33" conflat viewports through which they exit the chamber after their first pass. The PM fibers through which these beams are introduced to the machine are plugged into receptacles which are mounted on a standard 16 mm cage, which is screwed into a custom-machined 316 stainless steel collar which is firmly attached to the 1.33" conflat flange with set screws. The fiber outputs are initially collimated with $f = 25$ mm aspherical lenses to have ~ 7.5 mm diameters, and the polarization of the beams are set to be σ^- with respect to the quantization axis on the side of the field-zero closest to the entrance viewport using a single quarter waveplate[7]. All of these optics are mounted on the 16 mm cages. The Gaussian beam profile is clipped by the 0.6" clear aperture of the 1.33" conflat windows. The retro-reflection mirror and waveplate[8] are similarly cage-

[7]The output of the fiber is linearly polarized as the fiber is PM.

[8]A quarter waveplate is used to maintain the light polarization with respect to its own k-vector, and

mounted to the opposing 1.33" conflat flanges. The focus of these beams is empirically adjusted to maximize the magnetic-trap-loading rate.

The "vertical" MOT beam cannot be canted at a 16° angle due to the pumping manifold. It enters the main chamber from underneath the pumping manifold at an 11° angle. The fiber through which this beam is introduced to the machine is collimated with similar cage-mounted optics, but is mounted on the optical table and redirected up through the lower 8" conflat window using standard optics. The retro mirror and waveplates are mounted on the breadboard above the main chamber.

4.4.4 Reservoir magnetic trap

During the operation of the MOT, atoms leak into the $^3P_2$,$^3P_1$ and $^3P_0$ states through the $^1D_2$ state (see Section 4.1 for a discussion of this decay pathway). This limits the lifetime of a ground-state atom in the MOT to $\sim 50,000$ photon-scattering events, which, at the powers used in the MOT, corresponds to a lifetime of ~ 20 ms. Due to this reason, the MOT fluorescence quickly saturates, while the number of atoms that are magnetically trapped grows. The ratio of the number of atoms in the MOT and the number of atoms in the magnetic trap can be as high as 1 : 1000, as the lifetime of the magnetic trap can be ~ 20 s. The growth of the magnetic trap number is limited due to interactions between the ground-state atoms trapped in the MOT and the excited state atoms trapped in the magnetic trap. It is also plausible that blackbody radiation at 3 μm (particularly from the hot oven, which has a line-of-sight to the magnetic trap during the MOT loading) causes parasitic "repumping" to the $5s4d\,^3D_2$ state, and thereby reduces the effecitve lifetime of the magnetically-trapped $^3P_2$ state atoms.

thus also the quantization axis on the side of the MOT which is closer to the retro-window.

4.5 Intercombination line laser cooling

To laser cool on the narrow-line $^1S_0 \rightarrow {}^3P_1$ 689 nm transition, the atoms must be quite cold to begin with. The optical molasses capture velocity ($\Gamma/2k$) for this transition is 1 mm/s, and for 2.5 mW beams in the same configuration and detuning as those in the 461 nm MOT, the 689 nm MOT capture velocity would be less than 2 m/s. The length scale of such a MOT, set by the magnetic-field gradient and the detuning, would be 70 μm. Thus, loading from the Zeeman-slowed atomic beam directly into the 689 nm MOT is not feasible. However, the 1 mK, magnetically-trapped cloud of atoms is suitable for capture in an intercombination-line MOT. To this end, the atoms are repumped out of the metastable $^3P_2$ states to the $^3P_1$ state, which decays to the ground-state. This repumping is executed by using a transition to the $5s6d\,^3D_2$ state with 403 nm light. Post-repumping, the atoms are captured in a 689 nm MOT, which runs through two phases: an initial capture phase, in which the MOT beams are broadened in frequency space to capture a wide range of velocities of atoms, and a final cooling stage, in which the frequency range of the MOT beams is reduced, ultimately to a single frequency that is near resonance.

4.5.1 Repumping

There are many options for repumping magnetically trapped metastable Sr, as discussed in Section 4.1. We chose to use the 403 nm transition to the $5s6d\,^3D_2$ state, since it only requires one laser, and is available directly from a GaN-based laser diode. We initially planned to use the 497 nm transition to the $5s5d\,^3D_2$ state, as demonstrated by the Florence and Innsbruck groups, and worked on a home-built second-harmonic generation (SHG) set up for doubling the light from a home-built 994 nm external-cavity diode laser (ECDL). We later abandoned this project in favor of constructing a 403 nm ECDL, and

this decision was subsequently justified by the measurement of a 98% repump efficiency using this transition by the Innsbruck group [72][9]. When this repumper is shone on the MOT, the MOT fluorescence can improve by 50 times, as the lifetime can be as high as 1 s and is limited by the un-repumped leak into the $^3P_0$ state. A further improvement in magnetic-trap-loading rate can be achieved by the use of a "depumping" laser, to shelve atoms that leak into the $^3P_1$ state into the $^3P_2$ state before they decay to the ground-state [73].

After the 461 nm MOT and Zeeman slower beams are turned off, the magnetic trap is held for 500 ms[10], during which the magnetic-field gradient is ramped down to 22.5 G/cm[11]. After the ramp, the repump beam is applied for 18 ms, a time that was determined by maximizing the atom number in the capture phase of the 689 nm MOT. The beam has a power of $\sim$ 2 mW and a beam diameter of $\sim$ 7.5 mm. It is mounted on a 16 mm cage, which is attached to the flange of a 1.33" conflat window, using a collar similar to those used for the 461 MOT beams[12]. We found that the 689 MOT number improved slightly upon retro-reflection of the repump beam, which we achieved using a mirror mounted to the main-chamber breadboard.

4.5.2 689 nm MOT capture phase

The 689 nm MOT is operated with 3 retro-reflected beams, and the beam paths are mirrored from those of 461 nm MOT. The 689 nm MOT light is coupled into a custom

[9]The 497 nm repumper has a theoretical efficiency of 99.95%.

[10]The atomic beam shutter is closed, and the mini-MOT coil is turned off. See Sections 6.3.3 and 6.4.3 for details on the atomic beam shutter and the mini-MOT coil respectively.

[11]This rampdown is to speed up the eventual reduction from the magnetic trap magnetic-field gradient to the 689 nm MOT magnetic-field gradient. This of course leads to a reduction in the density of the magnetically-trapped cloud, but the 689 nm MOT improves the density by several orders of magnitude, so this is a reasonable sacrifice. The final field was chosen empirically, and corresponds to a force about twice that of gravity for the $m_F = 1$ state.

[12]The cage includes a 90° reflection, which is necessary for the 403 nm fiber to avoid a conflict with the main-chamber breadboard.

non-polarization maintaining 3 : 3 Oz Optics fiber splitter[13]. These 3 retro-reflected beams are turned on during the repumping flash (which lasts 18ms long) and the capture and compression phases of the 689 nm MOT (which are 200 ms long each). During the repump flash and the capture phase, the frequency of the light is broadened by applying a 30 kHz frequency modulation to the radio frequency (RF) signal that is used to drive an acouso-optic modulator (AOM) that the 689 nm MOT light passes through immediately before entering the 3 : 3 fiber splitter. This modulation has an amplitude of 4.91 MHz, and effectively produces 164 sidebands spaced by 30 kHz on the MOT light. The mean frequency during this modulation is 2.72 MHz red detuned from the transition, and the highest frequency sideband is 265 kHz detuned from the transition. The initial MOT beam power is 2.2 mW, and the MOT beam diameter is $\sim$ 7.5 mm, giving a saturation parameter of $\sim$ 1900 per beam, and $\sim$ 10 per sideband per beam. Thus the power-broadened linewidth of the transition is larger than the sideband spacing, and the MOT initially consists of overlapping shells corresponding to each sideband. The magnetic-field gradient dropped to 5.1 G/cm at the end of the repump flash. The power of the MOT beams is held constant at 2.2 mW each during the repump flash, and then ramped down to 1.3 mW during the capture phase of the MOT. Ramping down the power of the MOT beams has the effect of reducing the scattering rate of MOT photons, and thus reduces the temperature of the MOT[14]. At the end of the capture phase, the cloud atom number is typically $\sim 4 \times 10^6$, and the cloud temperature is $\sim 5\,\mu$K with a phase-space density of $\sim 10^{-5}$.

The "horizontal" MOT beams enter the main chamber through upper 1.33" conflat

[13]A 3 : 3 fiber splitter allows for co-trapping ^{87}Sr, which requires two frequencies of 689 nm light due to hyperfine structure, and a bosonic isotope. Oz Optics was not able to produce a 3 : 3 polarization maintaining fiber splitter. We later purchased one from ComCore but have yet to install it on the machine as polarization drift has not been a siginificant issue.

[14]This can be thought of as reducing the power-broadened linewidth of the transition, which reduces the Doppler temperature. See Section 2.1.3 for a discussion of power-broadening, and Section 2.2.1 for a discussion of the Doppler temperature.

flanges on the same side of the main chamber as the entrance of the atomic beam. The beams are retro-reflected back through the lower 1.33" conflat flanges through which they exit the main chamber after their first pass. The horizontal beam fiber receptacles and collimating and polarizing optics are mounted very similarly to the horizontal 461 nm MOT beams, on 16 mm cages mounted on 316 stainless steel custom-machined collars that are fixed to the 1.33" conflat flanges using set screws. A fast aspheric lens collimates the beams to a diameter of $\sim$ 7.5 mm. Two waveplates are used per fiber, as the polarization of the light emitted from the fibers is arbitrary. The mounting of the retro-mirror and waveplate are identical to those for the 461 nm MOT. The vertical MOT beam is similarly canted at 11° to the direction of gravity in order to preserve that axis for imaging[15]. The retro-mirror and waveplate are mounted on the breadboard above the main chamber.

4.6 Conservative trapping and evaporative cooling

Due to the low temperatures and high phase-space densities of the 689 nm MOT, it is possible to directly capture the atoms in a crossed optical dipole trap (XODT) with reasonable powers and trap volume. The second phase of the 689 nm MOT, the compression phase, is operated in conjuction with the XODT, and results in a high phase-space density of $\sim 10^{-2}$. Due to the favorable s-wave scattering length of ^{84}Sr ($a_{\mathrm{s}} = 123a_0$), runaway evaporation proceeds upon trap-weakening, and the phase-space density of the cloud increases by two orders-of-magnitude despite a decrease in atom number of up to an order-of-magnitude. This results in a Bose-Einstein condensate (BEC) of up to 10^5 atoms, a number density of more than 10^{13} per cm^3 and a temperature $\sim$ 20 nK.

[15]The vertical MOT beams of the 461 nm MOT and the 689 nm MOT are at $\sim 22^\circ$ to each other.

4.6.1 689 nm MOT compression phase

The second phase of the 689 nm MOT increases the density of the cloud, while slightly decreasing its temperature. The optical dipole traps (ODTs) that form the crossed optical dipole trap (XODT) are ramped on during this phase, and the final cloud is primarily held against gravity by this trap. This phase lasts 200 ms and during it the magnetic-field gradient is ramped up to 11.2 G/cm and the MOT power is reduced to 0 mW. The amplitude of the frequency modulation of the MOT light is ramped linearly to zero, while the mean frequency is ramped up to 175 kHz red detuned of the transition. The increase in magnetic-field gradient and reduction in detuning compresses the cloud, and "pushes" the atoms into the XODT. The resulting cloud number is as high as 0.7×10^6, temperatures of ~ 4 μK and phase space densities of 10^{-2}. This temperature is higher than those achieved by other experiments ($\sim 1\,\mu$K), which we believe is due to the linewidth of our laser, which is not cavity-narrowed. Our final detuning, below which we cannot go without introducing stochastic atom loss, and the final temperature, suggest a linewidth of 200 kHz.

4.6.2 XODT and evaporative cooling

The XODT is formed by two 1064 nm laser beams that are each focused to waists of $\sim 50\,\mu$m, and each have a power of ~ 4 W. They are introduced to the main chamber through two 2.75" viewports, and are thus horizontal, and are chosen to be at 90° to one another. The peak trap depth of one of these ODTs is 55 μK, and therefore the peak trap depth in the vertical dimension is 110 μK. The trap frequencies are thus 468 Hz in the horizontal dimensions, and 663 Hz in the vertical dimension. However, we found that our highest phase-space-density clouds were obtained when the ODTs were both slightly defocused, so the trap depth and trap frequencies are likely lower than these estimates.

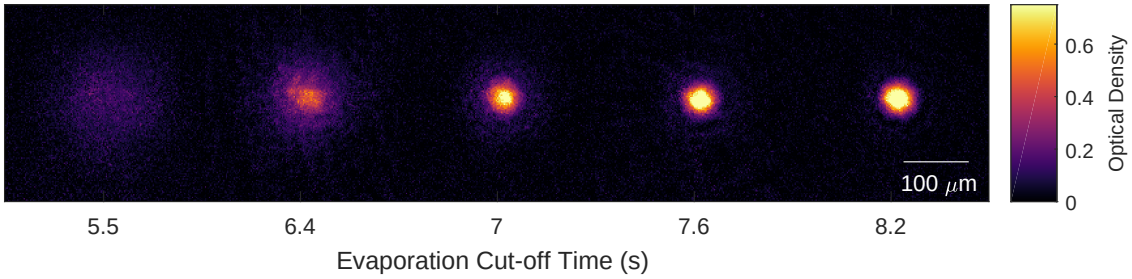

Figure 4.3: A series of absorption images of clouds of ^{84}Sr atoms after 13 ms of expansion from the XODT, taken after variable durations of evaporation. A condensate begins to form after 6 seconds of evaporation, and after 8.2 seconds of evaporation an almost pure condensate of $\sim 3 \times 10^4$ atoms is formed.

The improved clouds in this situation are most likely due to an increase in trap volume for the slightly defocused ODTs.

We force evaporation by lowering the powers in the ODT beams exponentially over the course of 8 s, with a time constant of 2 s. The initial single-particle elastic scattering rate (see Section 2.1.6 for a discussion of scattering rates) for ^{84}Sr with these conditions is 15 kHz. The final powers in the ODTs are $\sim$ 250 mW, giving a trap depth of 3.4 μK and trap frequency of 117 Hz in the horizontal dimensions, and a trap depth of 6.9 μK and trap frequency of 166 Hz in the vertical dimension. At this power, the ratio of the vertical confinement to gravity is 1.4, and the traps cannot be weakened much further without dropping the atoms[16]. With this final trap geometry, and a final atom number of 10^5, the Bose-Einstein condensation transition temperature is 276 nK. A Bose-Einstein condensate (BEC) forms during the evaporation process (after approximately 6.75 seconds of evaporation), and by the end of the 8s of evaporation the condensate fraction is close to 1, and temperature of the thermal fraction is $<$ 100 nK. Figure 4.3

[16]This metric is the ratio of the dipole and gravitational potentials at 1σ of the Gaussian beam. The 1σ point was chosen as this is where the derivative of a Gaussian is maximal.

shows absorption images of clouds of Sr atoms after varying durations of evaporation. The Thomas-Fermi radii of the cloud are 6.8 μm in the horizontal plane and 4.8 μm in the vertical plane. From here we proceed with experiments, by loading the BEC into an ODT or a lattice, by ramping down the XODT while ramping on the new trap, over a long timescale, such as 100 ms.

Chapter 5

Lithium experimental design & construction

The Li apparatus consists of an approximately 2 m long ultra-high vacuum (UHV) system which is mounted on a 4' by 8' optical table, known as the machine table. A computer-aided-design (CAD) depiction of the machine table components is shown in Figure 5.1. The UHV chamber is divided into two halves, which can be pressure-cycled independently: the oven, which produces a high-flux beam of hot atoms, and the main chamber, where the atoms are trapped and cooled. These two parts are connected via the Zeeman slower tube. Most of the resonant laser light is produced on a separate 4' by 8' optical table, known as the laser table, and delivered to the machine table via optical fibers. In addition to these tables, there are a few electronics racks used to mount power supplies, switching electronics, and radio frequency sources for acousto-optic modulators (AOMs), electro-optic modulators (EOMs) and the antenna used to address RF magnetic dipole transition. Control over all of these elements is accomplished by using digital and analog outputs produced by National Instruments cards installed in a desktop computer. A software suite, known as Cicero, that was developed by the Ketterle group at MIT is

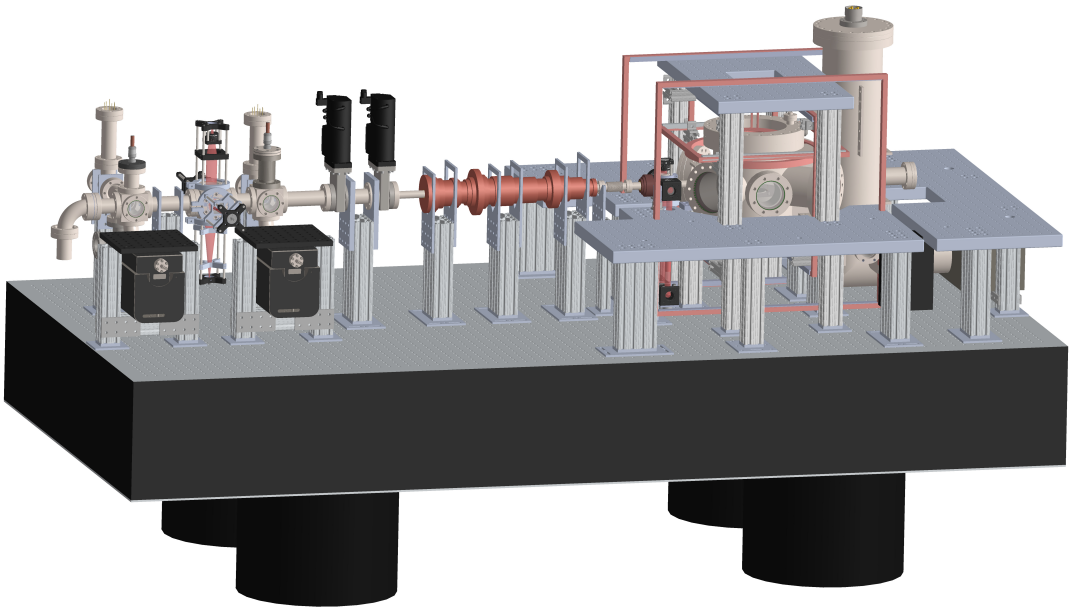

Figure 5.1: CAD depiction of Li machine table. The oven manifold is on the left and the main chamber is on the right. The two vacuum chambers are connected via the Zeeman slower tube.

used to produce the desired sequence of analog and digital outputs [74]. Water cooling is required by many of our electromagnets, and this is accomplished by a closed-cycle chilled water supply, and water-distribution manifolds mounted above the machine table enclosure.

5.1 Apparatus overview

The machine table is the heart of the experiment. It is enclosed using a home-built enclosure, constructed using 80/20 stock and plastic panels to which we attached wheels to allow us to slide the panels horizontally. The temperature and humidity inside this

enclosure is controlled via an air handling system that was installed during the renovation of our lab space. The enclosure temperature is typically stable to less than 1 °F. We aimed to have no non-fiber coupled resonant light on the machine table to avoid resonant light sources near the atoms that cannot be completely turned off. However, due to power constraints, we were eventually forced to install a slave laser diode and a tapered amplifier on the machine table. Light-tight enclosures were built around these lasers, and mechanical shutters were used to ensure complete turn-off of the laser beams which enter the chamber. The non-resonant 1064 nm and 532 nm high-power lasers are housed on the machine table, in metal light-tight enclosures for laser safety. The laser table is entirely enclosed, apart from the spectroscopy cell which is uncovered due to thermal management considerations. This is accomplished with a 5" high enclosure made of 80/20 stock and plastic panels. Both the machine and laser table top surfaces are made from 316 stainless steel (SS)[1], and the tables are floated using compressed air for vibrational isolation. Both tables have "clouds" made of Unistrut stock and painted fiber-board panels that descend from the ceiling, which are used to mount laser drivers, water-cooling-related hardware and other miscellaneous electronics. Three large ducts penetrate the machine table cloud and deliver temperature-and-humidty-controlled laminar-flow air to the space inside the machine table enclosure.

The vacuum chamber is mounted using 80/20 stock and tabs that were welded to the custom-built main chamber. Custom Al mounting clamps were used to connect other parts of the machine, such as the oven vacuum chamber, ion pumps, gate valves and Zeeman slower magnets, to the 80/20 stock. We installed custom additional breadboards on the machine table at a convenient height to access the horizontal windows of the main chamber, and above the main chamber to allow for access to the vertical windows. The breadboards were custom-designed, and then machined by the UCSB Machine Shop out

[1]316 SS is preferred over the more common 304 SS due to its favorable magnetization properties.

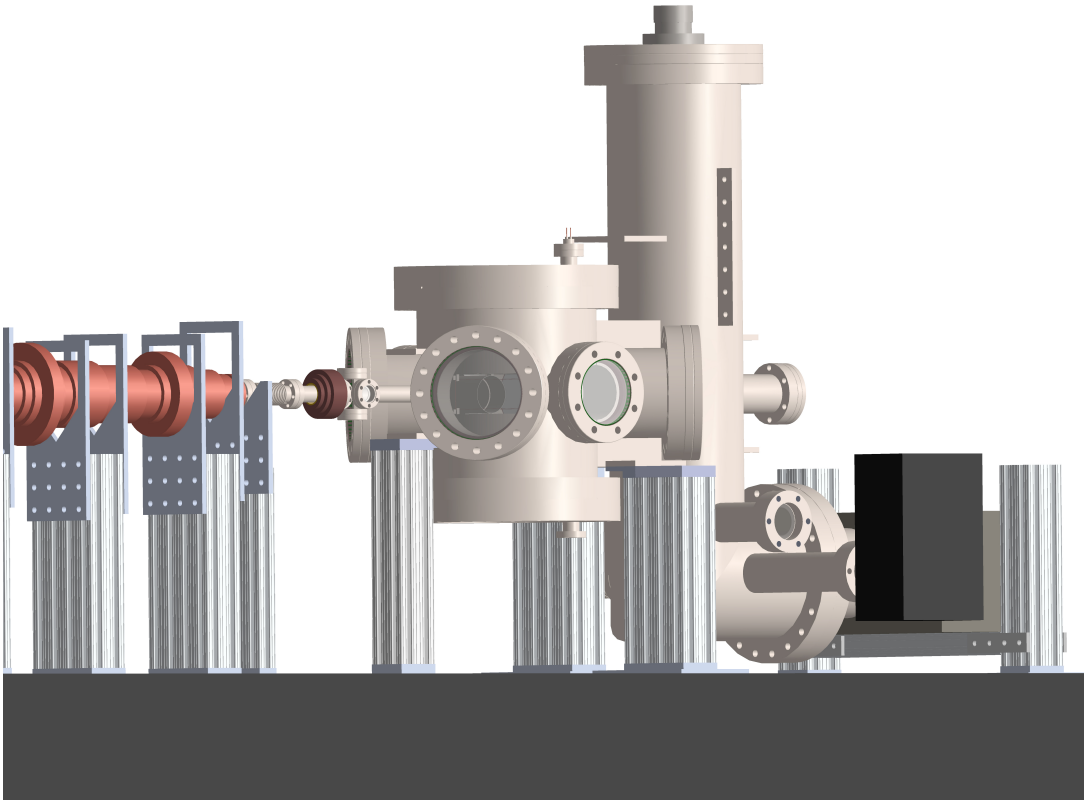

Figure 5.2: CAD depiction of Li main chamber. The vertical Ti-sub chimney and the horizontal ion pump pumping manifold are visible. The horizontal re-entrant window is visible through the large 6" window. The feedthroughs used to connect to the in-vacuum RF antennae are visible on the top and bottom re-entrant windows.

of Mic 6 alloy Al from Alcoa[2]. The breadboards are 1.5" thick, and are mounted on 80/20 stock.

5.2 Li main chamber

The Li main chamber was custom-designed, and was fabricated by the UCSB Machine Shop out of 316 stainless steel[3]. Figure 5.2 shows a CAD depiction of the main chamber. The most important considerations in the design of the main chamber were

[2]Al was chosen due to it being non-magnetic. Mic 6 has favorable vibrational properties.
[3]316 SS was chosen due to its favorable magnetic properties.

UHV compatibility and vacuum conductance, and magnetic and optical access to the atoms. We decided to work with a stainless steel chamber instead of a glass cell due to our misgivings about the structural integrity of the latter. We use a 75 l/s Agilent ion pump with optical baffles as the only active pump for the main chamber. The pump does not have a line-of-sight to the trapping region of the atoms, but the vacuum pathway from the pump to this region was chosen to be as short as possible and to have a cross-sectional area that was close to the cross-sectional area of the pump flange (6" conflat). Additonal pumping is achieved with a titanium sublimation pump (Ti-sub), that, when activated, deposits a Ti layer on the steel walls of the chamber. The deposited Ti acts as a getter, and a fresh layer of Ti has a pumping speed of a few liters per second per square centimeter. The Ti-sub is housed in a large chimney, and has a high-conductance pathway to the atoms, but not a direct line-of-sight.

To produce the magnetic field gradients required for the MOT and the magnetic trap, and the magnetic fields required to tune the atom-atom interactions using the Feshbach resonance, we use a pair of toroidal electromagnets which are positioned relative to each other close to the Helmholtz condition. Each magnet was designed to be approximately 1" from the atoms. We used a pair of large custom-designed re-entrant, or "bucket" windows made by the UKAEA to allow us to mount the magnets so close to the trapping region, while keeping them outside the vacuum chamber. These re-entrant windows were mounted with their axis of cylindrical symmetry along the dimension of gravity, thereby ensuring that the largest magnetic field-gradient produced by the magnets is in this dimension. A 1.33" conflat electrical feedthrough was mounted through the flange of each re-entrant window. These feedthroughs connected to two in-vacuum rectangular loops of Cu wire that were designed to be antennae for frequencies around 80 MHz. The loops were mounted to the re-entrant windows with macor screws and nuts. Figure 5.3 shows a photograph of the two RF antennae, as well as the macor screws used to hold

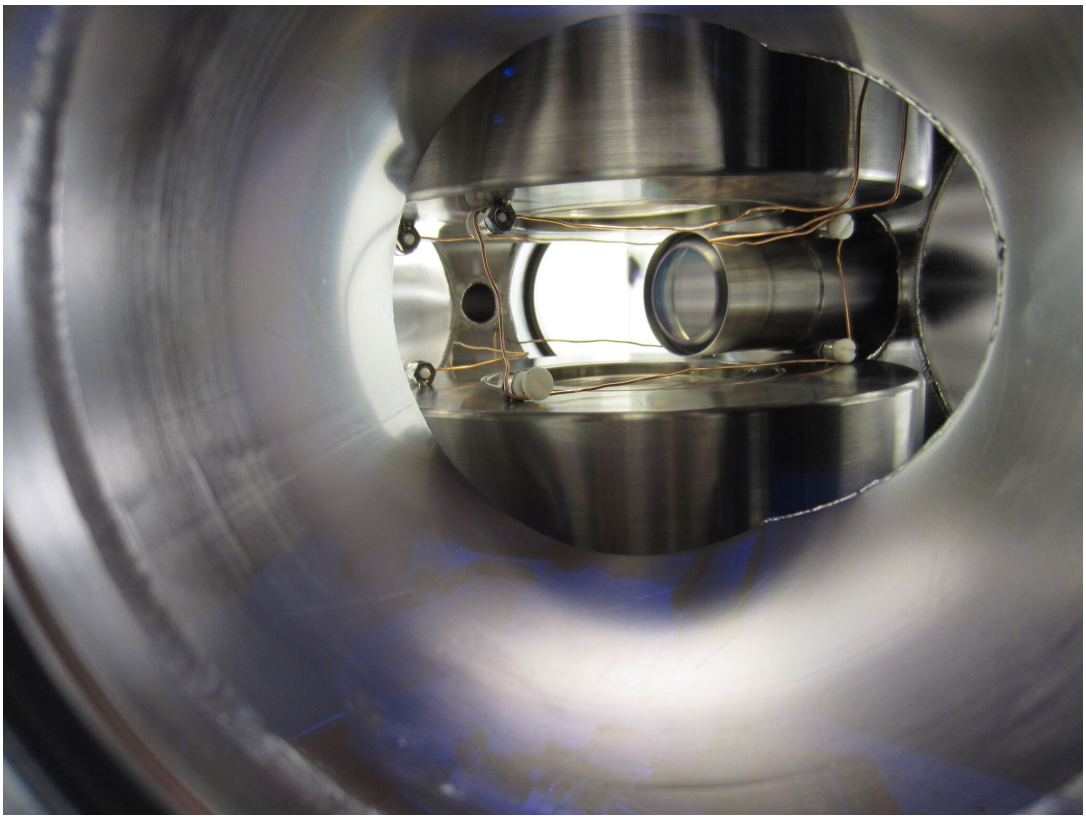

Figure 5.3: A photograph showing the two RF antennae wound inside the Li main chamber. The two antennae are rectangular and are threaded between the top and bottom re-entrant windows, to which they are affixed with macor screws. The side re-entrant window is also visible.

them in place. These antennae were never used in the experiment. One of the antennae became shorted to the main-chamber during pump-down, and the external leads of the feedthrough on the other antennae snapped off during an attempt to connectorize them. In addition, we decided to address radio frequency transitions between the two ground-state hyperfine manifolds, at and above 803.5 MHz[4]. For this purpose we use a loop antenna that is outside of vacuum.

The main chamber traping region can be accessed by 7 horizontal windows, which can be seen in the top-down CAD depiction in Figure 5.4. One is a 2.75" window that

[4]A transition from the magnetically trapped $|F = 2, m_F = 2\rangle$ state to the untrappable $|F = 2, m_F = -1\rangle$ state would require multiple photons, unlike the single photon transition to the untrappable $|F = 1, m_F = 1\rangle$ state.

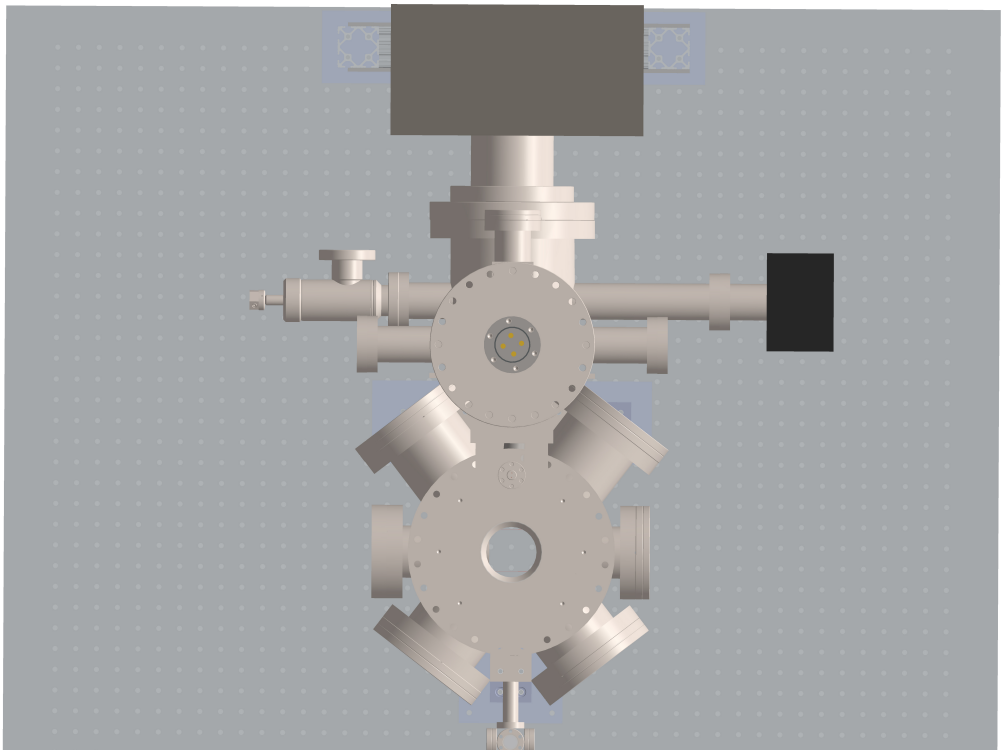

Figure 5.4: Top-down CAD depiction of the Li main chamber. Note the six horizontal windows that give access to the trapping region. The trapping region is also accessible through the pair of re-entrant windows along the vertical axis, which here is into the page. The four pairs of MOT beams enter the chamber through these eight windows. The seventh horizontal window, the Zeeman slower window, is along the atomic beamline, which here is vertical, and near the ion pump, which is at the top of the figure.

allows for the entrance of the Zeeman slower laser beam, which is counter-propagating to the atomic beam. A re-entrant window along the horizontal axis orthogonal to the atomic beam allows for the positioning of an objective at a distance of 34 mm to the atoms. A 4.5" window is placed along this axis on the other side of the main chamber. Four 6" windows were included in the design for the introduction of the four horizontal MOT beams. Due to the proximity of the side re-entrant window to the trapping region, and due to the desire for the ability to produce lattices with threefold symmetry, the

angle between the horizontal MOT beams and the atomic beams was designed to be an unusually shallow 31.5°. This was an unfortunate choice, as we were eventually forced to introduce a fourth pair of MOT beams long the side re-entrant window axis to increase the MOT confinement in this dimension.

5.3 Li oven

Lithium is the lightest metal, is soft, and reacts with water, producing a red flame. It is a solid at room temperature, and has a melting temperature of 180.5 ℃. In order to capture on the order of 10^{10} ^{7}Li atoms in the MOT over a reasonable load time of approximately 10 s, it is necessary to have a flux of atoms below the capture velocity (v_c) of the MOT that is at least 10^9 atoms/s[5]. The distribution of speeds v in an ideal gas is given by the Maxwell-Boltzmann distribution, $f(v)$

$$f(v) = \left(\frac{m}{2\pi k_B T}\right)^{3/2} 4\pi v^2 \exp\left(-\frac{mv^2}{2k_B T}\right), \tag{5.1}$$

where m is the mass of the atom, k_B is Boltzmann's constant and T is the temperature of the gas. The average speed of an atom in an ideal gas is therefore

$$\bar{v} = \int_0^\infty \mathrm{d}v\, v f(v) = \sqrt{\frac{8k_B T}{\pi m}}, \tag{5.2}$$

and the flux, Φ_v, of atoms with velocity, v, through a unit suface in unit time is

$$\Phi_v = \frac{n}{4\pi}\int_0^\infty \mathrm{d}v \int \mathrm{d}\Omega\, v\cos(\theta) f(v) = \frac{n\bar{v}}{4}, \tag{5.3}$$

where n is the number density of the gas, $\mathrm{d}\Omega$ is an infinitesimal solid angle, and θ is

[5]In this estimate we have swept loss processes from the MOT under the rug, but it serves as a useful minimium flux.

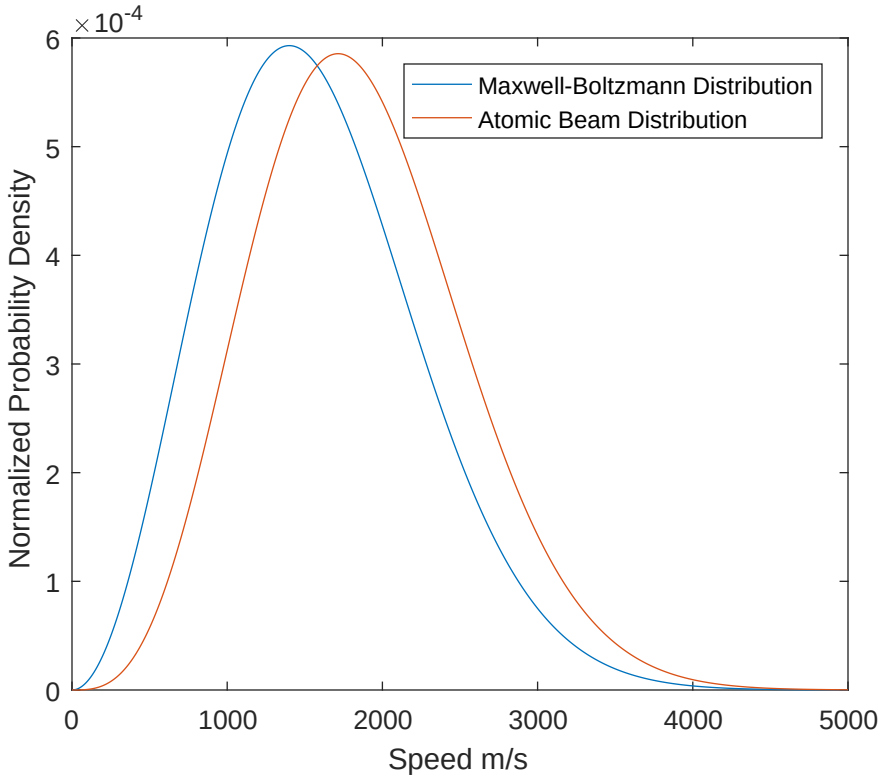

Figure 5.5: The Maxwell-Boltzmann distribution for a Li gas at 550 °C, and the speed distribution for a Li atomic beam at 550 °C. The percentages of atoms with speeds less than a MOT capture velocity of 50 m/s are 3.4×10^{-3}% and 8.1×10^{-5}% respectively. The percentages of atoms with speeds less than a Zeeman slower highest addressed velocity of 1000 m/s are 20.4% and 9.33% respectively.

the azimuthal angle. The atoms that do move through this area have a modified speed distribution $f_v(v)$, since the faster moving atoms have a higher flux. This is simply the flux sans integration over velocity, which, when normalized, is

$$f_v(v) = \left(\frac{m}{k_{\mathrm{B}}T}\right)^2 \frac{v^3}{2} \exp\left(-\frac{mv^2}{2k_{\mathrm{B}}T}\right) \tag{5.4}$$

and is more skewed towards higher velocities than the Maxwell-Boltzmann distribution. These two distributions are plotted for a gas and beam of Li atoms at 550 °C in Figure 5.5. Note the small populations of atoms with speeds $< v_{\mathrm{c}}$ and even < 1000 m/s.

In order to efficiently load a MOT, the number density of the gas n, and the population of atoms with velocity $v < v_c$ must be sufficiently high. Unfortunately, as

$$n = \frac{N}{V} = \frac{P}{k_B T}, \tag{5.5}$$

and the vapor pressure of a solid is typically exponentially increasing in T, these two desires are in competition. For certain species, such as Rb, the vapor pressure of the solid is sufficiently high at low temperatures, and the speed of the atoms is sufficiently low that MOTs can be loaded simply from the background gas produced by the low temperature solid. However, with Li the vapor pressure is low, requiring significant heating to produce sufficient number density. Due to this heating and the low mass of Li, the velocity distribution must be modified before a reasonable number of atoms can be captured. We chose to do this with a Zeeman slower, which requires an atomic beam which is collimated enough to have a sufficient flux of atoms through the MOT capture region.

5.3.1 Oven Nozzle

In order to produce a gas of Li atoms at a reasonable pressure and therefore number density and flux, it is necessary to heat it significantly above the melting point. The vapor pressure in torr in the solid (V_s) and liquid (V_l) phases at a temperature T are [75]

$$\begin{aligned} \log_{10} P_s &= -54.87864 - \tfrac{6450.994}{T} - 0.01487480\,T + 24.82251 \log_{10} T, \\ \log_{10} P_l &= -10.34540 - \tfrac{8345.574}{T} - 0.00008840\,T - 0.68106 \log_{10} T, \end{aligned} \tag{5.6}$$

and are ploted in Figures 5.6 and 5.7 respectively. The vapor pressure of solid Li peaks at a little over 10^{-10} torr at just below the melting point, which produces a flux of $\sim 5 \times 10^{10}$ atoms/s through a circular orifice with diameter 1 cm. However, such an orifice does not

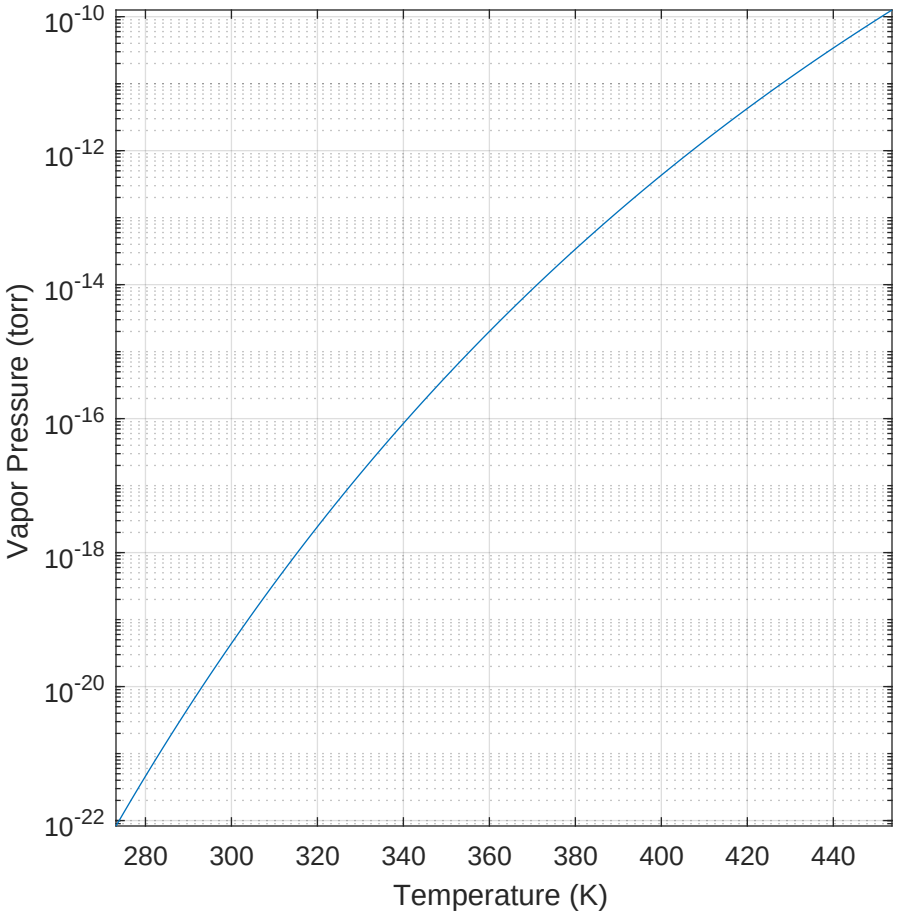

Figure 5.6: Vapor pressure of solid Li, plotted as a function of temperature, from the melting point of water, to the melting point of Li.

collimate the beam at all (the atoms are emitted into a solid angle of 2π steradians), and the flux through a solid angle subtended by the MOT capture region (~ 2 cm wide) at a distance of 2 m away is only $\sim 3 \times 10^6$ atoms/s[6]. Additionally, a Zeeman slower that is designed to slow atoms below, say, 1000 m/s to v_c will only capture 23.7% of the speed distribution if working perfectly, giving a slow flux of 7×10^5 atoms/s. To recover a flux of $\sim 5 \times 10^{10}$ slow atoms/s through the MOT capture region, the temperature must be increased to 365 °C. However, this increase in T increases the total flux out of the orifice,

[6]This assumes a uniform angular distribution of atom directions, which is a reasonable approximation.

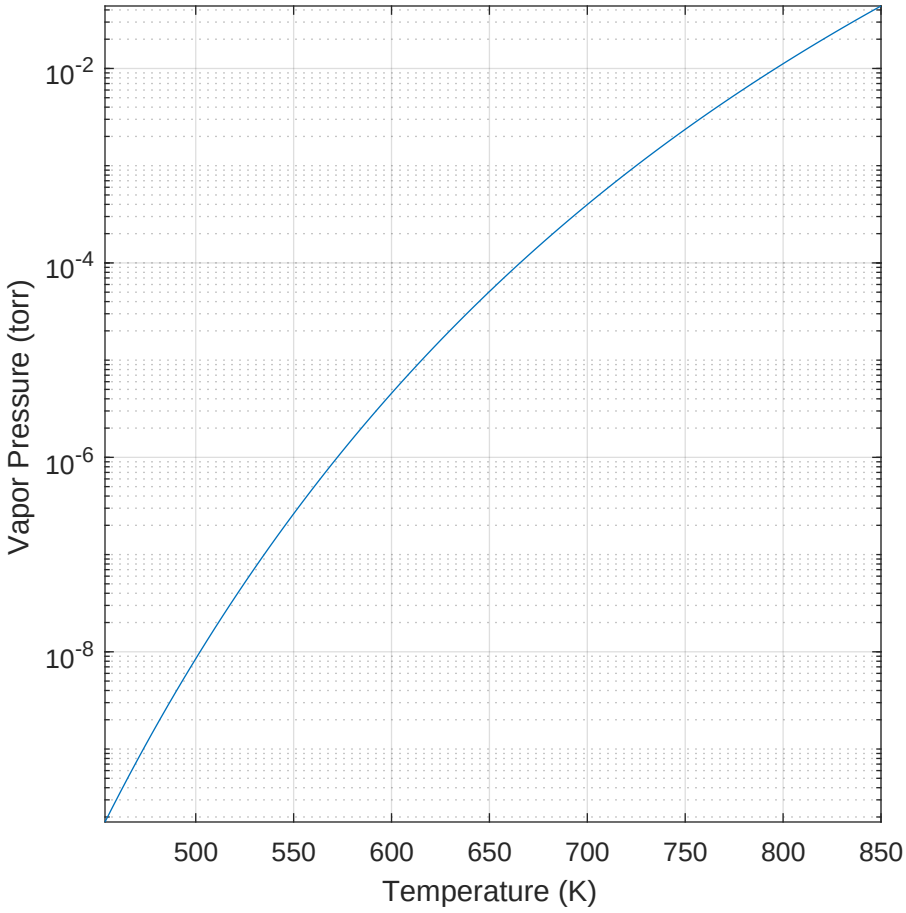

Figure 5.7: Vapor pressure of liquid Li, plotted as a function of temperature, from the melting point of lithium to 850 K.

leading to a reduction in lifetime of the oven, given a fixed supply of Li. Assuming an original supply of 25 g of Li, this oven would last just over 8 years at this temperature. In practice the Zeeman slower does not operate at perfect efficiency, particularly in Li where beam explosion is particularly large, and the repump light is not on resonance for all locations in the slower. These experimental realities reduce the lifetime of an oven, already an uncomfortably short time on the timescale of a professorial career, to an uncomfortably short time on the timescale of a graduate education.

The lifetime of an oven can be increased by replacing the orifice in our hypothetical

design with a collimating nozzle, the most simple of which is a tube with circular cross-section, and length much longer than the cross-sectional diameter. If we at first assume that all atoms that collide with the inner walls of the tube are returned to the oven, the atoms are now limited to a solid angle defined by the aspect ratio of the tube, which drastically improves the collimation, measured as the ratio of the solid angle subtended by the MOT and the solid angle into which the atoms are emitted. However, the class of atoms that pass through the tube without colliding with the walls decreases as the aspect ratio is increased, leading to an overall decrease in flux. Atoms which do collide with the walls undergo a random walk along the long dimension of the tube, until they reach either end of the tube and escape. Since the atoms are more likely to collide with the walls closer to the end through which they entered than the other end, they are more likely to exit from that end back into the oven, thereby recycling atoms that would have not reached the MOT region. Some atoms do escape after collisions with the walls towards the MOT, and this leads to an uncollimated shelf of atoms emitted into 2π steradians. The percentage of atoms in the central collimated peak increases as aspect ratio is increased, at the cost of flux. A simple compromise between these two conflicting demands is to have many tubes, each with a high aspect ratio.

Such multi-channel nozzles have been in use for many decades, and have been used in cold atom experiments for at least a decade. We chose to use 33RW gauge 304 stainless steel (SS) microcapillaries purchased from MicroGroup, Inc. These microcapillaries have circular cross-section and have an external diameter of 0.008" and an internal diameter of 0.004", and were cut to a 5 mm length and deburred prior to shipment. We developed a new nozzle design which holds these microcapillaries tightly in a hexagonal array enforced by the boundary condition of an orifice with the cross-sectional shape of an equilateral triangle. This design overcame the challenge of constraining hundreds of these small microcapillaries to be co-parallel. We published this design in an article in *Review of*

Scientific Instruments, which is reproduced in Appendix A. Subsequently this design or variants on this design have been implemented by at least ten other groups.

2-dimensional simulations suggested that a tube with this aspect ratio would permit 4% of atoms that impinged on one entrance to the tube with uniform angular distribution to exit the other side. This suggests a total flux of 2.3×10^{14} atoms/s out of a hexagonally-packed triangular array of 550 such tubes, and a lifetime of 292 years for a 25 g source, when there is a gas of Li atoms at 525 °C impinging upon the nozzle from one side[7]. Through absorption measurements of the atomic beam, we measured a flux of 1.2×10^{14} atoms/s in a collimated beam at this temperature. Additionally, the transverse velocity distribution we measured was consistent with that expected at this temperature given the aspect ratio of the tubes. Our simulations suggest that a significant proportion of the atoms are in a non-Gaussian shelf that includes high-angle atoms which collide with the walls near the exit of the microcapillaries, and this is consistent with the reduced flux measured in the collimated atomic beam.

5.3.2 Li reservoir and heating

The Li is contained in a cup[8], which is mounted such that the axis of symmetry of the cup is parallel to the direction of gravity. A 90°elbow connects this cup to the rest of the machine beamline, which is horizontal. This is necessary to ensure that the molten Li will not flow out of the cup, and particularly onto any conflat (CF) gaskets, which it could corrode. The micro-capillary array was assembled in a custom-machined double-sided

[7]Here we have assumed that no atoms move through the nozzle in between the hexagonally-packed tubes. The aspect ratio of these "tubes" is even higher than that of the microcapillaries, so this will not affect the flux through the nozzle substantially. We have also simply extended the result from our 2d simulation to the 3d case by taking the square of the percentage from the 2d case - i.e. 0.16% of the atoms pass through the nozzle. This agrees to within an order of magnitude with the Knudsen molecular flow conductance calculations for a collection of parallel tubes. The mean free path of Li atoms at this temperature is 0.2 mm, which is large compared to the entrance to the tubes, but not compared to the length of the tubes.

[8]The cup is an SS conflat half-nipple that has an SS plate welded across the nipple opening.

blank that was sandwiched between the elbow and a short nipple. This short nipple was used to absorb the thermal gradient from the nozzle, which is currently held at 550 °C. Stainless steel has a very poor thermal conductivity, and can maintain a thermal gradient of hundreds of degrees across a few inches. As long as there is not much of a gradient across a conflat flange, this is not a problem. We use grooved Ni gaskets purchased from Vacs SEV throughout the heated sections of the oven manifold, as Li vapor can corrode Cu gaskets. These Ni gaskets are harder than Cu ones, so require 316 SS conflat flanges. Therefore the cup, elbow, nozzle double-sided blank and short nipple to connect to the rest of the oven manifold were all custom parts made from 316 SS.

The cup and the CF flange connections between the cup and the elbow, and the elbow, the nozzle and the short nipple are directly heated using three Tempco Mi-plus band heaters. The entire heated section is wrapped in Al foil and fiber-glass insulation. It is critical to maintain the nozzle as the hottest point of this section. This is to ensure that Li does not deposit on the microcapillaries and clog them. To this end, we maintain a 100 °C temperature gradient from the cup heater to the nozzle heater[9]. We reduce the temperatures of each heater by 150 °C when the machine is not in use to extend the lifetime of the oven[10].

5.3.3 Oven manifold

After being produced by the nozzle, the atomic beam passes through several stages before entering the Zeeman slower. These stages block high-angle atoms, allow for transverse cooling and shuttering of the atomic beam, and implement differential pumping to maintain a pressure differential between the hot and relatively high-pressure oven and

[9]The set-points of the cup, cup flange and nozzle heaters are 450, 500 and 550 °C respectively.

[10]Complete thermal cycling to room temperature is not advisable. Kevin Mertes at Los Alamos National Laboratory, who implemented our nozzle design to produce a Li atomic beam, reported to us that leaks would develop in the nozzle after some amount of use. After discussion, we hypothesized that this may be due to their practice of completely cooling the nozzle to room temperature every night.

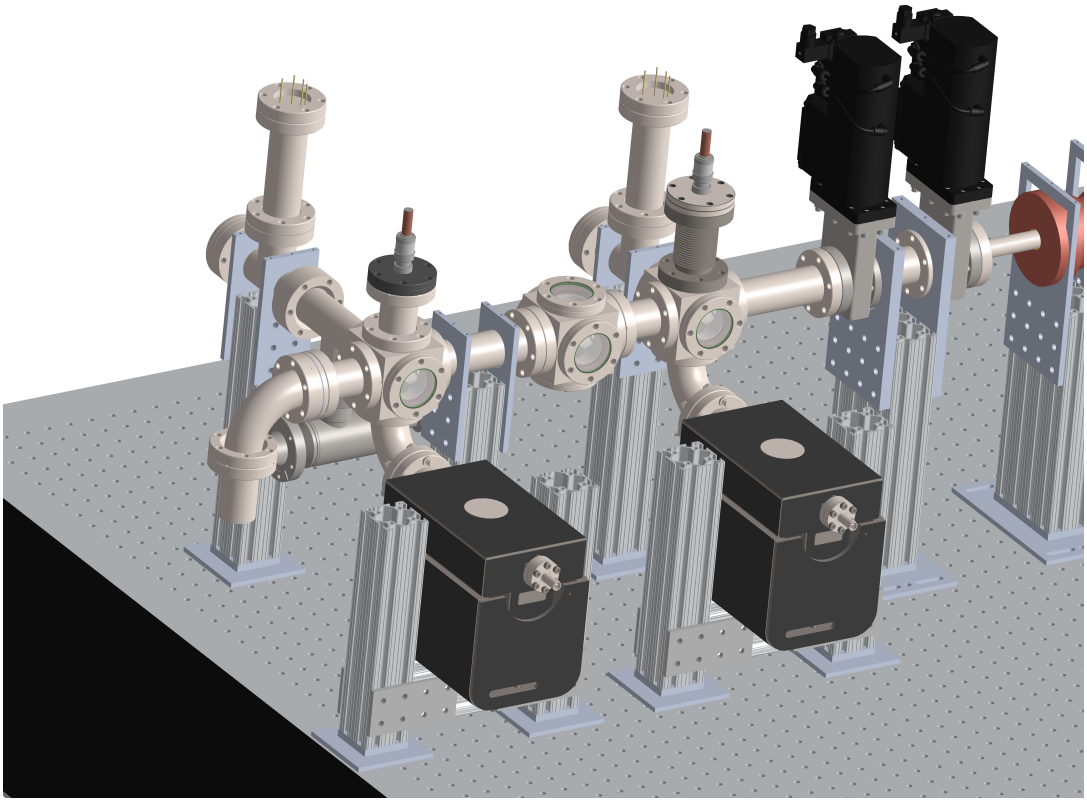

Figure 5.8: A CAD depiction of the Li oven manifold. The Li reservoir and nozzle flange are on the left, and the atomic beam travels towards the right, passing through the coldplate cube, the first differential pumping tube, the transverse cooling cube, the stopper cube, the second differential pumping tube and gate valves before entering the Zeeman slower.

the main chamber, where we target pressures on the order of 10^{-11} torr. The heated oven and these stages are collectively referred to as the oven manifold, a CAD depiction of which is shown in Figure 5.8.

The first vacuum component that the atomic beam line extends through, after the short nipple connected to the nozzle, is a 2.75" CF cube. A 45 l/s Gamma ion pump is connected to this cube via a 90° elbow, and a turbo pump may be connected to the manifold via a Kalrez elastomer[11] angle valve, which is connected to the cube via a CF T. A Varian UHV-24p ion gauge is connected to this T, and anti-reflection (AR) coated

[11]Kalrez is an expensive elastomer that outgasses less than the more common and less dear Viton.

windows allow for transverse interrogation of the beam. The last feature is a "coldplate," which is not actively cooled and consists of a 304 SS plate with a large hole machined through it. It is suspended in the cube by virtue of being screwed into a Cu rod, which is part of a re-purposed high-current electrical feedthrough, using vented SS screws to avoid virtual leaks[12]. This plate prevents high-angle atoms from coating the windows. We have observed some deposition on the cube window in places that have direct line-of-sight to the short nipple that connects to the nozzle.

This cube is connected to the next cube - one used for transverse cooling - via a full nipple which has a SS tube welded co-axially with the beamline[13]. This is one of two differential pumping tubes (DPTs) along the beamline that allows us to maintain a pressure difference between the two largely independently pumped sections that it connects. This is important because the pressure in the first cube is elevated due to being above room temperature due to the heat load from the heated parts of the oven manifold and the Li gas load through the nozzle. Differential pumping will be discussed in detail in Section 5.3.4.

The next cube has four AR-coated windows that allow for the application of 2d optical molasses beams for transverse cooling, or beam collimation. This cube is connected via a short nipple (short simply to reduce the total beamline length) to another cube, which is connected via an elbow to another 45 l/s Gamma ion pump, that pumps on the section between the two DPTs. An arm similar to that on the first section connects this section to another UHV-24p ion gauge with a T. Two AR-coated windows permit transverse interrogation of the atomic beam. The top flange of the cube is connected via a hydroformed bellows to another high-current electrical feedthrough. At the tip of this

[12]A virtual leak is a pocket of gas inside the chamber which is trapped via some low-conductance path to the rest of the chamber. It continuously leaks gas into the chamber, and is indistinguishable from a leak.

[13]The tube is held with a plate that is welded across the face of the nipple on one side. The only vacuum connection from one side of the nipple to the other is through the DPT.

feedthrough is a simple 304 SS block which blocks the atomic beam in its native state. The flexibility of the bellows allows for the feedthrough and the block to move out of the way of the atomic beam when actuated with a solenoid[14], forming a crude atomic beam shutter, which prevents the hot atomic beam from disturbing the trapped atoms after the MOT loading stage. From here the oven manifold is connected via the second DPT to the rest of the machine.

Two[15] Kalrez elastomer gate valves (with a short nipple between them) allow for separating the oven manifold from the main chamber. This allows for preservation of the vacuum of one side of the machine if the other side needs to be vented and re-baked.

5.3.4 Differential pumping

The conductance Q through a tube of radius r and length l in the molecular flow regime[16] when $l \gg r$ is given by the Knudsen formula [76, 77],

$$Q = \frac{8\pi}{3}\frac{r^3}{l}\sqrt{\frac{k_\mathrm{B}T}{2\pi m}}. \tag{5.7}$$

The conductance of hydrogen[17] through a full nipple (inner diameter (ID) ~ 1.5" and length ~ 5") at room temperature is thus ~ 185 l/s[18]. In order to model the functioning of a DPT, consider a chamber at negligibly low pressure connected to a pump with speed S and, through a tube with small conductance Q, to another chamber at a much higher

[14]Finding a solenoid with sufficient but not excessive stroke and force was a surprisingly difficult task. We use an Uxcell a14052100ux1279 solenoid purchased on Amazon.com, which is a pull-type solenoid with a stroke of 20 mm and "force" of 8 kg. We attached the solenoid slug to the external tip of the feedthrough with string or wire, and actuated the solenoid with a 3.3V TTL (transistor-transistor logic) signal sent to a solid-state relay or MOSFET.

[15]For redundancy.

[16]The molecular flow regime is when the mean free path of the particles is large compared to the size of the chamber

[17]After a successful bake the major contribution to the pressure is the partial pressure of H_2 molecules.

[18]For room temperature N_2 the conductance is ~ 50 l/s, and for room temperature Li the conductance is ~ 100 l/s. For 550 °C Li the conductance is ~ 160 l/s.

pressure P_{high} [78]. The major gas load onto the low pressure chamber is due to a leak through the tube from the high pressure chamber, which causes a pressure increase of

$$P_{\text{low}} = \frac{P_{\text{high}} Q}{S}. \tag{5.8}$$

From this relationship we can infer that the ratio of the pressures of the two chambers is

$$\frac{P_{\text{high}}}{P_{\text{low}}} = \frac{S}{Q} \tag{5.9}$$

For a chamber with a large pumping speed and a tube with small conductance, this ratio can be very high. In practice, the conductance of the tube has a minimum value set by the diameter required to allow a clear aperture for the atomic beam.

In our system we use two DPTs. The first is located between the cold plate section and the transverse cooling/atomic beam shutter section, and is a SS tube with ID 0.18" and length 6", and therefore a conductance of 0.29 l/s for room temperature hydrogen[19]. The effective pumping speed for a chamber connected to a pump with pumping speed S by a connection with conductance Q is S_{eff} is

$$\frac{1}{S_{\text{eff}}} = \frac{1}{S} + \frac{1}{Q}. \tag{5.10}$$

In our system, a 45 l/s pump is attached to the chamber via a 2.75" CF 90° elbow, the conductance of which we estimate by half the conductance of a straight tube of length equal to the inner length of the elbow. This gives a conductance of ~ 15.9 l/s for hydrogen at room temperature[20], which gives an S_{eff} of ~ 11.25 l/s[21]. Thus the pressure

[19]The conductance of room temperature Li is 0.15 l/s, and the conductance of 550 °C Li is 0.26 l/s.

[20]For room-temperature Li the conductance is ~ 8.5 l/s and for 550 °C Li the conductance is ~ 14.0 l/s.

[21]The effective pumping speed of room-temperature Li is ~ 7.1 l/s and of 550 °C Li is ~ 10.7 l/s.

ratio supported by the DPT is ~ 39[22].

The second DPT is between the atomic beam shutter cube and the gate valve manifold, through which it is connected to the Zeeman slower and the main chamber. It is also an SS tube, but with ID 0.3" and length 6". The increased diameter was chosen to accomodate the increased atomic beam diameter at this location without any clipping. This tube has a conductance of 1.4 l/s for room-temperature hydrogen. It is more complicated to calculate the pressure ratio that this DPT can support, as it is necessary to estimate the pumping speed of the main chamber due to the Ti-sublimation pump (Ti-sub), and because the Zeeman slower tube restricts conductance in a similar way to a DPT. A cm^2 of deposited Ti can pump a few l/s of chemically active gases. Estimating the coated area to be a few 1000 cm^2, and the conductance of the rectangular-cross section tube connecting the Ti-sub to the main chamber to be a few 1000 l/s, we can safely estimate that the effective pumping speed of the main chamber is on the order of 1000 l/s. The Zeeman slower is approximately 1 m long, and has an ID ~ 0.6", giving a conductance of 1.6 l/s. Thus the total conductance through the DPT and the Zeeman slower is ~ 0.75 l/s. This gives a DPT-supported pressure ratio on the order of 750.

The combined pressure ratio from the two stages of differential pumping give a ratio of $\sim 3 \times 10^4$. In practice, this is a higher differential pumping ratio than required, as the pressure measured by the oven-section ion pumps are $\sim 2 \times 10^{-8}$ torr[23] when the oven nozzle is held at 550 °C, and we have bottomed out our ion gauge on the main chamber at 5×10^{-12} torr after a fresh deposition of Ti.

5.3.5 Zeeman slower window

The atoms that are not collected in the MOT pass through the trapping region

[22]For room-temperature Li the pressure ratio is ~ 47 and for 550 °C Li the pressure ratio is ~ 41.
[23]The ion gauges read a pressure of $\sim 5 \times 10^{-}9$ torr.

and the majority of them eventually collide on the window through which the counter-propagating Zeeman slower laser beam enters the chamber[24]. This is an issue because Li is deposited on this glass and can reduce the transmission of the window significantly. If left unchecked, over a long period of use it could reduce the effective power in the Zeeman slower beam to the point where the MOT loading rate is insufficient. The only solution at this stage is to vent the main chamber and replace the window with a new one[25]. We do two things to reduce the amount of Li deposited on this window. The first is that we keep the slower window heated to approximately 150 °C. In order to keep the window uniformly heated to avoid cracking the glass, we keep it enclosed in a cylinder made of spring steel. The cylinder is end-capped on one end by the slower window, and on the other side another window[26]. A band-heater is slipped around the cylinder and the entire region is insulated with Al foil and fiber-glass. The second thing we do is shine a high-power 405 nm light-emitting diode (LED) onto the window. Through the process of light-induced atomic desorption (LIAD), Li atoms that are deposited on the glass are removed. LIAD has been used to load MOTs of Rb [79, 80]. We have observed a substantial and repeatable spike in the main chamber pressure when this LED is turned on.

5.4 Li Zeeman slower

As discussed in Section 5.3, it is not possible to load a sizeable MOT from the background pressure of Li due to its low vapor pressure and mass. In order to produce a

[24]To counter this issue some machines include a mirror at 45° to the beamline. The Zeeman slower laser is introduced along a line that is orthogonal to the beamline and is reflected off of the mirror and up the Zeeman slower. Since atoms colliding with the mirror do not obey the law of reflection, this window does not get substantially coated. However, the reflectivity of the mirror may be modified over time due to adsorption of atoms from the atomic beam.

[25]Or get some huge source of laser power.

[26]Note that there is no vacuum between these two windows.

sufficient flux of Li atoms through the MOT-capture region, the Li liquid must be heated to several hundreds of degrees Celsius, leading to a negligible proportion of the atoms having velocity lower than the capture velocity of the MOT. Therefore some modification of the speed distribution of the atoms must be made - i.e. some fraction of the atoms must be slowed. There are a couple of methods that have been used in Li to achieve this. The first is a Zeeman slower, which, as discussed in Section 2.2.2, requires an atomic beam, counter-propagating resonant light, and a spatially varying magnetic field along the length of the slowing region to counter the varying Doppler shift as the atoms are slowed down. The second is a 2d MOT, which is a MOT with one axis of lasers and magnetic field gradient removed, or alternatively, transverse cooling with a quadrupolar magnetic-field gradient in the plane perpendicular to the beam direction. A "push" resonant laser beam can be applied orthogonally to the beamline to push atoms trapped and cooled in that dimension towards the main chamber with a relatively low velocity. This has the advantage of not requiring the hot atomic beam to enter the 3d MOT chamber. A 2d MOT has been used to load a 3d MOT with 10^{10} ^{6}Li atoms from a hot atomic beam [81]. We considered both options in the early stages of planning the Li apparatus, and we chose to use a Zeeman slower based on our confidence in the technology's ability to deliver a high flux of low-velocity atoms and our familiarity with the technology.

Given the choice to build a Zeeman slower, this necessitated a sophisticated atomic oven to produce a collimated atomic source that is capable of delivering atoms to the MOT from approximately 2 m away. This design is discussed in Section 5.3. Assuming that we have such a collimated atomic beam, we began to design the Zeeman slower. We considered both electromagnet-based and permanent magnet-based solutions to produce the spatially-varying magnetic field. Electromagnets have the advantage of being able to be turned off after the MOT loading stage, while permanent magnets have the advantage of simplicity and, depending on the configuration, the virtue of not being topologically

captured by the vacuum hardware, and thus allowing complete replacement without breaking vacuum. We chose to use an electromagnet-based solution, both due to the advantage of being able to turn it off[27], and due to our familiarity with the winding of electromagnet Zeeman slowers. We did experiment with permanent-magnet based Zeeman slowers [82].

5.4.1 Decreasing-field spin-flip Zeeman slower

We decided to design the Zeeman slower to slow all atoms traveling ≤ 1000 m/s to 50 m/s. This decision was made based on the feasibility of the magnetic field strengths and light shifts required, as well as the fact that this would give us a significant fraction of the speed probability distribution (see Figure 5.5)[28]. Using the result from equation 2.38, the minimum length required to slow an atom from 1000 m/s to 50 m/s is 0.31 m. Using an η parameter of 2 to be conservative, we planned for a Zeeman slower with length ~ 0.6 m. The Doppler shift of the frequency of a 671 nm photon that is enountered by a Li atom traveling at 1000 m/s is 1.49 GHz (see equation 2.34). Using the transition shift for the $|F = 2, m_F = 2\rangle \rightarrow |F' = 3, m_{F'} = 3\rangle$ transition in Table 3.3, we find that the required magnetic field to compensate for this Doppler shift is 1064 G[29]. The Doppler shift of the frequency of a 671 nm photon that is encountered by a Li atom traveling at 50 m/s is 74.5 MHz. For the same transition, the required magnetic field to compensate for this Doppler shift is 53 G.

Naively, the exit field of this slower should be 53 G. In practice the slower magnets will have some drop off beyond this, and further slowing is possible in this fringe-field.

[27] μ-metal shielding can be used to shield the magnetic fields from permanent magnets, but it can be a temperamental technology.

[28] We initially planned for a beam distribution with temperature lower than the eventual 550 °C that we settled upon empirically.

[29] At high field (such as 800 G), the Zeeman shift is determined solely by the electron spin, so this is a good approximation of the Zeeman shift for 4 out of 8 of the ground states. Half of the 1000 m/s atoms are thus lost to the slowing process from the entrance of the slower.

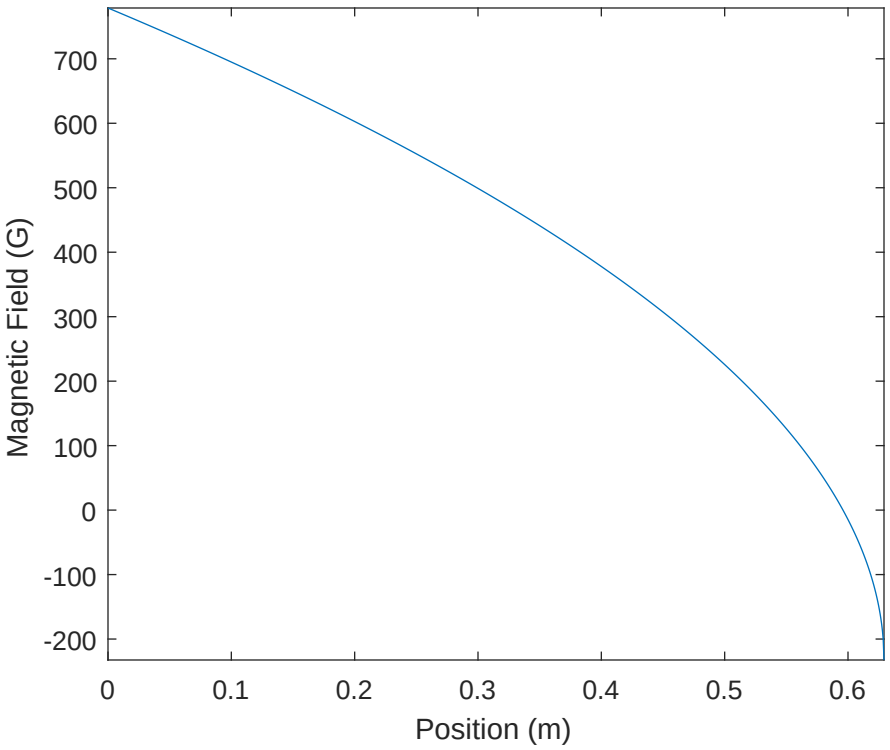

Figure 5.9: Desired magnetic field profile for Li Zeeman slower.

To avoid any atoms being slowed to a stop or even turned around, it is a good idea to end the slower at a moderately high absolute field[30]. Therefore, we chose to have a spin-flip or zero-field section in the latter half of the Zeeman slower. Thus the entrance of the Zeeman slower was designed to be at 778 G, and the exit field was designed to be -233 G[31]. This choice of offset is equivalent to a resonance detuning of 400 MHz. This low-field region of the slower leads to issues with the laser-cooling. In the excited state manifold, the electron and nuclear spin are decoupled for fields greater than ~ 20 G, so the cycling transition is closed at such fields ($\Delta m_I \neq 0$ transitions are forbidden). However, at lower fields the the electron and nuclear spins are coupled, and m_I changing transitions to the

[30]One could operate a slower on the σ^- transition, and thereby end at a very large field, but this is not ideal due to the large fringe field effects on the MOT field gradient.

[31]The magnetic-field gradient changes sign at the end of the slower, ensuring that atoms will not be slowed beyond this point.

$F = 1$ manifold are allowed, and the re-cycling laser is required to re-cycle the atoms to the $F = 2$ manifold[32].

Given these considerations, the desired magnetic field profile of the Zeeman slower is

$$B_{\mathrm{ZS}}(z) = (B_{1000} - B_{50})\left(1 - \frac{2\,\eta\,a_{\max}\,z}{v_{\max}^2 - v_{\mathrm{c}}^2}\right)^{1/2} + B_{50} - B_{\mathrm{offset}}, \tag{5.11}$$

where $B_{1000} = 1064$ G, $B_{50} = 53$ G, $\eta = 2$, $v_{\max} = 1000$ m/s, $v_{\mathrm{c}} = 50$ m/s, and $B_{\mathrm{offset}} = 286$ G. This magnetic field profile is ploted in Figure 5.9. This field configuration would require σ^+ cycling ($|F = 2, m_F = 2\rangle \rightarrow |F' = 3, m_{F'} = 3\rangle$) and re-cycling ($|F = 1, m_F = 1\rangle \rightarrow |F = 2, m_F = 2\rangle$) light that is detuned red of the zero-field transitions by 400 MHz respectively. This detuning is conveniently near the zero-field resonance.

5.4.2 Zeeman slower construction

Given the profile obtained in section 5.4.1, we set out to construct such a field profile with an electromagnet. The most straightforward design to produce such a field is a tapered solenoid. In order to make winding the slower more convenient, we split it into four separate segments: three for the decreasing field section, and one for in the increasing (absolute) field section. This also enabled us to run different currents in each segment. The wire we used has square cross-section to enable easy stacking of solenoid coils and is hollow to allow for water flow for heat management. It is made from Cu alloy 101, has an external square side length of 0.1875" and a wall thickness of 0.032", and is insulated with Daglass[33]. Using these dimensions, we simulated the magnetic field produced for various coil arrangements, and optimized the coil configuration to match the desired magnetic

[32]The re-cycling transition is $|F = 1, m_F = 1\rangle \rightarrow |F' = 2, m_F = 2\rangle$ transition, which has a significantly larger transition shift than the cycling transition (see Table 3.4). Therefore the re-cyler is only on resonance at low magnetic fields. Power-broadening is your friend.

[33]This insulation was one of the temperature limiting factors in our bakes, as it is rated to 180 °C.

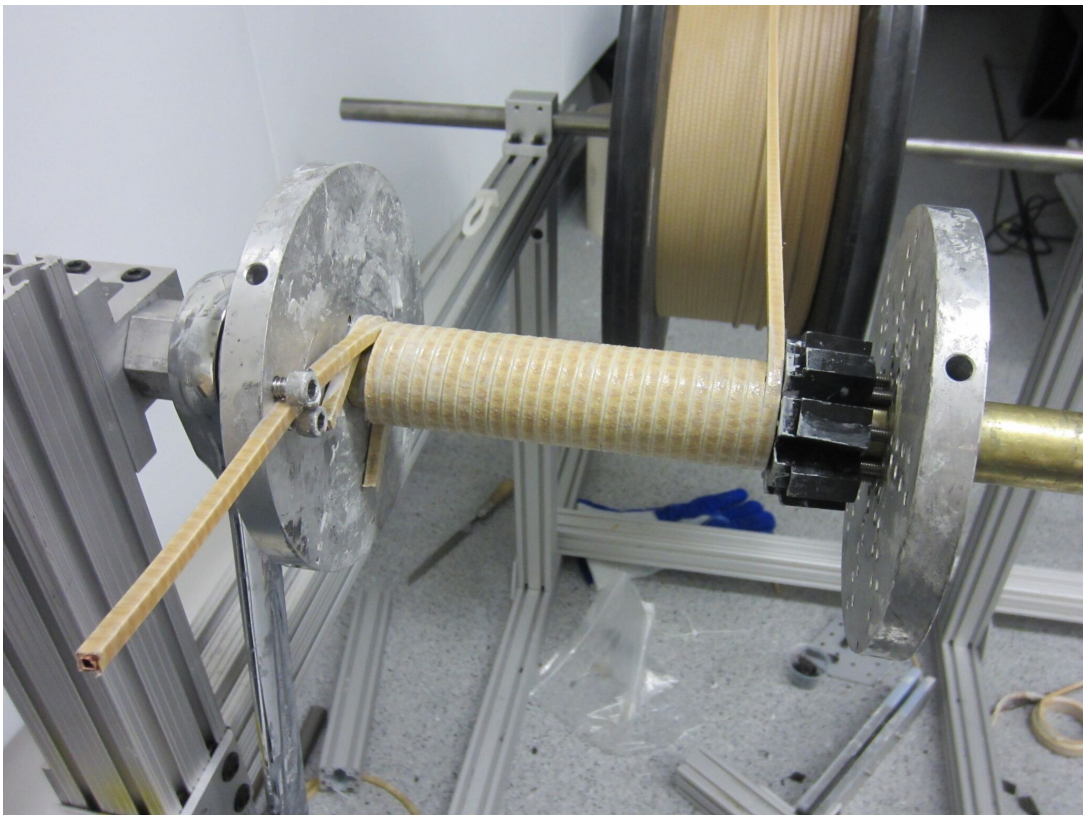

Figure 5.10: A photograph taken midway through the slower winding process. The winding rig, the wire spool, and the brass tube on to which the slower was wound are visible. At the time at which this photograph was taken, the first layer of the slower segment being wound was complete, and lateral confinement was being applied by using plastic blocks on the ends of set screws.

field profile and to be feasible to construct.

We then wound the wires on a brass tube with an outer dimension (OD) of 1". This was chosen to easily slip over the SS tube with OD 0.75" that connects the gate valve manifold to the main chamber without making contact with it[34]. The winding was done on a rig made of a mixture of custom-machined parts, and stock from 80/20 Inc. The spool of wire and the brass tube were mounted on axles, and a wrench was used to turn the brass tube axle and thereby wrap the wire around the brass tube. Thermally

[34]The brass tube cannot, however, slip over the 1.33" conflat flanges on the SS tube. We used custom split-ring flanges to allow us to slip the Zeeman slower segments onto the SS tube before making conflat connections. We ensured that we left enough room to fit in a wrench to tighten the bolts on these CF connections.

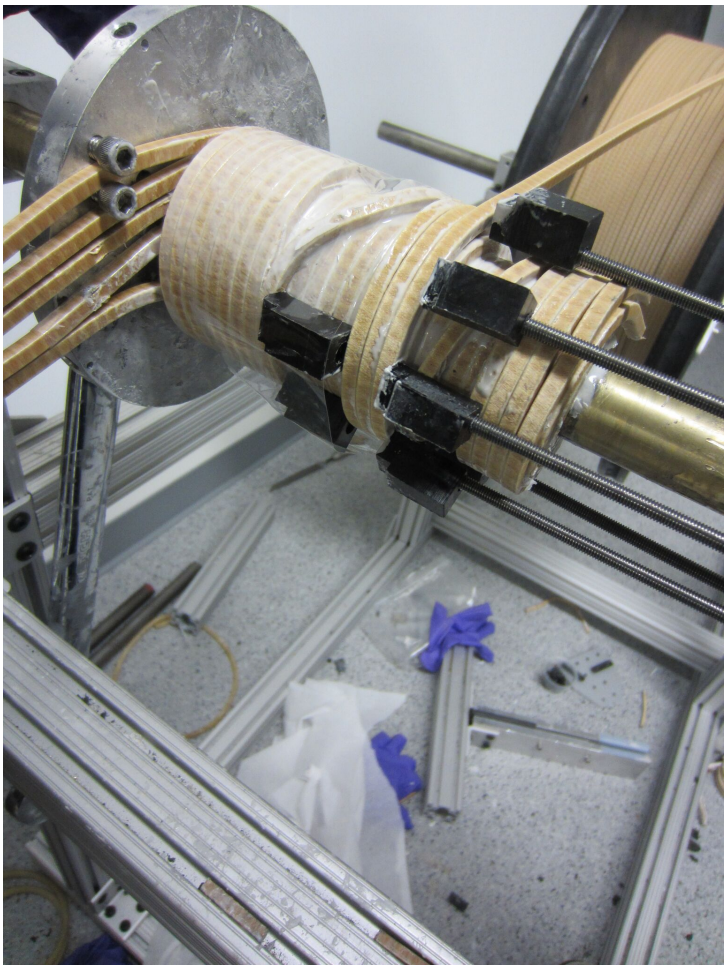

Figure 5.11: A photograph taken midway through the slower winding process. This photograph was taken after the completion of the fifth layer of the same slower segment as shown in Figure 5.10. Note the implementation of a gap between coils in this layer.

conductive epoxy (Duralco NM-25) was used to epoxy the coils to the brass tube, and to each other. This epoxy has a 24 hour cure time at room temperature, so we wound one layer per day, and left the rig under tension while it cured. Lateral confinement of the coils was provided by squeezing the coils between a plate that was slipped onto the brass tube and long set screws that were screwed into threaded holes in another such plate. The threaded holes were postioned along the perimeter of circles around the brass tube, with radii corresponding to each layer of coils. The plates were affixed to the brass tube with set screws. Care had to be taken to avoid tearing the insulation of the coils; the

first Zeeman slower segment that we wound had a fatal short buried inside the coil stack. To avoid tearing the insulation we used plastic blocks on the tips of the set screws and on the tips of all tools we used to apply force on the wire during the winding process. Figure 5.10 shows a photograph of the winding process after the completion of the first layer of a slower segment, and Figure 5.11 shows a photograph of the winding process after the completion of a higher layer on the same slower segment. Once a segment was completed, we used a hacksaw to saw off the excess brass tube as close as possible to the coil position on the bottom layer. We followed this method to wind the Zeeman slowers and MOT coils (which were wound on mandrels instead of brass tubes) for both experiments.

5.4.3 Zeeman slower electronics

The four Zeeman slower sections are powered with four separate DC power supplies, and each have a current that is in the 10s of A (see Table 5.1 for the current for each section). By the initial design the currents in sections A and D were highest, and we used Sorensen DLM 8-75 power supplies rated to 75 A at 8V for these sections. Sections B and C had more modest requirements, so we used Acopian W8LTU6400 power supplies rated to 64 A at 8 V. Both of these power supplies are specified to have low ripple noise.

The power supplies are connected to the slower sections with 10 AWG (American Wire Gauge) stranded battery cable via Al lugs that are clamped to the 3/8" OD circular-cross-section hollow Cu tube that is soldered to ends of the square cross-section electromagnet wire (see Section 5.4.4 for a discussion of this solder connection). The lug is a rectangular block with two circular holes milled out of it. One hole accepts the 10 AWG battery cable, and has a threaded hole for a screw that is used to press the cable firmly against the Al walls. The other hole fits around the circular-cross-section tube. Since the circular tube

Slower Section	Design Current(A)	Actual Current (A)
A	65	28.7
B	45	55.7
C	27	28.4
D	72	45.0

Table 5.1: Currents used in the four sections of the Li Zeeman slower.

is Swageloked on one end and soldered to the magnet wire on the other end, it would be impossible to slip the tube on or off of this tube after it has been Swageloked. To get around this issue, and to provide a way to clamp the lug around the tube, a notch is milled out of the wall of this hole, large enough such that the square-cross-section magnet wire can slip into it, but the circular-cross-section Cu tube cannot slip out of it. The lug is slipped on to the magnet wire behind the tube, and then slid onto the tube. A bolt is then passed through clearance holes drilled through the notch, and is tightened with a nut, clamping the lug around the Cu tube.

The gaps between the 3 slower segments in the decreasing field section of the slower led to dips in the measured magnetic field profile. These were countered by winding shim coils with 22 AWG, polyimide-insulated, circular-cross-section motor wire. They carry low currents through many turns, and are powered by bench-top GWInstek power supplies. The currents of the four slower segments and the shim coils were set empirically, by optimizing the load rate in the MOT. To do this we would flash on the MOT beams for a short ($\sim$ 1 s) period of time repeatedly while measuring the MOT fluorescence on a photodiode. The current phase-space would be explored while trying to maxmize the peak fluorescence signal for a fixed load time.

Switching of the high-current slower section power supplies is achieved using solid-state relays (Crydom D1D40 and D1D80, rated to 40 and 80 A respectively) with high-power diodes (Powerex CS240650 and CS241210, rated to 50 and 100 A respectively) in a ring-down-circuit configuration. The slower shim coils are not switched.

5.4.4 Zeeman slower thermal management

The high currents run through the four slower sections lead to substantial resistive heating of the solenoids. The power, P_{h}, of resistive heat production is simply

$$P_{\mathrm{h}} = I^2 R = \frac{I^2 \rho L}{A_{\mathrm{cond}}} = \frac{I^2 L}{\sigma A_{\mathrm{cond}}}, \tag{5.12}$$

where I is the current, L is the length of the wire, A_{cond} is the cross-sectional area of the conductor, and ρ and σ are the resitivity and conductivity of Cu respectively. The conductivity of the Cu alloy 101 is $1.01 \times 5.8 \times 10^7$ S/m, and the cross-sectional area of the conductor in our hollow square wire is 1.28×10^{-5} m^2.

To calculate the liquid flow through a tube with non-circular cross-section it is common to define the hydraulic diameter, D_{H}, which is [83]

$$D_{\mathrm{H}} = \frac{4 A_{\mathrm{water}}}{p}, \tag{5.13}$$

where A_{water} is the cross-sectional area of the tube, and p is the perimeter of this area. For a square cross-section, the hydraulic diameter is simply the length of the side of the square, d. In terms of the hydraulic diameter, the flow Q through the Cu tube in cm^3/s

$$Q = 8000 \sqrt{\frac{\Delta P D_{\mathrm{H}}}{L}} d^2 \tag{5.14}$$

where ΔP is the pressure differential across the tube in atm, and D_{H}, d and L are in cm.

If we assume that all of the generated heat is absorbed by the water, then the equilibrium rise in temperature of the water in °C is given by

$$\Delta T = \frac{P_{\mathrm{h}}}{c_{\mathrm{w}} Q} = \frac{P_{\mathrm{h}}}{4.186 \times Q} \tag{5.15}$$

Slower Section	Length (m)	Power (W)	ΔT (°C)
A	19.7	19.1	0.3
B	29.2	120	2.0
C	13.2	14 .1	0.2
D	1.91	5.14	0.1

Table 5.2: Length, power consumption, and temperature rise (ΔT) of cooling water of each slower section. Temperature rise calculation assumes that all slower sections are connected in hydraulic series, which gives a flow rate of ~ 14 cm^3/s at 100 psi.

where c_w is the specific heat of water in J/g·°C, where we have used that the density of water is 1 g/cm^3. Using this result we can calculate the expected rise in temperature for the water in each slower section, given that our lab chilled water supply pressure is set to 100 psi[35]. The calculated temperature rise for each slower section is listed in Table 5.2. Water cooling is only strictly necessary for section B.

In order to connect hydraulic lines to the solenoid wire, we had to overcome the proverbial challenge of fitting a square peg in a round hole or vice versa. Eventually we came upon an easy and reliable method to solder a Cu tube with circular cross-section onto the square-cross-section wire[36]:

- Strip away the insulation on all four sides of the magnet wire. This is most easily accomplished with a Dremel with a carbide tip. Strip the insulation away from a length $\sim 2-3$".

- Slip on a $\sim 2-3$" length of round Cu tubing (we use 3/8" OD) onto the stripped magnet wire. For this purpose it is useful to select a tube with ID that is close to the diagonal length of the magnet wire, otherwise the Cu tube tends to slip all the way down the magnet wire. Ideally the length of this tube is about a 1/4" shorter than the stripped section, one edge abuts the boundary of where the insulation

[35]This assumes that the total pressure drop is across the solenoid. One can calculate the total flow rate including the effects of the tubes used to connect to the slower sections, but this effect is negligible.

[36]This method is known as Dylanization in our group, as it was developed by Dylan Kennedy.

begins, and the stripped magnet wire pokes a short distance out of the other end.

- Wrap the Cu tube/insulated magnet wire interface with a small amount of Al foil, and tie it off tightly with some wire.
- Heat the Cu tube with a blowtorch and melt solder into the gaps between the Cu tube and the stripped magnet wire, taking care not to drip any solder into the magnet wire itself. Fill the gaps completely.
- Unwrap and discard the foil wrapper at the base of the Cu tube. Polish the Cu tube with isopropyl alcohol and steel wool to return the Cu tube to its pre-blowtorch finish.
- Fasten a Swagelok to the free end of the Cu tube. The free end of the stripped magnet wire will poke into the Swagelok to some extent, but this is not a problem.

These connections have proved to be incredibly reliable. In the history of our lab, only one such connection has ever leaked, and that was due to some extreme and ill-advised torquing of one of the solder joints.

5.5 Li magnets

Magnetic-field gradients or magnetic fields are necessary for MOTs, magnetic traps and the tuning of the scattering length via a magnetic Feshbach resonance. Due to the varied needs of each of these stages, electromagnets are almost always used in ultracold atom experiments to achieve these field profiles. Furthermore, it is often desirable to switch a magnetic field or field gradient on or off as quickly as possible. Turning on a magnetic-field gradient quickly is critical to minimizing the expansion of the atomic cloud between the gray molasses and magnetic trapping stages. Turning off a magnetic-field

gradient quickly is necessary to minimize expansion of the atomic cloud beween the MOT and gray molasses, as well as to perform time-of-flight (TOF) thermometry measurements out of a magnetic trap, which is very useful during the optimization of the magnetic trap loading and forced RF-assisted evaporation. To this end the electromagnets used should have low inductances to minimize switching time, and therefore are typically designed to have few turns but run high currents. Thermal management is thus a critical aspect of magnet design.

In order to use the highly-desirable Feshbach resonance in the ^{7}Li $^2S_{1/2}$ $|F = 1, m_F = 1\rangle$ state, one must be able to produce uniform magnetic fields up to the resonance field of 737 G (see Sections 2.1.7 and 3.3 for a discussion of Feshbach resonances). It is critical that this field gradient is uniform on the scale of the ultracold atom cloud, as field-gradients apply forces on the atoms with non-zero m_F. For this reason it is common to use a pair of Helmholtz coils to produce a magnetic field profile with minimum curvature. A pair of circular coils, each with radius a, is said to be in the Helmholtz condition if their separation is a. For such a pair of coils with currents flowing in the same direction in each coil, this condition generates a magnetic field with zero curvature at the point midway between the coils along the axis of symmetry. If the current in one of the coils is reversed, a quadrupolar magnetic field is produced, with a magnetic-field and magnetic-field-gradient-curvature zero at the point midway between the coils along the axis of symmetry. Therefore it is convenient to use the same pair of coils to produce the MOT and magnetic trap quadrupolar fields, and the Feshbach uniform field.

5.5.1 Helmholtz and anti-Helmholtz coils

The magnetic field in free space produced by a right-handed current loop with current I and radius a, centered about the origin and resting in the $z = 0$ plane, is given by [84]

$$B_z(r, z, I) = \frac{\mu_0 I}{2\pi} \frac{1}{\sqrt{(r+a)^2 + z^2}} \left(\frac{a^2 - r^2 - z^2}{(a-r)^2 + z^2} E(k) + K(k) \right) \tag{5.16}$$

in the z-direction and

$$B_r(r, z, I) = \frac{\mu_0 I}{2\pi} \frac{z}{r\sqrt{(r+a)^2 + z^2}} \left(\frac{a^2 + r^2 + z^2}{(a-r)^2 + z^2} E(k) - K(k) \right) \tag{5.17}$$

in the radial direction (r), where μ_0 is the magnetic permeability of free space, $K(k)$ and $E(k)$ are complete elliptic integrals of the first and second kind respectively, and k is

$$k = \sqrt{\frac{4ar}{(a+r)^2 + z^2}}. \tag{5.18}$$

The magnetic field in a Helmholtz configuration (where the two loops have the same I and are in the $z = a/2$ and $z = -a/2$ planes respectively) is given by

$$\begin{aligned} B_z^{\mathrm{H}}(r, z, I) &= B_z(r, z + a/2, I) + B_z(r, z - a/2, I) \\ B_r^{\mathrm{H}}(r, z, I) &= B_r(r, z + a/2, I) + B_r(r, z - a/2, I). \end{aligned} \tag{5.19}$$

It can be shown that the curvature of the magnetic field (second spatial derivative) vanishes at $z = r = 0$, where

$$\begin{aligned} B_z^{\mathrm{H}} &= \frac{8\mu_0 I}{5\sqrt{5}a} \\ B_r^{\mathrm{H}} &= 0. \end{aligned} \tag{5.20}$$

The magnetic field in an anti-Helmholtz configuration (where one loop is in the $z = a/2$ plane and has current I and the other loop is in the $z = -a/2$ plane and has current -I) is given by

$$\begin{aligned} B_z^{\mathrm{AH}}(r,z,I) &= B_z(r,z+a/2,I) + B_z(r,z-a/2,-I) \\ B_r^{\mathrm{AH}}(r,z,I) &= B_r(r,z+a/2,I) + B_r(r,z-a/2,-I) \end{aligned} \tag{5.21}$$

It can be shown that the magnetic field and the curvature of the magnetic field gradient (third spatial derivative) both vanish at $z = r = 0$, where

$$\left.\frac{\partial B_z^{\mathrm{AH}}}{\partial z}\right|_{z=r=0} = \frac{48\mu_0 I}{25\sqrt{5}a^2} = \frac{6}{5a}B_z^{\mathrm{H}}, \tag{5.22}$$

and

$$\left.\frac{\partial B_r^{\mathrm{AH}}}{\partial r}\right|_{z=0,r\to 0} = -\frac{24\mu_0 I}{25\sqrt{5}a^2} = -\frac{1}{2}\left.\frac{\partial B_z^{\mathrm{AH}}}{\partial z}\right|_{z=r=0}. \tag{5.23}$$

The 2:1 ratio between the axial field gradient and the radial field gradient hold for any field profile that contains a field zero along an axis of azimuthal symmetry, since $\vec{\nabla}\cdot\vec{\mathbf{B}} = 0$.

5.5.2 Li magnet design

For a realistic coil separation of ~ 2", the field-gradient increases by 42 mG/cm per amp turn. To achieve our target field gradient for the magnetic trap of 400 G/cm, this would require 10^4 amp turns. To operate at a reasonable current such as ~ 500 A, we must use ~ 20 turns. Since the turns have non-zero size, not all of them can be exactly at the Helmholtz condition[37]. Given such experimental realities, the best design would include coils that are closer together than the Helmholtz condition (sub-Helmholtz) and

[37] To satisfy the Helmholtz condition for all twenty turns, the radii of the coils would get very large, and would require more current or more turns.

coils that are farther apart than the Helmholtz condition (super-Helmholtz), and thereby minimize the curvature of the magnetic field at the center of the coils.

Our design for the Li magnets consists of 32 turns of square-cross-section wire[38] arranged into a block that is 8 turns wide and 4 turns high. There are 8 layers, as defined as turns that have the same radius (there are 4 turns per layer), which are enumerated from 1 through 8, starting with the innermost layer. Each set of two layers are wound from one continous wire, and are thus in series. The magnet consists of 4 of these separate sections of 8 turns each. The separation of the two magnets, as defined as the shortest distance between them, was designed to be 1.96", and ID of the magnet was designed to be 3.1". The peak (i.e. at 500 A) magnetic field at the center of the Helmholtz configuration of this design is 1790 G and the peak magnetic-field gradient at the field zero of the anti-Helmholtz configuration is 427 G/cm.

With these dimensions, the curvature of the Helmholtz field is positive for the first two layers, and negative for the second two layers. However, an increase in the separation of the two coils of only 0.5" - 0.25" further away from the windows for each magnet - would make the curvature have equal sign for all of the coils. We have empirically determined, by observing the effects of the supposedly uniform magnetic field on the BEC, that the curvature of each set of coils have the same sign, and this is likely due to the coils being installed too far apart. This has led to the need to develop further sets of compensation coils to attempt to cancel residual field-gradients.

5.5.3 Li magnet construction

The magnets were wound using the same cable, epoxy and winding rig that were used for the Zeeman slower magnets (see Section 5.4.2). A similar arrangement of two plates

[38] We used the same hollow Cu cable that we used for the slower, which was 0.1875" a side. As with our slower designs, we estimated 0.2" per wire, including the insulation and epoxy.

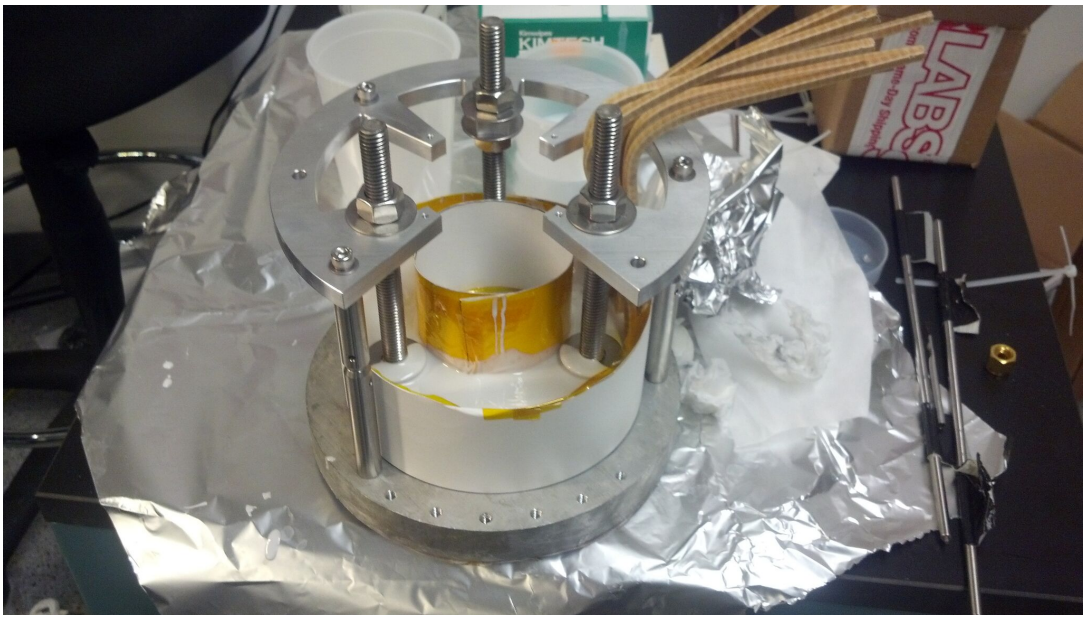

Figure 5.12: A photograph taken midway through the potting process on a test magnet. Note the still-visible washers used to increase the structural integrity of the connection.

with set screws between them was used to maintain lateral tension during curing. A major difference is that the magnets, unlike the Zeeman slower magnets, are not wound around a tube[39]. Therefore we wound the magnets around a custom-machined Al mandrel that was designed to have an OD equal to the desired ID of the magnet. The mandrel was coated in Kapton film to prevent the magnet from becoming epoxied to it. Despite this, it was difficult to remove the completed magnet from the mandrel, and eventually we developed a technique of synchronously beating the two sides of the magnet with rubber mallets until they came off. This procedure did not seem to do any damage to the magnets.

Since the magnets are not wound on a tube, and are designed to be inside re-entrant "bucket" windows, it is challenging to mount them. We accomplish this by "potting" three 1/2"-13 threaded 316 SS rods in approximately 1.5" of epoxy which covers the

[39]This is to preserve as much optical access through the magnets as possible.

entire annular shape of the external surface of each magnet. Each of these threaded rods is affixed to a custom water-jet-cut Al plate that screws into the re-entrant window flanges. In addition to the three 1/2" through-holes in these plates, there are 4 4-40" threaded holes that can be used to mount standard 2" cage optics. All unnecessary material was cut away to leave as much access for optics as possible. The "potting" was done by screwing in the rods to the desired height into the plate, temporarily mounting the plate horizontally using 1/2" optics posts, placing the magnet underneath the rods, and pouring epoxy onto the top surface of the magnet. Construction-paper molds were used to prevent the epoxy from spilling over the top of the magnet. Nuts and washers were added to the bottom of the threaded rods to give the rods a flared profile underneath the epoxy, which improves the structural integrity of the connection. Figure 5.12 shows a photograph of the potting process. Installation of the bottom magnet into the bottom re-entrant window is only possible if the depth of the bucket is less than the height of the window flange above the optical table. This was considered in the design of the re-entrant window.

5.5.4 Li magnet electronics

The magnets are designed to operate between 0 and 500 A. To run 500 A through both magnets, a total voltage difference of 17 V must be applied across them, not including voltage drops in the cables and connections to the power supply or any of the switching electronics[40]. The voltage required by each pair of layers in one of the magnets is listed in Table 5.3. In our lab we have access to 208 V 3-phase power, and high-current power supplies for this AC Voltage are typically limited to $\sim$ 10 kW. We therefore use two separate high current power supplies to run the magnets. The innermost 4 layers of each

[40] We measured the voltage drop across the 3/0 gauge stranded welding cable that we use to be 0.8V/10 ft. The voltage drop across each connection between the 3/0 cable and the magnet wire is 0.1V.

Magnet Layers	Length (m)	Voltage (V)
1 & 2	2.44	1.62
3 & 4	2.95	1.96
5 & 6	3.45	2.30
7 & 8	3.96	2.64

Table 5.3: Lengths of and voltage drops at 500 A across the four sections of the Li magnets.

magnet are connected to the same power supply, a TDK-Lambda ESS 20-500, and the outermost 4 layers of each magnet are connected to the same power supply, a TDK-Lambda Genesys 20-500, which are both rated to 20 V at 500 A. The currents in these two isolated electrical circuits had to be calibrated to be equal to avoid the magnetic-field zero moving during magnetic-field-gradient ramping.

The connections between the power supplies and the magnets were made using 3/0 gauge stranded welding cable. This cable is only rated to 350 A, but since we only run a few 10s of A during the machine steady-state (MOT), this is not an issue. Connections to the magnets were originally made with custom-made Al screw lugs that were similar in design to the lugs used to connect the 10 AWG battery cable to the slower magnets (see Section 5.4.3). The difference in the thermal expansion coefficient of the Cu wire, the Al lug and the steel scew which was used to hold them together tightly would eventually lead to loosening of the lug connection. This in turn would lead to an increased voltage drop across the connection, leading to heating and oxidation of the Cu wire. This runaway process would eventually consume much of the cable, and we have seen several feet of insulated cable be oxidized over time. We eventually switched techniques to use commercially available compression lugs that are designed for 3/0 gauge cable. These lugs are made of Cu and the crimp connection[41] is much less susceptible to loosening over time. We screw these compression lugs into custom-machined Al lugs that attach

[41]The crimp connection is made with a very large crimp tool which is designed for such low gauge connections.

to Cu tubes which are soldered to the magnet wire (see Section 5.4.3 for a discussion of this technique).

Switching of the magnets can be accomplished in a couple of ways. Slow control (10s of ms) can be achieved by simply adjusting the analog input voltage to either power supply. Fast turn-on of the magnets can be accomplished using a high voltage capacitor bank, which discharges a pulse of current into the magnets while the power supplies respond more slowly to the raised analog voltage[42]. Fast turn-off ($\sim 250\,\mu$s) of the magnets can be accomplished using a Powerex CM600HA-24A[43] insulated gate bipolar transistors (IGBTs). Vishay Spectrol VS-SD1100C12C[44] high-power diodes are used in a ring-down circuit, and Littelfuse V661BA60[45] varistors are used liberally across the magnets, the power supply terminals and the IGBTs. Clamping of the magnets is typically only required when the magnets are in the anti-Helmholtz configuration; it is done between the compressed MOT and gray molasses, and is done to prior to imaging the MOT or magnetic trap. We avoid clamping the magnetic trap at peak field gradient, as this can[46] break the IGBT.

Switching between the anti-Helmholtz and Helmholtz configurations is done using relays. We use two sets of four Kilovac LEV200A4NAA[47] contactors in an H-bridge configuration to switch the polarity of the bottom magnet after the magnetic trap in preparation for the application of the Feshbach field. Since, as installed, each of the 4 sets of 2 layers has the same sign of magnetic-field curvature, we run current in the

[42]The 500 V capacitor bank is charged with a 500 V power supply, with a time constant of $\sim$ 2.5s. Two IGBTs are used to connect the capacitors to the high voltage power supply and the magnets respectively. Discharging the capacitor bank into the inner section of the magnets ramps the magnetic-field gradient to 80 G/cm in 100 μs, which is sufficient to capture the atomic cloud after gray molasses in a magnetic trap.

[43]Rated to 600 A, 1200V.

[44]Rated to 1400 A, 1.2 kV.

[45]Rated to 70 kA, 1050V

[46]And has.

[47]Rated to 500 A, 12 V.

innermost 2 layers in the opposite direction to those in the outer 6 layers during the application of the Feshbach field. This allows us to reduce the field curvature while still being able to reach the required magnetic field strength[48].

5.5.5 Li magnet thermal management

The high currents run through the magnets lead to substantial resistive heating of the magnets themselves, as well as the cables and switching electronics. The magnets were wound with the same square-cross-section hollow Cu wire that was used for the Li Zeeman slower, and therefore have the same resistive and hydraulic properties as the slower (see Sections 5.4.2 and 5.4.4). The calculated temperature rise for the cooling water flowing through each magnet section is listed in Table 5.4. Note the rise in temperature of the cooling water as the coil radius increases[49]. Since the current running in the magnets varies significantly during the experimental sequence, so do the temperatures of the magnets. Unbalanced heating of the magnets, due to the energizing of only half of the magnet coils during the application of the Feshbach field, was observed to misalign the quadrupole trap plug beam (which has a beam waist of 10 μm). This was overcome by ensuring that the entire magnet was energized whenever significant currents are used. The IGBTs are water-cooled by means of Lytron cold plates.

5.6 Li laser systems

As discussed in Chapter 3, the Li experiment requires three wavelengths of light: resonant light at 671 nm, for laser cooling, trapping, spin polarization and imaging, red-detuned light, for optical trapping and the production of optical lattices, and blue-

[48] This does not completely solve the issue, and we use compensation coils to further reduce the field curvature.

[49] $\Delta T \propto \sqrt{R}$.

Magnet Layers	Length (m)	Power (kW)	Flow Rate (cm^3/s)	ΔT (°C)
1 & 2	2.44	0.81	73.6	2.6
3 & 4	2.95	0.98	67.0	3.5
5 & 6	3.45	1.15	61.8	4.4
7 & 8	3.96	1.32	57.7	5.5

Table 5.4: Length, power consumption, flow rate and temperature rise (ΔT) of cooling water of each section of one magnet coil, assuming a current of 500 A and cooling water pressure of 100 psi. Temperature rise calculation assumes that all magnet sections are connected in hydraulic parallel.

detuned light, for plugging the magnetic quadrupole trap. The resonant light consists of a master laser, the frequency of which is referenced to the atomic transition, and several stages of frequency shifting and amplification. The master laser is an external cavity diode laser (ECDL). Our trapping light is produced by an Nd:YAG fiber laser and amplifier, and is at 1064 nm. Our plugging light is produced by a diode-pumped solid-state (DPSS) laser, which produces green light by frequency doubling light in the YAG band. Therefore our plug wavelength is 532 nm.

5.6.1 671 nm laser system

The 671 nm laser system occupies the entirety of the laser table, as well as portions of the machine table. A diagram of the layout of this system, and a chart of all of the produced frequencies may be found in Zachary Geiger's dissertation [29]. The 671 nm master laser is a Toptica TA Pro, which consists of an ECDL and a tapered amplifier (TA). While this laser system was originally specified to 500 mW, trouble with the diodes and TA chips at this wavelength led Toptica to downgrade the specification to 300 mW. In addition to this TA, we use three other TAs and two injection-locked slave laser diodes to produce the required power for the entire experimental sequence. With the exception of the Zeeman slower light, and the gray molasses cooling and D1 optical pumping light, all of the resonant light is produced on a 4' by 8' optical table, and then conveyed via

optical fibers to the experiment. Switching of the light on fast ($\sim 1\,\mu$s) time scales is achieved by gating the radio frequency (RF) signal used to drive acousto-optic modulators (AOMs)[50], which effectively deflects the laser beam. Such switching does not completely block the laser beams, so home-built mechanical shutters which actuate on $\sim 10\,\mu$s time scales are used for complete shuttering.

We use separate tapered amplifiers[51] to produce the cycler and re-cycler light. The frequency shifts are accomplished using acousto-optic modulators AOMs. These TAs produce the cycler and re-cycler light used for transverse cooling, the MOT and imaging, which are all fiber-coupled. A separate pathway of master light produces the light required for the Zeeman slower, and for gray molasses cooling and D1 optical pumping. Some of this light is used to injection-lock a slave laser diode[52] that produces close to 100 mW of laser power, which is used for the Zeeman slower. This light is passed through a home-built electro-optic modulator, which produces sidebands at 813.5 MHz, one of which addresses the re-cycling transition. In order to perform gray molasses cooling and D1 optical pumping, we produce light near the D1 transitions, which are 10.052 GHz red-shifted from the D2 transitions. Most of this large frequency shift is achieved by using a New Focus EOM, which operates at 9.2 GHz. The red-sideband is used to injection-lock a slave laser diode, which serves the purpose of amplifying the light, and spectrally purifying the light by eliminating the carrier and blue-sideband frequencies[53]. The output of

[50] Almost all of our AOMs were purchased from Intra-action.

[51] One is a Toptica BoosTA, and the other is a home-built TA, using an Eagleyard EYP-TPA 0670-00500-2003-CMT02-0000 TA chip. Each produce approximately 300 mW of light, with approximately 50 mW of input light.

[52] We use HL6535GM diodes that are centered at 660 nm, and are specified to produce 120 mW of light. The diode is mounted in an Arroyo 224 laser-diode mount. We use the integrated thermo-electric cooler (TEC) to heat the diode to ~ 70°C, which pulls the center wavelength to the desired wavelength. A few 100 μW are used for injection-locking the slave diode. The frequency output is monitored on a Thorlabs Fabry-Perot interferometer with a 1.5 GHz free spectral range and finesse of 200.

[53] This slave diode set up is very similar to the Zeeman slower slave set up. The slave can be injection-locked with any of the three frequency components of the post-EOM light, and the locking-currents for these three frequencies are separated by 2-3 mA.

the slave is fiber-coupled and used to seed another home-built TA, which produces the 300 mW of light used for gray molasses and D1 optical pumping. Another home-built EOM puts sidebands at 803.5 MHz on this light, to produce light that addresses both ground-state hyperfine manifolds.

The master laser is frequency-locked to an aborption signal produced by performing saturated absorption spectroscopy on a hot gas of Li atoms. This gas is produced by heating a reservoir of Li to 350 °C in a small vacuum chamber, which was originally pumped down to 10 mtorr and then sealed[54]. The gas is addressed by roughly counter-propagating beams, one of which has a high power, and is known as the pump beam, and the other of which has a lower power, and is known as the probe beam. As the frequency of the master laser is scanned through the resonance, the transmitted power of each beam traces out a Doppler absorption profile, which is centered at the resonance frequency, but is very broad[55], due to the broad distribution of velocities in the projection of the Maxwell-Boltzmann distribution onto one dimension. For an atom with a single ground state, the counter-propagating beams are only co-resonant for the class of atoms that have zero velocity component along the dimension of the laser beams[56]. Since the pump beam excites many of these atoms to the excited state, in which they no longer undergo stimulated absorption from either beam, the probe beam absorption signal has a linewidth-limited Doppler-free saturated absorption peak at the location of the resonance.

For atoms with two hyperfine manifolds in the ground state, there are two overlaid Doppler profiles, and there are two Doppler-free saturated absorption peaks[57]. In ad-

[54]Ar was used as an inert buffer gas.

[55]In particular, much broader than the linewidth of the transition. The projection of the Maxwell-Boltzmann distribution onto one dimension is a Gaussian with $\sigma = \sqrt{k_B T/m}$. For ^{7}Li at 350 °C, $\sigma = 860$ MHz, and the full-width at half-maximum of the distribution is 2 GHz.

[56]If the pump and the probe beam are detuned with respect to one another, the two beams are co-resonant for a velocity class determined by that detuning

[57]This assumes that the splitting between transitions from the two ground-state hyperfine manifolds is less than the Doppler width, as is the case for ^{7}Li at 350 °C.

dition to these peaks, there is a "cross-over" dip halfway between these peaks. At this frequency, the pump and probe are resonant with different transitions for the same atom; each with a transition from one of the ground-state hyperfine states. The pump decreases the population of ground-state atoms in the hyperfine manifold that it is resonant with, thereby increasing the population of ground-state atoms in the other ground-state hyperfine manifold, due to spontaneous emission from the excited state. Thus the population of atoms that are resonant with the probe is increased at this frequency, leading to a linewidth-limited dip in the aborption profile.

Due to the hyperfine structure of the ground-state, we observe two Doppler-free absorption peaks, corresponding to D2 transitions from the $F = 2$ and $F = 1$ manifolds, as well as a cross-over dip halfway between these two peaks. Since the cross-over peak is larger than the absorption peaks, and since we need to produce light to address both ground-state hyperfine manifolds, it is convenient to lock the frequency of the laser to the cross-over dip, which we accomplish with a Toptica Digilock 110, which implements a lock-in amplifier and a feedback circuit. The frequency is locked through an electronic feedback circuit. The lock-in amplifier effectively takes the derivative of the absorption signal, converting the cross-over dip to a slope, which can be used to generate a feedback signal using a PID circuit[58]. The frequency modulation (FM) that is used for the functioning of the lock-in amplifier is generated by the Digilock 110, and is added to the probe light with an acousto-optic modulator (AOM)[59].

[58] A PID feedback circuit takes two inputs, and gives one output that is a sum of terms that are proportional to the difference (P), integral of the difference (I), and deriviative of the difference (D), of these two signals.

[59] The FM is applied to the radio frequency (RF) signal that is used to drive the AOM.

5.6.2 1064 nm laser system

The 1064 nm laser light is produced by a single-mode Orbits Lightwave Nd:YAG fiber laser, which produces up to 100 mW of fiber-coupled laser light. This fiber is directly connected to a Nufern fiber amplifier, which is specified to produce up to 50 W of laser light with a single spatial-mode (TEM_{00}). Two 60 dB optical isolators are used to prevent retro-reflected light from entering the amplifier. AOMs are used to offset the frequencies of the two XODT trapping beams with respect to each other. Additionally, these AOMs are used to switch the beams, as well as to feedback on the power of the beam, as measured downstream with a beam-sampler and a photodiode. Home-built PID feedback circuits are used for this purpose. Waveplate rotators from Pacific Laser Equipment are used to channel power towards the lattice beams in the final 400 ms of optical evaporation. The lattice beams are similarly gated using AOMs.

5.6.3 532 nm laser system

The 532 nm laser light is produced by a single-spatial-mode, multi-longitudinal-mode Lighthouse Photonics Sprout G frequency-doubled DPSS, which produces 10 W of laser light. A Pacific Laser Equipment waveplate rotator is used to reduce the power in the beam from the maximum to a few 100 mW over the course of a few hundred ms.

Chapter 6

Strontium experimental design & construction

The Sr apparatus consists of an approximately 1.5 m long ultra-high vacuum (UHV) system which is mounted on a 5' by 10' optical table, known as the machine table. A computer-aided-design (CAD) depiction of the machine table is shown in Figure 6.1, and a photograph of the vacuum system taken after baking is shown in Figure 6.2. The UHV chamber is divided into two halves, which can be pressure-cycled independently: the oven, which produces a high-flux beam of hot atoms, and the main chamber, where the atoms are trapped and cooled. These two parts are connected via the Zeeman slower tube. The 461 nm and 403 nm resonant laser light is produced on a separate 4' by 10' optical table, known as the laser table, and delivered to the machine table via optical fibers. In addition to these tables, there are two electronics racks used to mount power supplies, switching electronics, and radio frequency sources for acousto-optic modulators (AOMs). Control over all of these elements is accomplished by using digital and analog outputs produced by National Instruments cards installed in a desktop computer. A software suite, known as Cicero, that was developed by the Ketterle group at MIT is used to

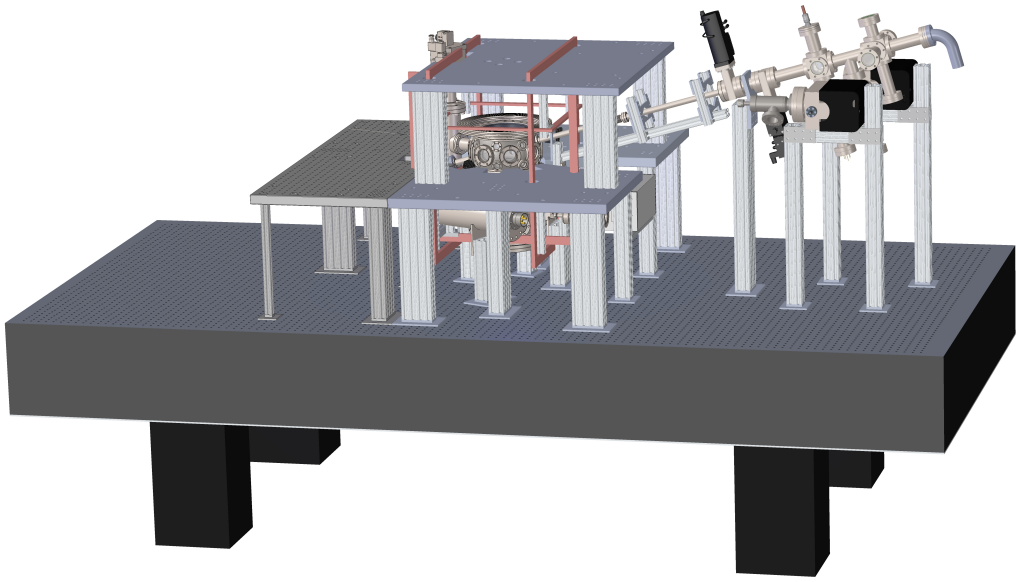

Figure 6.1: CAD depiction of Sr machine table. The oven manifold is on the right and the main chamber is on the left. The two vacuum chambers are connected via the Zeeman slower tube. The Zeeman slower coils are not included in this CAD depiction. The atomic beam is at a 16° angle above the horizontal.

produce the desired sequence of analog and digital outputs. Water cooling is required by many of our electromagnets, and this is accomplished by a closed-cycle chilled water supply, and water-distribution manifolds mounted above the machine table enclosure.

6.1 Apparatus overview

The machine table is the heart of the experiment. It is enclosed using a home-built enclosure, constructed using 80/20 stock and Al panels to which we attached wheels to allow us to slide the panels horizontally. The temperature and humidity inside this

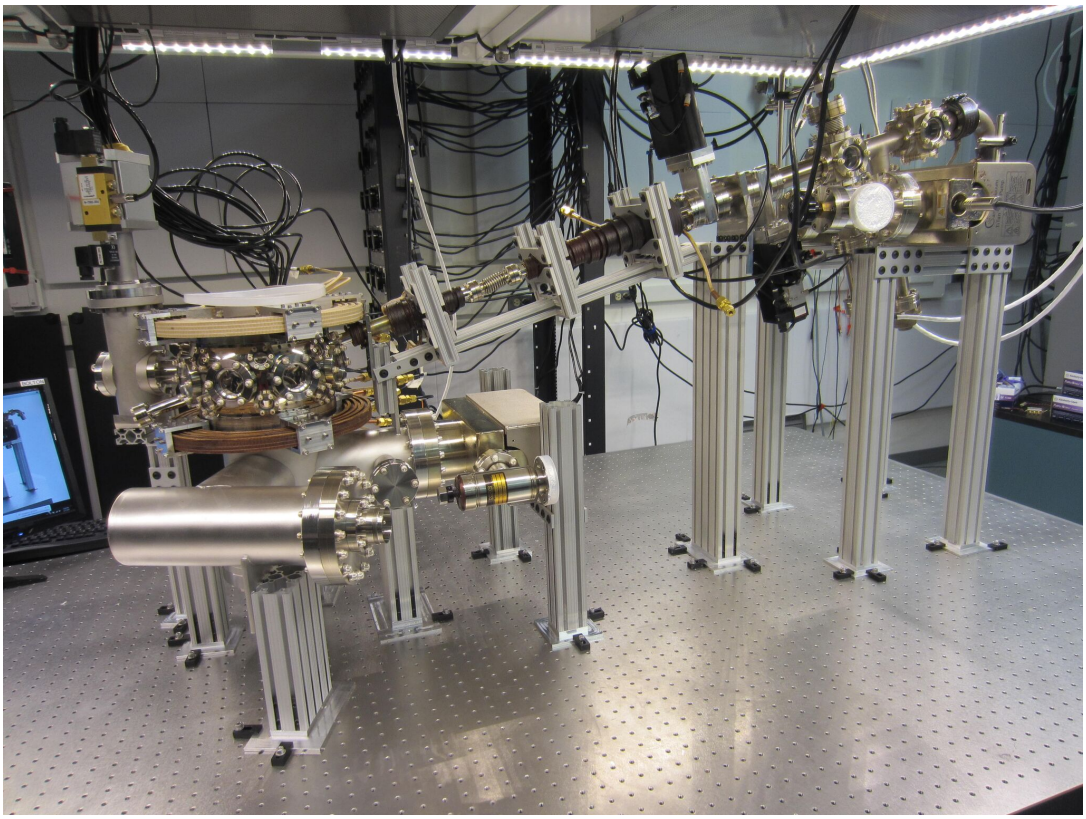

Figure 6.2: A photograph of the Sr vacuum system after baking both the oven manifold and the main chamber.

enclosure is controlled via an air handling system that was installed during the renovation of our lab space. The enclosure temperature is typically stable to less than 1 °F when the experiment is not running[1]. Due to concerns over the stability of the 689 nm laser system, it is housed on the machine table in its own plastic enclosure. The non-resonant 1064 nm high-power laser is housed on the machine table, in an Al light-tight enclosure for laser safety. The 915 nm laser system is also housed on the machine table, currently on a temporary breadboard. The top surface of the machine table is made from 316 stainless steel (SS)[2]. A "cloud" made of Unistrut stock and painted fiber-board panels descends from the ceiling above the machine table, and is used to mount laser drivers, water-

[1]The Sr experiment has experienced temperature stability issues due to the large thermal load of the 280 A that are run in steady-state to produce the MOT currents.

[2]316 SS is preferred over the more common 304 SS due to its favorable magnetization properties.

cooling-related hardware and other miscellaneous electronics. Three large ducts penetrate the machine table cloud and deliver temperature-and-humidity-controlled laminar-flow air to the space inside the machine table enclosure.

The 461 nm and 403 nm laser systems are entirely housed on the laser table, and are enclosed, apart from the 461 nm spectroscopy cell which is vented due to thermal management considerations[3]. This is accomplished with a 6" high enclosure made of 80/20 stock and plastic panels. We inherited the optical table used for the laser table from David Cannell's laboratory, and the top surface is made of 304 SS. The laser table does not have a cloud, so we recently constructed a shelf over part of the table with 80/20 stock and painted fiber-board. Both the machine and laser tables are floated using compressed air for vibrational isolation.

The vacuum chamber is mounted using 80/20 stock and tabs that were welded to the custom-built pumping manifold. Custom Al mounting clamps were used to connect other parts of the machine, such as the oven vacuum chamber, ion pumps, gate valves and Zeeman slower magnets, to the 80/20 stock. We installed custom additional breadboards on the machine table at a convenient height to access the horizontal windows of the main chamber, and above the main chamber to allow for access to the vertical window. The breadboards were custom-designed, and then machined by the UCSB Machine Shop out of MIC6 alloy Al from Alcoa[4]. The breadboards are 1" thick, and are mounted on 80/20 stock. Due to the proximity of the lower magnet, the Sr breadboards are less thick than those on the Li experiment, and the laser beam height was designed to be 1.5", not our lab-standard of 2". Tabs that are thinner and approach the main chamber windows over the magnet were included so that we can mount lenses very close to the windows.

[3]The 689 nm spectroscopy cell is also on the laser table, to avoid another source of heat on the machine table

[4]Al was chosen due to it being non-magnetic. MIC6 has favorable vibrational properties.

6.2 Sr main chamber

In the interest of expediency, we decided to use an off-the-shelf 316 SS Kimball spherical octagon as our main chamber. A CAD depiction of the spherical octagon and the associated pumping manifolds are shown in Figure 6.3. It has two 8" conflat (CF) flanges on the "cylinder" end-faces, and 8 uniformly distributed 2.75" CF flanges on the curved surface. The centers of these 8 flanges define a plane that is orthogonal the axis of cylindrical symmetry of the 8" flanges. The point of intersection of this plane, which we chose to be horizontal, and this (therefore vertical) axis is the trapping region. In addition to these flanges, there are 8 pairs of 1.33" CF flanges. The axis defined by the centers of a pair of these windows pierces the trapping region, and is at a 16˚angle to the horizontal plane. The horizontal 2.75" viewports are used for non-resonant trap and lattice beams. We attached an all-metal VAT gate valve to one of the 2.75" flanges to allow us add a "science" chamber to the apparatus in the future without losing vacuum in the main chamber. See Section 8.2 for details on the planned science chamber for single-lattice-site-resolution imaging.

We chose to pump the chamber out of one of the large 8" ports, through a custom-designed 316 SS pumping manifold made by A & N. This pumping manifold is connected to the lower 8" flange, and has connections to a 75 l/s Gamma ion pump, and an Agilent titanium sublimation pump (Ti-sub), while maintaining a clear aperture to an 8" CF window. The ion pump and Ti-sub therefore do not have line-of-sight access to the trapping region, but nonetheless have high conductances to the main chamber. We added a port for a UHV-24p ion gauge, as well as an extra port for a residual gas analyzer, that we decided against purchasing later in the construction sequence. We also included 2 pairs of 2.75" CF flanges arranged in a cross formation along a horizontal plane. We have not used these windows so far, but in principle it is possible to use them to interrogate

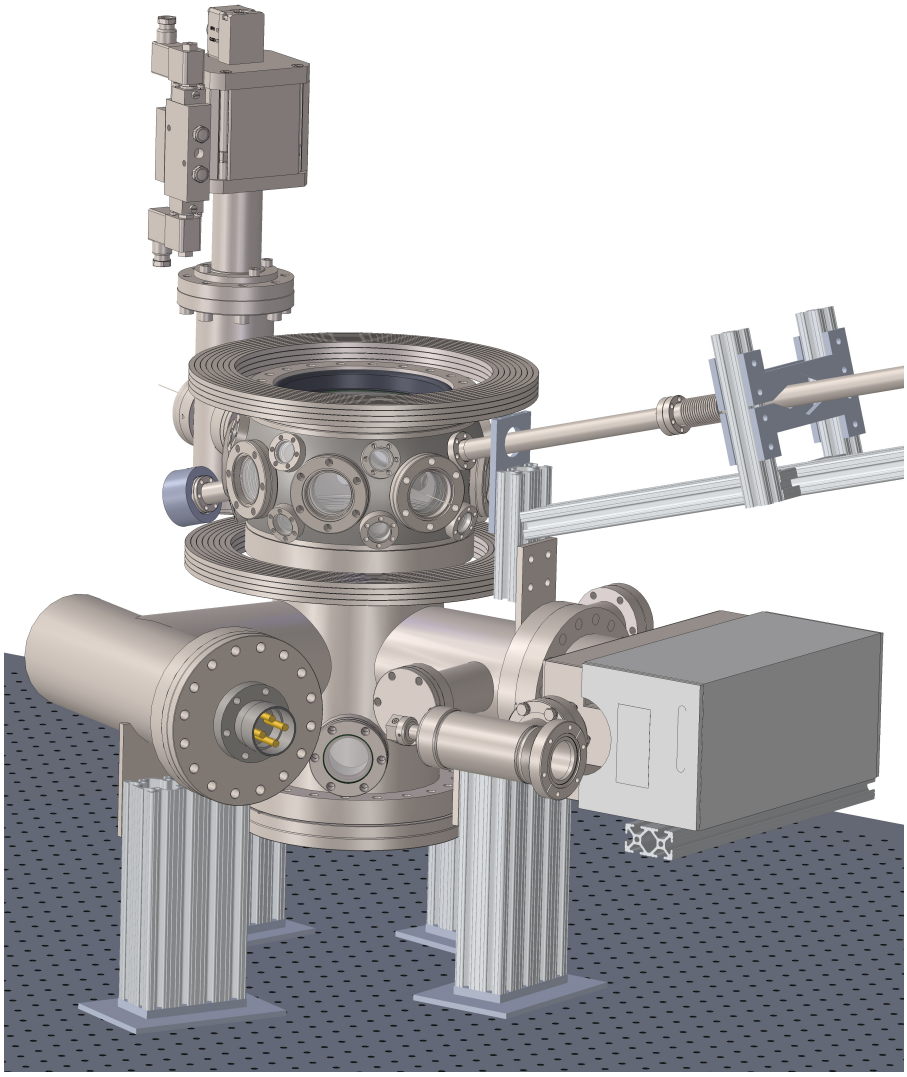

Figure 6.3: CAD depiction of Sr main chamber. The Ti-sub and the ion pump are visible and attached to the lower pumping manifold. One of the four windows included on the pumping manifold is visible. The Zeeman slower tube is connected to one of the upper 1.33" CF flanges, and the Zeeman slower window is attached (via a short nipple) to the diametrically opposite 1.33" CF flange. The VAT gate valve is behind the Kimball chamber as depicted.

the atoms after a long time-of-flight[5].

[5]At least one of these windows has a direct line-of-sight to the Ti-sub, and therefore must have a Ti coating at this stage.

6.3 Sr oven

Strontium is an alkaline-earth metal which oxidizes in air and reacts gently with water. It is a solid at room temperature, and has a melting temperature of 777 °C. In order to capture on the order of 10^7 ^{84}Sr atoms in the magnetic trap over a reasonable load time of approximately 10 s, it is necessary to have a flux of all Sr isotopes below the capture velocity (v_c) of the MOT that is at least 10^8 atoms/s[6]. As discussed in Section 5.3, the velocities in an atomic beam are distributed according to a modified Maxwell-Boltzmann distribution, which is more skewed towards higher velocities. The Maxwell-Boltzmann distribution and the velocity distribution for an atomic beam are plotted for a gas and beam of Sr atoms at 650 °C in Figure 6.4. Note the small percentages of the distributions that are below a v_c of 50 m/s.

As is the case for Li, it is necessary to heat Sr substantially to produce a vapor with number density high enough to load significant numbers of atoms into the magnetic trap. The number density implied by the vapor pressure is reduced by a factor of ~ 200 due to the natural abundance of ^{84}Sr. At the high temperatures required to produce a sufficiently-high number density of ^{84}Sr atoms, the fraction of atoms with low enough velocity to be captured by the MOT is negligibly low. Thus, in order to capture these atoms we must modify the velocity distribution of the atoms, and, as in the Li experiment, we chose to do this using a Zeeman slower, which requires an atomic beam which is collimated enough to have a sufficient flux of atoms through the MOT capture region.

6.3.1 Oven Nozzle

In order to produce a gas of Sr atoms at a reasonable pressure and therefore number density and flux, it is necessary to heat the solid significantly. The vapor pressure of

[6]In this estimate we have swept loss processes from the MOT, and from the MOT-to-magnetic-trap transfer under the rug, but it serves as a useful minimum flux.

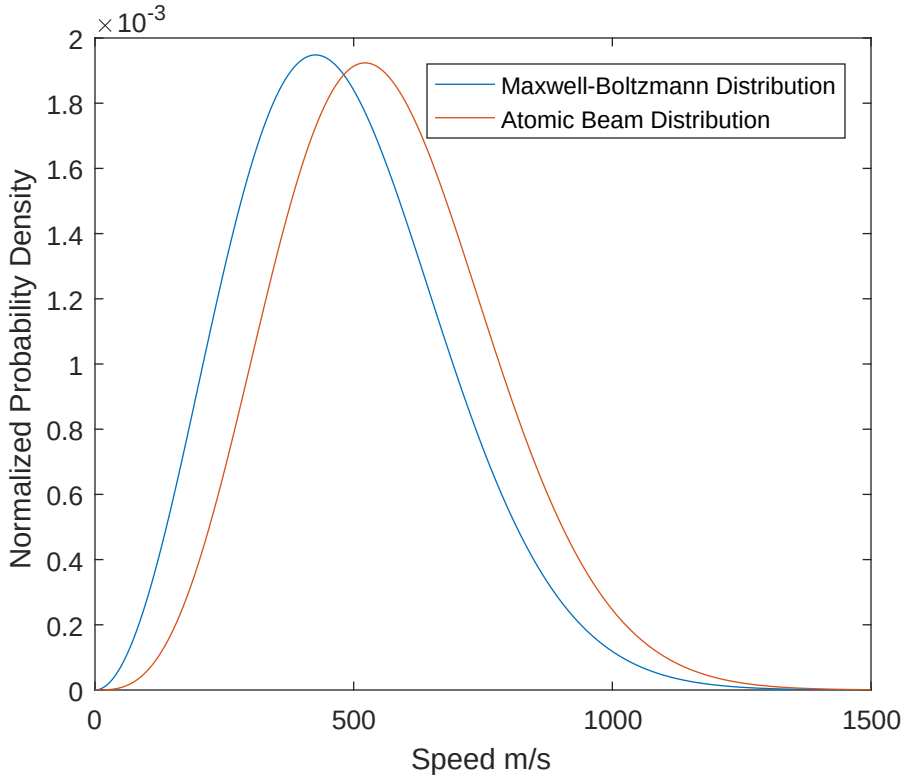

Figure 6.4: The Maxwell-Boltzmann distribution for a Sr gas at 650 °C, and the speed distribution for a Sr atomic beam at 650 °C. The percentages of atoms with speeds less than a MOT capture velocity of 50 m/s are 0.12% and 0.01% respectively. The percentages of atoms with speeds less than a Zeeman slower highest addressed velocity of 600 m/s are 73.4% and 58.9% respectively.

solid Sr in torr is [85][7]

$$\log_{10} P_s = 2.88 + 4.75 - 7720/T \tag{6.1}$$

and is plotted in Figure 6.5. Due to the considerations discussed in Section 5.3.1, a nozzle is required to collimate the beam. We used the same triangular, hexagonally-packed, multi-capillary array design as used in the Li experiment for the Sr nozzle. Operating at 650 °C, this nozzle should produce a flux of $\sim 9.3 \times 10^{12}$ ^{84}Sr atoms. Given an initial reservoir for 25 g, we predicted a lifetime of just over 3 years. We had to reload the

[7]We heard of some disagreement between the published vapor pressure curve for Sr and the experience of other Sr groups. We have not observed any clear discrepancy.

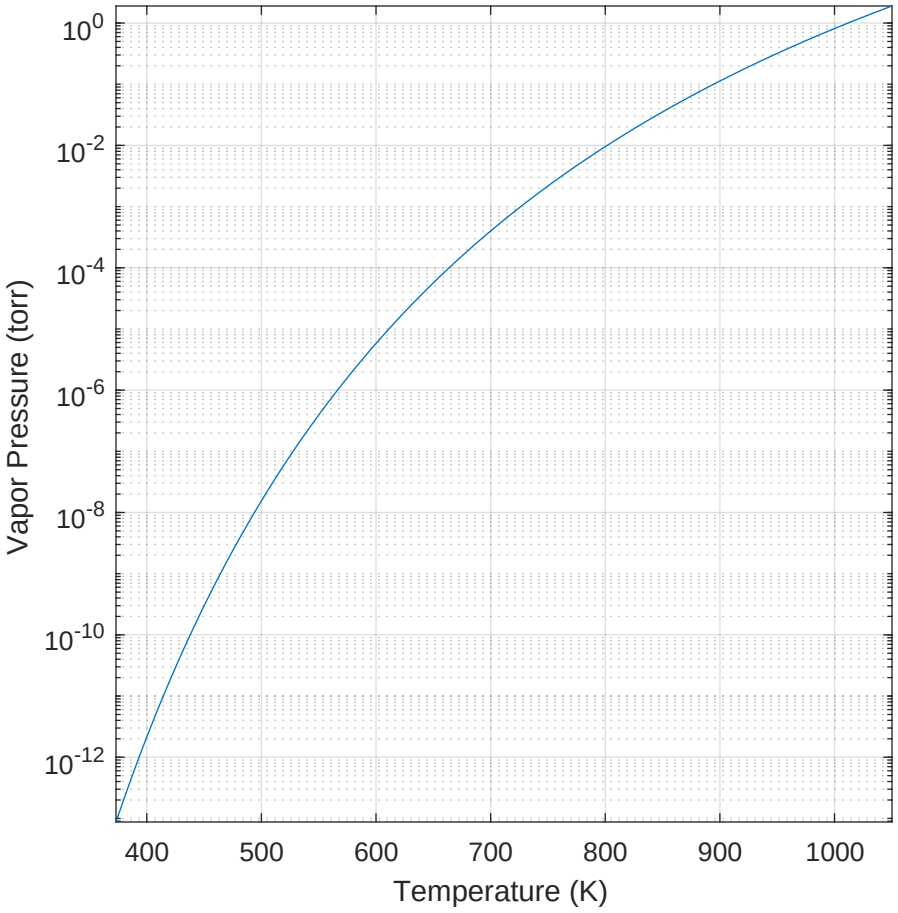

Figure 6.5: Vapor pressure of solid Sr, plotted as a function of temperature, from the boiling point of water to the melting point of Sr.

oven with Sr in the winter of 2016/7 (after approximately 1.75 years of operation at approximately $\sim$ 50% duty cycle), though when the oven was opened we found some amount of Sr still in the reservoir. Perhaps inadequate heating led to the drop in oven flux[8]. We reloaded the oven with 100 g of Sr, which should last $\sim$ 13 years.

[8]Post-re-bake we discovered that one of the oven thermocouples was being read incorrectly. This was discovered because the flux of atoms was still low, despite a new reservoir of Sr. We found that the thermocouple reader was set to the wrong type of thermocouple, implying that our oven temperature was actually more than 100 °C below the reading. Once we fixed this, the oven roared back to life.

6.3.2 Sr reservoir and heating

The Sr is contained in a custom one-flanged SS CF component that combines a cup with a 90° elbow. This was modified from the Li design described in Section 5.3.2 to remove the flange between the cup and the elbow[9]. As will be discussed in section 6.3.3, the entire beamline of the Sr experiment is at 16° to the horizontal, with the oven elevated above the main chamber. This necessitated a fairly deep cup to hold the Sr without it spilling over onto the nozzle[10]. As in the Li experiment, the micro-capillary array was assembled in a custom-machined double-sided blank that was sandwiched between the elbow and a short nipple. All of these components are made from 316 SS, as we use Ni gaskets as in the Li oven to avoid corrosion.

The cup and the flange connection between the elbow and the nozzle are directly heated using Tempco Mi-plus bandheaters[11]. The entire heated section is wrapped in Al foil and fiber-glass insulation. As in the Li oven, it is necessary to maintain the nozzle as the hottest part of the oven. To this end, we maintain a 50 °C temperature difference between the cup heater and the nozzle heater. We reduce the temperatures of each heater by 325 °C when the machine is not in use to extend the lifetime of the oven.

6.3.3 Sr oven manifold

The Sr oven manifold consists of stages for transverse cooling and shuttering the atomic beam, as well as for differential pumping. In many respects it is very similar to

[9]This was desirable as we heat the flanges beyond the highest temperature to which they are rated (450 °C), and having one less flange gave us one less thing to worry about.

[10]This is not as much of an issue as it would be with Li, since we do not heat the Sr above its melting point

[11]We have placed additional thermocouples on various parts of the elbow and cup, and have found that the temperature of the elbow is lower than the cup and the nozzle. We have wrapped heating tape around this section, but we have not had need to energize them as of yet. In the future if the beam flux decreases, it may be prudent to heat this section, as it is quite likely that a large quantity of Sr is deposited there.

the Li oven manifold discussed in Section 5.3.3. The main striking difference is that the oven atomic beamline is at 16° to the horizontal, with the oven elevated above the main chamber. This was necessitated by the desire to use one of the 1.33" CF flanges on the Kimball spherical octagon that serves as the main chamber, and thereby preserve another pair of 2.75" CF flanges for windows. However, this difference only mainly affected the mounting of the oven manifold. A more substantial difference is that we decided to not have a coldplate section in order to minimize the length of the oven manifold, and to perform transverse cooling as early as possible along the beamline - i.e. in the first 2.75" CF cube that the atomic beam enters. This led to the unfortunate consequence of much of the transverse cooling windows being sputtered with Sr. Deposition occured in areas that had line-of-sight to the short nipple. This deposition rendered the transverse cooling cube useless, and we were forced to perform 1d transverse cooling in the atomic beam shutter cube further down the beamline. The original Sr oven manifold design is shown in Figure 6.6.

During the Sr replenishing that occured in the winter of 2016/17 we completely deconstructed and reconstructed the oven manifold up to the gate valves. During this reconstruction, we replaced the short nipple that connected the nozzle to the first 2.75" CF cube with a standard length nipple. This would allow the end of the nipple attached to the cube to be at a lower temperature, and would increase the chance of atoms sticking to the walls of the nipple, instead of bouncing on to the windows. We also used four nipples to recess the four windows on the cube to further reduce the chance of Sr coating the windows[12]. We discussed welding an annular plate into this nipple to act as a coldplate, but we considered the risk of Sr depositing and occluding the orifice to be too high. A CAD depiction of the second iteration of the Sr oven manifold is shown in Figure

[12]The nipple used for the top window had to be a short nipple as a standard-length nipple would not have fit underneath the machine table cloud. Standard-length nipples were used for the remaining three windows.

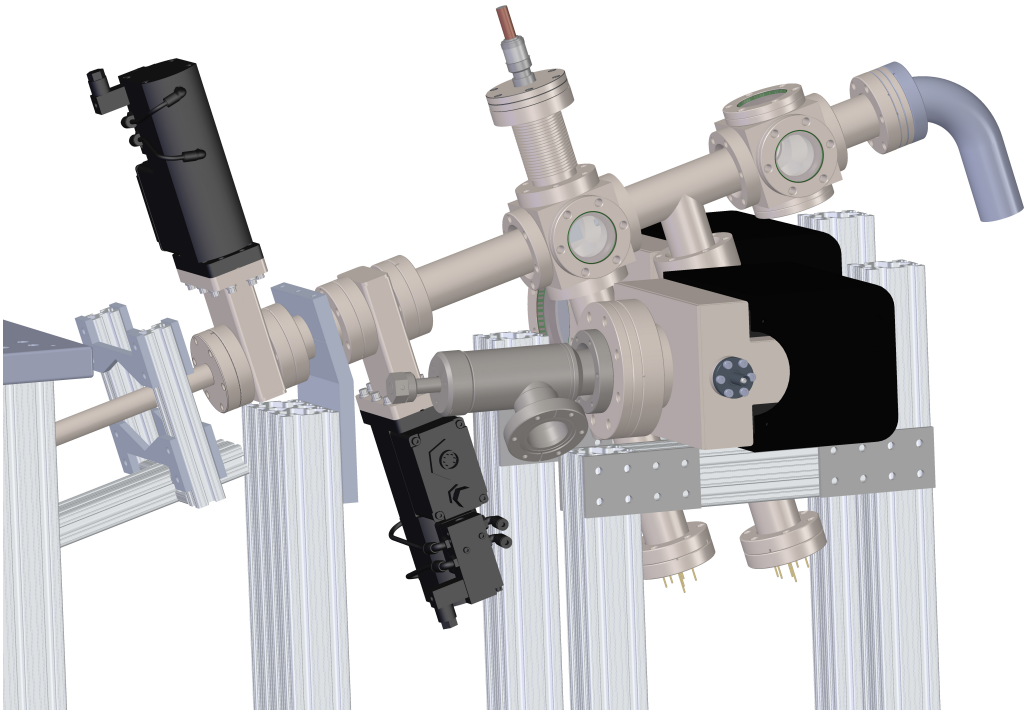

Figure 6.6: CAD depiction of the first iteration of the Sr oven manifold. The Sr reservoir and nozzle flange are on the right. The atomic beam travels downwards and to the left through the transverse cooling cube, first differential pumping tube, stopper cube, second differential pumping tube and gate valves, before entering the Zeeman slower. The four transverse cooling windows became occluded with deposited Sr, making transverse cooling in this cube impossible.

6.7. While these design changes have been successful in terms of preventing Sr from depositing on the transverse cooling windows, we are still unable to use these windows for transverse cooling, as there is an optically dense background gas of Sr atoms in the transverse cooling cube that completely absorbs the limited transverse cooling power that we have. This suggests that high-angle atoms are still bouncing off of the nipple walls and forming a diffuse gas in the transverse cooling cube. We still perform 1d transverse cooling in the atomic beam shutter cube.

As in the Li oven manifold we have two stages of differential pumping. The dimensions

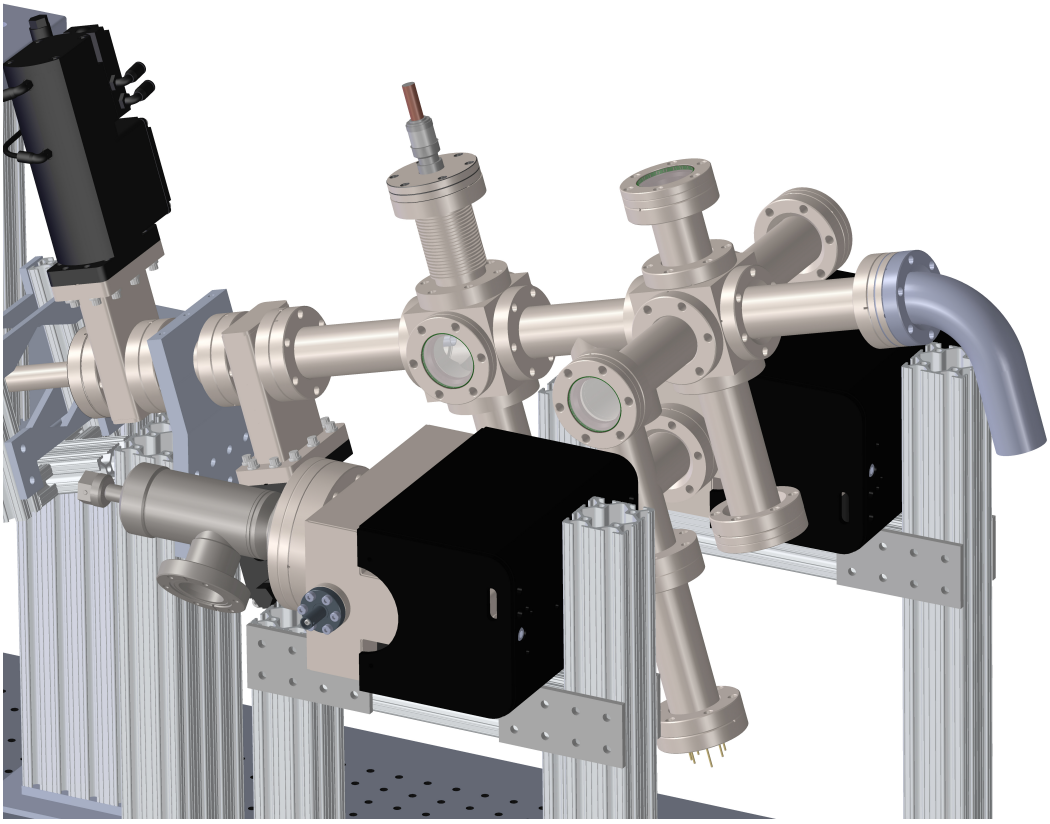

Figure 6.7: CAD depiction of the second iteration of the Sr oven manifold. The four transverse cooling windows were recessed on nipples, and the short nipple that connected the nozzle flange to the transverse cooling cube was replaced with a standard length nipple. These improvements ensured that the transverse cooling windows did not become occluded with deposited Sr. Nonetheless, we are unable to perform transverse cooling in this cube as the background vapor of Sr has too high of an optical density.

of the DPTs are the same as those in the Li experiment. We have two 35 l/s Gamma ion pumps on either side of the first DPT, connected to the cubes via CF Ts. A Kalrez elastomer angle valve is attached to an auxiliary port on the transverse cooling ion pump. The differential pumping ratio supported between the oven and the main chamber is similar to that calculated in Section 5.3.4. Varian UHV-24p ion gauges measure the pressure in these two sections. The ion pump and ion gauge in the transverse cooling section read pressures of the order of 10^{-8} torr, while those in the atomic beam shutter

section read pressures of the order of 10^{-9} torr. The main chamber ion gauge reads a pressure in the 10^{-11} torr regime. Two Kalrez elastomer gate valves separate the main chamber from the oven. During the oven replacement we discovered that one of these gate valves leaked, and therefore our choice to have two gate valves for redundancy was justified.

6.4 Sr Zeeman slower

As discussed in Section 6.3, it is not possible to load a sizeable magnetic trap of ^{84}Sr from the background pressure of Sr due to its low vapor pressure and the low natural abundance of this isotope. In order to produce a suficient flux of Sr atoms through the MOT-capture region, the Sr solid must be heated to several hundreds of degrees Celsius, leading to a negligible proportion of the atoms having velocity lower than the capture velocity of the MOT. Therefore some modification to the speed distribution of the atoms must be made - i.e. some fraction of the atoms must be slowed. While I do not know of any Sr degenerate gas experiments that do not use a Zeeman slower of some kind, it should, in principle, be possible to load a sizeable magnetic trap with a 2d MOT alone. Many Sr experiments today use a commercial oven, Zeeman slower and 2d MOT from AO Sense, and we considered this option. However, due to the price, the fact that at that point in time the AO Sense source was not yet well-evaluated by other groups working on Sr, and our experience in building ovens and Zeeman slowers, we decided to pursue a home-built solution. We again toyed with the idea of using a permanent-magnet Zeeman slower, but again chose to use electromagnets (see Section 5.4 for a discussion of this choice in the context of the Li experiment).

6.4.1 MOT-field-compensated Zeeman slower

The choices discussed above, and the eventual Zeeman slower design, were also largely influenced by our MOT magnet design. Since we decided to use an off-the-shelf Kimball spherical octagon as the main chamber, and decided to eschew re-entrant windows, our MOT magnet design ID had to be 9.1". These very large anti-Helmholtz coils have a large fringe field. In particular the axis of the Zeeman slower tube (which is angled upwards from the main chamber at 16° to the horizontal) passes within $\sim$ 1" of the top magnet, and experiences a peak axial field of over 600 G at the MOT coil design current of 352 A. Since it is desirable to have the exit of the Zeeman slower be as close to the MOT as possible, we had to include the effects of this large fringe field in our Zeeman slower design.

Figure 6.8 shows the fringe field, desired total field for Zeeman slowing and the difference between these two field profiles that must be supplied by the Zeeman slower magnets. The peak absolute value of magnetic field in the fringe field occurs at the point of closest approach of the slower axis to the MOT coil. Ideally the exit of the Zeeman slower would coincide with this location, as the change in sign of the field gradient at this point would bring the atoms off of resonance. However, due to the geometric constraint, not many coils of wire can fit at this location, so we would not be able to suitably modify the magnetic-field profile for Zeeman slowing. This forced the exit of the Zeeman slower away from this point, which in turn required a few coils to be wound at this point of closest approach to change the sign of the field gradient and bring the atoms off of resonance. This requires very high currents, and we constrained this to be equal to the MOT coil current (352 A) to avoid requiring a separate power supply. This small cancellation coil was thus christened the "mini-MOT" coil. Figure 6.9 shows a photograph of the mini-MOT coil in relation to the magnet coils. The magnetic field profile for the region

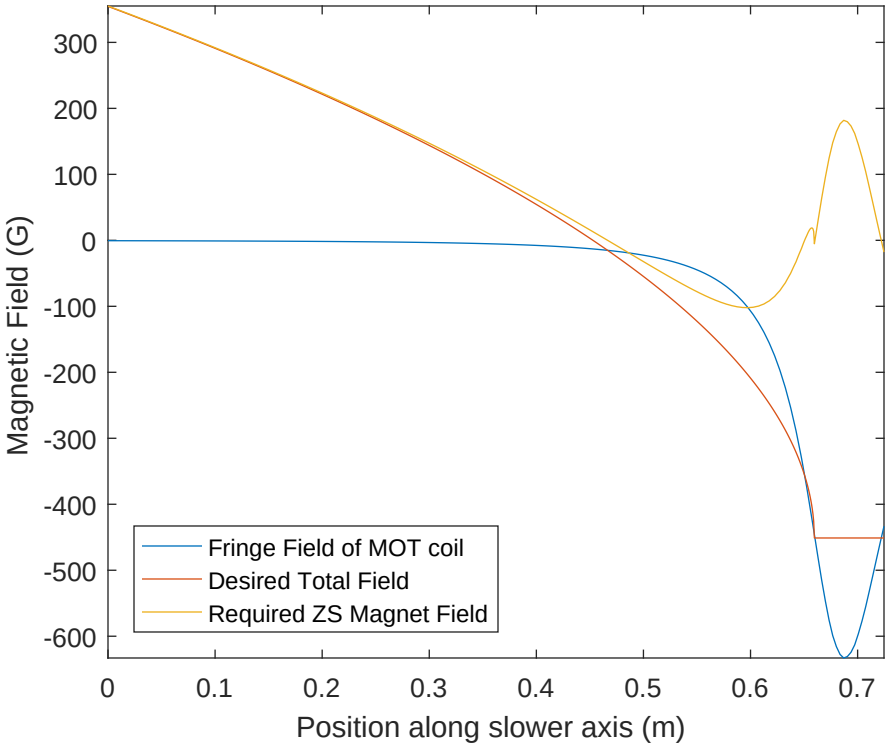

Figure 6.8: The fringe field of the MOT coil along the slower axis, the desired field profile for Zeeman slowing, and the required field from the Zeeman slower magnets. The MOT field is for a current of 352 A. Given the polarity of the MOT coils, the field strength plotted is defined to point away from the MOT. The desired field profile is for a maximum entrance velocity of 570 m/s, an exit velocity of 50 m/s, and a detuning of 750 MHz.

where the slowing occurs has a zero-field crossing point, and therefore it naturally broke up into two sections, the first, positive-field[13] section, A, and the second, negative-field section, B. In between these two sections we introduced a few-inch gap to accomodate a hydroformed bellows to allow for flexibility between the main chamber and the oven manifold. During this zero-field section the slowed atoms should scatter few photons.

[13]The actual direction of the magnetic field is completely arbitrary, as long as the MOT coils and slower coils are wired up consistently with each other. We chose to run current in our MOT coils such that the magnetic field points towards the MOT in the vertical dimension. This is consistent with the slower field in section A pointing towards the MOT.

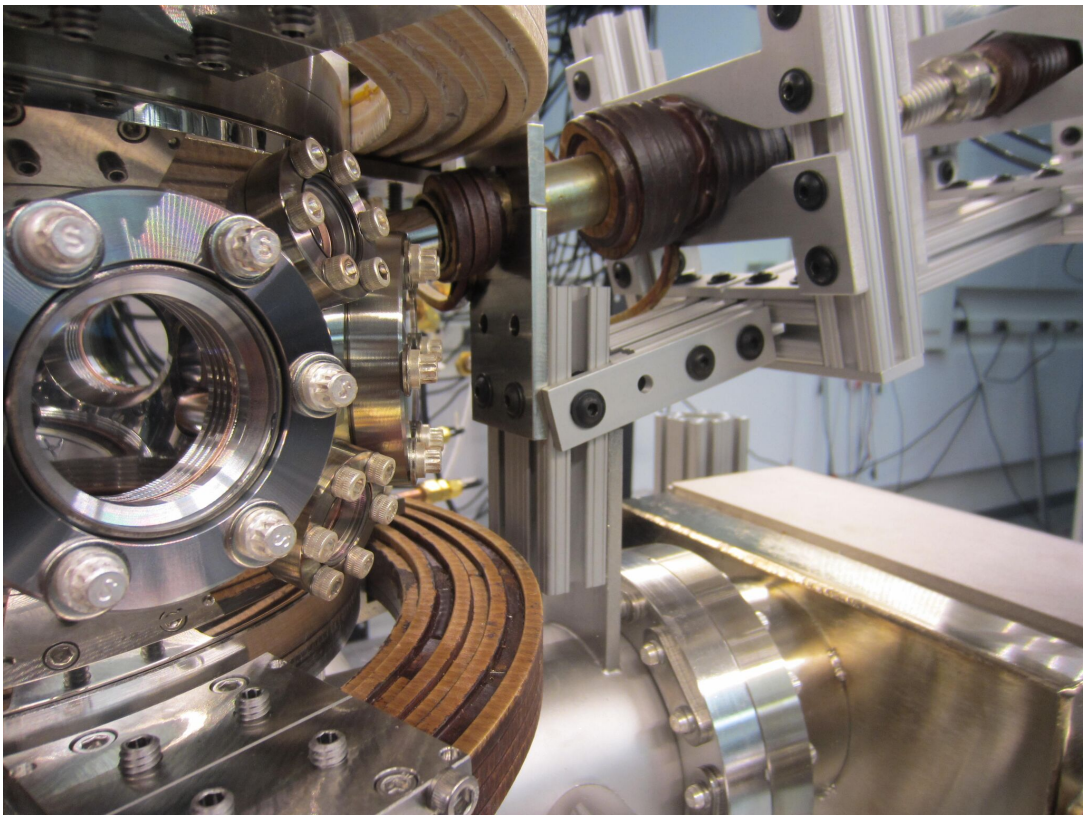

Figure 6.9: A photograph showing the position of the mini-MOT coil in relation to the top magnet coil. Slower sections A and B are also visible, as well as the bellows connecting the two parts of the slower tube.

6.4.2 Zeeman slower construction

The construction of the Sr Zeeman slower was largely identical to the Li Zeeman slower, which is chronicled in Section 5.4.2. One difference is that Zeeman slower section B and the mini-MOT coil were wound on the same brass tube to ease mounting of the latter. This meant that the distance between section B and the mini-MOT was fixed when we wound the sections, and this led to the largest difference between our achieved field profile and our target field profile. However simulations run on *in situ* measurements of the combined field of the MOT coils and the slower magnets suggested that this was workable.

Slower Section	Design Current(A)	Actual Current (A)
A	35	39.1
B	25	25.4
mini-MOT	352	127

Table 6.1: Currents used in the three sections of the Sr Zeeman slower.

6.4.3 Zeeman slower electronics

Zeman slower sections A, B and the mini-MOT are powered with three separate DC power supplies. Sections A and B were designed to run currents in the 10s A, while the mini-MOT was designed to run at the same current as the MOT coils (see Table 6.1 for the design and actual current of each section). Sections A and B, which have fairly modest current requirements, are powered by Acopian Y08LXU4000 power supplies rated to 40 A at 8 V. In practice we found that the constraint of having the same current in the mini-MOT and MOT coils was limiting our magnetic trap loading rate, and therefore we eventually installed a separate Power10 P63C-15440 high-current power supply rated to 440 A at 15 V for the mini-MOT coil. Optimization of the slower currents was done while looking at the fluoresence of the repumped MOT.

Electrical connections to sections A and B are made identically to those in the Li Zeeman slower (see Section 5.4.3). The electrical connections between the mini-MOT coil and the high-current power supply are made using 3/0 gauge stranded welding cable, which is what is used to wire both pairs of MOT coils in the two experiments. See Section 5.5.4 for details on such connections. Switching of the slower sections A and B can be achieved with Crydom D1D40 solid state relays (rated to 40 A) with Powerex CS240650 diodes (rated to 50 A) in a ring-down-circuit configuration. In practice we do not switch sections A and B, because their fringe field has a positive effect on our 689 MOT size. The mini-MOT coil is switched by simply toggling the analog input voltage to the power supply between 0 and a voltage set with a potentiometer with an external TTL

Slower Section	Length (m)	Power (W)	ΔT (°C)
A	20.3	43.1	0.5
B	5.06	10.8	0.1
mini-MOT	0.44	9.41	0.1

Table 6.2: Length, power consumpion and temperature rise (ΔT) of cooling water of each slower section. Temperature rise calculation assumes that all slower sections are connected in hydraulic series, which gives a flow rate of ~ 23 cm^3/s at 100 psi.

(transistor-transistor logic) signal. While this turn off is slow ($\sim$ 10 ms), it is shorter than the timescale of our magnetic trap hold ($\sim$ 100 ms).

6.4.4 Zeeman slower thermal management

All three Sr Zeeman slower magnets are water cooled, although it is only strictly necessary for the mini-MOT coil. The expected rise in water temperature in each section is listed in Table 6.2. The water connections were made in the same fashion as those on the Li Zeeman slower (see Section 5.4.4).

6.5 Sr magnets

Strontium has a non-magnetic ground state[14], which therefore cannot be magnetically trapped. In addition, no ground-state-ground-state magnetically tunable Feshbach resonances exist. For these reasons, the magnetic requirements of a Sr experiment are quite relaxed. A magnetic field-gradient is required for the MOT, and the magnetic trap of the metastable $5s5p\,^3P_2\,|m_J = 2, 1\rangle$ states. A relatively gentle gradient of $\sim$ 50 G/cm is sufficient for both of these stages. For this reason, and to expedite construction by using off-the-shelf vacuum components, we decided to prioritize optical access in the

[14] Apart from ^{87}Sr, which has ten degenerate nuclear spin states in the ground manifold. However since g_I is small, these states have effectively zero Zeeman shift at experimentally accessible magnetic-field gradients.

construction of the Sr main chamber. No re-entrant bucket windows were used in the design of the main chamber, and therefore the point of closest approach between the pair of anti-Helmholtz coils is 5.25", corresponding to a Helmholtz-condition ID of 9.5". Such large coils require large currents to produce modest magnetic-field gradients, and produce large fringe fields outside of the chamber. The heat generated by the 3/0 gauge cables that carry current to and from the magnets has been a continual worry during operation of the Sr experiment. The fringe field from the top Sr magnet largely influenced the Sr Zeeman slower design, as discussed in Section 6.4.

6.5.1 Sr magnet design & construction

The Sr magnets were designed to produce a magnetic-field gradient of ~ 50 G/cm. Given the minimum separation of 5.25" and an ID of 9", this required a current of ~ 350 A for the same 32-turn, 4×8 block of coils that were used in the Li magnet (see Section 5.5.2 for further details on this design). As the magnets would never be used to produce a uniform field, maintaining low field curvature was not a priority.

The Sr magnets were wound using the same square-cross-section, hollow Cu wire and 80/20 winding rig that were used for the Li Zeeman slower and magnets (see Sections 5.4.2 and 5.5.3). The mandrel, and plates used to provide lateral confinement increased in size in the radial dimension according to our design requirements. We also used set screws from both plates to provide the confinement, adjusting the position of each screw according to the helicity of the coil.

6.5.2 Sr magnet electronics

The magnets are designed to operate between 0 and 400 A. To run 400 A through both magnets, a total voltage difference of 31 V must be applied across them, not including

Magnet Layers	Length (m)	Voltage (V)
1 & 2	6.61	3.51
3 & 4	7.12	3.79
5 & 6	7.63	4.06
7 & 8	8.14	4.33

Table 6.3: Lengths of and voltage drops at 400 A across the four sections of the Sr magnets.

voltage drops in the cables and connections to the power supplies. The voltage required by each pair of layers in one of the magnets is listed in Table 6.3. Since the power required to energize both of the magnets entirely would require more than the 15 kW available from a 208 V 3-phase high-current power supply, we use two separate high-current power supplies to run the magnets. The innermost 4 layers of each magnet are connected to the same power supply, a PowerTen P63C-25400[15], and the outermost 4 layers of each magnet are connected to the same power supply, a TDK-Lambda 30-500[16]. The currents in these two isolated elctrical circuits had to be calibrated to be equal to avoid the magnetic-field zero moving during magnetic-field-gradient ramping.

The connections between the power supplies and the magnets were made using the same 3/0 gauge stranded welding cable and screw lugs that were used for the Li magnets (see Section 5.5.4). This cable is only rated to 350 A, and is typically at ~ 60 °C when running the MOT currents of 288 A. This leads to substantial heating of the Sr machine table enclosure, and a temperature rise of 1 °C or more is common when running the experiment. A future technical upgrade of the apparatus will involve replacing large sections of this 3/0 gauge wire with water-cooled Cu tubing, and replacing all of the screw lugs with compression lugs.

Switching of the magnets is accomplished through analog voltages that are sent to the power supplies. Such control of the magnets can ramp down the magnetic-field gradient

[15]Rated to 400 A, 25V.
[16]Rated to 500A, 30V

Magnet Layers	Length (m)	Power (kW)	Flow Rate (cm^3/s)	ΔT (°C)
1 & 2	6.61	1.40	44.7	7.5
3 & 4	7.12	1.51	43.1	8.4
5 & 6	7.63	1.62	41.6	9.3
7 & 8	8.14	1.73	40.3	10

Table 6.4: Length, power consumption, flow rate and temperature rise (ΔT) of cooling water of each section of one magnet coil, assuming a current of 400 A and cooling water pressure of 100 psi. Temperature rise calculation assumes that all magnet sections are connected in hydraulic parallel.

to zero in ~ 20 ms, and we find this is sufficient for the transfer from the magnetic trap to the 689 MOT.

6.5.3 Sr magnet thermal management

The high currents run through the magnets lead to substantial resistive heating of the magnets themselves, as well as the cables used to connect to them (for a discussion of the heating of the cables, see Section 6.5.2). The magnets were wound with the same square-cross-section hollow Cu wire that was used for the Li Zeeman slower, and therefore have the same resistive and hydraulic properties as the slower (see Sections 5.4.2 and 5.4.4). The calculated temperature rise for the cooling water flowing through each magnet section is listed in Table 6.4. The observed steady-state temperature rises during the MOT (when the magnets have 288 A running through them) are as high as 15 °C, suggesting that the calculated flow-rate is an over-estimate.

6.6 Sr laser systems

As discussed in Chapter 4, the Sr cooling sequence requires us to address three optical transitions, at 461 nm, 689 nm and 403 nm. We use two non-resonant red-detuned lasers to produce traps and lattices, one at 1064 nm, and the other at 915 nm.

6.6.1 461 nm laser system

The 461 nm laser is a Toptica SHG Pro, which consists of an ECDL at 922 nm, a TA and a frequency-doubling cavity. While the laser origially produced over 600 mW of blue light power, it produces up to 400 mW currently[17]. We believe this is due to reduction in power of the TA output (which is now up to 1 W) and a change in the TA output mode, which would have to be compensated for by adjusting the TA output coupling lens. The doubling cavity is locked with a Pound Drever Hall (PDH) lock, that is implemented by a Toptica FALC. This cavity lock has given us much trouble over the years. The cavity is susceptible to going out of lock due to acoustic and vibrational noise, from the lab door being opened, and from mechanical shutters on the optical table being actuated. A water absorption line at around half of the frequency of the 461 nm resonance frequency leads to power loss inside the cavity, and can make it impossible to lock the cavity. To overcome this, we use packets of dessicant provided by Toptica to absorb any water vapor in the cavity. These packets have to be periodically replaced[18]. We have had to clean the cavity mirrors with iso-propyl alcohol and a lens cloth a couple of times, due to a decrease in output power. We have also had to replace one of the cavity mirrors, as the piezoelectric transducer (PZT) that was used to adjust the position of that mirror, and thereby provide feedback to the cavity, broke.

The 461 nm laser system is set up on a 4' by 10' optical table, and all of the 461 nm light is delivered to the experiment via PM optical fibers. AOMs are used to achieve all of the required frequency shifts, and to gate the light on fast time scales. Mechanical

[17] One of the TA incoupling mirrors drifts on the few-day time scale, and thus has to be adjusted at the start of the day to maximize output power.

[18] The frequency with which we have to replace the dessicant packets is variable. At it's worst (typically in the early months of the year when rain is more common in Santa Barbara) we have to replace the dessicant packets on a few-day time scale. At other times we do not replace the dessicant packet for several months. The dessicant packets can be re-used, by baking them for a prolonged period to drive out water bound to the dessicant.

shutters are used for complete shuttering on slow time scales. The isotope shifts of the ${}^1S_0 \rightarrow {}^1P_1$ transition are all less than 271 MHz (for the stable isotopes), and by adjusting the RF used to drive two AOMs in the spectroscopy pathway, the laser set up can be used to produce MOTs of each isotope. Since imaging light is only required when the MOT light is turned off, we use the MOT AOM zero-order light to produce the imaging light.

The laser is frequency-referenced to the atomic transition by performing saturated absorption spectroscopy on a heated vapor of Sr atoms in a spectroscopy cell very similar to that used in the Li experiment (see Section 5.6.1 for details on saturated absoprtion spectroscopy and frequency-locking). We lock to the ^{88}Sr Doppler-free absorption peak as it provides the largest signal, and because the istope shift between ^{88}Sr and ^{84}Sr is easily spanned using AOMs. The laser is stabilized by PID feedback to the diode laser current. The PID circuit input is a slope which is produced by a lock-in amplifier, both of which are implemented by a Toptica Digilock 110. The frequency modulation required for the lock-in amplifier is applied to the light with a double-passed AOM which is in the spectroscopy light pathway. This laser lock is by far the least stable in either experiment, and has to be relocked on a 30 minute timescale. However, the frequency does not wander by more than a few 100 MHz, so re-locking is relatively painless.

6.6.2 689 nm laser system

The 689 nm laser is a Toptica DL Pro. We requested a longer-than-standard ECDL cavity, which was specified to have a linewidth of 30 kHz. While this linewidth is still larger than the ${}^1S_0 \rightarrow {}^1P_1$ transition linewidth (7.4 kHz), it can be used to produce clouds with sufficiently-high PSD to reach quantum degeneracy via evaporation. The laser produces close to 30 mW of 689 nm light, which is directly used to seed a home-

built TA, which uses a Eagleyard EYP-TPA-0690-00500-2003-CMT02-0000 chip. While this TA originally produced over 350 mW, it currently produces 200 mW. This light is used for spectroscopy and to produce the MOT beams. The 689 nm laser is on the same optical table as the vacuum chamber, but the MOT light is fiber-coupled into an Oz Optics non-polarization maintaining 3 : 3 fiber splitter which produces the three fiber-coupled light sources for the three MOT beams (see Section 4.5.2 for details on this splitter and the MOT beam set up). AOMs are used to produce the required frequency shifts, and are used in conjuction with mechanical shutters to gate the MOT beams before they are fiber coupled. Separate optical pathways were constructed to produce the ^{88}Sr and ^{84}Sr MOT light, which are separated by 351.49 MHz. The optical power can be routed between these two pathways by turning a waveplate.

We perform saturated absorption spectroscopy on a heated vapor of Sr atoms, and lock to the Doppler-free absorption peak of ^{88}Sr, as it is the most abundant isotope. We use a Toptica DLC pro to produce a slope and a feedback signal to the laser diode current. The frequency modulation used to produce the slope is applied to the pump light[19], via a double-passed AOM in the optical pathway. Since the linewidth of, and therefore the scattering cross-section for, this transition is more than 3 orders of magnitude smaller than that of the 461 nm transition, we use a separate spectroscopy cell to perform saturated absorption spectroscopy. This cell was initially pumped to a lower pressure than the 671 nm and 461 nm spectroscopy cells - around 0.1 mtorr. This leads to an increased partial pressure of Sr atoms, and therefore optical density (OD), at a given temperature. To avoid coating the windows of the cell due to this increased partial pressure, we extended the length of the cell and initially water-cooled the tube near the windows to increase the probability that Sr would stick to the walls in these regions, instead of bouncing off of the walls and later colliding with and sticking to the windows.

[19]This is known as modulation transfer spectroscopy

However this large temperature gradient led to substantial mass transport of Sr from the heated reservoir to the water-cooled regions of the tube. The deposition was so large that it could occlude the spectroscopy laser beams. Additionally, the reduced quantity of Sr in the heated region would require higher temperatures to produce a sufficiently high OD vapor. Sustained heating to over 700 °C led to periodic failure of the heating tape used to heat the cell. Recently, we removed the water-cooling plates and have begun heating the formerly cooled regions of the tube. We now can achieve a strong Doppler absorption signal at temperatures below 400 °C, but there is the possibility that the windows will become occluded over time.

6.6.3 403 nm laser system

The 403 nm laser is a Sacher Lynx ECDL. It produces close to 30 mW of 403 nm light. We use an AOM and mechanical shutter to gate the light before it enters a fiber, through which it is delivered to the main chamber. The laser is brought to resonance by observing the effect of the light on the 461 nm MOT (there is a substantial increase in fluorescence). We correct for drift in the laser frequency via an offset lock. Some of the 403 nm light and 461 nm light are coupled into the same Thorlabs scanning Fabry-Perot interferometer. The cavity PZT is scanned through less than the 1.5 GHz free spectral range (FSR), to produce one transmission peak each for the 403 nm light and the 461 nm light. A digital feedback loop implemented in Labview maintains the separation between these peaks (in terms of cavity PZT voltage) by providing feedback to the 403 nm laser PZT voltage. The cavity PZT voltage offset must be manually adjusted periodically as the cavity length drifts over the course of the day to ensure that we continue to detect the same pair of peaks[20]. The lock is reliable as long as the 403 nm laser has a stable

[20]Each laser has multiple transmission peaks, each separated by 1 FSR. The change in cavity length, and therefore PZT voltage, that corresponds to 1 FSR is different for the two lasers, and they are related

mode, and the 461 nm laser remains locked to the atomic transition.

6.6.4 1064 nm laser system

The 1064 nm laser light is produced by an NKT Koheras AdjustiK Nd:YAG fiber laser. The AdjustiK has a built-in pre-amplifier, and can produce up to 100 mW of single spatial and transverse mode, low linewidth laser light. This is directly used to seed an NKT Koheras BoostiK fiber amplifier, that is specified to output 15 W of optical power. After two stages of optical isolation, we obtain 12 W of power. This is used to produce the two trapping beams that produce the XODT. The XODT beams are free-space coupled to the atoms, and the power in the beams is monitored and stabilized by a photodiode and PID circuit which adjusts the RF power delivered to the AOMs that are used to control the power in each beam. Pacific Laser Equipment waveplate rotators are used to divert power away from the XODT beams and towards other trap or lattice beams during the final second of evaporation. Oz Optics high-power fibers and collimaters are used to deliver trap and lattice power to the chamber for experiments. The power emitted from these fibers are monitored with photodidodes, and this signal is used to stabilize the beam power with a PID circuit which controls the RF power used to drive AOMs.

6.6.5 915 nm laser system

The 915 nm laser light is produced by a Sacher Lynx ECDL. The laser produces 100 mW of optical power, which is used to seed a home-built TA using an Eagleyard EYP-TPA-0915-01500-3006-CMT03-0000 TA chip. An AOM is used to gate the light before it

by the ratio of the wavelengths of the lasers. Therefore, the splitting between 403 nm peaks and 461 nm peaks is different for each pair of peaks. We choose a convenient pair of peaks, and adjust the cavity PZT offset voltage to maintain those two peaks within the cavity scan.

is coupled into an Oz Optics high-power fiber and delivered to the chamber. The power emitted from the fiber is monitored with a photodiode and is used to stabilize the beam power with a PID circuit which controls the RF power used to drive AOMs.

Chapter 7

Quantum simulation of ultrafast dynamics using trapped ultracold atoms

One avenue of research on the Sr experiment is the quantum simulation of ultrafast processes that occur in atoms or molecules subject to short, intense laser pulses. This new type of quantum simulation experiment hinges upon an analogy between electrons bound in a Coulomb or molecular potential, and atoms bound in an optical or magnetic trap. While details such as the charge of the particles and the shape of the potential are different, the Hamiltonian of bound electrons experiencing an oscillating electric field can be shown to have the same form as that of bound atoms experiencing inertial forces. One advantageous difference between these two analogous physical scenarios is that the energy density of the cold atom system is much lower, leading to a difference in the relevant timescales of these two systems of up to 12 orders of magnitude. Therefore dynamics that occur on femtosecond timescales for a trapped electron occur on millisecond timescales for trapped atoms. This temporal magnification allows for susbtantial simplification of

experimental requirements on pulse generation and detection.

We performed a series of experiments in which we applied inertial forces to the atoms in the ground-state of a single optical dipole trap. This was achieved by loading a BEC of $\sim 2 \times 10^4$ ^{84}Sr atoms into the ground state of a horizontal ODT with a waist of $\sim$ 15 μm, an optical power of $\sim$ 30 mW, and a radial trap frequency of $\sim$ 400 Hz. Inertial forces were applied to the atoms by moving the trap center, by frequency-modulating the radio frequency drive of an acousto-optic modulator (AOM) that was placed in the beampath. The light was delivered to the breadboard in an Oz Optics high-power fiber, with an output beam diameter of $\sim$ 1 mm. The light was immediately passed through the AOM, and then through two telescopes in an $8f$ configuration from the AOM crystal, which expanded the beam diameter to 20 mm. The $8f$ system mapped AOM defelection to an angular deflection on a $f = 150$ mm objective lens that was used to focus the collimated beam onto the atoms. This angular deflection at the lens leads, to first order, to a translation of the beam focus position. The RF drive was modulated by applying a tunable voltage to the voltage controlled oscillator (VCO) that was used to produce it. This tunable voltage was produced by a National Instruments (NI) PCI 6713 analog output board, and the waveform was specified in Cicero. The results of this experiment are published in *Nature Communications* [30], and the manuscript is included as the remaining part of this Chapter.

7.1 Abstract

Ultrafast electronic dynamics are typically studied using pulsed lasers. We demonstrate a complementary experimental approach: quantum simulation of ultrafast dynamics using trapped ultracold atoms. Counter-intuitively, this technique emulates some of the fastest processes in atomic physics with some of the slowest, leading to a temporal

magnification factor of up to twelve orders of magnitude. In these experiments, time-varying forces on neutral atoms in the ground state of a tunable optical trap emulate the electric fields of a pulsed laser acting on bound charged particles. We demonstrate the correspondence with ultrafast science by a sequence of experiments: nonlinear spectroscopy of a many-body bound state, control of the excitation spectrum by potential shaping, observation of sub-cycle unbinding dynamics during strong few-cycle pulses, and direct measurement of carrier-envelope phase dependence of the response to an ultrafast-equivalent pulse. These results establish cold atom quantum simulation as a complementary tool for studying ultrafast dynamics.

7.2 Introduction

The study of ultrafast-equivalent electronic and vibrational dynamics is a natural but largely unexplored application of cold-atom quantum simulation techniques [21, 24, 22, 23, 86]. Quantum simulation experiments often rely on an analogy between trapped neutral atoms and electrons in matter [87, 88, 89]. Although these two systems have vastly different energy densities and constituents which differ in mass and charge, they can often be described by equivalent Hamiltonians, which give rise to equivalent physics. This analogy has been used to explore equilibrium solid-state phenomena from Mott insulators to antiferromagnets [10, 15], and dynamical phenomena from Bloch oscillations to many-body localization [11, 17]. Here we extend this analogy to quantum simulation of ultrafast dynamics, with the aim of realizing an alternate experimental approach to open questions in a vibrant and expanding area of science [90, 91, 92], testing approximate theories [93, 94, 95, 96, 97], and pushing into experimentally unexplored regimes.

The quantum simulator we describe consists of an artificial atom or molecule made from a trapped quantum gas. The analogue of the atomic or molecular binding potential

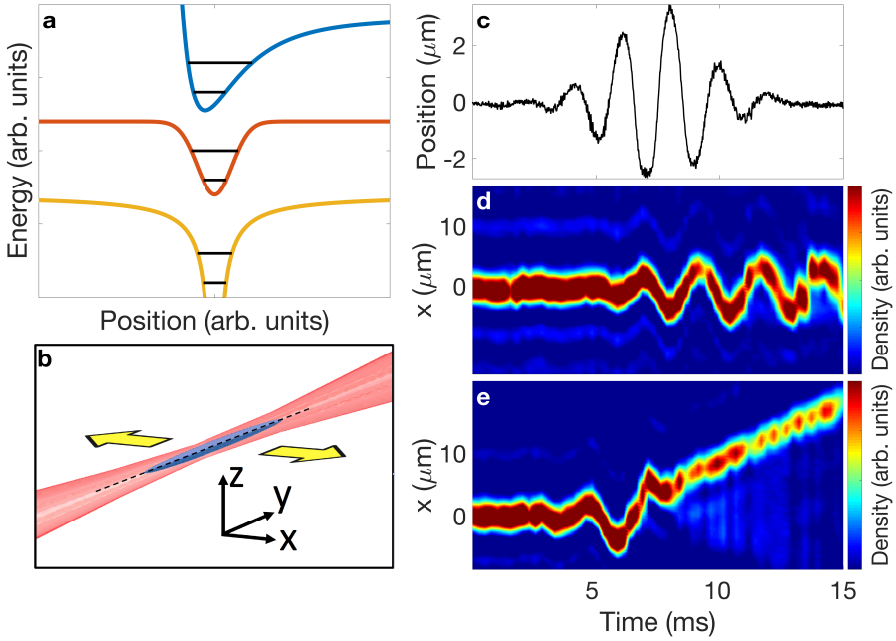

Figure 7.1: **Quantum simulation of ultrafast dynamics.** **a:** Schematic bound states of Lennard-Jones, Gaussian, and $1/r$ potentials (offset for clarity). **b:** Diagram of optical trap (red), which is shaken in the $\hat{\mathbf{x}}$ direction to generate inertial forces on the condensate (blue). **c:** Measured trap position $\alpha(t)$ during a pulse. **d:** Response to a weak pulse. Colourmap shows density distribution after time-of-flight as a function of time. Pulse carrier frequency is 450 Hz, pulse envelope width is 3.76 ms, pulse amplitude is 0.6 μm, and carrier-envelope phase is 0, as defined in Eq. 7.2. **e:** Response to a stronger pulse. Unbinding occurs near 8 ms, after which the atoms propagate with constant velocity. Pulse amplitude is 2.4 μm. All other pulse parameters are identical to those in **d**.

is the tunable AC Stark potential of an optical trap (see Fig. 7.1a), and the analogue of the pulsed laser's electric field is an inertial force arising from rapid trap translation (see Fig. 7.1b). The time-dependent Gross-Pitaevskii equation describing the evolution of the condensate wavefunction $\Psi(\mathbf{r}, t)$ is [21]

$$\left[-\mathrm{i}\hbar\partial_t - \frac{\hbar^2\nabla^2}{2m} + V(\mathbf{r} + \alpha(t)\hat{\mathbf{x}}) + gN|\Psi|^2\right]\Psi = 0, \tag{7.1}$$

where m is the atomic mass, $g = 4\pi\hbar^2 a_\mathrm{s}/m$ parameterizes interactions among N atoms, a_s is the scattering length, and the optical potential $V(\mathbf{r})$ is shaken in the $\hat{\mathbf{x}}$ direction

with waveform $\alpha(t)$ (see Fig. 7.1c for a sample waveform). Crucially, the same equation also describes the evolution of the wavefunction of an atomic electron interacting with a linearly-polarized laser field in the Kramers-Henneberger frame of reference [21], taking m to be the electron mass, V the nuclear potential including screening effects, and $g \to 0$. For dipolar excitations like those in the experiments we present, the impact of the atoms' nonzero g is minimized due to Kohn's theorem. Very similar dynamics have been theoretically predicted [21] for the cold-atom and ultrafast realizations of Eq. 7.1. A closely related equivalence is described in [24]. This equivalence between the evolution of condensate and electron wavefunctions motivates cold atom quantum simulation of ultrafast dynamics, much as the Bose-Hubbard model motivated early quantum simulation of Mott insulators [10].

Though very little of the growing body of quantum simulation work has addressed ultrafast phenomena, a robust toolkit exists for controlling and measuring excitations in trapped gases. Collective excitations in Bose condensates were a major focus of early experimental and theoretical research [8, 9, 98, 99, 100, 101], and the analogy between degenerate trapped gases and individual atoms was noted at that time [102, 103, 21]. Ultrafast probes have recently been used to study many-body dynamics in Rydberg atoms [104], and recent theoretical proposals have suggested the use of cold atoms to simulate ultrafast dynamics in atoms [24, 86], molecules [23], and solids [22].

Cold gases offer unique capabilities for dynamical quantum simulation. Due to the extremely low energy scales, the dynamics are slowed, or magnified, with respect to atomic or molecular timescales by as much as twelve orders of magnitude, allowing the observation of ultrafast-equivalent processes in ultra-slow-motion [24]. This extreme temporal magnification — quantum gas chronoscopy — enables simple and complete control over all parameters of an applied force pulse, as well as straightforward measurement of the artificial atom's or molecule's response, with time resolution much faster than all relevant

dynamics. The excitation spectrum itself can also be controlled by trap shaping. Using this toolkit of capabilities, we demonstrate experimentally that cold atom quantum simulation can be used to probe complex phenomena of ultrafast science such as the effect of carrier-envelope phase and pulse intensity on unbinding dynamics. Fig. 7.1d-e show examples of experimentally observed sub-cycle unbinding. These experiments demonstrate a new application for cold-atom quantum simulation and establish a potentially fruitful connection between ultrafast and ultracold atomic physics.

7.3 Results

7.3.1 Ultrafast-equivalent pulse synthesis

The experiments we describe use a Bose condensate of $N \simeq 20,000$ atoms of ^{84}Sr [105], with a scattering length $a_s \simeq 6.5$ nm. Rapid trap translation gives rise to time-dependent inertial forces designed to have the same approximate functional form, and the same effect of driving dipole-allowed transitions, as the electric field of an ultrafast pulsed laser (see Fig. 7.1b for diagram of experimental set up). This is achieved by applying a trap which depends on x and t as $V(x,t) = -V_{\text{trap}} \times \exp\left[-2(x-\alpha(t))^2/w^2\right]$, where w is the $1/e^2$ trap waist and

$$\alpha(t) = A \,\text{sech}\left[\eta\,(t-t_0)\right] \sin\left[2\pi f\,(t-t_0) + \phi + \pi\right]. \tag{7.2}$$

Control over the pulse is effectively arbitrary; variable parameters include amplitude A, carrier frequency f, pulse full-width at half-maximum $\tau = (2\ln(2+\sqrt{3}))/\eta$, and carrier-envelope phase ϕ. The measured trap centre translation as a function of time during a typical pulse is shown in Fig. 7.1c. All data reported here use pulse amplitudes well below the trap width. The effective Keldysh parameter in such an experiment

is $\gamma_{\mathrm{K}} = \sqrt{V_{\mathrm{trap}}/2U_{\mathrm{p}}}$, where the optical trap depth V_{trap} corresponds to the ionization energy and the ponderomotive potential $U_{\mathrm{p}} \simeq m\overline{\dot{\alpha}^2}/2$ is the time-averaged kinetic energy imparted to the atoms by the pulse. The use of inertial forces enables realization of Keldysh parameters of order unity and greater. Keldysh parameters much less than 1 could be straightforwardly attained by using a time-varying optical potential gradient rather than trap motion to apply the simulated electric field.

7.3.2 Spectroscopy of tunable collective excitations

We performed initial spectroscopic characterization of our quantum simulator by applying pulses of constant length much greater than a drive period and variable carrier frequency f. After each pulse, the atoms that had not been unbound from the trap were counted with absorption imaging. The resulting plots of bound fraction versus pulse frequency characterize the collective excitation spectra of the trapped condensate. Nonlinear effects are straightforwardly probed by increasing the pulse intensity.

Excitation spectra for one particular trap are shown in Fig. 7.2a. The resonance at ∼750 Hz corresponds to dipole oscillation in the trap and is at the same frequency as the resonance for a non-interacting gas. As the pulse amplitude is increased, higher modes are excited and power broadening is observed. Since our trap is deeply in the Thomas-Fermi regime, these modes are anharmonic and strongly collective. Fig. 7.2b shows a 2d amplitude-frequency spectrogram.

The excitation spectrum can be tuned by adjusting the trap shape, enabling the study of ultrafast-equivalent dynamics in systems with specific spectral characteristics such as mode degeneracies. The results of such tuning of the excitation spectrum are presented in Fig. 7.3a-c. We observe good agreement with analytic predictions for dipole-allowed collective resonance positions in the broadened and unbroadened trap [101]. Note that the

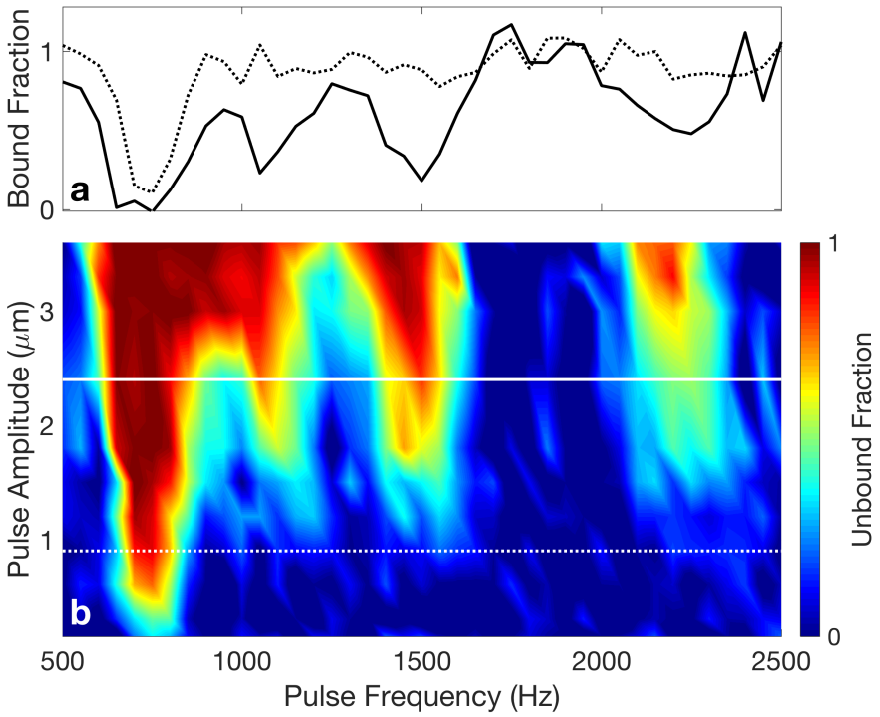

Figure 7.2: **Spectroscopy of the quantum simulator. a:** Remaining bound fraction as a function of carrier frequency for pulses with $\tau = 250$ ms, $\phi = \pi$ and amplitudes of 0.9 μm (dotted) and 2.4 μm (solid). Note the emergence of higher-order peaks and power broadening at larger amplitudes. **b:** Unbound fraction as a function of applied pulse frequency and amplitude, for a 250 ms pulse. Lines indicate cuts plotted in panel **a**.

frequencies of these complex anharmonic modes are not simply rescaled by broadening, but disperse at different rates; this enables tunable creation of mode degeneracies. This tunability of the collective excitation spectra is a key feature of cold-atom based quantum simulation of ultrafast dynamics. Static adjustments like those demonstrated here enable the realization of desired spectral properties, and rapid tuning of mode degeneracies could enable the study of controllably diabatic or adiabatic dynamics. Future experiments could use this ability for quantum simulation of molecular energy relaxation mechanisms in the vicinity of tunable mode degeneracies similar to conical intersections [106].

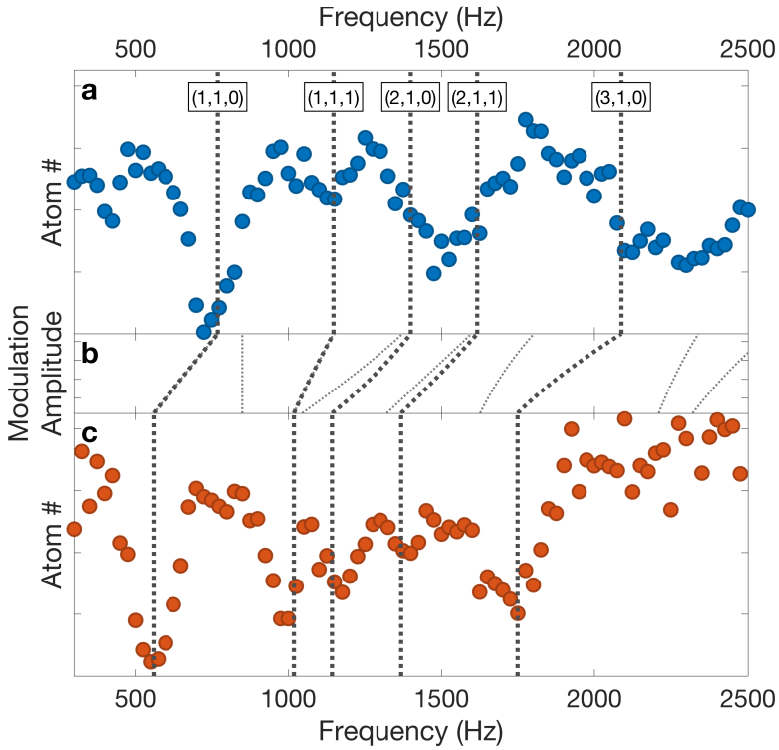

Figure 7.3: **Tunable excitation spectra via trap shaping. a:** Bound fraction after a 1-second pulse as a function of excitation frequency for an unmodified trap. Bold dotted lines are theoretically predicted frequencies of collective resonances expected to couple to our drive. Labels on theory lines indicate the quantum numbers (k, β, γ), using the notation of [101]. β and γ are parity quantum numbers, and k indicates the form of the nodal surface for the excitation. The quantum number m is 1 for all resonances plotted. The only inputs to this theory are the three trap frequencies. The resonance at half the fundamental frequency is believed to be due to parametric excitation of a dipole oscillation in the direction of gravity. Pulse amplitudes were increased from 0.6 μm at low frequency to 3 μm at the highest frequency to maximize peak visibility. **b:** Evolution of predicted resonances under continuously increasing trap broadening. Thinner dotted lines represent resonances which are not dipole-allowed for this drive polarization. **c:** Bound fraction after a 1-second pulse as a function of excitation frequency for a trap broadened in one direction as described in the methods section.

7.3.3 Momentum-resolved sub-cycle unbinding dynamics

Having demonstrated quasi-CW spectroscopy of bound states with tunable energy spectra, we turn to the use of this tool for quantum simulation of ultrafast dynamics during few-cycle pulses [107]. In ultrafast streaking measurements, the electric field of a

few-cycle femtosecond pulse deflects photoelectrons produced by an attosecond extreme ultraviolet pulse striking an atom, allowing characterization of both the pulses and the atom [90, 108, 109]. In the quantum simulator, qualitatively similar techniques allow high-resolution measurement of sub-cycle quantum dynamics. Here, instead of using photoionization to terminate the dynamics, the experimenter can simply instantaneously turn off the trapping potential at any point before, during or after the pulse. The atoms then propagate freely in space, and their instantaneous momenta at the time of trap removal are mapped onto their positions after some time of flight. Varying the time at which the trap is removed enables measurement of the time evolution of the bound quantum system with time resolution far below a drive period. This experimental technique, while commonplace in ultracold atomic physics, represents a powerful and general tool for the study of ultrafast-equivalent dynamics in our quantum simulator.

Fig. 7.4a-e presents the results of such measurements for both off-resonant and near-resonant pulses. The Bose-condensed atoms initially occupy mainly a single eigenstate of the transverse trapping potential. Quantum dynamics during and after the pulses shown in Fig. 7.4a and Fig. 7.4c can be tracked by direct momentum-space imaging of the atoms. Fig. 7.4b and Fig. 7.4d show the density distribution after time-of-flight, integrated over the directions transverse to the excitation, as a function of time. For a pulse carrier frequency significantly below the dipole oscillation frequency ν_x in the dimension of driving (see Fig. 7.4a for pulse waveform), the momentum of the BEC evolves coherently during and after the pulse, as shown in Fig. 7.4b. Incoherent heating due to the pulse is observed to be minimal on the few-cycle time scales we probe. The atoms respond to the pulse at ν_x — a higher frequency than the carrier — but remain bound. During a pulse with carrier frequency near ν_x, however, qualitatively different is observed. Fig. 7.4d shows momentum evolution during a near-resonant pulse for an amplitude near the unbinding threshold (see Fig. 7.4c for pulse waveform). In this parameter regime, atoms do not leave

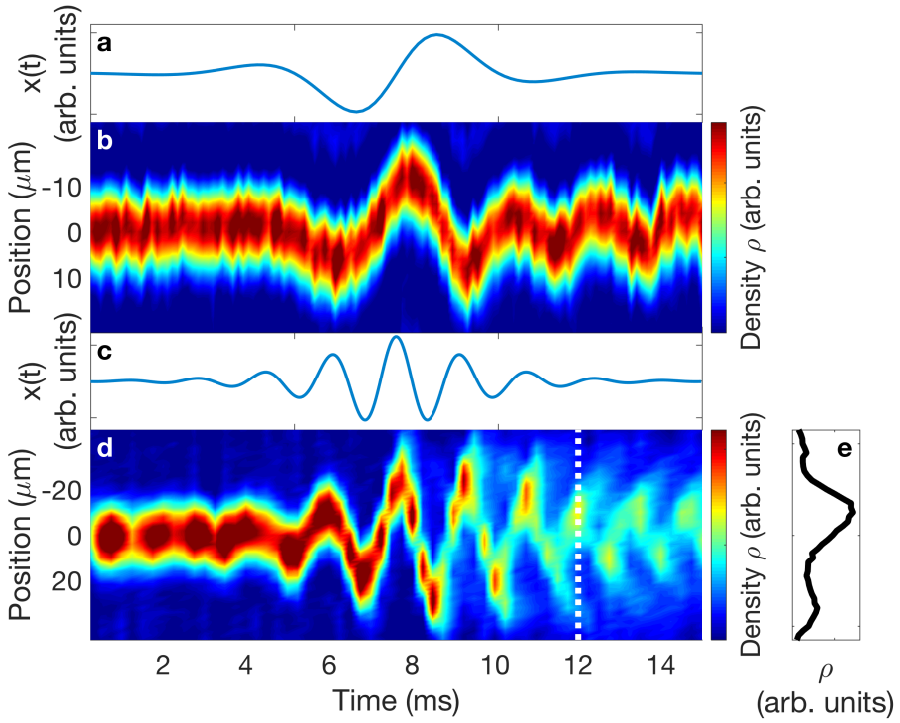

Figure 7.4: **Sub-cycle dynamics during off-resonant and near-resonant pulses. a:** Trap minimum position as a function of time for a pulse with $\tau = 3.76$ ms, $f = 200$ Hz, $A = 3\mu$m and $\phi = \pi$. **b:** Post-time-of-flight integrated spatial density distribution versus trap turn-off time during the off-resonant pulse depicted in panel **a**. Here $\nu_x = 450$ Hz. **c:** Trap minimum position as a function of time for a pulse with $\tau = 3.76$ ms, $f = 550$ Hz, $A = 1.5\mu$m and $\phi = \frac{3\pi}{2}$. **d:** Post-time-of-flight integrated spatial density distribution versus trap turn-off time during the near-resonant pulse depicted in panel **c**. Here $\nu_x = 600$ Hz. **e:** Density distribution at the time indicated by the dashed line in panel **d**. Peaks from bound and ejected atoms are visible.

the trap all at once, but do not incoherently heat either; instead, ejection starts at the time of the pulse peak, with additional bursts of atoms emitted during each subsequent half-cycle of the pulse. Fig 7.4e shows one such burst. This unbinding process models ionization or molecular disintegration during an ultrafast laser pulse.

7.3.4 Varying pulse amplitude and carrier-envelope phase

The ability to precisely measure the population and momenta of unbound states as a function of pulse parameters and time opens up the possibility of flexible quantum

simulation of ultrafast unbinding dynamics. As an initial application of the quantum simulator presented herein we have measured the dependence of simulated ionization yield or photodissociation on both pulse amplitude and carrier-envelope phase. This represents a complementary method of testing the effects of two parameters central to numerous experimental and theoretical studies of ultrafast multiphoton ionization and bond-breaking processes [93, 94, 95, 110, 111, 112].

Both the precise unbinding time during an applied force pulse and the final unbound momentum depend sensitively and non-monotonically on pulse amplitude. In the quantum simulator, the amplitude of the pulse can be straightforwardly varied over a wide range, keeping the carrier-envelope phase, carrier frequency, and total pulse time constant. As the amplitude is increased from that used in Fig. 7.4d, the unbinding dynamics change drastically. Fig. 7.5a shows the momentum distribution of the atoms (measured by detecting the position distribution after 2 ms time of flight) after few-cycle pulses with amplitudes from 0 up to 6 μm. Fig. 7.5b-e show the full time evolution of the momentum distribution during few-cycle pulses of selected amplitudes. Below a critical amplitude, no atoms are ejected from the trap. For some intermediate amplitudes, the behaviour mirrors that shown in Fig. 7.4d, with bursts of atoms unbinding at different points during the pulse. Above that intermediate regime, all of the atoms unbind at one well-defined time and continue to move with constant momentum after unbinding. Strikingly, as the amplitude is increased further, the momentum of the unbound atoms reverses sign, as they unbind half a drive cycle earlier, in an oppositely-directed simulated electric field.

Even for fixed pulse amplitude, the final state of the initially bound system after the force pulse depends sensitively and non-trivially on the carrier-envelope phase ϕ (CEP). In the pulsed-laser experimental context, the advent of few-cycle pulses with adjustable, stabilized CEP [113] has enabled advances such as probes of the effects of CEP on ultrafast dynamics [114, 115], study of interference patterns in multiparticle ioniza-

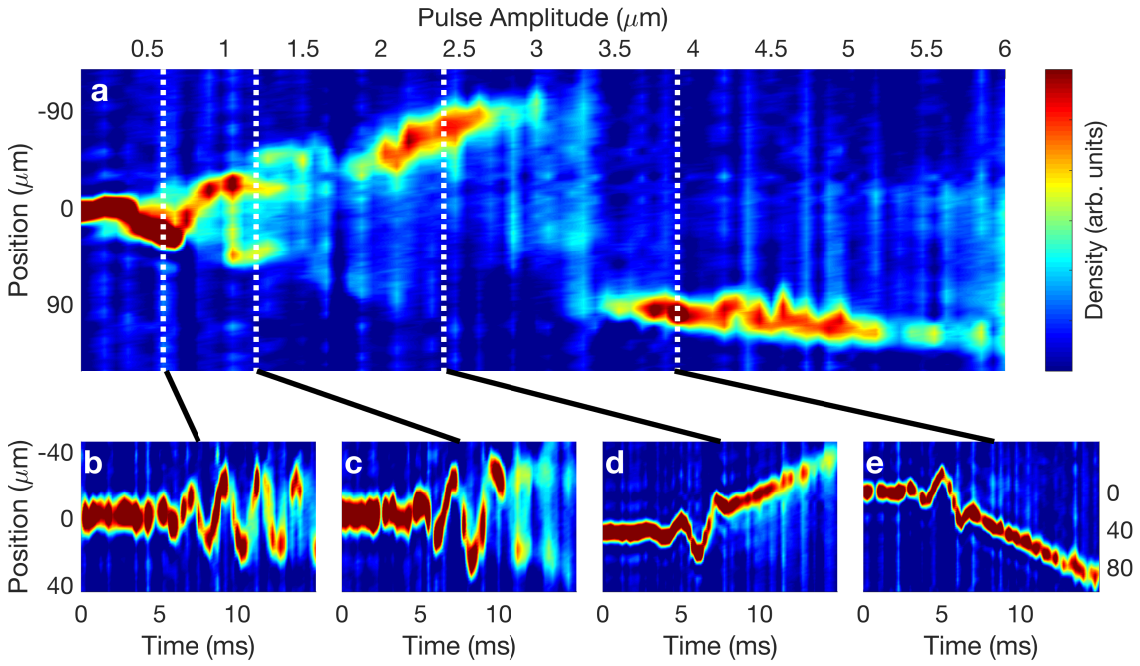

Figure 7.5: **Dependence of unbinding dynamics on pulse amplitude. a:** Integrated spatial density distribution after application of a near-resonant 480 Hz pulse with $\tau = 3.76$ ms and $\phi = 0$ followed by 2 ms time-of-flight, versus pulse amplitude A. **b-e:** Integrated spatial density distribution versus time during pulses with the indicated amplitude. Panels **d** and **e** have an expanded y-axis (indicated at right) to track the unbound atoms. Note the momentum of the unbound atoms changing sign as the pulse amplitude increases.

tion signals [116], and control of recollision processes in molecular ions [117, 118]. The nearly arbitrary pulse-shape control available in the cold-atom quantum simulator makes it a flexible tool for probing the dependence of ultrafast-equivalent dynamics on CEP. Fig. 7.6a shows a measurement of post-pulse momentum distribution (again detected via time of flight) as a function of the carrier-envelope phase of a near-resonant applied pulse. Changing the CEP from 0 to π flips the sign of all forces during the pulse, and results in inversion of the momentum of the unbound atoms. As shown in Fig. 7.6b-d, the pulses at integer values of ϕ/π have sine-like character, possessing odd symmetry under reflection in time around the pulse centre. Pulses with a CEP of $3\pi/2$ have cosine-like character and give rise to very different unbinding dynamics at this pulse amplitude, populating more

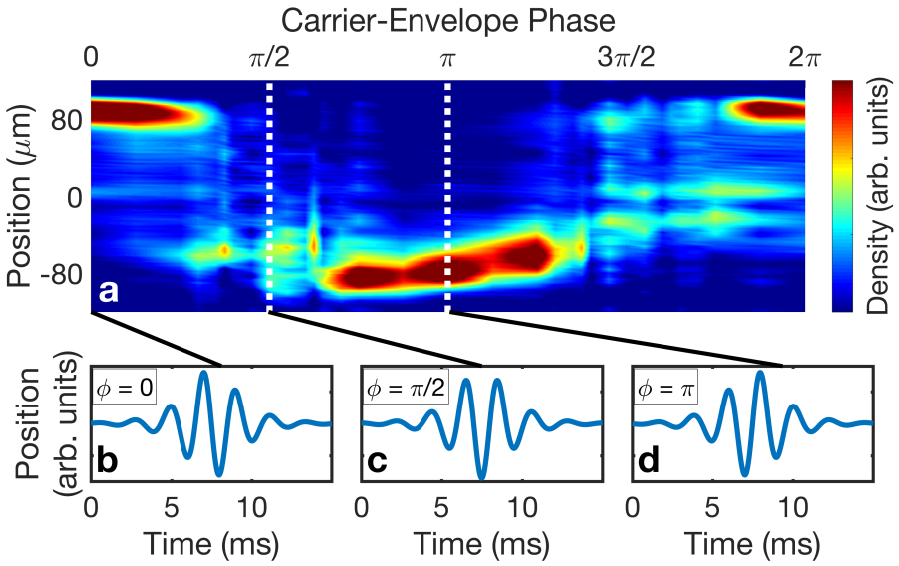

Figure 7.6: **Carrier-envelope phase dependence of final momentum. a:** Integrated spatial density distribution after application of a near-resonant 450 Hz pulse with $\tau = 3.76$ ms and $A = 2.4$ μm followed by 3 ms of time-of-flight, versus CEP. **b-d:** Pulse waveforms (force versus time) for CEP values indicated in the inset.

than one momentum class of unbound atoms. More complex dynamical phenomena are also visible in Fig. 7.6: the inward slope of the unbound momentum as CEP increases in the neighborhood of $\phi = \pi$ can be understood as the consequence of the force at the first unbinding peak sliding down the pulse envelope, and the observed asymmetry between $\phi = \pi/2$ and $\phi = 3\pi/2$ indicates a violation of inversion symmetry in the potential. The most likely cause of this symmetry-breaking is slight trap aberration; this points the way to future work elucidating the effects of potential shape on unbinding dynamics.

7.4 Discussion

The results presented here open the door to a broad class of quantum simulation experiments investigating ultrafast nonequilibrium phenomena, with numerous possible scientific targets. Emulation of pump-probe experiments, multichromatic light fields, and non-physical (for example, half-cycle) pulse shapes impossible to create with lasers would

require no techniques beyond those demonstrated here apart from changing the form of $\alpha(t)$.

Additional possibilities require only modest extensions of the experimental approach reported here. The simplest such extension would be to replace the inertial forces used to emulate electric fields with time-varying Zeeman or Stark potential gradients. This would allow ultrafast quantum simulation in the regime of Keldysh parameter γ_{K} less than one, and enable the direct experimental investigation of open questions of current interest in ultrafast science. Potential scientific targets include the creation of photoelectron vortices with circularly-polarized pulses [119], the demonstration and study of strong-field stabilization, wherein the ionization probability becomes a decreasing function of pulse amplitude [120], and detailed quantitative measurement of sub-cycle tunnel ionization timing effects [121, 122, 123, 124].

Other extensions to the basic technique are also possible. The use of traps with multiple minima could enable modelling of more complex molecular configurations [23]. Ultrafast quantum simulation could also be pursued with small numbers of trapped fermions [125], making a more direct analogue of atomic electrons. However, the use of Bose condensates and the analogy of Eq. 7.1 does greatly magnify the signal, making experiments feasible with bosons that would be very challenging with fermions. Finally, an expansion of the analogy underlying these quantum simulation experiments beyond atoms and molecules could enable the study of ultrafast-equivalent dynamical phenomena relevant to nuclear excitations [126] and strong-field dynamics in solids [22].

In summary, we present experimental results from a cold-atom quantum simulator of ultrafast phenomena, including nonlinear spectroscopy of collective excitations, control of the energy spectra of the bound states of the simulator, imaging of sub-cycle dynamics during an unbinding process similar to ultrafast ionization, and measurement of the effects on unbinding dynamics of pulse amplitude and carrier-envelope phase. Such cold

atom quantum simulation of ultrafast dynamical phenomena has the potential to enable benchmarking of relevant theories and explorations of experimentally challenging regimes, in an approach complementary to both ultrafast theory and pulsed-laser experiments.

7.5 Methods

7.5.1 Preparation of a Bose-Einstein condensate in an optical trap

During the computer-controlled experimental sequence [74], atoms from an effusive source are collimated by a nozzle [31], Zeeman-slowed, trapped and pre-cooled by sequential magneto-optical traps using the 461 nm and 689 nm ground-state transitions, and evaporatively cooled to degeneracy in a crossed-beam 1064 nm optical dipole trap (ODT) [105]. In the emulation stage of the experiment, the resulting condensate of 2×10^4 ^{84}Sr atoms is adiabatically loaded into a single-beam ODT with a waist of 15 μm. The trap depth can be varied across a wide range; a typical value used in the work presented here is 10 μK. The s-wave scattering length of ^{84}Sr is 6.5 nm.

7.5.2 Temporal magnification of the quantum simulator

Varying the power and shape of the trap beam yields transverse trap frequencies ν_x and ν_z between 300 and 1000 Hz, and an axial trap frequency ν_y between 5 and 15 Hz. Drawing the analogy between the optical trap and a single hydrogen atom, the energy difference $h\nu_x$ between the ground and first relevant excited states (typically $\simeq$500 Hz) is analogous to the 2.47 PHz Ly-α line. Although the detailed energy spectrum of the ODT differs from that of hydrogen due to the different potential shapes, comparison of these two frequency scales indicates an approximate temporal magnification factor of 5×10^{12}.

Emulation of molecular vibrational excitations or cluster dynamics leads to a ratio of up to 10^{11} between characteristic timescales of the emulator and emulated system.

7.5.3 Application of time-varying inertial forces

An acousto-optic modulator (AOM) can translate the trap centre in the x-direction (see Fig. 7.1b for axis definitions) at amplitudes up to 6 μm and frequencies from DC up to hundreds of kHz. Because of the direction of translation and the wide separation between transverse and axial frequency scales, the axial degree of freedom is irrelevant to the results we present. Under the assumption that the atoms remain near the centre of the trap during the pulse, which we observe to be true until unbinding, the effective applied force is $m\ddot{x} = F(t) = -dV(x,t)/dx|_{x=0}$. $\ddot{x}$ can be specified as desired; for the particular functional form chosen, $\ddot{x}(t)$ has a similar enveloped-pulse shape to $x(t)$.

7.5.4 Tuning the trap geometry

Shaping of the trap is achieved most simply by periodic translation on much faster time scales than the dynamics of the BEC, so that the atoms experience a time-averaged potential. For this purpose, the trap AOM's RF drive frequency was sinusoidally modulated at 500 kHz, giving rise to a maximum trap translation amplitude of 4.2±0.3 μm.

Chapter 8

Further work with Sr

8.1 Quasiperiodic lattices

Quasicrystals are solids that have discrete diffraction peaks but no translational symmetry. They were first discovered in 1982, and this discovery was subsequently awarded the Nobel Prize in Chemistry in 2011 [127]. Such a quasiperiodic lattice may be thought of as a projection of a periodic lattice in a higher dimension into a lower dimension along some vector that is not a crystal vector of the periodic lattice. Quasicrystals exhibit order on all length scales, and therefore have fractal energy spectra. Due to the lack of either periodicity or true disorder, the nature of the localization of the wavefunctions, excitations and conductivity of quasicrystals are incompletely understood theoretically.

Ultracold atom systems, which have been highly successful in the quantum simulation of periodic and disordered condensed matter systems, are well-suited for the study of quasiperiodic systems. A quasiperiodic lattice may be arranged in a few ways. Geometrically enforcing rotational symmetry that violates the crystallographic restriction theorem (i.e. 5-fold or 7-fold or higher rotational symmetries) can produce a 2d quasiperiodic lattice [128]. Our group has also proposed to implement a 1d quasiperiodic lattice

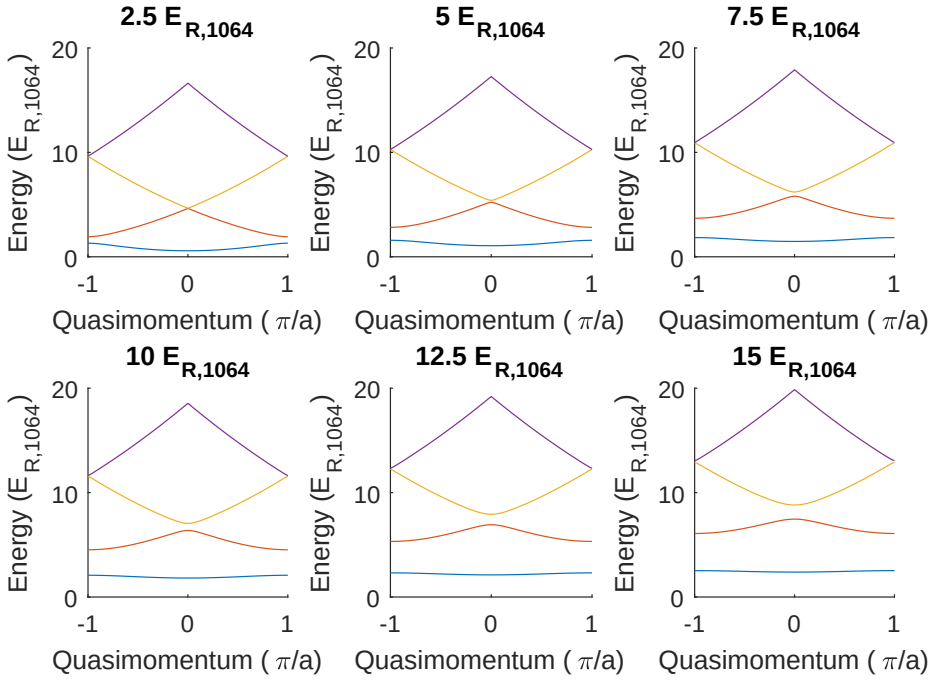

Figure 8.1: First four bands of a retro-reflected 1064 nm lattice for six different lattice depths.

via a suitable projection of a 2d square lattice [129]. Lastly, it is possible to engineer a quasiperiodic lattice by simply spatially overlapping two 1d lattices with different periodicities[1]. If the ratio of the periodicities of the two lattices is irrational, a quasiperiodic lattice is produced. For sufficiently small system-sizes, it is possible to ensure that the periodicity is larger than the system size for non-irrational ratios. The effect of such a non-irrational ratio is to reduce the size of the Brillouin zone from the case of the monochromatic case. The Bloch bands are folded in quasi-momentum space to accomodate this reduction. Figures 8.1 and 8.2 show the band structures of monochromatic 1064 nm retro-reflected lattices and bichromatic 1064 nm and 912 nm retro-reflected lattices (a periodicity ratio of $7:6$).

Such systems have been successfully used as a proxy for disorder in cold atom quantum

[1]This is known as a bichromatic lattice

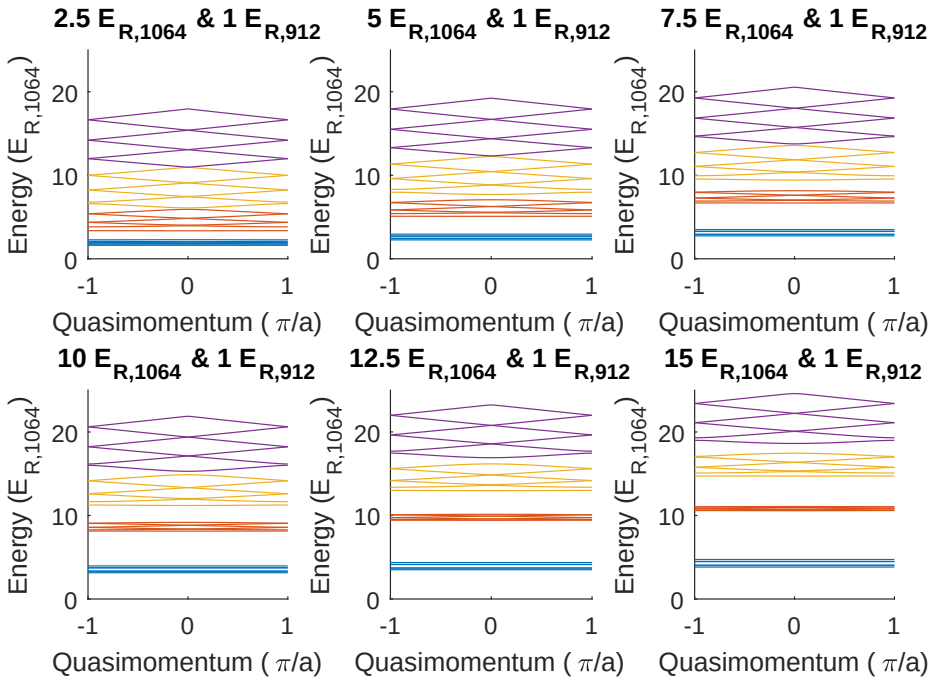

Figure 8.2: Band structure of 1d bichromatic lattices consisting of a strong 1064 nm retro-reflected lattice and a 1 $E_{\mathrm{R},912}$ 912 nm retro-reflected lattice. The size of the Brillouin zone is reduced by a factor of six from that in Figure 8.1, and therefore each band is folded over 6 times.

simulation experiments [12, 17]. A bichromatic lattice for which one of the lattices is weak realizes the 1d Aubry-André Hamiltonian[2], which is

$$H = J\sum_{i=1}^{N} c_i c_{i+1}^{\dagger} + \text{h.c.} + \sum_{i=1}^{N} \Delta\cos(2\pi\alpha i + \phi) c_i^{\dagger} c_i, \tag{8.1}$$

where c_i and $c_i^{\dagger}$ are annihilation and creation operators at site i of a 1d lattice with N sites, and J is the tunneling energy between neighboring sites. The parameter α is the periodicity ratio between the two lattices that form the bichromatic lattice, Δ is strength of the modulation in lattice-site depth due to the weak lattice beam, and ϕ defines a relative phase between the two lattices.

[2]A similar Hamiltonian is known as the Harper Hamiltonian.

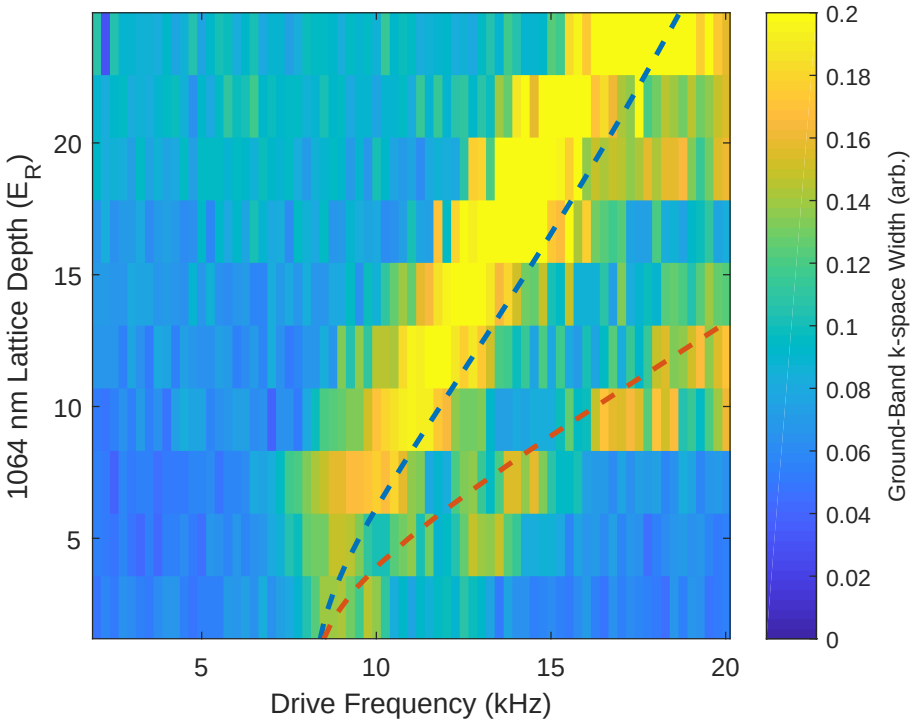

Figure 8.3: Excitation spectrum for phononic driving of a bichromatic lattice with variable 1064 nm lattice depth, and a 915 nm lattice with depth equal to 1 $E_{\mathrm{R},915}$. Plotted in red is the calculated transition frequency for zero-quasi-momentum states from the first band to the third band of the 1064 nm lattice band structure. Plotted in blue is the calculated transition frequency for zero-quasi-momentum states from the first band to the second band of the 1064 nm lattice band structure.

8.1.1 Phasonic spectroscopy

Our current experiments using quasiperiodic lattices focus on the ϕ parameter. This corresponds to a phasonic degree of freedom which exists in quasicrystals and represents long-range rearrangments of the lattice, but does not exist in crystals. The phasonic degree of freedom is believed to have significant impact on the transport properties of quasicrystals, but is difficult to study in solid-state experiments. We have performed experiments where we have periodically driven this phase parameter, which we dubbed "phasonic" driving. This was accomplished by producing a bichromatic lattice consisting of a strong 1064 nm lattice and a weak 915 nm lattice, which gives an approximate period

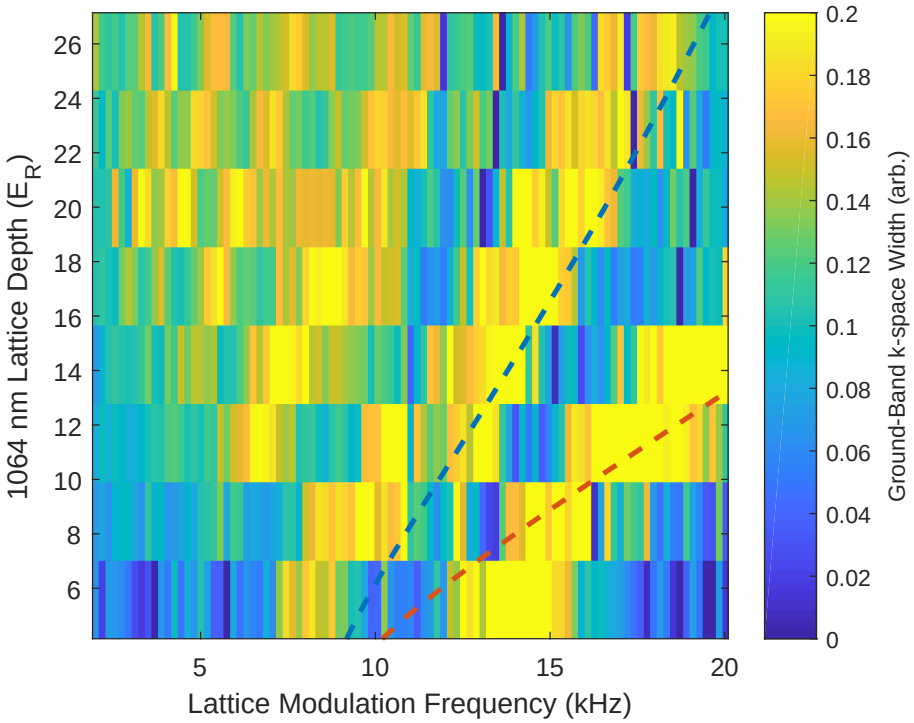

Figure 8.4: Excitation spectrum for phasonic driving of a bichromatic lattice with variable 1064 nm lattice depth, and a 915 nm lattice with depth 2 $E_{\mathrm{R},915}$. Plotted in red is the calculated transition frequency for zero-quasi-momentum states from the first band to the third band of the 1064 nm lattice band structure. Plotted in blue is the calculated transition frequency for zero-quasi-momentum states from the first band to the second band of the 1064 nm lattice band structure.

ratio of 43/50[3], and modulating the position of the retro-mirror used to produce the 915 nm lattice. We have also performed experiments where we have periodically modulated the phase of both lattices (with a fixed relative phase), by using the same retro-mirror for both lattice beams. We dubbed this type of modulation "phononic" driving.

The mirror is epoxied to a piezoelectric transducer (PZT), which itself is epoxied to a home-built Cu slug that was filled with lead. The mirror and PZT have the same shape (square), and are light. This design allowed us to push the resonance frequency of the mirror-PZT assembly to be above 40 kHz. The PZT was chosen to have a low

[3]The size of our initial condensate is roughly 20 μm and therefore is smaller than effective period of the bichromatic lattice

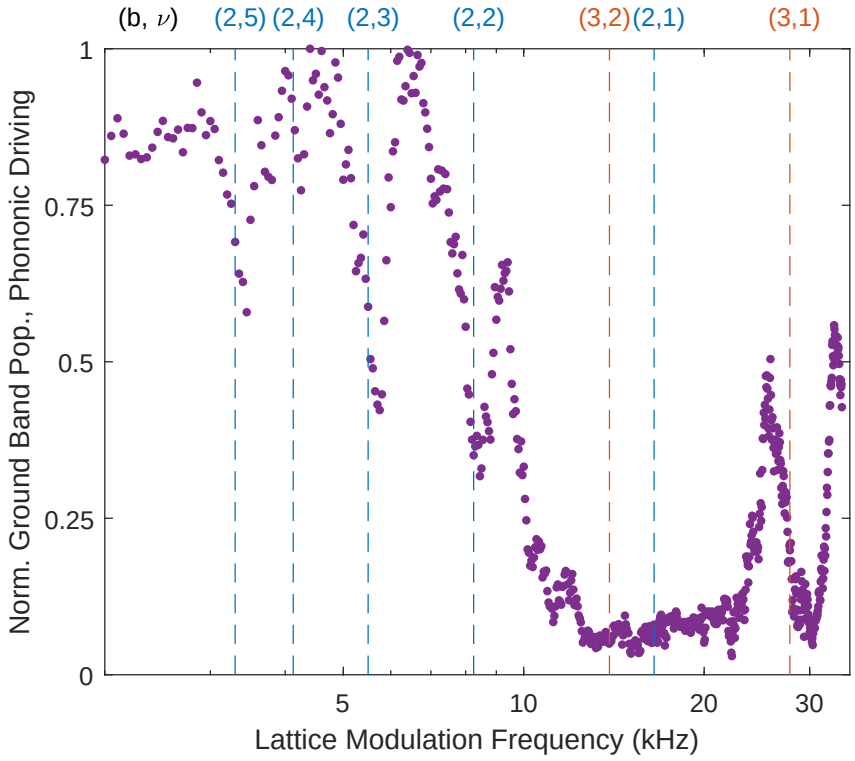

Figure 8.5: Excitation spectrum for phononic driving of a bichromatic lattice with a 1064 nm lattice depth of 20 $E_{\mathrm{R},1064}$, and a 915 nm lattice with depth 1 $E_{\mathrm{R},915}$. Pulse amplitude (in terms of the PZT displacement) was scaled inversely with frequency according to $\frac{2.5}{f} \times \frac{915\,\mathrm{nm}}{2}$, where f is the driving frequency in kHz. Vertical dashed lines are theoretically expected frequencies for zero-quasi-momentum transitions from the ground band to the second and third bands of the 1064 nm lattice band structure, and are labeled (b, ν), where b labels which excited band is involved in the transition and ν labels the number of drive photons that are absorbed during the excitation.

capacitance, and we can drive it with a sinusoidal voltage produced by an AA Labs PZT driver without too much loss in fidelity up to 30 kHz for small drive amplitudes.

Figures 8.3 and 8.4 show preliminary results from experiments where we modulated the phononic and phasonic degrees of freedom of the lattice respectively. In each case, we applied a driving pulse[4] for 10 ms to the bichromatic lattice at varying frequencies as well as 1064 nm lattice depths. The pulse amplitudes were chosen in a non-systematic way in order to resolve the excitations. In order to measure the excitation strength, we

[4]The waveform of the pulse was chosen to gently ramp the modulation on and off.

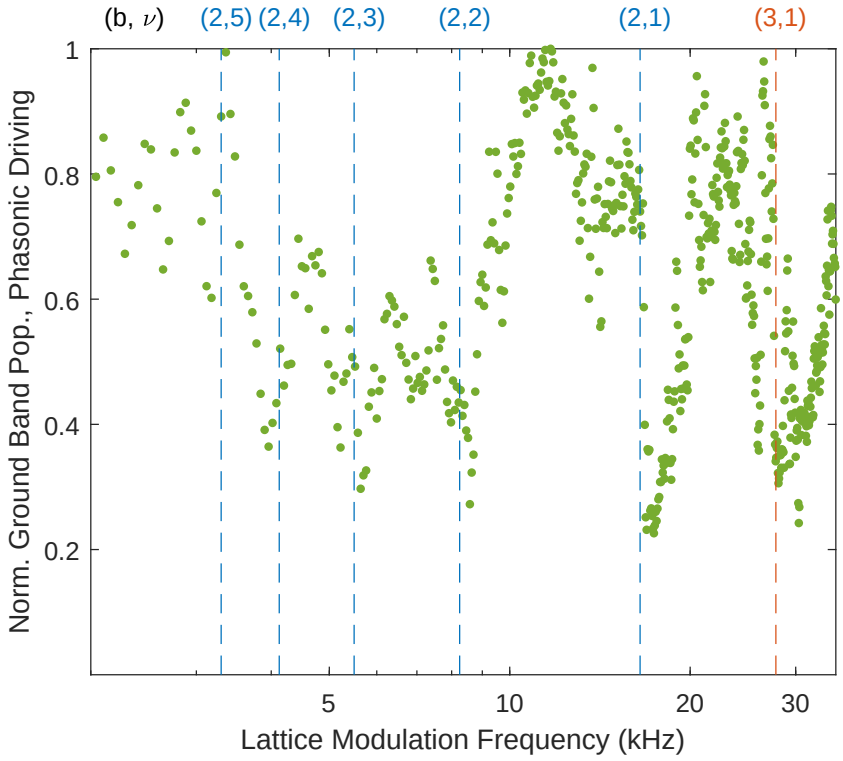

Figure 8.6: Excitation spectrum for phononic driving of a bichromatic lattice with a 1064 nm lattice depth of 20 $E_{\mathrm{R},1064}$, and a 915 nm lattice with depth 1 $E_{\mathrm{R},915}$. Pulse amplitude (in terms of the PZT displacement) was scaled inversely with frequency according to $\frac{3.5}{f} \times \frac{915\,\mathrm{nm}}{2}$, where f is the driving frequency in kHz. Vertical dashed lines are theoretically expected frequencies for zero-quasi-momentum transitions from the ground band to the second and third bands of the 1064 nm lattice band structure, and are labeled (b, ν), where b labels which excited band is involved in the transition and ν labels the number of drive photons that are absorbed during the excitation.

band-mapped[5] the atoms over a few 100 μs and measured the width of the ground band atom cloud. Our results suggest that phasonic driving excites the ground-to-third-band transition more strongly than phononic driving. This is understandable as phasonic driving does not have defined parity, unlike phononic driving, which has odd parity. In addition to this result, we have observed that phasonic driving excites harmonics of both the ground-to-second-band and ground-to-third-band transitions more strongly

[5]Band-mapping involves adiabatically lowering the lattice depth to map quasi-momentum onto momentum. This effectively unfolds the first Brillouin zone onto the free-particle dispersion relation. Subsequent time-of-flight expansion maps momentum onto position, and the atom occupation of each band of the lattice may be directly imaged [130].

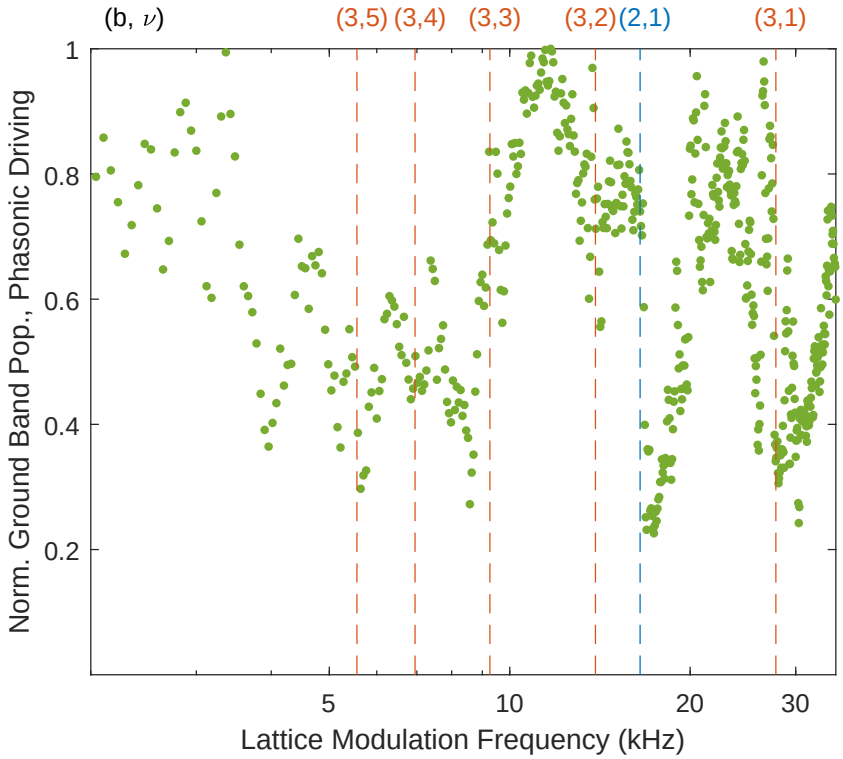

Figure 8.7: Excitation spectrum for phononic driving of a bichromatic lattice with a 1064 nm lattice depth of 20 1064 nm photon recoil energies, and a 915 nm lattice with depth 1 $E_{\mathrm{R},915}$. Pulse amplitude (in terms of the PZT displacement) was scaled inversely with frequency according to $\frac{3.5}{f} \times \frac{915\,\mathrm{nm}}{2}$, where f is the driving frequency in kHz. Vertical dashed lines are theoretically expected frequencies for zero-quasi–momentum transitions from the ground band to the second and third bands of the 1064 nm lattice band structure, and are labeled (b, ν), where b labels which excited band is involved in the transition and ν labels the number of drive photons that are absorbed during the excitation.

than phononic driving. This is also understandable, as phasonic driving is not a dipole excitation, and should contain higher mulitpole components than phononic driving.

Finer scans as a function of frequency at a 1064 nm lattice depth of 20 $E_{\mathrm{R},1064}$ support these findings. Figure 8.5 shows ground band atom number in after a 100 ms phononic pulse for a bichromatic lattice consisting of a 20 $E_{\mathrm{R},1064}$ 1064 nm lattice and a 1 $E_{\mathrm{R},915}$ 915 nm lattice. The amplitude of the pulse was scaled inversely with frequency and chosen to be sufficiently large to excite harmonics of the ground-to-second

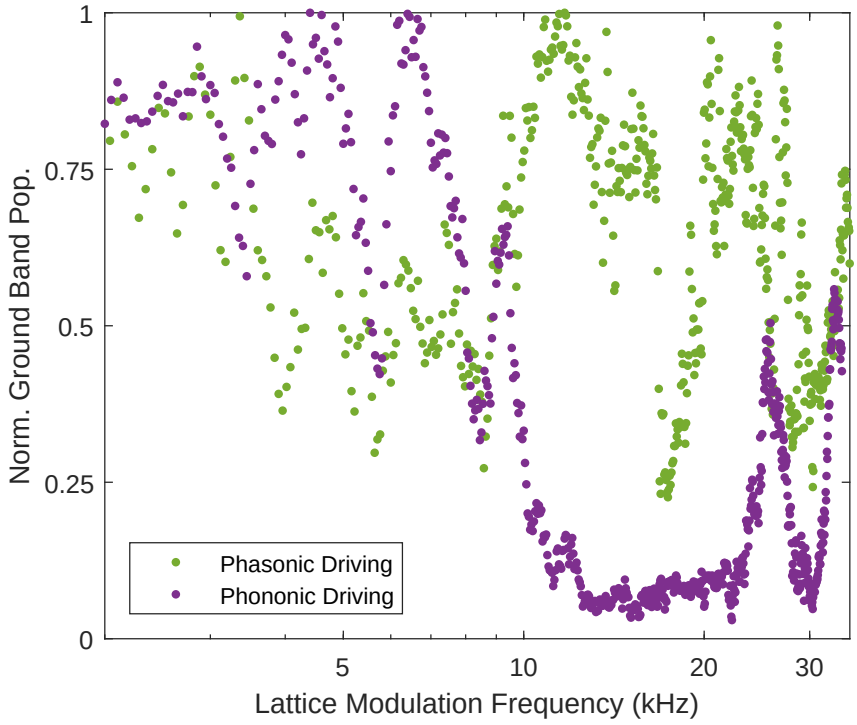

Figure 8.8: Overlaid data from Figures 8.5 and 8.6.

band transition. At these amplitudes the fundamental ground-to-second band transition is completely saturated and is power-broadened. The width of the fundamental ground-to-third band transition is substantially narrower, indicating that the excitation strength of the ground-to-second band is higher than that of the ground-to-third band. Figures 8.6 and 8.7 show data from an experiment with similar conditions for phasonic driving. In this case, harmonics of both the ground-to-second band and ground-to-third band transitions are observed, and appear to have excitation strengths closer to those of their respective fundamental transitions than in the case of phononic driving. Figure 8.8 shows the two sets of data overlaid on the same axes to clearly demonstrate the differences between the relative excitation strengths of the ground-to-second and ground-to-third band transitions, and between the relative excitation strengths of the fundamental transitions and their harmonics for phononic versus phasonic driving.

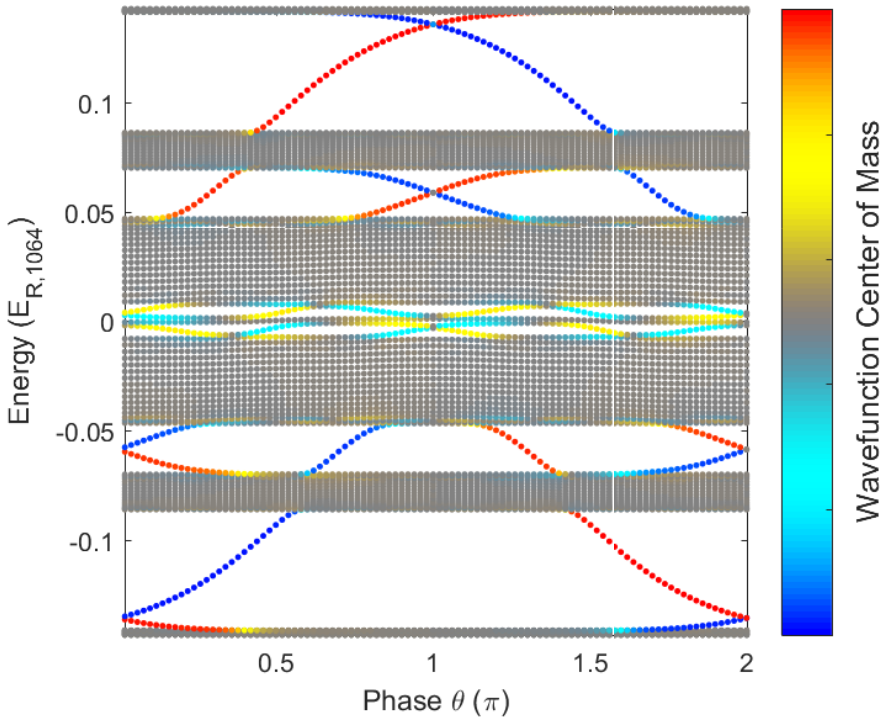

Figure 8.9: Energies of eigenstates of of the tight-binding Hamiltonian for a 106 site bichromatic lattice consisting a strong 1064 nm retro-reflected lattice and a weak 915 nm retro-reflected lattice with hard walls for $\Delta/J = 1$. Here the depth of the strong lattice was chosen to be 5 $E_{\mathrm{R},1064}$, which sets the 915 nm lattice depth to be very small (given by the span of eigenenergies). The colorbar indicates the center-of-mass of each eigenstate in position space, with red and blue indicating opposite edges of the system.

Further work will investigate the relative strengths of the harmonic excitations, particularly as a function of the periodicity ratio, which can be adjusted by adjusting the wavelength of the 915 nm ECDL. We are also interested in studying the effects of driving on the Aubry-André localization transition. Furthermore, for a finite-sized system the Aubry-André Hamiltonian supports edge states. These edge states can be adiabatically pumped from one edge of the lattice to the other by a ramp of the relative phase of the two lattices. By applying hard walls on the lattice with blue-detuned beams, we hope to observe these edge states and pump them across the lattice by ramping the phase of the

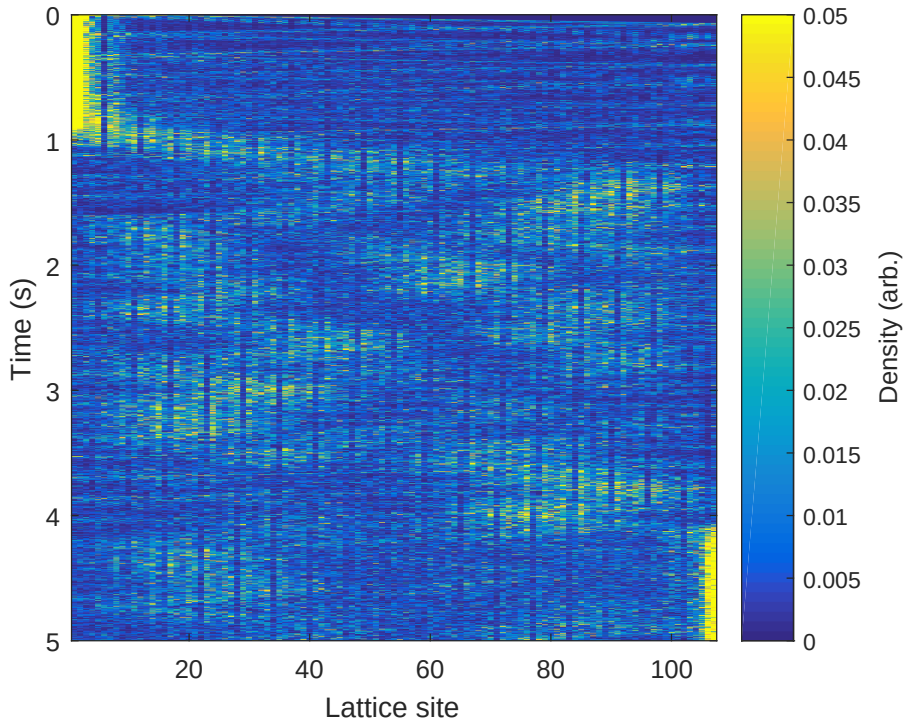

Figure 8.10: A simulation of an adiabatic pumping experiment for an edge-state in a 106 site bichromatic lattice consisting a strong 1064 nm retro-reflected lattice and a weak 915 nm retro-reflected lattice with hard walls for $\Delta/J = 1$. Here the depth of the strong lattice was chosen to be 5 $E_{\mathrm{R},1064}$. The phase parameter ϕ is ramped linearly between $\pi/2$ and $3\pi/2$ between 0.675 and 4.325 s, during which the initially-loaded edge-state is adiabatically pumped to the other edge of the lattice.

weak lattice.

8.1.2 Edge-state pumping

For finite-sized systems with hard walls, the Aubry-André Hamiltonian has solutions that are localized on the edges of the sample. Figure 8.9 shows the energies of eigenstates of the tight-binding Hamiltonian for a 106 site bichromatic lattice consisting a strong 1064 nm retro-reflected lattice and a weak 915 nm retro-reflected lattice with hard walls for $\Delta/J = 1$. The edge-states are indicated by having non-zero center-of-mass in position space, and traverse the "band-gaps" in the energy spectrum as the phase ϕ is varied.

These edge-states are robust to some degree of "softening" of the hard-wall boundary condition. If an edge-state is populated and the phase is adiabatically ramped, one can initate mass-transfer across the system by "pumping" the atoms from one edge to the other. Such edge-state pumping has been observed in photonic crystals [131][6]. In principle it should be possible to observe this phenomenon with cold atoms. Figure 8.10 shows the results of a simulation[7] of an adiabatic pumping experiment for the energy spectrum shown in Figure 8.9. The edge-state with energy $\sim -0.1E_{\mathrm{R},1064}$ for $\phi = \pi/2$[8] is loaded by projecting a tight Gaussian packet of atoms onto eigenstates of the bichromatic lattice Hamiltonian at time zero. The phase is held constant for the first 625 ms, and then linearly ramped over 3.75 s to $3\pi/2$, after which it is held constant for 625 ms. This procedure pumps the edge-state from one side of the lattice to the other. Longer pump times result in more efficient mass transfer, but are difficult to implement experimentally.

8.1.3 Aubry-André localization

For an irrational α the Aubry-André Hamiltonian exhibits a transition at $\Delta/J = 2$ between eigenstates that are delocalized in position space (at low disorder strength) and eigenstates that are localized to a lattice site (at high disorder strength). Figure 8.11 shows the tight-binding energy spectrum for the same Hamiltonian as in Figure 8.9, except that $\Delta/J = 2$. The centers-of-mass of the energy eigenstates are now non-zero for many of the non-edge states, indicating localization. For non-irrational α, the value of Δ/J at which the transition occurs increases [12].

Figure 8.12 shows relevant contours of Δ as a function of J for ^{84}Sr atoms in the ground-band of a strong 1064 nm retro-reflected lattice spatially-modulated by a weak

[6] A quantized bulk mass-pumping effect in a bichromatic lattice known as Thouless pumping has been observed using cold atoms [132].

[7] This simulation consisted of decomposing the time evolution into small steps and exactly diagonalizing the resulting Hamiltonian at each step.

[8] This is the blue edge-state between the first and second "bands" in Figure 8.9.

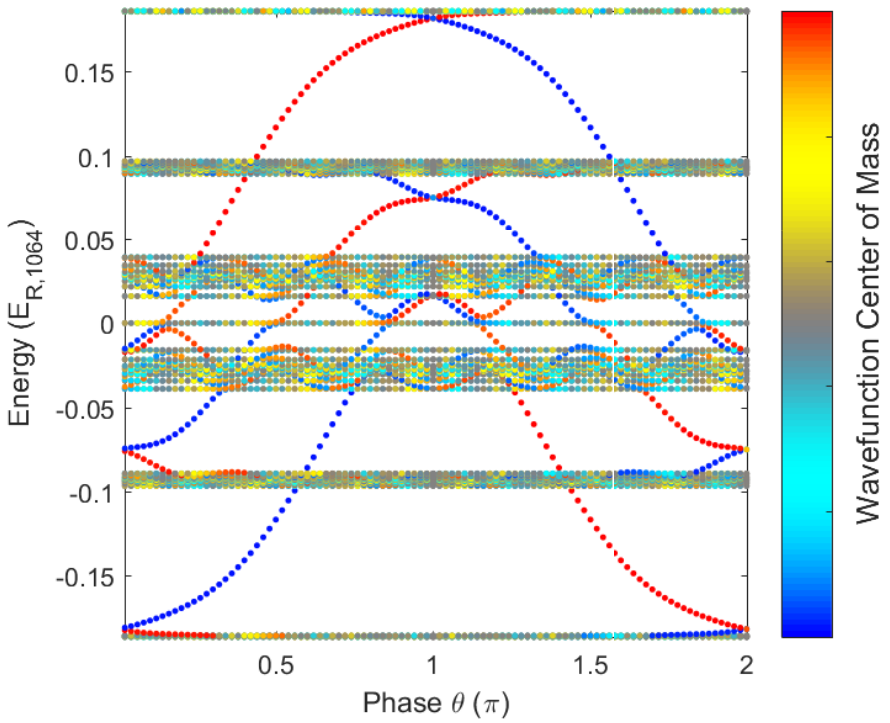

Figure 8.11: Energies of eigenstates of of the tight-binding Hamiltonian for a 106 site bichromatic lattice consisting a strong 1064 nm retro-reflected lattice and a weak 915 nm retro-reflected lattice with hard walls for $\Delta/J = 2$. Here the depth of the strong lattice was chosen to be 5 $E_{\mathrm{R},1064}$. The colorbar indicates the center-of-mass of each eigenstate in position space, with red and blue indicating opposite edges of the system. A significant proportion of the non-edge states have non-zero centers-of-mass, indicating the onset of localization.

915 nm retro-reflected lattice. Figure 8.13 shows the same for the first excited band of the strong 1064 nm lattice. The observation of the localization transiton in the excited band would allow for investigation of the excitation spectrum of the Hamiltonian in three distinct regimes: between delocalized bands, between localized bands, and between the localized ground band and the delocalized excited band.

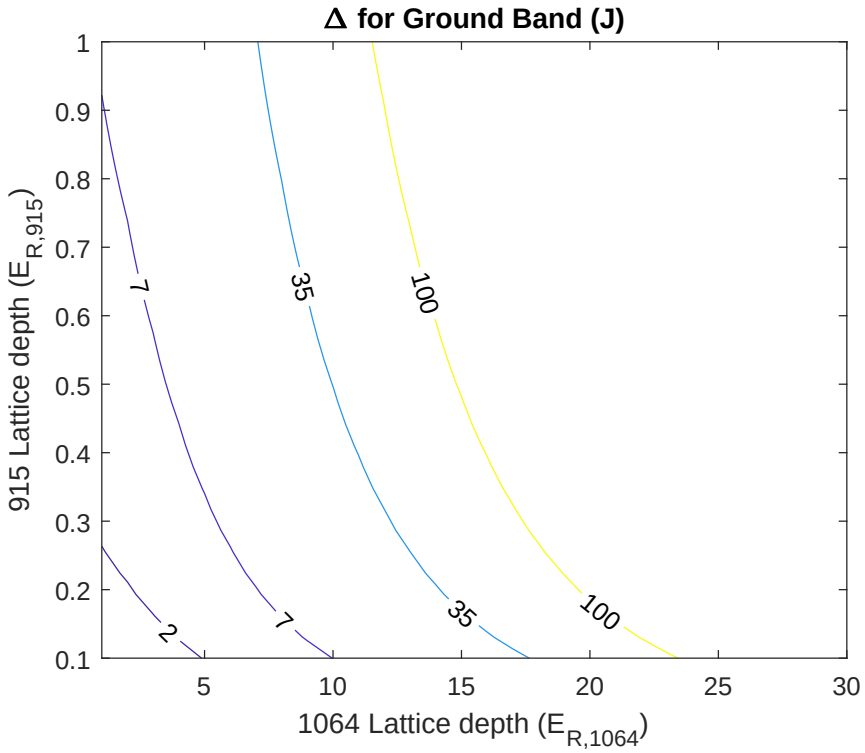

Figure 8.12: Contours of disorder strength Δ in units of J for an Aubry-André system of ^{84}Sr atoms produced by a strong 1064 nm retro-reflected lattice and a weak 915 nm retro-reflected lattice. For non-interacting atoms and an irrational periodicity ratio, the Aubry-André localization transition ocurs at $\Delta/J = 2$. We observed the onset of localization at approximately $\Delta/J = 35$ for these lattice conditions with ^{84}Sr atoms which have an s-wave scattering length of 123 a_0. The Inguscio group observed the localization transition to occur at $\Delta/J = 7$ for non-interacting atoms in a strong 1032 nm retro-reflected lattice and a weak 832 nm retro-reflected lattice [12].

8.2 Quantum gas microscope

We have designed an additional science chamber to be connected to the main chamber through the all-metal VAT gate valve. This chamber is designed to add the capability of high-resolution imaging and single-lattice-site resolution to the experiment [133, 134]. A computer-aided-design (CAD) depiction of this chamber and its associated pumping manifold is shown in Figure 8.14. The chamber design is a 6" Kimball spherical octagon, with 8 2.75" conflat ports and no 1.33" conflat ports. Additionally a similar pumping

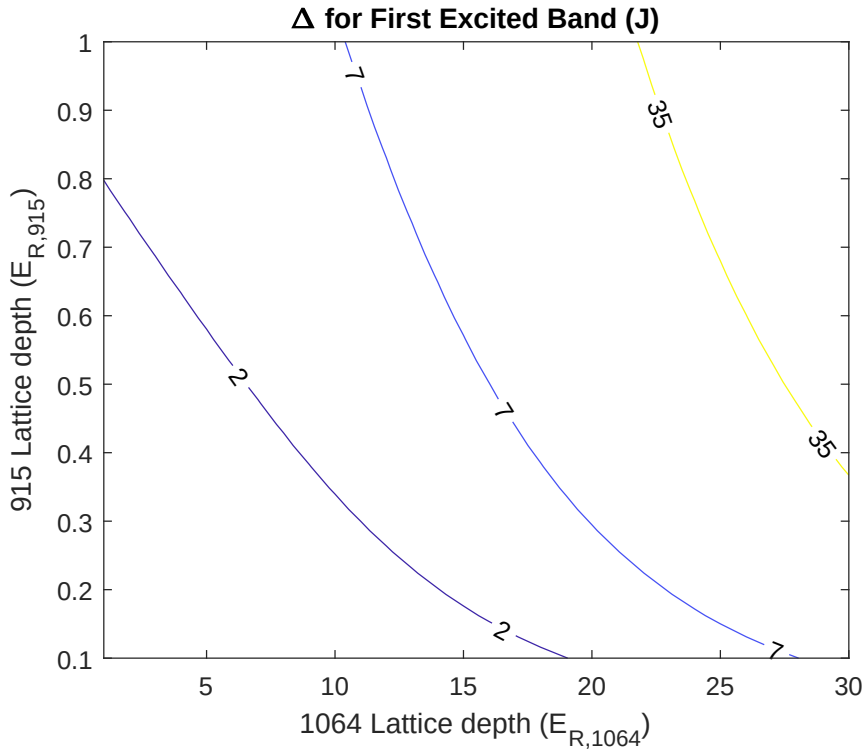

Figure 8.13: Contours of disorder strength Δ in units of J for an Aubry-André system of ^{84}Sr atoms in the first excited band of a strong 1064 nm retro-reflected lattice which is spatially modulated by a weak 915 nm retro-reflected lattice. For non-interacting atoms and an irrational periodicity ratio, the Aubry-André localization transition ocurs at $\Delta/J = 2$.

manifold to that used in the current apparatus was designed and fabricated. We plan to install a re-entrant window on the top 6" flange to bring a glass surface close to the atoms. This will allow the objective lens of the microscope to have a short working distance. Since Sr has a non-magnetic ground-state, transport will have to be optical. One of our current strategies to achieve this transport is to have a phase-ramped optical lattice. The optical lattice will be formed by counter-propagating infra-red beams that will have a grazing-angle reflection off of the re-entrant window. This reflection will ensure that the atoms load into a lattice site that is a well-defined distance from the re-entrant-window glass surface. A long-period vertical lattice will be created with angled beams, which will allow us to address individual layers of the 3d lattice. The lattices will be made from

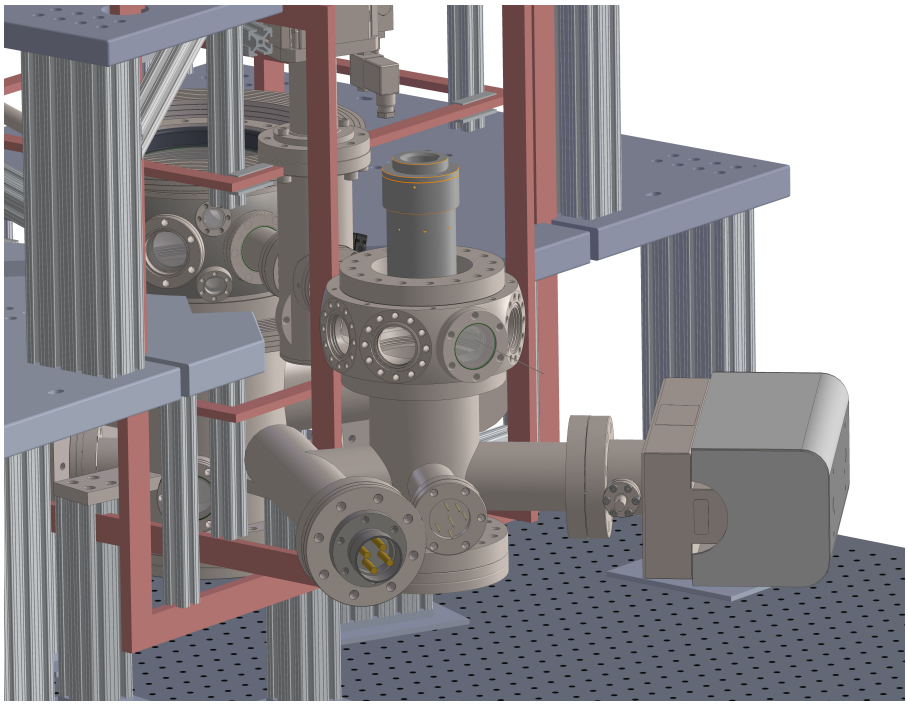

Figure 8.14: CAD depiction of the current design for the Sr QGM. The chamber is connected to the Sr main chamber via the VAT gate valve. A top re-entrant window allows access for the large, high-NA Special Optics objective. The Ti-sub and the ion pump are visible and attached to the lower pumping manifold.

915 nm light, which is a magic wavelength for the $^1S_0 \rightarrow {}^3P_1$ transition. An alternative magic wavelength for this transition is predicted to be near 513 nm, where more laser power is available. Imaging and cooling will occur simultaneously, potentially on the 461 nm and 689 nm transitions respectively. The 5-element objective is designed to work at each of these wavelengths, have an NA of ~ 0.8, and a working distance of 1 mm of air, 5 mm of glass and 4 mm of vacuum. It was custom-built by Special Optics.

8.3 Kitaev Chain

A goal of the Sr experiment is to simulate the Kitaev chain Hamiltonian, in order to produce Majorana fermions [135]. The Hamiltonian is given by

$$H_{\text{Kitaev}} = \sum_i \Big[- J(a_i^\dagger a_{i+1} + a_{i+1}^\dagger a_i) - \mu(a_i^\dagger a_i - \frac{1}{2}) + \Delta a_i a_{i+1} + \Delta^* a_i^\dagger a_{i+1}^\dagger \Big]. \qquad (8.2)$$

The unusual feature in the Hamiltonian is a pair-wise creation (and a pair-wise annihilation) term for neighboring lattice sites along the 1d chain. We plan to accomplish this by having two 1D chains that are formed by diagonal chains on a square 2d lattice. One of these chains will be the primary chain, and the other will the reservoir chain. By controlling the phase of the four lattice beams independently, it should be possible to engineer the relative lattice depths between the primary and reservoir chain such that tunneling for bosons between the primary and reservoir chain and vice versa is only possible in a pairwise fashion due to the conservation of energy. For fermions the picture is more challenging, and perhaps some Floquet band-hybridization will be required to engineer the required band-structure.

Appendix A

Effusive atomic oven nozzle design using an aligned microcapillary array

As discussed in Sections 5.3 and 6.3, we designed and constructed an oven nozzle consisting of a hexagonally packed array of microcapillaries. This design ensured that the microcapillaries in the nozzle were co-parallel. We wrote and published a paper in *Review of Scientific Instruments* on this design and its construction and evaluation.

A.1 Abstract

We present a simple and inexpensive design for a multichannel effusive oven nozzle which provides improved atomic beam collimation and thus extended oven lifetimes. Using this design we demonstrate an atomic lithium source suitable for trapped-atom experiments. At a nozzle temperature of 525°C the total atomic beam flux directly after the nozzle is 1.2×10^{14} atoms per second with a peak beam intensity greater than

5.0×10^{16} atoms per second per steradian. This suggests an oven lifetime of several decades of continuous operation.

A.2 Introduction

Effusive sources have been a common feature of molecular and atomic beam experiments for decades [136]. Such sources are useful in trapped-atom experiments on low-vapor-pressure species such as lithium, in which the background vapor pressure is inadequate to trap large numbers of atoms. The capture efficiency of an atomic beam — the percentage of trappable atoms which enter the trapping region — is determined in part by the solid angle subtended by the beam. For traditional single-orifice nozzles, this solid angle can be as large as 2π sr, leading to a small capture efficiency. Such nozzle designs necessitate frequent oven changes in order to replenish the supply of atoms, leading to a disruptive periodic breaking of vacuum.

A popular approach to designing high-capture-efficiency atomic and molecular beams is to use nozzles composed of multiple tubes. If the mean free path is greater than the tube length, the angular spread of the beam is set by the tubes' aspect ratio [137]. Most particles that collide with the tube walls exit the tube on the same end that they entered (see Figure A.1). In practice, as discussed in Ref. [137], such nozzles are often operated in an intermediate regime in which the mean free path is less than the tube length but greater than the tube diameter. Operation at very small mean free paths can cause increased angular divergence and depletion of low-velocity atoms. In order to minimize the effects of inter-atomic scattering while maintaining minimal angular spread and high beam intensity, several groups have implemented nozzles consisting of numerous microchannels with diameters ranging from a few microns to a few hundred microns.

Multichannel nozzles were pioneered by Zacharias, who used alternate stacked layers

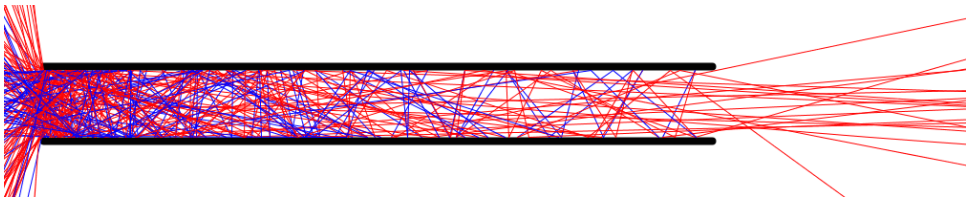

Figure A.1: Simulation of particle trajectories through a 2d tube. In this simple simulation, the particles enter on the left-hand side at uniformly distributed random angles, and assume a random angle upon each collision with a wall. Rightward-moving paths are colored red and leftward-moving paths are colored blue. Those particles that do not pass all the way through the tube without striking the walls have a higher probability of exiting the tube on the left rather than the right, because they are likely to strike the walls before reaching the midpoint of the tube. Thus the exit beam is collimated, and most particles that would not enter the trapping region are recirculated to the oven reservoir. In this figure the tube aspect ratio has been reduced from 50 to 10 for clarity.

of smooth and corrugated nickel foil to create a matrix of channels [138]. This technique was also used to form an intense beam of ammonia molecules in the construction of the first maser[139]. A non-exhaustive list of subsequent multichannel designs includes klystron grids, electrolytically etched plastic, photographically etched metal foil and short sections of hypodermic tubing compressed into an aperture [137, 140, 141, 142, 143]. An alternate approach to the realization of long-lived effusive ovens is to use a recirculating design. Recirculating ovens recover atoms that would not enter the trapping region by cooling them to the liquid state and returning them to the oven reservoir[144, 145, 146, 147, 148, 149, 150]. However, such designs add substantial complexity with little to no lifetime increase over multichannel designs.

In this paper we present an inexpensive and simple design for a multichannel array consisting of microcapillaries cut from hypodermic tubing. An important challenge in designing such a nozzle is to ensure that all of the microcapillaries are constrained to be parallel to the axis of the experiment. The absence of such constraint has been identified as a limiting factor for multichannel nozzles[143]. To the best of our knowledge no design that ensures this constraint has been published.

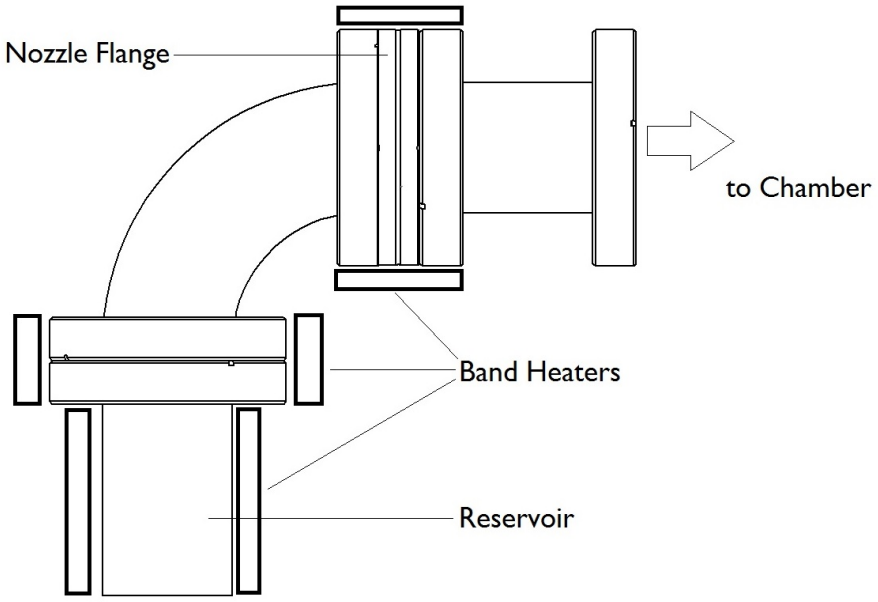

Figure A.2: Drawing of oven manifold, showing band heater placements.

A.3 Design

In our nozzle we constrain the microcapillaries to be parallel by stacking them in a hexagonally packed lattice. Such packing eliminates the possibility of gaps due to dislocations in the array. This is also desirable, since if such a gap had a width larger than the inner diameter of one of the microcapillaries it could dominate the conductance through the nozzle and thus the solid angle of the resultant atomic beam.

We enforced the hexagonal packing of the microcapillaries by appropriate design of the bounding walls of the array. This necessitates that the angle between adjoining boundary walls is either 60°or 120°. The simplest boundary design forms an equilateral triangle of microcapillaries and requires only one 60°angle to be machined. Since a large tooling radius at the apex of the triangle would disrupt the ordering of the array, we used wire-cut electrical discharge machining (EDM) for this step. The precision required

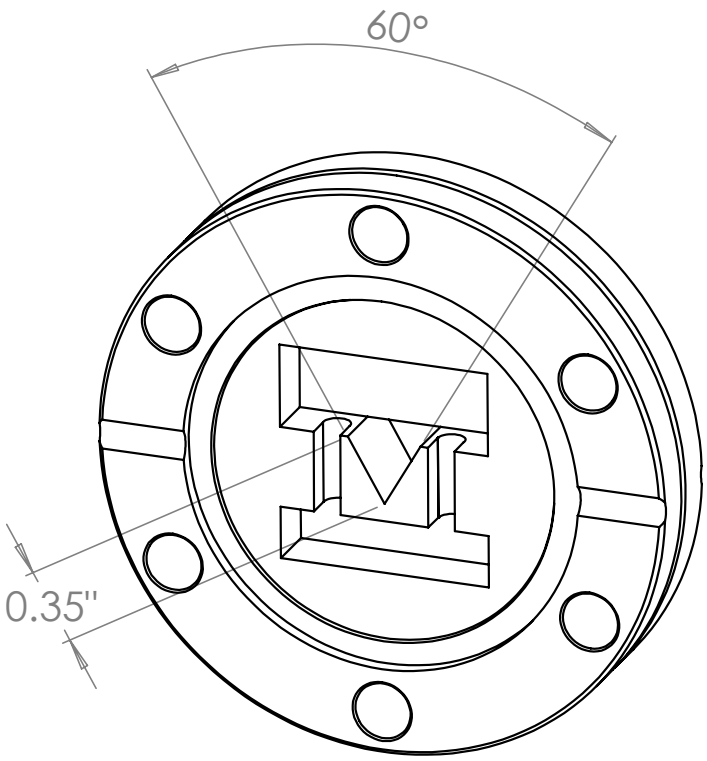

Figure A.3: Drawing of channel and clamping pocket machined in CF blank.

to ensure no defects in the hexagonally packed lattice over the length scale of a typical nozzle size is well within the capabilities of EDM.

The nozzle channel is machined out of a 2.75-inch-diameter double-sided ConFlat (CF) blank, which once assembled, was bolted between two flanges to connect the oven to the rest of the experiment. The nozzle channel is directly machined into the blank to maximize thermal conductance to the exterior, as the nozzle must be the hottest point in the oven manifold to discourage clogging. The oven manifold is heated using three band heaters, as depicted in Figure A.2. Nickel CF gaskets are used for all seals in the oven manifold. CF flanges are rated to 450 °C, but we have operated such flanges at temperatures over 600 °C without any adverse effects on our vacuum. Since the nozzle is machined out of a standard CF blank, it can be used in an oven manifold for any

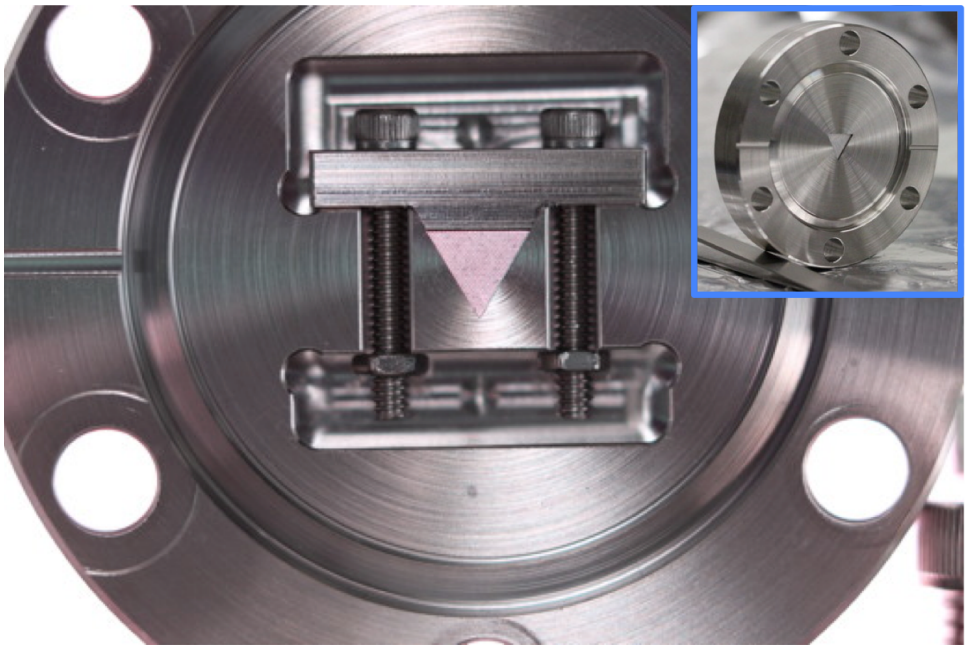

Figure A.4: The assembled nozzle, seen from the side opposite the oven. Inset shows the oven side of the nozzle.

atomic species that can be safely heated to required pressures within the limits of CF technology.

The microcapillaries are held in the channel by a single stainless steel clamp that fits into a pocket machined out of the blank. The clamp is precisely sized to firmly hold in 528 microcapillaries in 32 rows, and is tightened with two sets of stainless steel bolts and nuts housed in additional pockets. These pockets ensure adequate venting for vacuum purposes, so vented screws are not required. The design for the machining of the blank is shown in Figure A.3, while the completed nozzle is shown in Figure A.4. The hexagonal packing of the microcapillaries is evident in the closeup in Figure A.5.

The microcapillaries used were 5 mm lengths of 33RW gauge (100 μm inner diameter) type 304 stainless steel hypodermic tubing purchased from MicroGroup. This length and gauge were selected to ensure a suitable atomic beam solid angle and an atomic flux of the order of 10^{12} atoms per second at the trapping region (estimated by calculating the

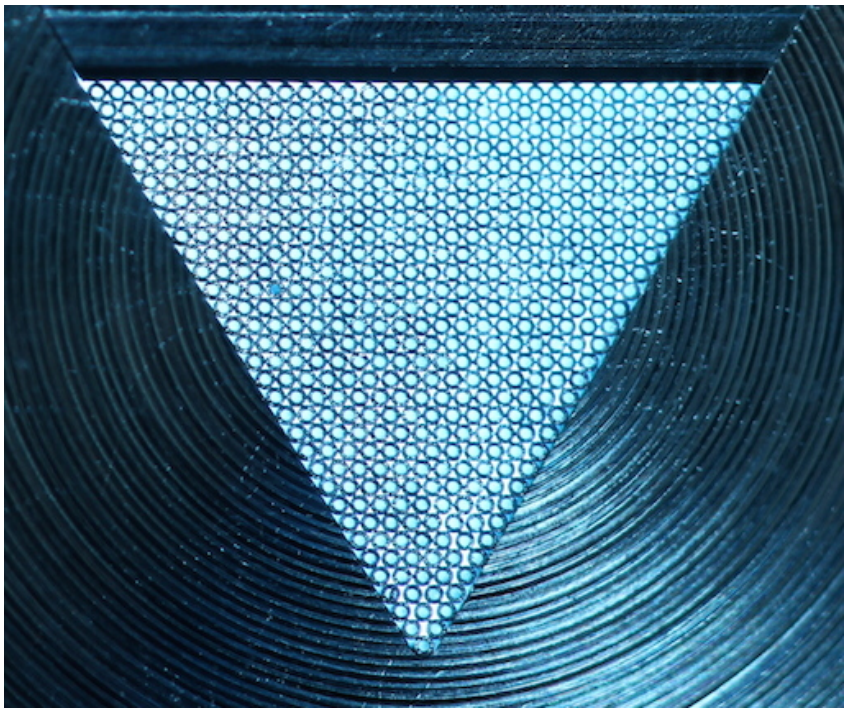

Figure A.5: Close-up of the microchannel array.

molecular flow conductance). The solid angle was chosen conservatively to be more than four times the angle subtended by the differential pumping tubes and the Zeeman slower, in order to minimize alignment sensitivity of the 1.7-meter-long machine.

A.4 Evaluation

The performance of the nozzle was evaluated in several ways. First, the collimation of the atomic beam and the atomic beam flux were measured approximately 3 inches downstream of the nozzle by recording the absorption of a weak probe laser beam operating on the ^{7}Li $2^2S_{1/2} \longrightarrow 2^2P_{3/2}$ transition. The probe beam included frequency components resonant with the transitions from both ground-state hyperfine manifolds in order to avoid optical pumping into a dark state. The nozzle was held at a temperature of 525 °C for these measurements, with the oven reservoir temperature typically 100 °C lower

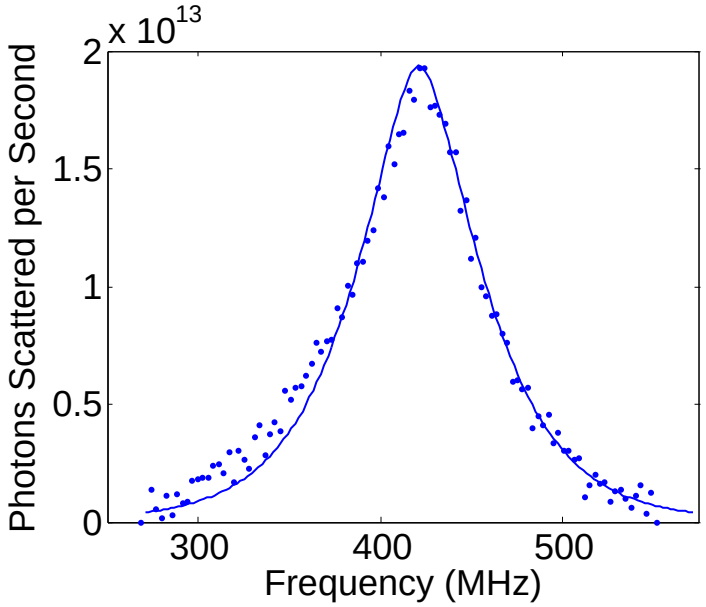

Figure A.6: (Color online). Measurement of velocity distribution of atomic beam. Points show photons scattered per second from a resonant transverse laser beam by the atomic beam, at a point three inches downstream of the nozzle. The solid curve shows the expected velocity distibution given the temperature of the oven and the expected divergence angle inferred from the tube aspect ratio. We attribute the asymmetry in the data to an angular deviation of the probe beam from the transverse direction.

to avoid clogging. No collimating apertures apart from the nozzle itself were present. The results of this measurement are plotted in Figure A.6, which shows the number of photons scattered per second by the center of the atomic beam as the laser frequency was scanned through resonance. The data are consistent with theory for an atomic beam at the nozzle temperature, with a divergence half-angle in the dimension parallel to the probe beam of 1.2°, set by the tube aspect ratio. Additional absorption measurements were taken at various locations along the axis orthogonal to both the atomic beam and the probe beam in order to measure the angular divergence in this dimension. The measured full-width at half-maximum of the spatial atomic beam distribution in this dimension is 5.8 mm. Taking into account the known diameter of the nozzle, this value is in accord with the same divergence half-angle of 1.2°. These measurements demonstrate that the

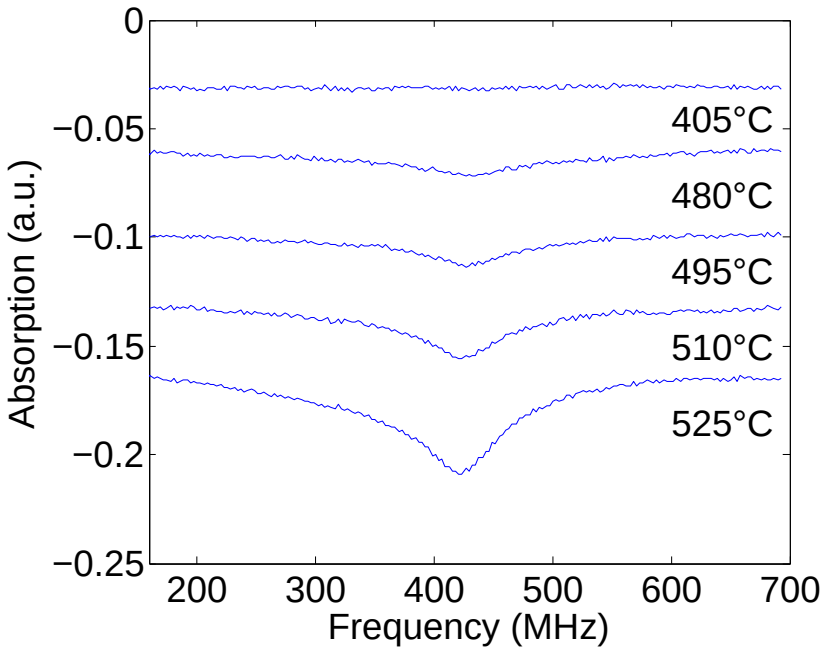

Figure A.7: (Color online). Measurement of angular distribution and temperature dependence. Absorption versus frequency of a transverse probe beam by the atomic beam at various nozzle temperatures. Data at different temperatures are offset for clarity.

collimation of the atomic beam is controlled by the aspect ratio of the microcapillaries, despite the fact that the calculated mean free path is in the intermediate range between the tube diameter and tube length. Physically, this can be explained by noting that the decrease in density along the length of the microcapillaries will lead to a substantial increase in mean free path, suggesting that interparticle interaction effects might not become important until the mean free path in the oven approaches the tube diameter.

These absorption data were also used to calculate a total atomic beam flux of 1.2×10^{14} atoms per second. However, our simulations indicate that the angular distribution of atoms from the high-aspect-ratio tubes has broad non-Gaussian shoulders in addition to the sharp central peak. Including the effects of these shoulders, we estimate an oven lifetime of over 50 years of continuous operation at these temperatures given an initial oven reservoir of 25 g of lithium. As an alternative measure of efficiency, we calculate

that the nozzle consumes roughly 200 times less lithium than a hole of the same area to produce a given beam flux in the central peak. We have observed no performance change in the atomic beam over nine months of operation, which suggests no clogging of the nozzle or unanticipated depletion of the reservoir.

Second, we investigated the performance of the oven nozzle at different temperatures. The absorption versus frequency of a transverse probe laser when aimed through the center of the atomic beam was measured as a function of nozzle temperature, up to 525 °C. Angled-beam velocimetry measurements indicate that the temperature of the atomic beam is close to the nozzle temperature. Transverse-beam data are plotted in Figure A.7, and show a monotonic increase in atomic beam flux, further supporting the conclusion that stalling is not yet important at these temperatures.

Finally, in conjunction with a Zeeman slower and a standard transverse cooling stage [151], the atomic beam was used to load a magneto-optical trap (MOT) of up to 1.2×10^9 atoms, located 1.7 m from the oven, at an initial loading rate of 3×10^8 atoms per second.

A.5 Conclusion

We have presented a simple and inexpensive method to implement a multi-tube effusive oven nozzle. The design ensures that all microcapillaries are parallel, eliminates stacking defects, is adequately vented, ensures sufficient thermal conductivity for effective heating, and can be adapted for other species. The nozzle produces a highly collimated lithium atomic beam of 1.2×10^{14} atoms per second with beam intensities over 5.0×10^{16} atoms per second per steradian while maintaining an expected oven lifetime of several decades.

Appendix B

Ultra-high vacuum and baking

Achieving ultra-high vacuum in a room-temperature chamber is difficult. Much care has to be exercised in the selection and design of vacuum components, and the entire system must be baked to high temperatures while pumping with an external vacuum pump in order to reach the required pressures. Since ultracold atom experiments involve many optics, electronics and water-cooling hardware in close proximity to the vacuum chamber, it is difficult to bake a chamber once it has been set up to perform experiments. Therefore the goal of most cold atom experimenters is to bake their main chamber a single time, and to avoid re-bakes at all costs. This leads to an amount of what David calls "bake voodoo," as we are forced to infer signal from low-N statistics, and therefore take several precautions without knowing whether they are indeed necessary. This appendix summarizes what we have learned over the course of six successful and one unsuccessful bake.

B.1 Vacuum hardware companies

There are a few different commercial options for vacuum components. We purchased much of the conflat hardware from Kurt J. Lesker Company, and a smaller amount of them from MDC Vacuum Products[1]. We used Lesker viewports and anti-reflection (AR) coatings for the Li main chamber[2]. We initially requested an AR-coating for 323 nm[3], in addition to coatings at 532, 671 and 1064 nm. However due to some error in the coating process, the coating at 323 nm was not applied. A further error in the coating procedure led to large splotches on these windows after baking the main-chamber. Due to this we had to get new windows and re-bake the Li main chamber. We decided to no longer use Lesker for AR coatings. For the Sr main chamber we bought the viewports from Lesker and had them shipped to Optical Filter Source to be coated. Apart from some of the coating runs not achieving quite the levels of anti-reflection that were quoted, we have not had any major issues with this company. We experienced a further issue with Lesker viewports in the case of the 1.33" conflat viewports on the Sr main chamber. Due to some change in the design of the Lesker viewports, the glass-to-metal seal protruded above the outer surface of the flange. The washers we used for the bolts would thus push on the glass-to-metal seal, and we cracked several of these viewports during the vacuum assembly. Figure B.1 shows a photograph of such a cracked viewport.

The Sr main chamber and the science chamber were purchased from Kimball Physics. Some spectroscopy cells, pumping manifolds and custom oven manifold parts were fabricated by A & N[4] and Applied Vacuum Technologies. We purchased some AR-coated viewports for spectroscopy cells from Larson Electronic Glass[5]. We purchased Cu gaskets

[1] Lesker tended to be cheaper except for valves.

[2] Apart from the re-entrant windows which were made and coated by the UKAEA.

[3] This is the ${}^2S_{1/2} \rightarrow {}^3P_{3/2}$ transition, which has been used for laser cooling [56].

[4] Now known as ANCORP

[5] We heard a horror story from another group about a glass-to-metal seal on a Larson viewport failing during a bake, so we subsequently avoided them for applications where baking is necessary.

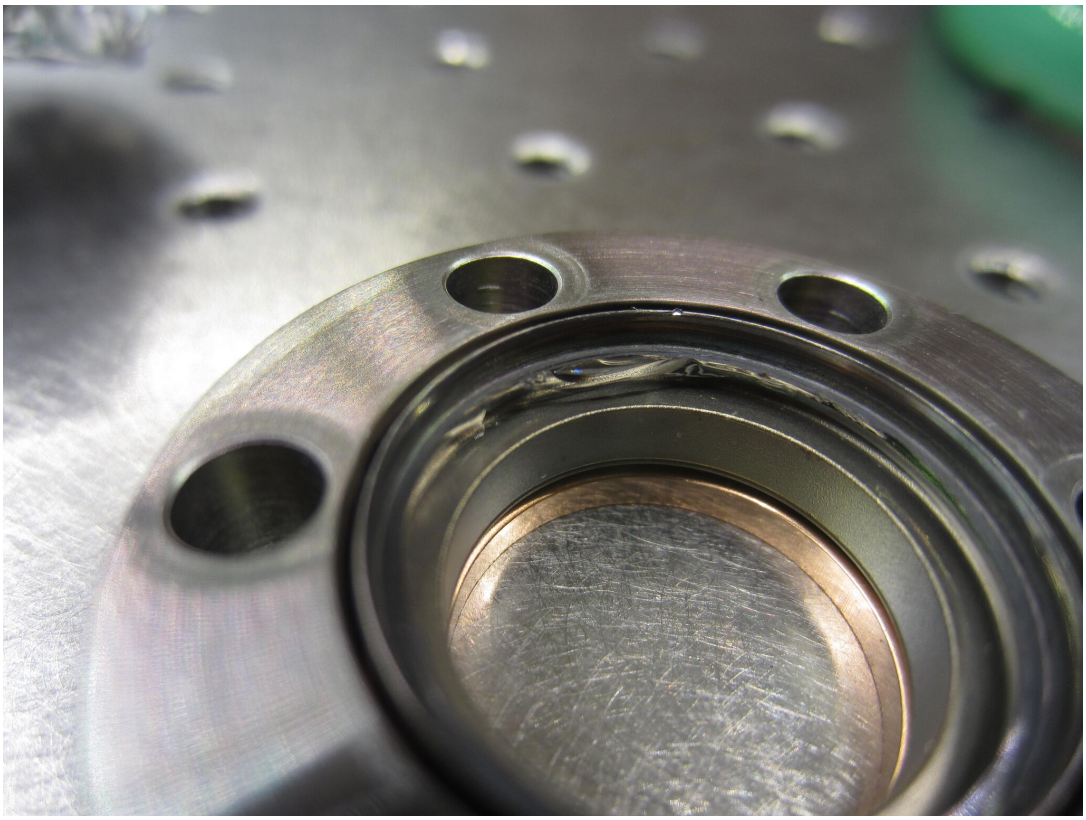

Figure B.1: A photograph showing the failure of the glass-to-metal seal in a Lesker 1.33" conflat viewport caused by washers pushing on the seal during tightening.

and silver-plated[6] stainless steel bolts from Duniway. We used plate-nuts as they are self-torquing and therefore more convenient than conventional nuts. In the case of the VAT valve, which is metric-threaded, we could not find the requisite silver-plated bolts and therefore used Loctite Food-Grade Anti-Seize to lubricate the bolts. We used grooved Ni gaskets from Vacs SEV for the heated flanges in the oven manifold. We purchased our UHV-24p ion gauges and gauge readers from Ideal Vac.

We bought our turbo-molecular pump and dry-scroll roughing pump from Edwards Vacuum. We used a Phoenix Oerlikon dry leak checker borrowed from the generous Martinis and Mazin Groups.

[6]Silver-plating acts as a lubricant.

B.2 In-vacuum components

We used all-metal valves for the main chambers of both experiments, and used elastomer valves for the oven manifold. Elastomers outgas, wihch is why we avoided using them with the main chamber where vacuum was critical. On the other hand, all-metal valves are expensive and can be cycled fewer times. We used the expensive Kalrez elastomer for the oven manifold valves, which supposedly outgasses less than Viton. For the gate valve between the Sr main chamber and the future science chamber we used an expensive VAT all-metal gate valve that may be cycled 10,000 times before servicing. We used vented stainless steel screws for attaching the coldplate and stoppers on to metal feedthroughs. We used UHV-compatible macor ceramic for the Li in-vacuum RF antennae as an electrical insulator. We used a mixture of Agilent (Varian) and Gamma ion pumps. The Gamma ion pumps' magnets were bakeable and thus left on during bakes. The Sr oven manifold ion pump that was closest to the Sr reservoir became non-functional[7]. During the re-build of the Sr oven manifold in the winter of 2016/7 we washed the inside of this ion pump with deionized water and baked it separately for a while[8]. The ion pump now functions normally.

B.3 Cleanliness

It is important to ensure that the in-vacuum components of the system are clean. To this end, we always use gloves, hairnets and plastic sleeves when handling exposed conflat flanges and gaskets. We also set up a temporary shroud around the machine table using shower curtains during vacuum assembly. Parts that were small enough to fit in our ultra-sonic cleaner (other than viewports) were sonicated for in a solution of

[7]We believe that Sr deposition between the ion pump electrodes led to high currents flowing in the pump, which led to the pump cable frying.

[8]This bake almost drowned our turbo-molecular pump. We disassembled it and dried it.

Alconox (a detergent), held in flowing deionized water, and then sonicated in acetone and iso-propyl alcohol. Each step would take approximately five minutes. For parts that could not be sonicated, we did some careful cleaning using solvents and lens cloths, and tried to vacuum up any visible contaminants. Many custom parts, such as the Li main chamber and the slower tubes of both experiments, were electro-polished by a local company named Electromatic.

B.4 Baking

In order to establish a vacuum in the region of 10^{-11} torr (particularly for a stainless steel chamber at room temperature), it is necessary to "bake" the chamber while pumping on it for a long period of time. This process removes water that is trapped within the steel, and which outgasses into the chamber when it is put under vacuum. It is typical to bake to temperatures $\sim$ 200°C for a water bake. It is also not uncommon to do a bake to much higher temperatures ($\sim$ 400°C) to remove hydrogen that is trapped within the steel[9].

Stainless steel (SS) is a terrible thermal conductor. Therefore using conduction as a means of heating an SS object is not a good method to achieve uniform heating. Our one failed bake (the first Li oven manifold bake) was caused by direct heating of the chamber with heating tapes. This led to non-uniform heating, causing the temperature at some viewports to go above the rated temperature, leading to a failure of the glass-to-metal seal. Figure B.2 shows a photograph of this failure and of our ill-advised heating technique. Luckily our constant vigilance allowed us to save our turbo-molecular pump from catastrophic failure.

We prefer to completely wrap the chamber in Al foil and fiberglass insulation

[9]We have never performed a hydrogen bake, and acheived pressures of 5×10^{-12} torr in the Li main chamber, and 2×10^{-11} torr in the Sr main chamber.

Figure B.2: A photograph showing the source of the failure in our first attempted Li oven bake. The glass-to-metal seal was heated above its rating, leading to the sealant melting. This was caused by non-uniform heating due to direct heating of the chamber.

(wrapped in Al foil since it is unpleasant to handle), and heat this using heating tapes. Figure B.3 shows a photograph of this technique implemented during one of our Li main chamber bakes. A second layer of insulation goes around the heating layer. Band heaters that are in direct contact with the SS can be used to heat lagging areas of the chamber which have a large thermal load. Bayonet-style thermocouples are preferrable for flanges, as they are spring-loaded against the chamber. For other thermocouples, we use hose-clamp to affix them to the chamber where possible, and Kapton or Al tape where not. We used over 50 thermocouples on various points of the machine during bakes, and used up to 34 heating elements at a time[10]. The thermocouples were read using

[10]This number was limited by the number of variable transformers we owned.

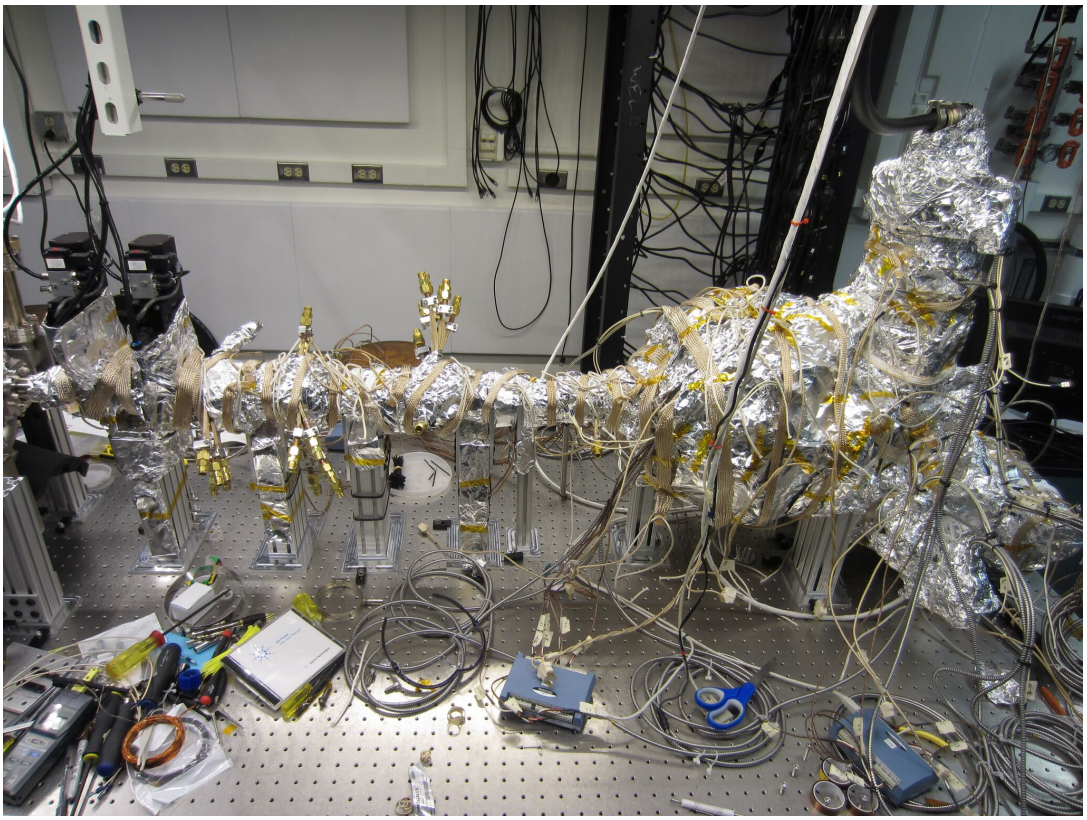

Figure B.3: A photograph showing the heating layer during one of our Li main chamber bakes. The inner layer of Al foil insulation allows the heaters to heat the chamber convectively rather than conductively. A second, thicker layer of insulation is applied on top of the heating layer before the heaters are engaged.

multiple USB-TC data acquisition modules from Measurement Computing. The temperatures were read into MATLAB and displayed in a graphical user interface, where we could see the temperatures of each part of the machine and plot graphs over time of the temperature of any selection of the thermocouples. We streamed the desktop of the bake-monitoring computer so that we could monitor the bake from home once the temperatures had equilibrated. A web-cam was used to monitor the turbo-molecular pump pressure gauge reading.

We have used metal mesh to protect glass from being contact with insulation (shown in a photograph in Figure B.4). We have used shims of thin metal between supports

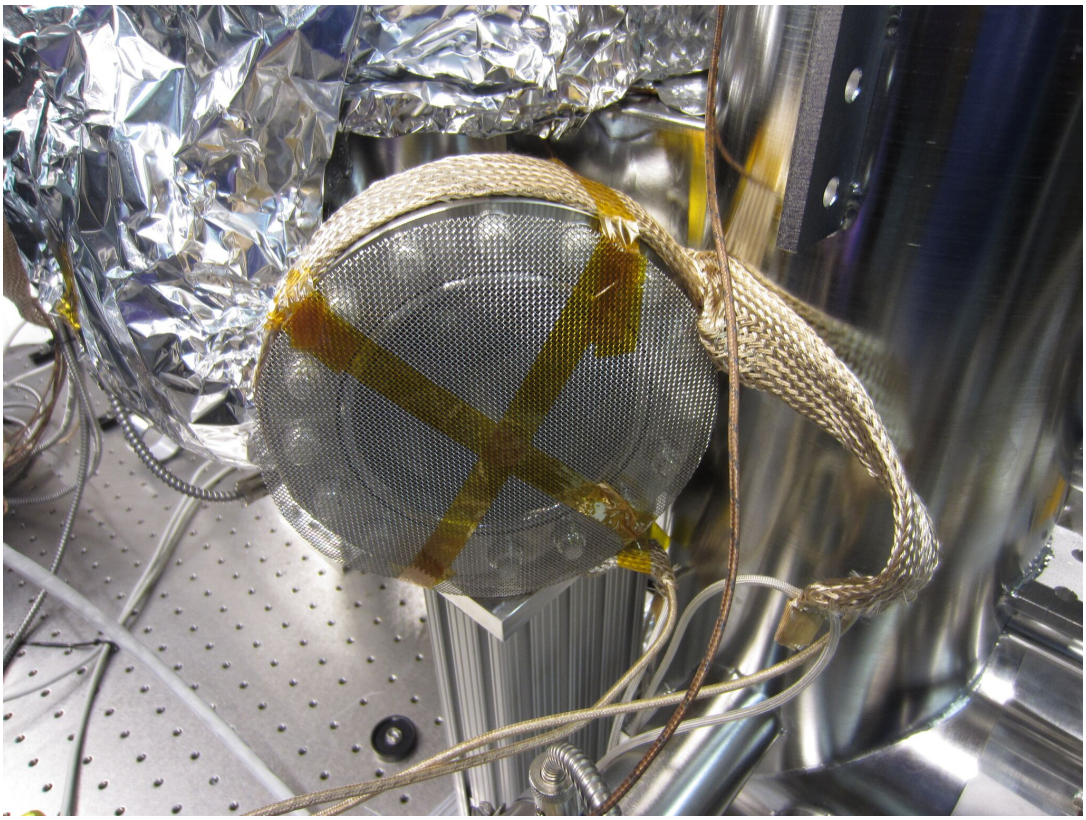

Figure B.4: A photograph showing an application of metal mesh to protect one of the 6" viewports on the Li main chamber during a bake. Note also the usage of a heating tape in direct contact with the large flange. Such direct application of heat was used only in cases where a section of the chamber with a large thermal load was lagging behind the rest of the chamber.

and the optical table to prevent heat sinking. We unclamp all but one of the supports from the optical table, to allow the chamber to expand under heating. We heat up to a temperature of about 180°C , and maintain this temperature for about 10 days. We heat up and cool down over the course of a couple of workdays. We degas the ion gauge filaments a few times during the middle of the bake. Typically the region of hottest temperature during a bake is thermally coupled to the region of lowest temperature[11].

Lastly it is crucial to have a good bake playlist.

[11]Otherwise you would have fixed the temperature discrepancy!

Appendix C

Experimental tips & tricks

1. **Sealing a conflat flange.** Conflat technology is over 50 years old and is very robust. I have seen conflat flanges bolted to one another at significant angles that have successfully held vacuum. Conflats can also withstand a large torque; a 2.75" conflat flange can hold up a 45 l/s ion pump against gravity. We would typically seal a conflat by tightening the bolts in a generalized "star" pattern to achieve a uniform sea. We initially used a torque-wrench[1] to ensure that we did not exceed the torque ratings while sealing a flange. Eventually we became experts at judging the required torque, and took off the training wheels.

2. **1.33" conflat flanges.** These flanges are very difficult to work with due to their small size, and are best avoided. It is easy to strip the bolt head, and the gasket often gets stuck on one of the flanges after disassembly, making the ability to reuse a 1.33" conflat flange a probabilistic affair. An RF feedthrough with a stuck gasket held up the assembly of the Li mainchaber. It is possible to remove these stuck gaskets by carefully using a vise-grip. I have heard from a Gamma sales

[1] In cases where our torque wrench would not fit, we used a fish-hook scale to measure the torque applied with a regular wrench.

representative that silver-plated Cu gaskets get stuck less often, but I have not confirmed this.

3. **Getting a MOT from scratch.** It is tempting to try and diagnose the Zeeman slower before attempting to get a MOT. However this is very difficult as it requires velocimetry of the atomic beam, which requires for a probe beam that scans through a large range of frequencies while the Zeeman slower beam frequency is held fixed. In my opinion it is best to try and achieve a MOT without doing any optimization of the Zeeman slower; we were able to see a Li MOT loaded from the low-velocity tail of the atomic beam without any slowing at all! Overlapping the MOT beams with each other and the magnetic-field zero are critical. Scanning the frequency of the laser through the resonance should reveal an expanding and contracting ring of fluorescence around the magnetic-field zero. With Sr this effect was readily observable on the broad 461 nm transition, to which our eyes are quite sensitive. We also saw this effect with Li when all of the MOT power was re-directed to a single beam that was transverse to the atomic beam. Irises can be used to ensure that the MOT beams are centered on the field-zero. Use a polarimeter to set the polarizations of the MOT beams.

4. **How to set up a $4f$ system.** A $4f$ optical system is a system of two lenses which maps a point source to a point, and a collimated source to a collimated beam. The first lens is placed at its focal length away from the source, and the second lens is placed at a distance equal to the sum of the focal lengths of the two lenses away from the first lens. The distance between the object plane and the image plane is equal to twice the sum of the focal lengths of the two lenses. When using a $4f$ system as a telescope it is best to have the planar side of planarconvex lenses on the interior surfaces of the telescope, as this obeys the Abbe sine criterion for an

input collimated beam.

5. **Si photodiodes and 1064 nm light.** The band gap of Si is 1.1 eV, which corresponds to a wavelength of just over 1100 nm. Since 1064 nm is close to the bandgap, the penetration depth of the light is very large. This leads to slow response times as electrons have to diffuse from deep within the material to the surface, where they are accelerated by the bias voltage. For applications where a response time in the μs regime is required, it is advisable to use photodiodes based on other semiconductors, such as InGaAs.

6. **Blue light.** Blue light can cause photochemistry in optics such as polarizing beamsplitter cubes and fiber tips. We have seen 300 mW of 461 nm light damage the interface of Thorlabs PBS101 cubes, causing 10+ mW to be scattered at the interface. We have seen periodic damage of the Sr Zeeman slower fiber exit tip[2]. We have heard the glass-capped fibers can alleviate this issue, but we have not been able to get good fiber-coupling efficiency with these fibers.

7. **High-power optics.** Use fused-silica lenses, since they have a lower coefficient of thermal expansion than BK-7.

8. **Setting up an imaging axis.** Make a collimated beam of resonant light and align it through the chamber. Use an iris to pick out the center of the imaging beam, and look for it perturb the MOT. For an optically dense MOT like the Li 671 nm MOT, you should be able to see the shadow the MOT in the imaging beam on the other side of the chamber. Set up a $4f$ imaging system on the other side of the chamber, between the MOT and a camera. You should be able to focus the system on the MOT fluorescence. Once you have taken absorption images of the atoms, it

[2]The Zeeman slower power is typically 80 mW.

is best to focus the imaging system on an ODT, as it gives you the smallest point source[3] to focus on.

9. **Aligning and focusing a non-resonant beam.** The best way to align a non-resonant beam to a cloud of cold atoms is to image the atoms along the axis of the non-resonant beam. Set up a $4f$ imaging system on the exit-side of the chamber using achromatic lenses[4]. Use a dichroic mirror[5] to mix the non-resonant light with the resonant imaging light on the entrance-side of the chamber. Typically the final focusing lens of the non-resonant beam will be after the dichroic, so use another lens to make sure that the imaging beam is collimated going through the chamber. Once the imaging system is focused on the atoms, focus the non-resonant beam on the camera. For a $4f$ imaging system this should focus the non-resonant beam on the atoms.

10. **Polarization in an AOM.** Use linear vertically polarized light through an AOM. Other polarizations are susceptible to polarization drift through the AOM on thermal time scales.

11. **Polarization-maintaining fibers.** Use a polarimeter, preferrably one capable of measuring extinction ratios. Place two quarter wave-plates before the fiber input. Look at the fiber output on the polarimeter. Stressing the fiber should cause the output polarization to walk along a circular path on the surface of the Poincare sphere. Use the two quarter waveplates to move the output polarization to the center of the circular path.

[3]Technically a point occlusion, but they can be thought of similarly due to Babinet's principle.

[4]If you don't use achromatic lenses, the imaging system will not be focused for the non-resonant light and the resonant light.

[5]Use reflection mode for the non-resonant beam, as you typically care more about its spatial mode than that of the imaging beam, which will only be used for alignment purposes.

Appendix D

Custom part designs

This appendix contains computer-aided design drawings for custom parts used in the Li and Sr oven manifolds.

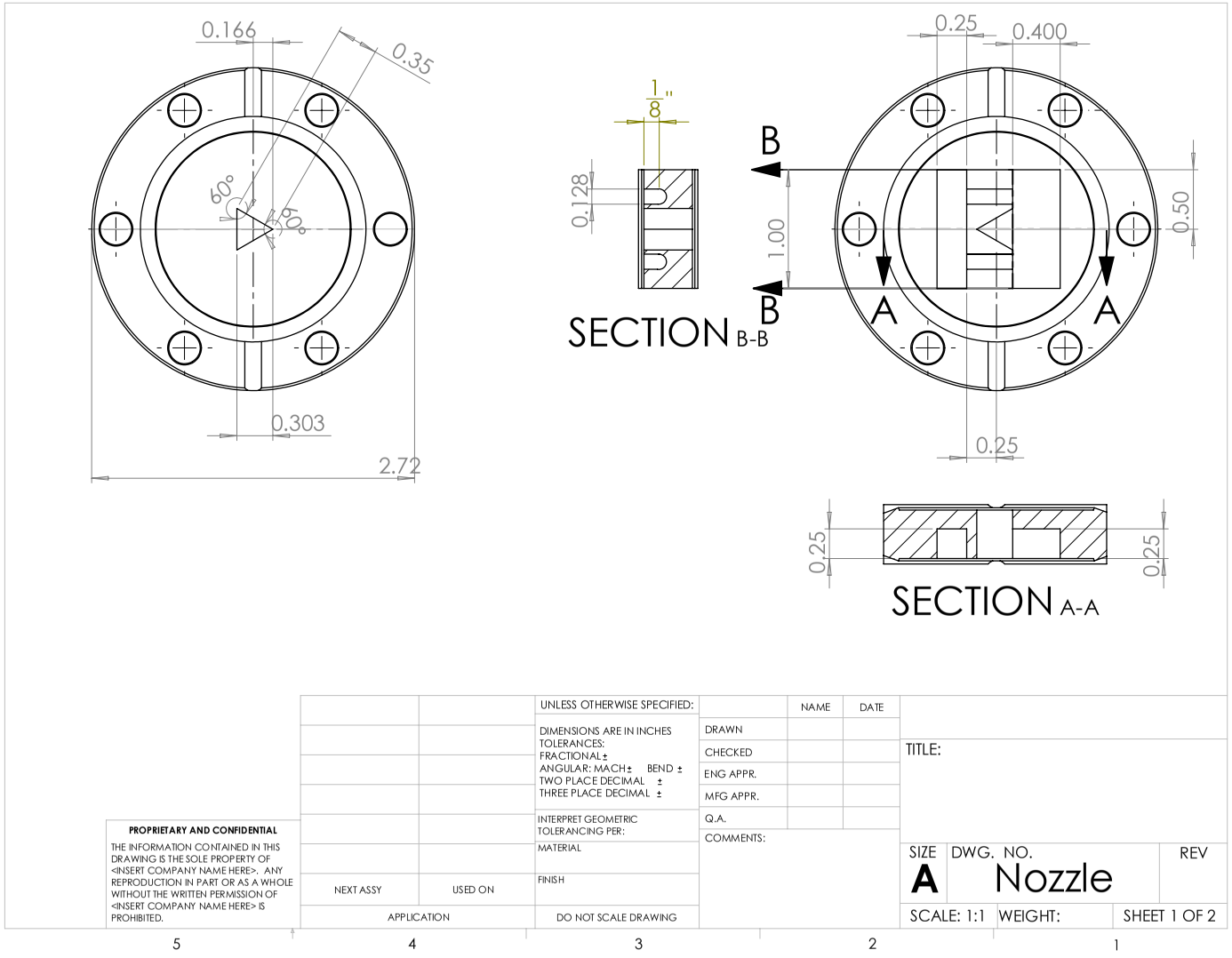

Figure D.1: Drawing of nozzle.

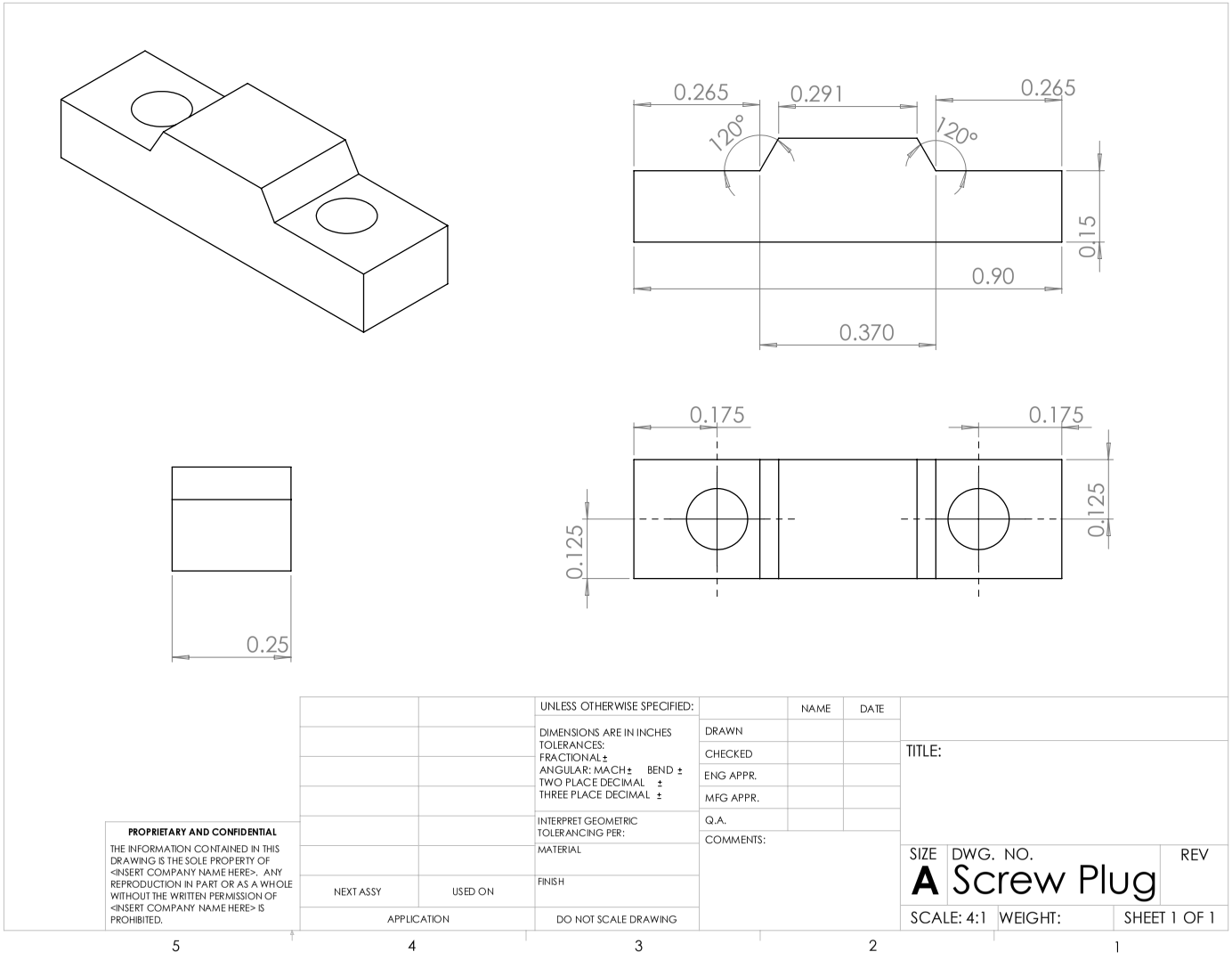

Figure D.2: Drawing of clamp used to hold microcapillaries in nozzle.

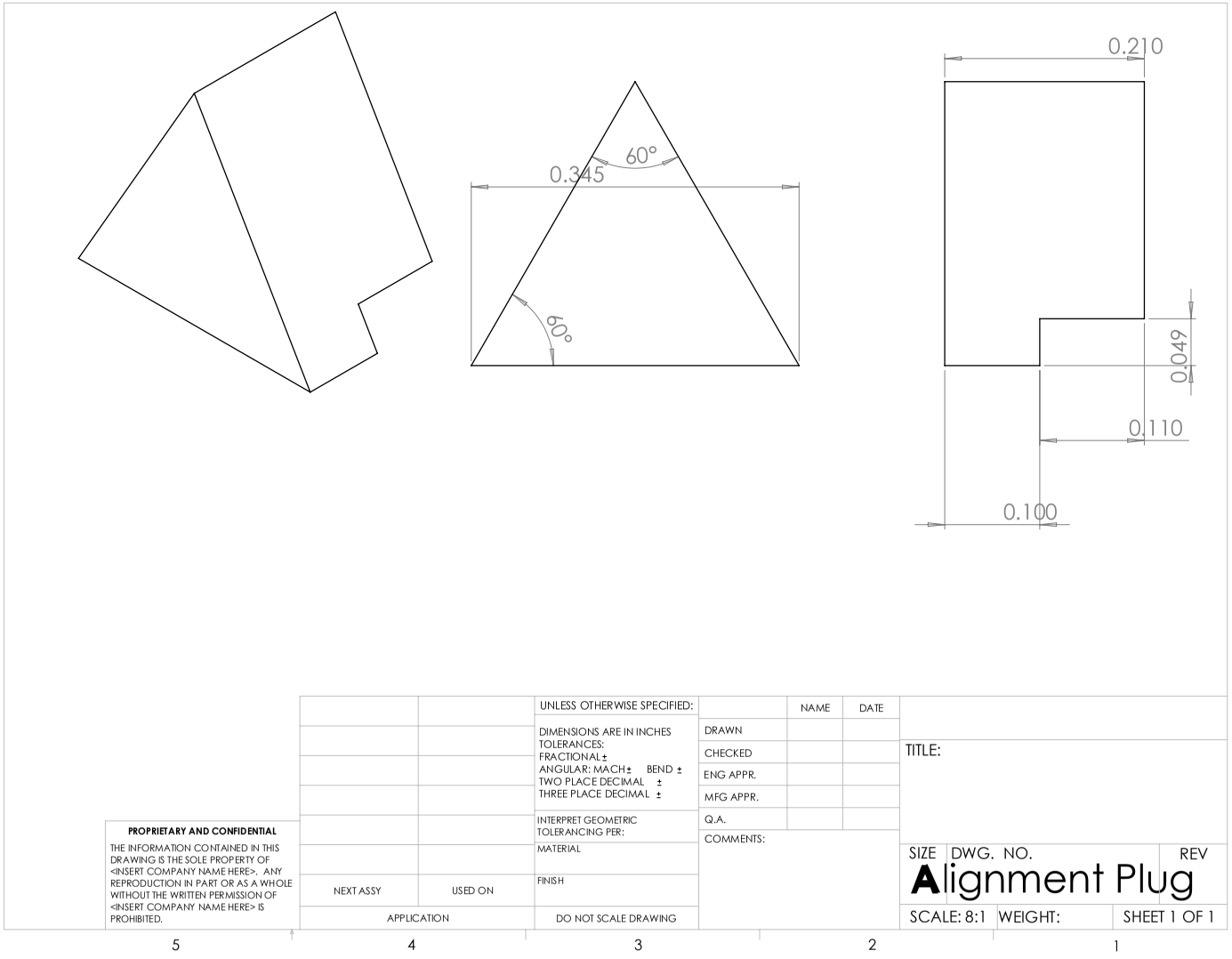

Figure D.3: Drawing of temporary alignment plug used to align microcapillaries before clamping.

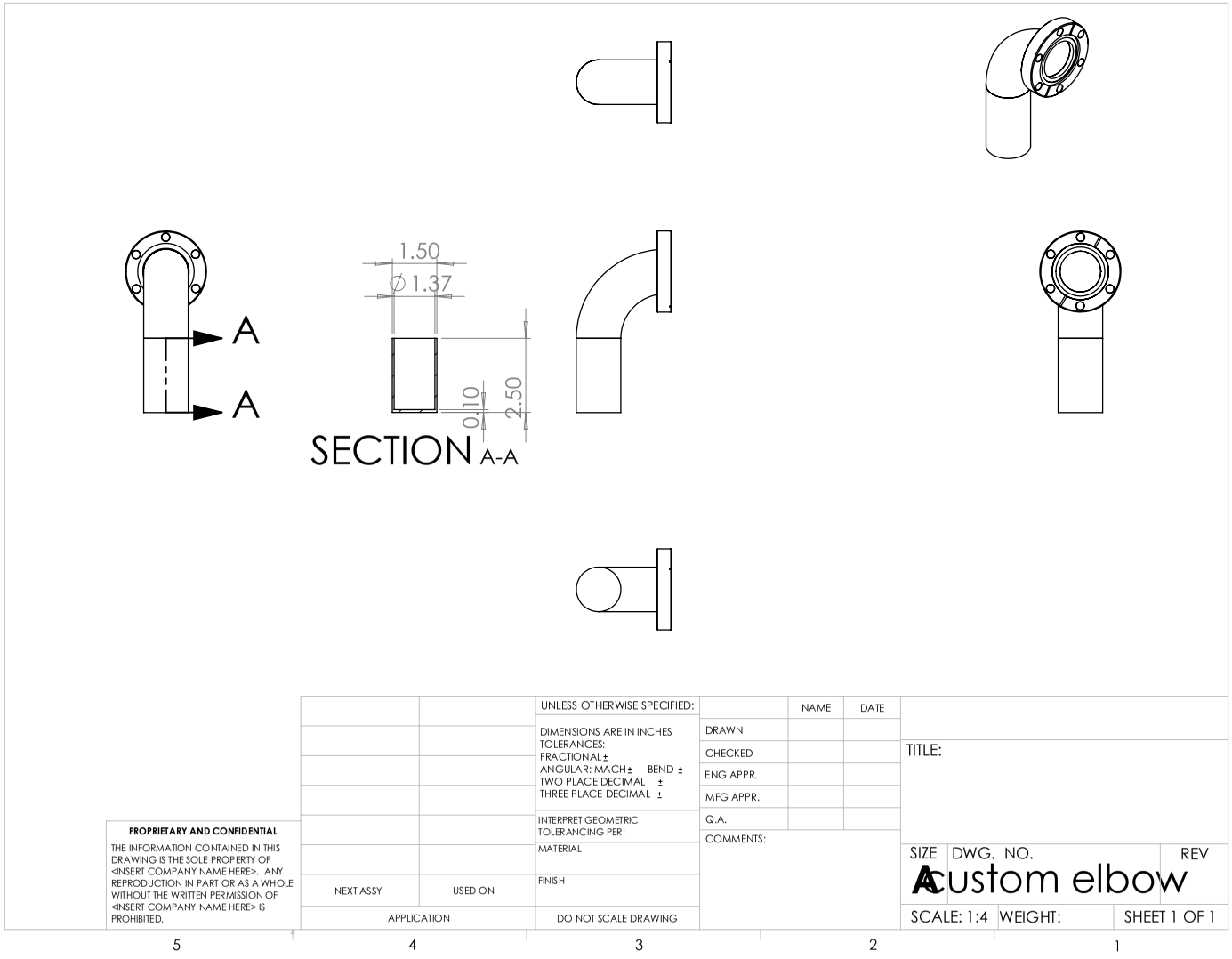

Figure D.4: Drawing of custom elbow used for Sr reservoir.

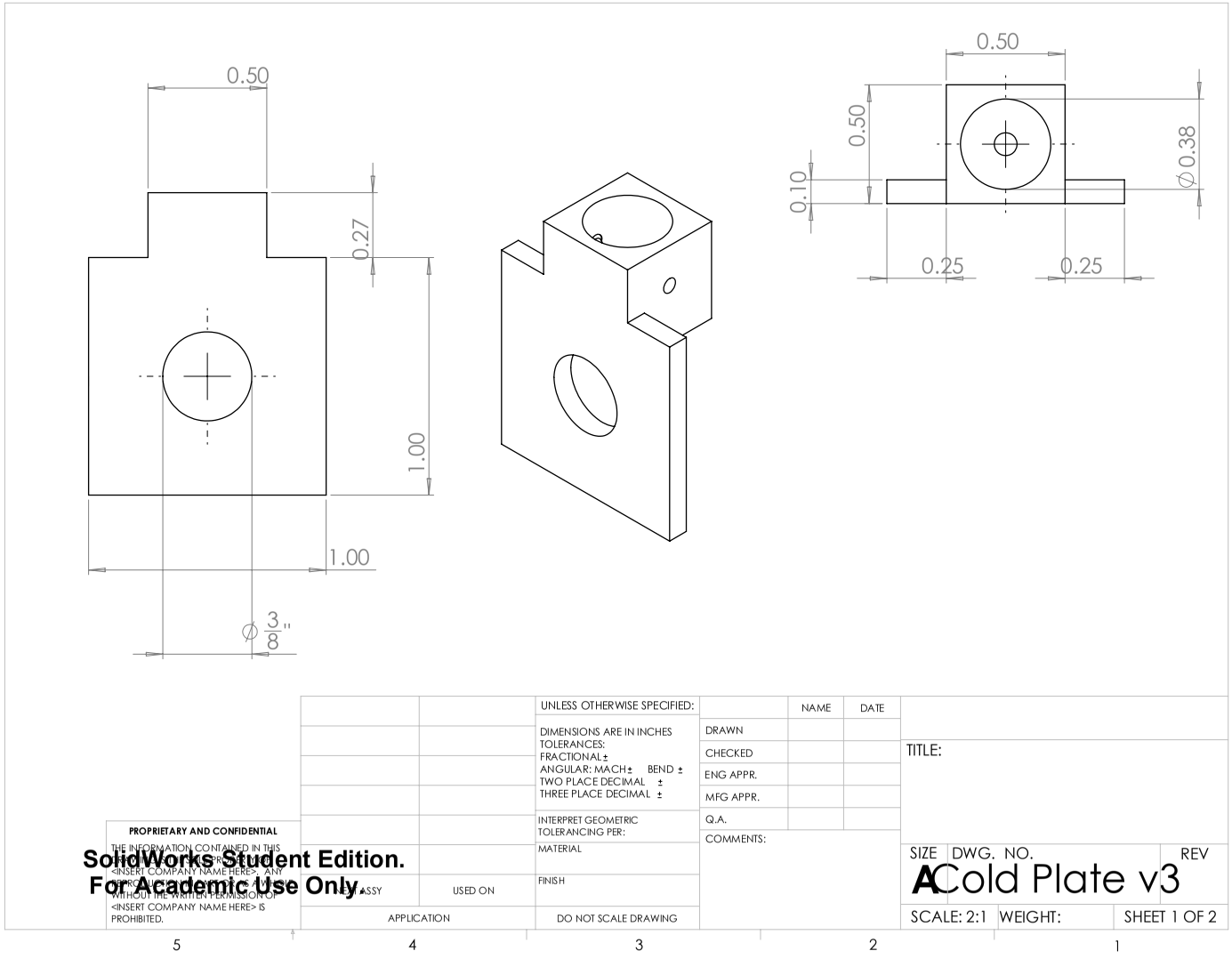

Figure D.5: Drawing 1 of 2 of Li coldplate.

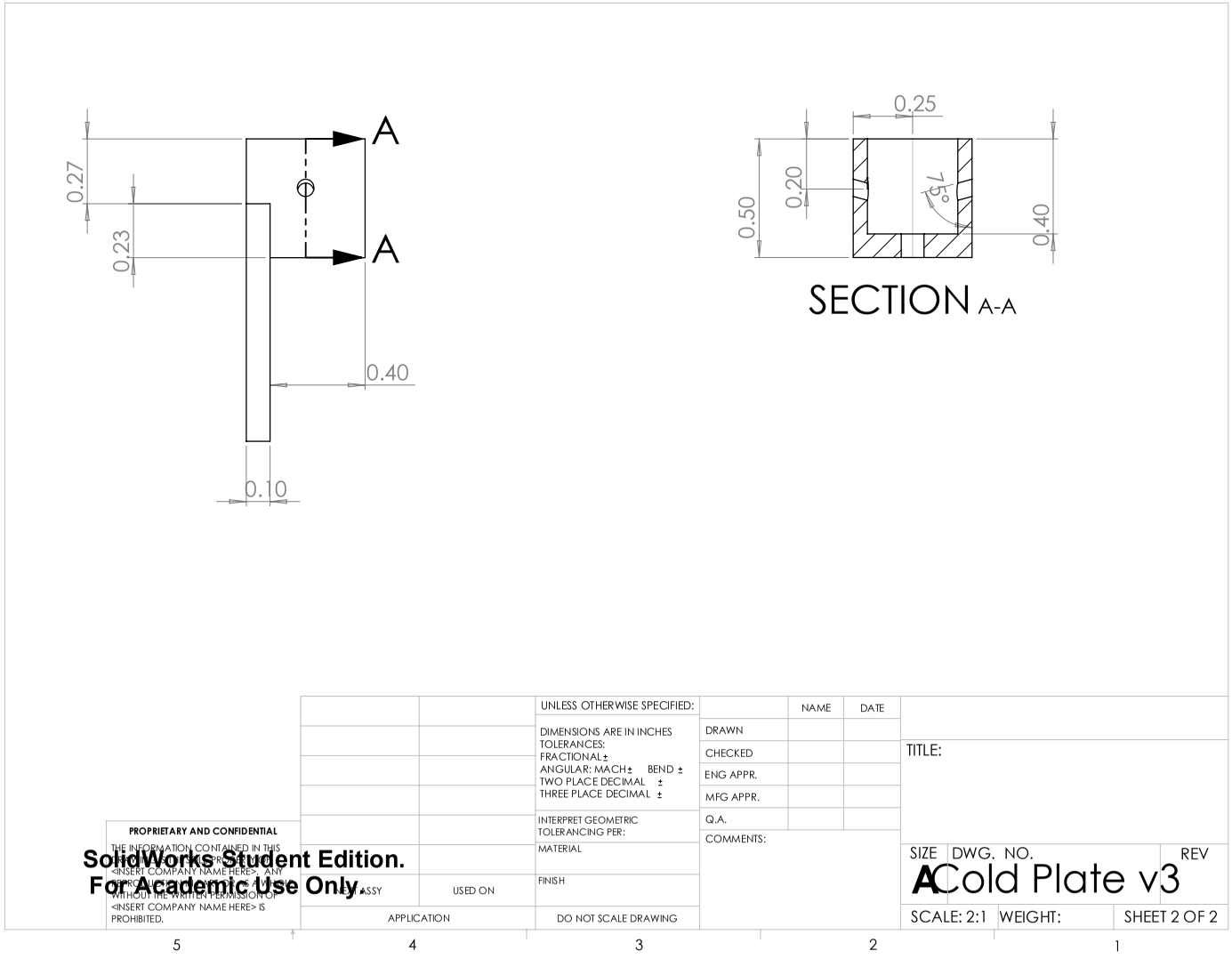

Figure D.6: Drawing 2 of 2 of Li coldplate.

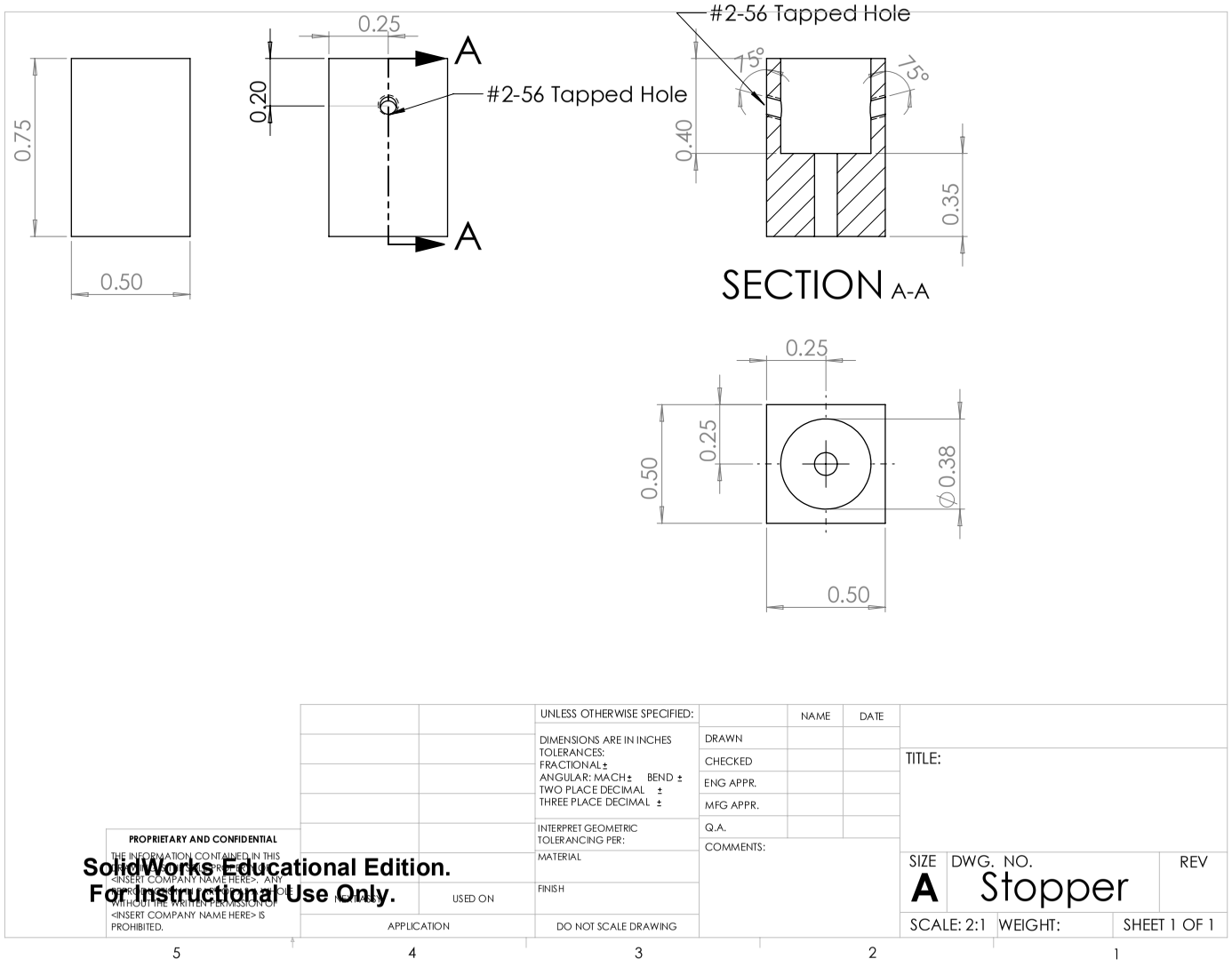

Figure D.7: Drawing of stopper block used for atomic beam shutters.

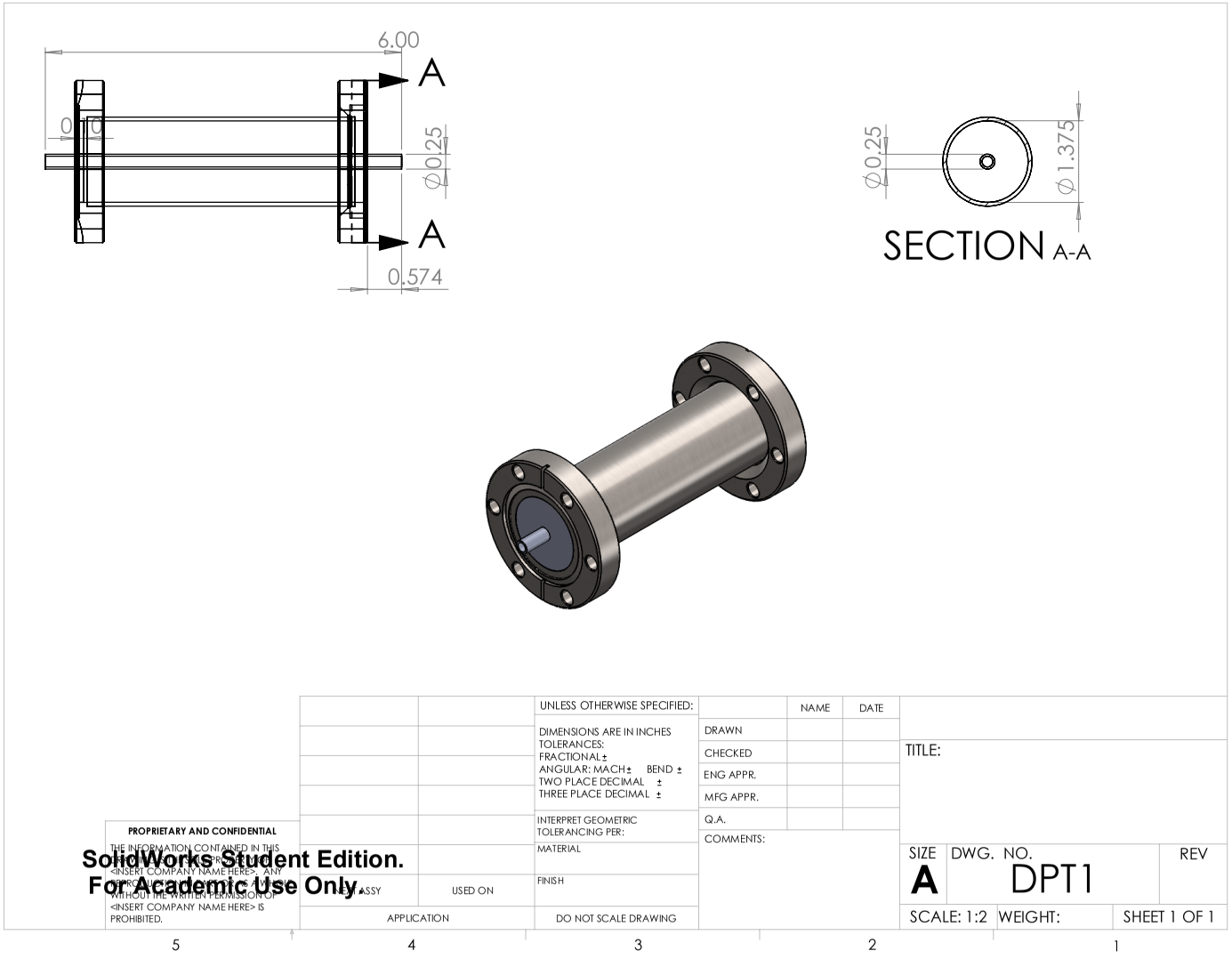

Figure D.8: Drawing of the first Li differential pumping tube.

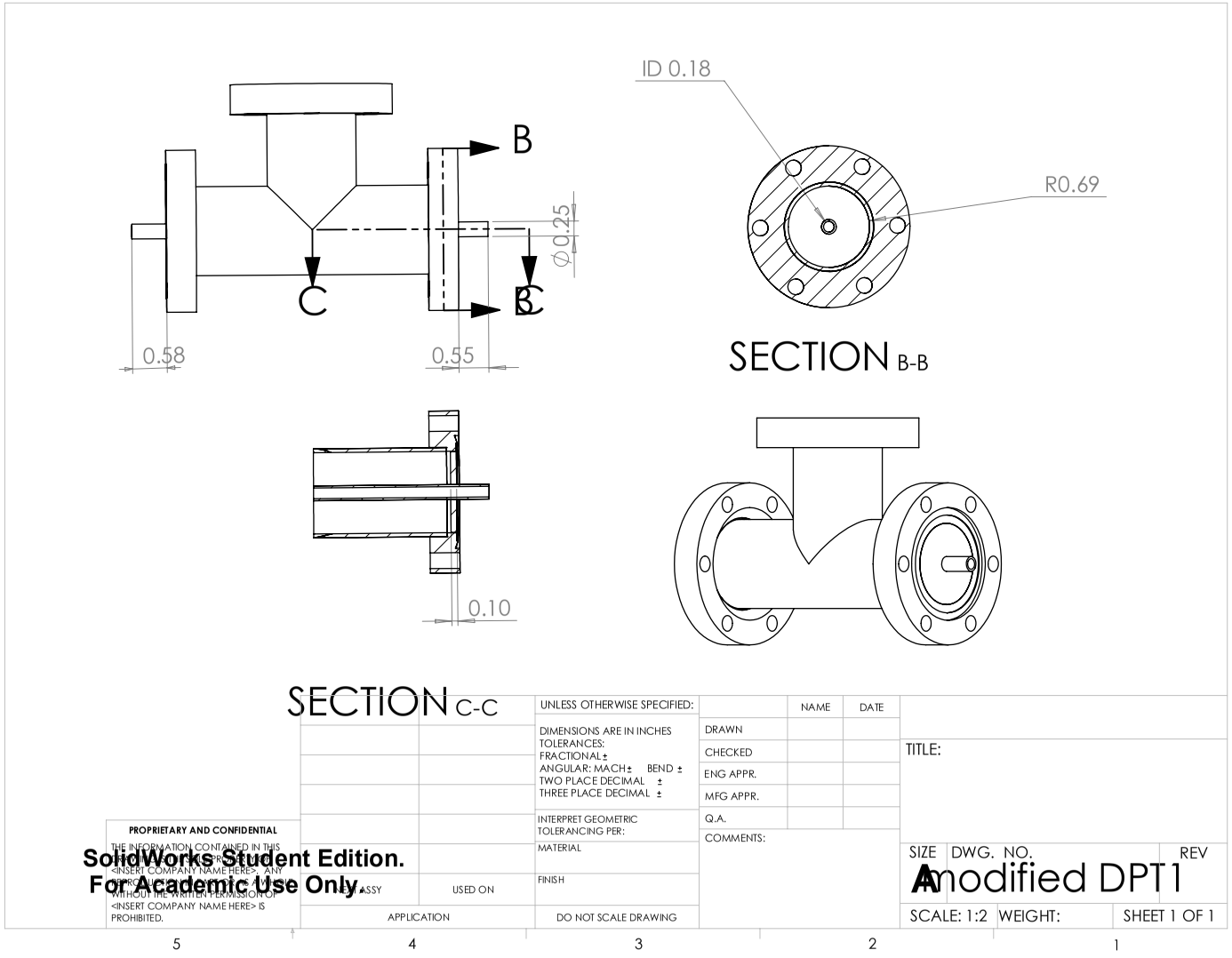

Figure D.9: Drawing of the first Sr differential pumping tube.

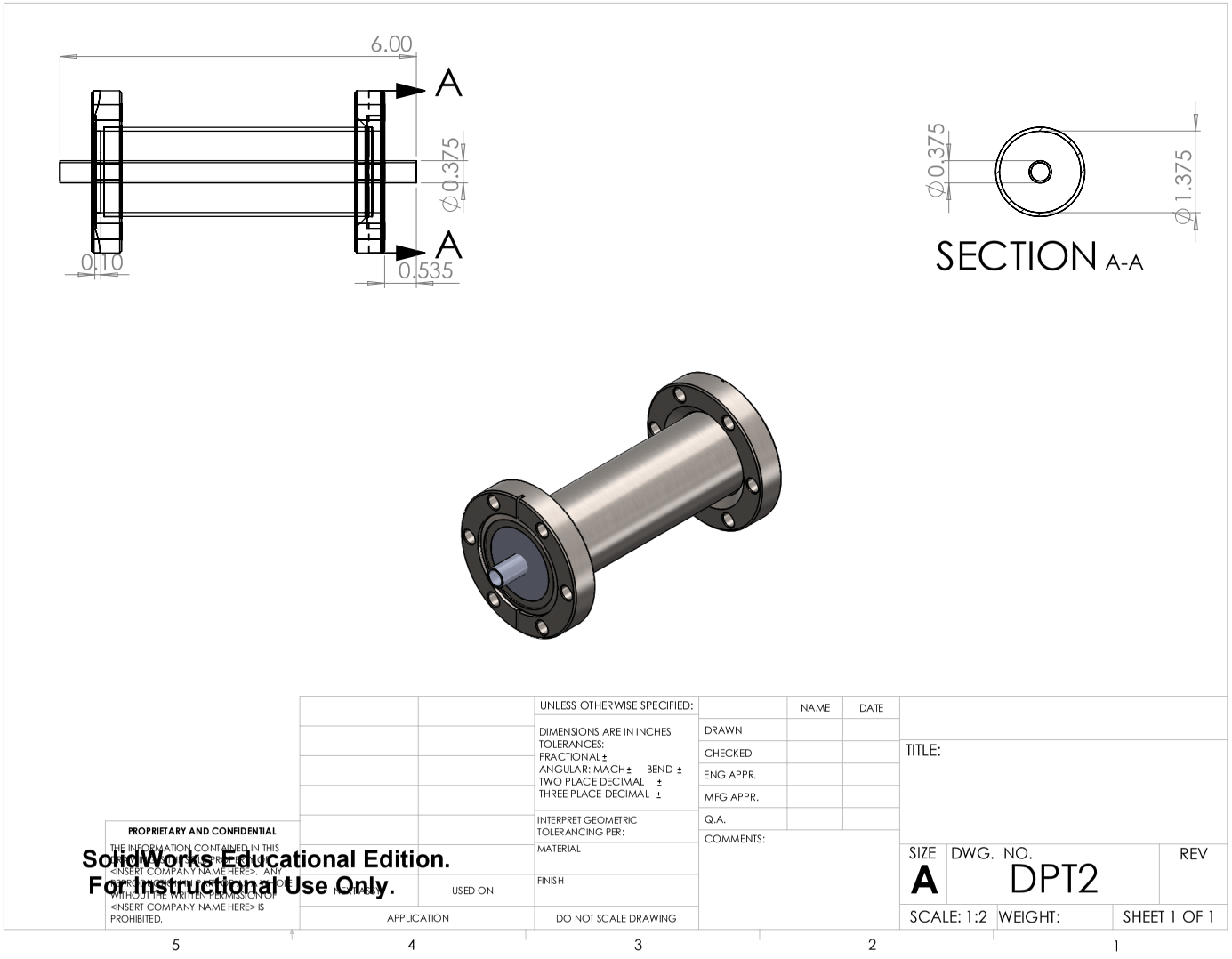

Figure D.10: Drawing of the second differential pumping tube for Li and Sr.

Bibliography

[1] T. H. Maiman, *Stimulated optical radiation in ruby*, *Nature* **187** (1960), no. 4736 493–494.

[2] W. D. Phillips and H. Metcalf, *Laser deceleration of an atomic beam*, *Physical Review Letters* **48** (1982), no. 9 596–599.

[3] S. Chu, L. Hollberg, J. E. Bjorkholm, A. Cable, and A. Ashkin, *Three-dimensional viscous confinement and cooling of atoms by resonance radiation pressure*, *Physical Review Letters* **55** (1985), no. 1 48–51.

[4] E. L. Raab, M. Prentiss, A. Cable, S. Chu, and D. E. Pritchard, *Trapping of neutral sodium atoms with radiation pressure*, *Physical Review Letters* **59** (1987), no. 23 2631–2634.

[5] M. H. Anderson, J. R. Ensher, M. R. Matthews, C. E. Wieman, and E. A. Cornell, *Observation of Bose-Einstein condensation in a dilute atomic vapor*, *Science* **269** (1995), no. 5221 198–201.

[6] K. B. Davis, M. O. Mewes, M. R. Andrews, N. J. Van Druten, D. S. Durfee, D. M. Kurn, and W. Ketterle, *Bose-Einstein condensation in a gas of sodium atoms*, *Physical Review Letters* **75** (1995), no. 22 3969–3973.

[7] S. Inouye, M. R. Andrews, J. Stenger, H. J. Mlesner, D. M. Stamper-Kurn, and W. Ketterle, *Observation of Feshbach resonances in a Bose-Einstein condensate*, *Nature* **392** (1998), no. 6672 151–154.

[8] D. S. Jin, J. R. Ensher, M. R. Matthews, C. E. Wieman, and E. A. Cornell, *Collective excitations of a Bose-Einstein condensate in a dilute gas*, *Physical Review Letters* **77** (1996), no. 3 420–423.

[9] M.-O. Mewes, M. R. Andrews, N. J. van Druten, D. M. Kurn, D. S. Durfee, C. G. Townsend, and W. Ketterle, *Collective excitations of a Bose-Einstein condensate in a magnetic trap*, *Physical Review Letters* **77** (1996) 988.

[10] M. Greiner, O. Mandel, T. Esslinger, T. W. Hänsch, and I. Bloch, *Quantum phase transition from a superfluid to a Mott insulator in a gas of ultracold atoms*, *Nature* **415** (2002), no. 6867 39–44.

[11] M. Ben Dahan, E. Peik, J. Reichel, Y. Castin, and C. Salomon, *Bloch oscillations of atoms in an optical potential*, *Physical Review Letters* **76** (1996), no. 24 4508–4511.

[12] G. Roati, C. D'Errico, L. Fallani, M. Fattori, C. Fort, M. Zaccanti, G. Modugno, M. Modugno, and M. Inguscio, *Anderson localization of a non-interacting Bose-Einstein condensate*, *Nature* **453** (2008), no. 7197 895–898.

[13] S. S. Kondov, W. R. McGehee, J. J. Zirbel, and B. DeMarco, *Three-dimensional Anderson localization of ultracold matter*, *Science* **334** (2011), no. 6052 66–68.

[14] J. Simon, W. S. Bakr, R. Ma, M. E. Tai, P. M. Preiss, and M. Greiner, *Quantum simulation of antiferromagnetic spin chains in an optical lattice*, *Nature* **472** (2011), no. 7343 307–312.

[15] R. A. Hart, P. M. Duarte, T. L. Yang, X. Liu, T. Paiva, E. Khatami, R. T. Scalettar, N. Trivedi, D. A. Huse, and R. G. Hulet, *Observation of antiferromagnetic correlations in the Hubbard model with ultracold atoms*, *Nature* **519** (2015), no. 7542 211–214.

[16] A. Mazurenko, C. S. Chiu, G. Ji, M. F. Parsons, M. Kanász-Nagy, R. Schmidt, F. Grusdt, E. Demler, D. Greif, and M. Greiner, *A cold-atom Fermi-Hubbard antiferromagnet*, *Nature* **545** (2017), no. 7655 462–466.

[17] M. Schreiber, S. S. Hodgman, P. Bordia, H. P. Luschen, M. H. Fischer, R. Vosk, E. Altman, U. Schneider, and I. Bloch, *Observation of many-body localization of interacting fermions in a quasirandom optical lattice*, *Science* **349** (2015), no. 6250 842–845.

[18] D. V. Else, B. Bauer, and C. Nayak, *Floquet Time Crystals*, *Physical Review Letters* **117** (2016), no. 9 1–5.

[19] P. Kapitza, *Dynamic stability of the pendulum with vibrating suspension point*, *Journal of Experimental and Theoretical Physics* **21** (1951), no. 5 588–597.

[20] M. Holthaus, *Floquet engineering with quasienergy bands oferiodically driven optical lattices*, *Journal of Physics B* **49** (2015), no. 1.

[21] R. Dum, A. Sanpera, K.-A. Suominen, M. Brewczyk, M. Kuś, K. Rzążewski, and M. Lewenstein, *Wave packet dynamics with Bose-Einstein condensates*, *Physical Review Letters* **80** (1998), no. 18 3899–3902.

[22] S. Arlinghaus and M. Holthaus, *Driven optical lattices as strong-field simulators*, *Physical Review A* **81** (2010), no. 6 1–4.

[23] Dirk-Sören Lühmann, C. Weitenberg, and K. Sengstock, *Emulating molecular orbitals and electronic dynamics with ultracold atoms*, *Physical Review X* **5** (2015), no. 3 1–8.

[24] S. Sala, J. Förster, and A. Saenz, *Ultracold-atom quantum simulator for attosecond science*, *Physical Review A* **95** (2017), no. 1 1–5.

[25] C. J. Foot, *Atomic Physics*. Oxford University Press, 2005.

[26] C. Cohen-Tannoudji and D. Guery-Odelin, *Advances in Atomic Physics: An Overview*. World Scientific, 2011.

[27] F. Schreck, *Mixtures of Ultracold Gases: Fermi Sea and Bose-Einstein Condensate of Lithium Isotopes*. PhD thesis, University of Paris IV, 2002.

[28] S. Stellmer, *Degenerate quantum gases of strontium*. PhD thesis, University of Innsbruck, 2013.

[29] Z. A. Geiger, *Apparatus for Dynamical Quantum Emulation Using Ultracold Lithium*. PhD thesis, University of California, Santa Barbara, 2018.

[30] R. Senaratne, S. V. Rajagopal, T. Shimasaki, P. E. Dotti, K. M. Fujiwara, K. Singh, Z. A. Geiger, and D. M. Weld, *Quantum simulation of ultrafast dynamics using trapped ultracold atoms*, *Nature Communications* **9** (2018), no. 1 2065.

[31] R. Senaratne, S. V. Rajagopal, Z. A. Geiger, K. M. Fujiwara, V. Lebedev, and D. M. Weld, *Effusive atomic oven nozzle design using an aligned microcapillary array*, *Review of Scientific Instruments* **86** (2015), no. 2 1–5.

[32] B. Pullman, *The Atom in the History of Human Thought*. Oxford University Press, 2001.

[33] A. Einstein, *Über die von der molekularkinetischen Theorie der Wärme geforderte Bewegung von in ruhenden Flüssigkeiten suspendierten Teilchen*, *Annalen der Physik* **322** (1905), no. 8 549–560.

[34] J. Perrin, *Mouvement brownien et réalité moléculaire*, *Annales de Chimie et de Physique* **18** (1909) 5–104.

[35] J. J. Sakurai and J. Napolitano, *Modern Quantum Mechanics*. Addison-Wesley, 2011.

[36] C. Chin, A. J. Kerman, V. Vuletić, and S. Chu, *Sensitive detection of cold cesium molecules formed on Feshbach resonances*, *Physical Review Letters* **90** (2003), no. 3 4.

[37] K.-K. Ni, S. Ospelkaus, M. H. G. de Miranda, A. Pe'er, B. Neyenhuis, J. J. Zirbel, S. Kotochigova, P. S. Julienne, D. S. Jin, and J. Ye, *A high phase-space-density gas of polar molecules*, *Science* **322** (2008), no. 5899 231–235.

[38] P. D. Lett, W. D. Phillips, S. L. Rolston, C. E. Tanner, R. N. Watts, and C. I. Westbrook, *Optical molasses*, *Journal of the Optical Society of America B* **6** (1989), no. 11 2084.

[39] D. Rio Fernandes, F. Sievers, N. Kretzschmar, S. Wu, C. Salomon, and F. Chevy, *Sub-Doppler laser cooling of fermionic ^{40}K atoms in three-dimensional gray optical molasses*, *Europhysics Letters* **100** (2012), no. 6.

[40] A. T. Grier, I. Ferrier-Barbut, B. S. Rem, M. Delehaye, L. Khaykovich, F. Chevy, and C. Salomon, *Λ-enhanced sub-Doppler cooling of lithium atoms in D1 gray molasses*, *Physical Review A* **87** (2013), no. 6 1–8.

[41] G. Salomon, L. Fouché, P. Wang, A. Aspect, P. Bouyer, and T. Bourdel, *Gray-molasses cooling of ^{39}K to a high phase-space density*, *Epl* **104** (2013), no. 6.

[42] P. Hamilton, G. Kim, T. Joshi, B. Mukherjee, D. Tiarks, and H. Müller, *Sisyphus cooling of lithium*, *Physical Review A* **89** (2014), no. 2 1–5.

[43] M. Weidemüller, T. Esslinger, M. A. Ol'shanii, A. Hemmerich, and T. W. Hänsch, *A novel scheme for efficient cooling below the photon recoil limit*, *Europhysics Letters* **27** (1994), no. 2 109–114.

[44] W. Wing, *On Neutral Particle Trapping in Quasielectrostatic Electromagnetic Fields*, *Prog. Quant. Elect.* **8** (1984) 181.

[45] R. Grimm, M. Weidemller, and Y. B. Ovchinnikov, *Optical dipole traps for neutral atoms*, vol. 42 of *Advances In Atomic, Molecular, and Optical Physics*, pp. 95 – 170. Academic Press, 2000.

[46] R. Roy, A. Green, R. Bowler, and S. Gupta, *Rapid cooling to quantum degeneracy in dynamically shaped atom traps*, *Physical Review A* **93** (2016), no. 4 1–7.

[47] G. H. Wannier, *The structure of electronic excitation levels in insulating crystals*, *Physical Review* **52** (1937), no. 3 191–197.

[48] N. Marzari and D. Vanderbilt, *Maximally localized generalized Wannier functions for composite energy bands*, *Physical Review B* **56** (1997), no. 20 12847–12865.

[49] D. Jaksch, C. Bruder, J. I. Cirac, C. W. Gardiner, and P. Zoller, *Cold bosonic atoms in optical lattices*, *Physical Review Letters* **81** (1998), no. 15 3108–3111.

[50] R. Walters, G. Cotugno, T. H. Johnson, S. R. Clark, and D. Jaksch, *Ab initio derivation of Hubbard models for cold atoms in optical lattices*, *Physical Review A* **87** (2013), no. 4 1–13.

[51] Bose, *Plancks Gesetz und Lichtquantenhypothese*, *Zeitschrift für Physik* **26** (1924), no. 1 178–181.

[52] R. K. Pathria and P. D. Beale, *Statistical Mechanics*. Elsevier, 1972.

[53] C. J. Pethick and H. Smith, *Bose-Einstein Condensation in Dilute Gases*. Cambridge University Press, 2002.

[54] L. P. Pitaevskii and S. Stringari, *Bose Einstein Condensation and Superfluidity*. Oxford University Press, 2016.

[55] A. Ludwig, *The Many Body Problem in Condensed Matter Physics II*. Lecture, University of California, Santa Barbara, 2013.

[56] P. M. Duarte, *Observation of antiferromagnetic correlations in the Fermi-Hubbard model*. PhD thesis, Rice University, 2014.

[57] E. R. I. Abraham, W. I. McAlexander, C. A. Sackett, and R. G. Hulet, *Spectroscopic determination of the s-wave scattering length of lithium*, *Physical Review Letters* **74** (1995), no. 8 1315–1318.

[58] E. R. I. Abraham, W. I. McAlexander, J. M. Gerton, R. G. Hulet, R. Côté, and A. Dalgarno, *Triplet s-wave resonance in ^6Li collisions and scattering lengths of ^6Li and ^7Li*, *Physical Review A* **55** (1997), no. 5 R3299–R3302.

[59] C. C. Bradley, C. A. Sackett, and R. G. Hulet, *Bose-Einstein condensation of lithium: Observation of limited condensate number*, *Physical Review Letters* **78** (1997), no. 6 985–989.

[60] W. I. McAlexander, *Collisional Interactions in an Ultracold Lithium Gas*. PhD thesis, Rice University, 2000.

[61] K. E. Strecker, G. B. Partridge, A. G. Truscott, and R. G. Hulet, *Formation and propagation of matter-wave soliton trains*, *Nature* **417** (2002), no. 6885 150–153.

[62] S. E. Pollack, D. Dries, M. Junker, Y. P. Chen, T. A. Corcovilos, and R. G. Hulet, *Extreme tunability of interactions in a ^7Li Bose-Einstein condensate*, *Physical Review Letters* **102** (2009), no. 9 3–6.

[63] S. Stellmer, B. Pasquiou, R. Grimm, and F. Schreck, *Laser cooling to quantum degeneracy*, *Physical Review Letters* **110** (2013), no. 26 1–5.

[64] S. L. Campbell, R. B. Hutson, G. E. Marti, A. Goban, N. Darkwah Oppong, R. L. McNally, L. Sonderhouse, J. M. Robinson, W. Zhang, B. J. Bloom, and J. Ye, *A Fermi-degenerate three-dimensional optical lattice clock*, *Science* **358** (2017), no. 6359 90.

[65] S. Kolkowitz, S. L. Bromley, T. Bothwell, M. L. Wall, G. E. Marti, A. P. Koller, X. Zhang, A. M. Rey, and J. Ye, *Spin-orbit-coupled fermions in an optical lattice clock*, *Nature* **542** (2017), no. 7639 66–70.

[66] A. V. Gorshkov, M. Hermele, V. Gurarie, C. Xu, P. S. Julienne, J. Ye, P. Zoller, E. Demler, M. D. Lukin, and A. M. Rey, *Two-orbital SU(N) magnetism with ultracold alkaline-earth atoms*, *Nature Physics* **6** (2010), no. 4 289–295.

[67] A. J. Daley, J. Ye, and P. Zoller, *State-dependent lattices for quantum computing with alkaline-earth-metal atoms*, *European Physical Journal D* **65** (2011), no. 1-2 207–217.

[68] M. Yasuda and H. Katori, *Lifetime measurement of the $^3P_2$ metastable state of strontium atoms*, *Physical Review Letters* **92** (2004), no. 15 14–17.

[69] R. Santra, K. V. Christ, and C. H. Greene, *Properties of metastable alkaline-earth-metal atoms calculated using an accurate effective core potential*, *Physical Review A* **69** (2004), no. 4 1–10.

[70] Y. N. Martinez De Escobar, P. G. Mickelson, P. Pellegrini, S. B. Nagel, A. Traverso, M. Yan, R. Côté, and T. C. Killian, *Two-photon photoassociative spectroscopy of ultracold ^{88}Sr*, *Physical Review A* **78** (2008), no. 6 1–8.

[71] A. Stein, H. Knöckel, and E. Tiemann, *Fourier-transform spectroscopy of Sr_2 and revised ground-state potential*, *Physical Review A* **78** (2008), no. 4 1–9.

[72] S. Stellmer and F. Schreck, *Reservoir spectroscopy of 5s5p $^3P_2$ - 5snd $^3D_{1,2,3}$ transitions in strontium*, *Physical Review A* **90** (2014), no. 2 1–14.

[73] D. S. Barker, B. J. Reschovsky, N. C. Pisenti, and G. K. Campbell, *Enhanced magnetic trap loading for atomic strontium*, *Physical Review A* **92** (2015), no. 4 1–8.

[74] A. Keshet and W. Ketterle, *A distributed, graphical user interface based, computer control system for atomic physics experiments*, *Review of Scientific Instruments* **84** (2013), no. 1 015105.

[75] M. E. Gehm, *Preparation of an Optically-Trapped Degenerate Fermi Gas of ^6Li: Finding the Route to Degeneracy*. PhD thesis, Duke University, 2003.

[76] M. Knudsen, *Die Gesetze der Molekularströmung und der inneren Reibungsströmung der Gase durch Röhren*, *Annalen der Physik* **333** (1909), no. 1 75–130.

[77] W. Steckelmacher, *A review of the molecular flow conductance for systems of tubes and components and the measurement of pumping speed*, *Vacuum* **16** (1966), no. 11 561–584.

[78] C. A. Stan, *Experiments with Interacting Bose and Fermi Gases*. PhD thesis, Massachusetts Institute of Technology, 2005.

[79] B. P. Anderson and M. A. Kasevich, *Loading a vapor-cell magneto-optic trap using light-induced atom desorption*, *Physical Review A* **63** (2001), no. 2 1–6.

[80] S. N. Atutov, R. Calabrese, V. Guidi, B. Mai, A. G. Rudavets, E. Scansani, L. Tomassetti, V. Biancalana, A. Burchianti, C. Marinelli, E. Mariotti, L. Moi, and S. Veronesi, *Fast and efficient loading of a Rb magneto-optical trap using light-induced atomic desorption*, *Physical Review A* **67** (2003), no. 5 6.

[81] T. G. Tiecke, S. D. Gensemer, A. Ludewig, and J. T. Walraven, *High-flux two-dimensional magneto-optical-trap source for cold lithium atoms*, *Physical Review A* **80** (2009), no. 1 1–12.

[82] V. Lebedev and D. M. Weld, *Self-assembled Zeeman slower based on spherical permanent magnets*, *Journal of Physics B* **47** (2014), no. 15.

[83] D. B. Montgomery, *Solenoid Magnet Design*. Wiley-Interscience, 1969.

[84] J. D. Jackson, *Classical Electrodynamics*. Wiley-Interscience, 1998.

[85] G. De Maria and V. Piacente, *Vapor pressures of calcium and strontium by transpiration method*, *Journal of Chemical Thermodynamics* **6** (1974), no. 1 1–7.

[86] S. V. Rajagopal, K. M. Fujiwara, R. Senaratne, K. Singh, Z. A. Geiger, and D. M. Weld, *Quantum emulation of extreme non-equilibrium phenomena with trapped atoms*, *Annalen der Physik* **529** (2017), no. 8 1–10.

[87] M. Lewenstein, A. Sanpera, V. Ahufinger, B. Damski, A. Sen, and U. Sen, *Ultracold atomic gases in optical lattices: Mimicking condensed matter physics and beyond*, *Advances in Physics* **56** (2007), no. 2 243–379.

[88] I. Bloch, J. Dalibard, and S. Nascimbène, *Quantum simulations with ultracold quantum gases*, *Nature Physics* **8** (2012), no. 4 267–276.

[89] C. Gross and I. Bloch, *Quantum simulations with ultracold atoms in optical lattices*, *Science* **357** (2017), no. 6355 995–1001.

[90] F. Krausz and M. Ivanov, *Attosecond physics*, *Reviews of Modern Physics* **81** (2009), no. 1 163–234.

[91] P. B. Corkum and F. Krausz, *Attosecond science*, *Nature Physics* **3** (2007), no. 6 381–387.

[92] T. Fennel, K. H. Meiwes-Broer, J. Tiggesbäumker, P. G. Reinhard, P. M. Dinh, and E. Suraud, *Laser-driven nonlinear cluster dynamics*, *Reviews of Modern Physics* **82** (2010), no. 2 1793–1842.

[93] L. V. Keldysh, *Ionization in the field of a strong electromagnetic wave*, *Journal of Experimental and Theoretical Physics* **20** (1964), no. 5 1307–1314.

[94] F. H. M. Faisal, *Multiphoton transitions. IV. Bound-free transition integrals in compact forms*, *Journal of Physics B* **6** (1973), no. 3 553–558.

[95] H. R. Reiss, *Gauges for intense-field electrodynamics*, *Physical Review A* **22** (1980), no. 2 770–772.

[96] P. B. Corkum, *Plasma perspective on strong field multiphoton ionization*, *Physical Review Letters* **71** (1993), no. 13 1994–1997.

[97] M. Lewenstein, P. Balcou, M. Y. Ivanov, A. L'Huillier, and P. B. Corkum, *Theory of high-harmonic generation by low-frequency laser fields*, *Physical Review A* **49** (1994), no. 3 2117–2132.

[98] C. Fort, M. Prevedelli, F. Minardi, F. S. Cataliotti, L. R. G. M. Tino, and M. Inguscio, *Collective excitations of a ^{87}Rb Bose condensate in the Thomas-Fermi regime*, *Europhysics Letters* **49** (2000), no. 1 8.

[99] S. Stringari, *Collective excitations of a trapped Bose-condensed gas*, *Physical Review Letters* **77** (1996), no. 12 2360–2363.

[100] P. Öhberg, E. L. Surkov, I. Tittonen, S. Stenholm, M. Wilkens, and G. V. Shlyapnikov, *Low-energy elementary excitations of a trapped Bose-condensed gas*, *Physical Review A* **56** (1997), no. 5 R3346–R3349.

[101] A. Csordás and R. Graham, *Collective excitations in Bose-Einstein condensates in triaxially anisotropic parabolic traps*, *Physical Review A* **59** (1999), no. 2 1477–1487.

[102] B. D. Esry, *Hartree-Fock theory for Bose-Einstein condensates and the inclusion of correlation effects*, *Physical Review A* **55** (1997), no. 2 1147–1159.

[103] R. Walsworth and L. You, *Selective creation of quasiparticles in trapped Bose condensates*, *Physical Review A* **56** (1997), no. 1 555–559.

[104] N. Takei, C. Sommer, C. Genes, G. Pupillo, H. Goto, K. Koyasu, H. Chiba, M. Weidemüller, and K. Ohmori, *Direct observation of ultrafast many-body electron dynamics in an ultracold Rydberg gas*, *Nature Communications* **7** (2016).

[105] S. Stellmer, M. K. Tey, B. Huang, R. Grimm, and F. Schreck, *Bose-Einstein condensation of strontium*, *Physical Review Letters* **103** (2009), no. 20 13–16.

[106] D. R. Yarkony, *Conical intersections: The new conventional wisdom*, *Journal of Physical Chemistry A* **105** (2001), no. 26 6277–6293.

[107] D. B. Milošević, G. G. Paulus, D. Bauer, and W. Becker, *Above-threshold ionization by few-cycle pulses*, *Journal of Physics B* **39** (2006), no. 14.

[108] M. Hentschel, R. Kienberger, C. Spielmann, G. A. Reider, N. Milosevic, T. Brabec, P. Corkum, U. Heinzmann, M. Drescher, and F. Krausz, *Attosecond metrology*, *Nature* **414** (2001), no. 6863 509–513.

[109] J. Itatani, F. Quéré, G. L. Yudin, M. Y. Ivanov, F. Krausz, and P. B. Corkum, *Attosecond Streak Camera*, *Physical Review Letters* **88** (2002), no. 17 4.

[110] S. L. Chin and N. R. Isenor, *Multiphoton ionization in atomic gases with depletion of neutral atoms*, *Canadian Journal of Physics* **48** (1970) 1–3.

[111] G. Mainfray and C. Manus, *Multiphoton ionization of atoms.*, *Reports on Progress in Physics* **229** (1991) 1345–1351.

[112] A. L'Huillier, L. A. Lompre, G. Mainfray, and C. Manus, *Multiply charged ions induced by multiphoton absorption in rare gases at 0.53 μm*, *Physical Review A* **27** (1983), no. 5 2503–2512.

[113] A. Baltuška, T. Udem, M. Uiberacker, M. Hentschel, E. Goulielmakis, C. Gohle, R. Holzwarth, V. S. Yakovlev, A. Scrinzi, T. W. Hänscht, and F. Krausz, *Attosecond control of electronic processes by intense light fields*, *Nature* **421** (2003), no. 6923 611–615.

[114] L.-Y. Peng and A. F. Starace, *Attosecond pulse carrier-envelope phase effects on ionized electron momentum and energy distributions*, *Physical Review A* **76** (2007), no. 4 043401.

[115] M. F. Kling, J. Rauschenberger, A. J. Verhoef, E. Hasović, T. Uphues, D. B. Milošević, H. G. Muller, and M. J. Vrakking, *Imaging of carrier-envelope phase effects in above-threshold ionization with intense few-cycle laser fields*, *New Journal of Physics* **10** (2008).

[116] M. Krüger, M. Schenk, P. Hommelhoff, and M. Kruger, *Attosecond control of electrons emitted from a nanoscale metal tip*, *Nature* **475** (2011), no. 7354 78–81.

[117] M. F. Kling, A. J. Verhoef, J. I. Khan, M. Schultze, Y. Ni, M. Uiberacker, M. Drescher, F. Krausz, and M. J. J. Vrakking, *Control of Electron Localization in*, *Science* **312** (2006), no. April 12–15.

[118] T. Rathje, A. M. Sayler, S. Zeng, P. Wustelt, H. Figger, B. D. Esry, and G. G. Paulus, *Coherent control at its most fundamental: Carrier-envelope-phase-dependent electron localization in photodissociation of a H^{2+} molecular ion beam target*, *Physical Review Letters* **111** (2013), no. 9 1–5.

[119] J. M. Ngoko Djiokap, S. X. Hu, L. B. Madsen, N. L. Manakov, A. V. Meremianin, and A. F. Starace, *Electron vortices in photoionization by circularly polarized attosecond pulses*, *Physical Review Letters* **115** (2015), no. 11 1–5.

[120] M. Pont and M. Gavrila, *Stabilization of atomic hydrogen in superintense, high-frequency laser fields of circular polarization*, *Physical Review Letters* **65** (nov, 1990) 2362–2365.

[121] D. Shafir, H. Soifer, B. D. Bruner, M. Dagan, Y. Mairesse, S. Patchkovskii, M. Y. Ivanov, O. Smirnova, and N. Dudovich, *Resolving the time when an electron exits a tunnelling barrier*, *Nature* **485** (2012), no. 7398 343–346.

[122] A. N. Pfeiffer, C. Cirelli, M. Smolarski, D. Dimitrovski, M. Abu-Samha, L. B. Madsen, and U. Keller, *Attoclock reveals natural coordinates of the laser-induced tunnelling current flow in atoms*, *Nature Physics* **8** (2012), no. 1 76–80.

[123] M. Uiberacker, T. Uphues, M. Schultze, A. J. Verhoef, V. Yakovlev, M. F. Kling, J. Rauschenberger, N. M. Kabachnik, H. Schröder, M. Lezius, K. L. Kompa, H. G. Muller, M. J. Vrakking, S. Hendel, U. Kleineberg, U. Heinzmann, M. Drescher, and F. Krausz, *Attosecond real-time observation of electron tunnelling in atoms*, *Nature* **446** (2007), no. 7136 627–632.

[124] M. Isinger, R. J. Squibb, D. Busto, S. Zhong, A. Harth, D. Kroon, S. Nandi, C. L. Arnold, M. Miranda, J. M. Dahlström, E. Lindroth, R. Feifel, M. Gisselbrecht, and A. L'Huillier, *Photoionization in the time and frequency domain*, .

[125] F. Serwane, G. Zürn, T. Lompe, T. B. Ottenstein, A. N. Wenz, and S. Jochim, *Deterministic preparation of a tunable few-fermion system*, *Science* **332** (2011), no. 6027 336–338.

[126] N. T. Zinner and A. S. Jensen, *Comparing and contrasting nuclei and cold atomic gases*, *Journal of Physics G* **40** (2013), no. 5.

[127] D. Shechtman, I. Blech, D. Gratias, and J. W. Cahn, *Metallic phase with long-range orientational order and no translational symmetry*, *Physical Review Letters* **53** (1984), no. 20 1951–1953.

[128] K. Viebahn, M. Sbroscia, E. Carter, and U. Schneider, *Experimental realisation of a two-dimensional optical quasicrystal for ultracold atoms*. 49th Annual Meeting of the APS Division of Atomic, Molecular and Optical Physics Meeting, 2018.

[129] K. Singh, K. Saha, S. A. Parameswaran, and D. M. Weld, *Fibonacci optical lattices for tunable quantum quasicrystals*, *Physical Review A* **92** (2015), no. 6 1–8.

[130] A. Kastberg, W. D. Phillips, S. L. Rolston, R. J. Spreeuw, and P. S. Jessen, *Adiabatic cooling of cesium to 700 nK in an optical lattice*, *Physical Review Letters* **74** (1995), no. 9 1542–1545.

[131] Y. E. Kraus, Y. Lahini, Z. Ringel, M. Verbin, and O. Zilberberg, *Topological states and adiabatic pumping in quasicrystals*, *Physical Review Letters* **109** (2012), no. 10 1–5.

[132] M. Lohse, C. Schweizer, O. Zilberberg, M. Aidelsburger, and I. Bloch, *A Thouless quantum pump with ultracold bosonic atoms in an optical superlattice*, *Nature Physics* **12** (2016), no. 4 350–354.

[133] W. S. Bakr, J. I. Gillen, A. Peng, S. Fölling, and M. Greiner, *A quantum gas microscope for detecting single atoms in a Hubbard-regime optical lattice*, *Nature* **462** (2009), no. 7269 74–77.

[134] J. F. Sherson, C. Weitenberg, M. Endres, M. Cheneau, I. Bloch, and S. Kuhr, *Single-atom-resolved fluorescence imaging of an atomic Mott insulator*, *Nature* **467** (2010), no. 7311 68–72.

[135] A. Kitaev, *Unpaired Majorana fermions in quantum wires*, .

[136] N. F. Ramsey, *Molecular Beams*. Oxford University Press, Oxford, 1956.

[137] K. J. Ross and B. Sonntag, *High temperature metal atom beam sources*, *Review of Scientific Instruments* **66** (1995), no. 9 4409–4433.

[138] J. G. King and J. R. Zacharias, *Some new applications and techniques of molecular beams*, *Adv. Electron. Electron Phys.* **8** (1956) 1–88.

[139] J. P. Gordon, H. J. Zeiger, and C. H. Townes, *The maser – new type of microwave amplifier, frequency standard, and spectrometer*, *Physical Review* **99** (1955), no. 4 1264–1274.

[140] J. A. Giordmaine and T. C. Wang, *Molecular beam formation by long parallel tubes*, *Journal of Applied Physics* **31** (1960), no. 3 463–471.

[141] J. C. Helmer, F. B. Jacobus, and P. A. Sturrock, *Focusing molecular beams of NH_3*, *Journal of Applied Physics* **31** (1960), no. 3 458–463.

[142] J. C. Johnson, A. T. Stair, and J. L. Pritchard, *Molecular beams formed by arrays of 3-40 μ diameter tubes*, *Journal of Applied Physics* **37** (1966), no. 4 1551–1558.

[143] M. Schioppo, N. Poli, M. Prevedelli, S. Falke, C. Lisdat, U. Sterr, and G. M. Tino, *A compact and efficient strontium oven for laser-cooling experiments*, *Review of Scientific Instruments* **83** (2012), no. 10.

[144] M. Lambropoulos and S. E. Moody, *Design of a three-stage alkali beam source*, *Review of Scientific Instruments* **48** (1977), no. 2 131–134.

[145] R. D. Swenumson and U. Even, *Continuous flow reflux oven as the source of an effusive molecular Cs beam*, *Review of Scientific Instruments* **52** (1981), no. 4 559–561.

[146] R. Drullinger, D. Glaze, and D. Sullivan, *A recirculating oven for atomic beam frequency standards*, *39th Annual Symposium on Frequency Control* (1985) 13–17.

[147] L. V. Hau, J. A. Golovchenko, and M. M. Burns, *A new atomic beam source: The "candlestick"*, *Review of Scientific Instruments* **65** (1994), no. 12 3746–3750.

[148] M. R. Walkiewicz, P. J. Fox, and R. E. Scholten, *Candlestick rubidium beam source*, *Review of Scientific Instruments* **71** (2000), no. 9 3342–3344.

[149] C. Slowe, L. Vernac, and L. V. Hau, *High flux source of cold rubidium atoms*, *Review of Scientific Instruments* **76** (2005), no. 10 1–10.

[150] A. Pailloux, T. Alpettaz, and E. Lizon, *Candlestick oven with a silica wick provides an intense collimated cesium atomic beam*, *Review of Scientific Instruments* **78** (2007), no. 2 023102.

[151] M. A. Joffe, W. Ketterle, A. Martin, and D. E. Pritchard, *Transverse cooling and deflection of an atomic beam inside a Zeeman slower*, *Journal of the Optical Society of America B* **10** (1993), no. 12 2257.